Measurements of the Electric Form Factor of the Neutron at $Q^2 = 1.7$ and 3.5 GeV^2

by

Seamus Patrick Riordan

A dissertation submitted in partial fulfillment of the requirements
for the degree of

Doctor of Philosophy

in the Department of Physics

Carnegie Mellon University

May 2008

Abstract

A measurement of the electric form factor of the neutron, G_E^n, was performed at $Q^2 = 1.3, 1.7, 2.4$, and 3.5 GeV^2 at Thomas Jefferson National Accelerator facility. This was done using a double polarization technique by measuring the helicity dependent quasielastic cross section asymmetry from the semi-inclusive reaction $^3\vec{\mathrm{He}}(\vec{e}, e'n)pp$. This asymmetry can then be directly related to the ratio of the electric and magnetic form factors of the neutron.In this analysis we present results for two of the measurements performed in this experiment, $Q^2 = 1.7$ and 3.5 GeV^2, which represent the first points analyzed for this experiment. The 3.5 GeV^2 point is of particular interest due to the lack of previous precision data above 2.0 GeV^2. We find the value for our lower momentum transfer point, $Q^2 = 1.7$ GeV^2, $G_E^n = 0.0342 \pm_{\mathrm{stat}} 0.0023 \pm_{\mathrm{sys}} 0.0040$, consistent with existing world data and our highest point, $Q^2 = 3.5$ GeV^2, $G_E^n = 0.0117 \pm_{\mathrm{stat}} 0.0030 \pm_{\mathrm{sys}} 0.0010$, consistent with the Galster parametrization.

Acknowledgments

This work wouldn't have been possible without the contributions from many people within and outside of physics. I feel that I've been exceptionally blessed with a large number of people who have supported me throughout the years as a person and as a scientist. Out of all the pages in this work, I think this has probably been the most difficult for me to write as I don't want to forget anyone. If I have, it is my hope that they already know my gratitude beyond what's written down here.

As I reflect on the path that I have taken, it's somewhat horrifying to realize without some of the seemingly small contributions from everyone, I wouldn't have reached this point today. For those I am extremely grateful. It was through many people that allowed me to complete this work, which of course is more than a summary and the results of an experiment, but also represents a completion of this phase of my life.

First and foremost I must thank my parents. I wouldn't be anywhere without them and they've contributed in so many ways I couldn't even begin to enumerate them. I especially thank my father for his sense of professionalism and duty that he's given me. I thank my mother for her hard work ethic and do-it-yourself attitude which has served me well as a scientist. I thank them for their trust and endless support throughout the years. Their unwavering belief that I could accomplish whatever I set out to do has been a solid foundation for my self-esteem. I also thank them for their financial support whenever I needed it. It relieved so many stressful periods I can't begin to count.

I thank my grandmothers for their support and love over the years. My paternal grandmother recognized a young scientist and went to special lengths to help nurture that side of me. The trips to the Des Moines Science Center and the Drake Observatory were some of my important first exposures to science and were greatly enjoyed. I also thank her for the endless supply of books over my fields of interest when I was young. They were my first textbooks and gave an immeasurable head start. My maternal grandmother provided me with my first computer which proved to start an early programmer on a successful career path. I can't thank her enough for that gift as it provided many fundamental skills I needed to succeed.

The Meade family has been a strong part of my life since I was very small, but I give special thanks to Becky Meade for starting my high school career at Central Academy and getting me to enroll there. Had I not attended, I'm convinced I would not have considered a scientific career. I thank my good friend Sean Wright, whose natural scientific curiosity inspired me to start studying physics well before I took any dedicated classes over the subject. Working with him academically was a great pleasure and has been missed. My time at Central was filled with an exceptional group of teachers, but I especially thank Scott Schoneberg and Linda Kuiken for their guidance, help, and support. They allowed me to pursue part of my education on my own and I am very grateful for their providing that freedom.

I thank all the faculty and staff in the physics department at Drake University while I was there. They provided me with my first rigorous physics education. I thank them for awarding me the Drake Physics Prize which paid for my undergraduate education, removing a huge practical burden from me. I'd like to thank all the professors there for their interesting and useful lectures. I thank Larry Staunton for the advice on learning, paraphrased "I won't understand something until I sit down

and really think about it on my own for a while," which has been particularly useful. I thank Klaus Bartschat for working with me and giving me my first research opportunities. I must especially thank Athanasios Petridis for his enthusiasm for teaching and working with students. His support for my independent projects as a student and continued support for my career in general has been greatly appreciated and helpful. His attitude and hard work in these matters has served as a guide and model for me. I also thank Morris Mason; my first interactions with him were at the Des Moines Science Center when I was small, and his presentations and demonstrations were memorable and interesting.

I thank all the faculty in the mathematics and computer science department at Drake University. Those two subjects both hold special places in my life and I sincerely enjoyed my time studying there. I must especially thank Ken Kopecky for his support of my projects and career there as a student. His guidance and enthusiasm inspired me to do work and research outside of my standard classes and his trust allowed me to carry out some ambitious work. I can't thank him enough for giving me those opportunities and support.

I made a number of friendships with my fellow students which helped me through my time there. It's impossible to put together an exhaustive list, but I especially thank Patty Graziano, Greg Ver Steeg, Aaron Plasek, Warren Baltz, Andrew Thompson, Oliver Couture, Angie Sowell, Allison Harris, and Sarah Ragan for their friendship and support at various times during my life.

At Carnegie Mellon University I solely dedicated myself to the study of physics and found my way as a scientist. I thank the entire physics department for giving me this opportunity and providing me with the academic and financial support I needed while I was a graduate student there. I especially thank the medium energy experiment group for engaging me to work with them. I thank Curtis Meyer, Brian Quinn, and Reinhard Schumaker for their patience and support. With them and Kent Paschke, I thank them for serving on my thesis committee, reading this document, and providing their useful feedback and criticisms.

I am incredibly indebted to my advisor, Gregg Franklin, without whom none of this would have been possible. His dedication to his students is remarkable and I am deeply appreciative of it. His open-door policy and willingness to answer questions was invaluable to me for completing my work. I genuinely find his willingness to work with students and the endless patience he has for them to be incredibly admirable and I believe them to be the most important qualities to have as an advisor.

I genuinely don't think I could have completed my work here without the help and friendship from my fellow graduate students. I'd like to thank my first office-mates Gavin Mendel-Gleason, Chang-Yu Hou, Jimmy Hutasoit, and Rafael Porto for their useful discussions and getting through homework together. I'd like to thank all of my fellow graduate students and post docs at CMU, as well as their spouses and girlfriends, for their support and friendship while I was there, especially Ryan and Kim Dickson, Julie Gardner, Mike Williams, Zeb and Krista Krahn, Matt Bellis and Heather Watson, Yves Van Haarlem, Fatiha Benmokthar, Mike and April McCracken, Diana and Brian Parno, Kei Moriya, Brian Vernarsky, Adam Lichtl, Bob Bradford, Kevin and Laura Bandura, Biplab Dey, and Joe Parker. I'd also like to thank Gary Wilkin and Hilary Homer for their friendship and help, as well as the company on smoke breaks.

While I was here I was given the opportunity to work with and learn from many of the professors here. I have a great appreciation for Roy Briere, who I was lucky enough to have for my outstanding nuclear and particle course. I must thank Bob Swendsen for taking some of his spare time over the course of a semester to help me understand thermodynamics on a graduate level. His volunteered help and patience was above and beyond his responsibilities and were greatly appreciated. I'd also like to thank Leonard Kisslinger for providing me with some smaller research opportunities on the theory side of medium energy physics, which was an interesting learning experience. Also, thanks to Helmut Vogel for his guidance and patience while I was a teaching assistant for him.

In 2004 I first went to Jefferson Lab in Newport News to start my work on the G_E^n experiment which would be the subject of my thesis. I'd like to thank the spokespeople I worked with, Bogdan Wojtsekhowski, Bodo Reitz, Nilanga Liyanage, and Gordon Cates, for designing, coordinating, and

running this experiment. Without their hard work and attention to detail I would have not had this excellent experiment to work on. I'd also like to thank them for giving me their trust to perform and complete this analysis and their patience with the mistakes I've made. I'd also like to thank Rob Feuerbach for his invaluable help during and after the experiment and for getting the analysis off the ground. Things would not have gone nearly as smoothly without him and he's saved us at least months of analysis time. I'd also like to thank everyone involved for their feedback and criticism while I was working with them. It has been invaluable and has helped me grow to be a better scientist.

I'd like to thank my fellow G_E^n graduate students Aidan Kelleher, Brandon Craver, Jon Miller, Ameya Kolarkar, and Sergey Abrahamyan for their hard work and friendship during this experiment. Things could not have been done without their labor and frequent late nights.

Finally, I'd like to thank the many people in my personal life who have been with me to this point. I couldn't begin to name everyone, but I'd like to give special thanks to my sisters Anne, Caitlain, and Ellie. Thanks to my aunts and uncles, Buff, Kevin, Dennis, Brian, Kathy, Co, Terry, Chuck, and Phyllis, and my great aunt and uncle Rosalie and Charlie Dunham. I'd like to thank Ben Oleson, Maren Braaksma, Brian Kirkman, Michelle Evans, and Tanner Strutzenberg for their continuous and valuable friendship. I thank the Cote family for welcoming me and letting me steal their daughter away to the other side of the country.

Last, I thank my beautiful girlfriend, Lyn, who probably experiences and endures the worst side of all of this. She puts up with me when my focus is on my work. She lives alone when I leave town. She has to live with all my aggravations, fears, and doubts. For this patience and love, I am eternally grateful, even if I don't always show it.

Contents

Chapter 1

Introduction

Particle physics represents the field of study which attempts to mathematically model the fundamental constituents and interactions of matter. These attempts date as far back as ancient Greece where it was hypothesized that matter was made up of indivisible units, which represents an early picture of the atom. By the end of the 19th century, a periodic table of over 100 elements had been developed classifying these basic building blocks of matter. In the late 19th and early 20th century, it was discovered that atoms themselves have structure.

The modern model of the atom began with Ernest Rutherford in the early 20th century, whose famous experiments showed that the atom was comprised of a dense, charged core surrounded by an electron cloud. Rutherford determined that this core, or nucleus, itself is comprised of smaller particles. Protons (hydrogen nuclei) were identified to be a fundamental component, as hydrogen is the lightest of all atomic nuclei and nuclear masses appear in near integer multiples of the proton mass. The neutron was discovered in 1932 by James Chadwick as another component, which earned him the 1935 Nobel Prize in physics. This discovery confirmed the existence of a particle close to the mass of the proton, but without charge, needed to reconcile the mass and the charge of the nuclei.

However, the nucleons themselves are found to have structure, as the measurements of their magnetic moments suggested. It was found that the proton and neutron had magnetic moments, μ, different from the prediction for point-like spin 1/2 particles

$$\mu = g\left(\frac{e}{2m}\right)\frac{\hbar}{2} \tag{1.1}$$

where g is the g-factor, close to 2 for a spin 1/2 point particle and predicted by quantum electrodynamics, e is the particle's charge, m is the mass of the particle, and $\hbar$ is Planck's constant divided by 2π. The proton was found to have a value of $\mu_p = 2.79$ and the neutron, $\mu_n = -1.91$, (in the units of nuclear magnetons, $\mu_N = \frac{e\hbar}{2M_p}$). These were different from the predicted values of 1 and 0, respectively, indicating that the nucleons are not point particles. Further evidence mounted from the elastic scattering cross section from protons, which was not in agreement with theoretical expectations for a point particle, which earned Hofstadter the Nobel prize in 1965.

The idea of describing the structure of hadrons in terms of point-like particles, called quarks, was first layed out by Gell-Mann in 1964 motivated by the organization of quantized values of properties such as isospin and strangeness. Reinforcement of the idea of point-like constituents was found in observations of scaling predicted in deep inelastic scattering hypothesized by Bjorken. Here, the idea of smaller constituents, called partons, each carrying some fraction of the momentum of a particle in the infinite momentum frame would produce a predictable behavior of the cross sections in deep inelastic scattering. Combined with the idea of asymptotic freedom by Gross, Wilczek, and Politzer, the connection of quarks and partons was made. As the momentum transfer from an electron to the quark becomes sufficiently high, the quark behaves as if it was a free particle, producing the scaling

behavior.

Today we have a theory of the strong nuclear force, the force which binds the protons and neutrons together in the nucleus as well as governs interactions between quarks, called quantum chromodynamics (or QCD). In this model, an intermediate boson called the gluon is the force carrier, analogous to the photon in quantum electrodynamics (QED). Each quark is assigned a quantum number called 'color', red, green, or blue. Through the idea of confinement, a composite system of quarks (called a hadron) must be a colorless object, either through the combination of all three colors (i.e. baryons) or through a color and its anti-color (i.e. mesons). Attempts to separate a quark from the system and create a new system with color requires an energy that is greater than a quark mass (Table 1.1) which is sufficient to produce additional quarks and subsequently colorless hadrons. To date, no isolated quark has been found.

The idea of color was motivated by the existence of hadronic states composed of three identical quarks. By the Pauli exclusion principle, such a state could not contain three identical fermions, so an additional quantum number had to be generated. Perhaps the strongest evidence of only three color states comes from the measured ratio of the high momentum-transfer electromagnetic production cross sections of $e^+e^- \rightarrow$ hadrons and $e^+e^- \rightarrow \mu^+\mu^-$

$$\frac{\sigma(e^+e^- \rightarrow \text{hadrons})}{\sigma(e^+e^- \rightarrow \mu^+\mu^-)} = \frac{\sum_f \sigma(e^+e^- \rightarrow q_f\bar{q}_f)}{\sigma(e^+e^- \rightarrow \mu^+\mu^-)} = 3\sum_f z_f^2 \tag{1.2}$$

where f is the flavor of a quark and z_f is the charge of a quark of flavor f. The strength of the electromagnetic interaction of each of these production channels is identical except for the charge of the product. The factor of 3 arises from the degeneracy of each flavor of quark from the three values of color.

QCD, when formulated in a perturbative fashion, has some significant differences from QED. Perhaps the most significant difference is the strength of the coupling for the two forces. For QED, the strength of the coupling is defined by the hyperfine coupling constant, $\alpha \approx 1/137$. Because this constant is much less than unity, one can successfully expand the QED Lagrangian in powers of α to perform tractable calculations of electromagnetic interactions. This has proven to be wildly successful in describing electromagnetic interactions, such as the successful calculation of various differential cross sections and the anomalous magnetic moment of the electron (the difference of the Landé g-factor from the leading order value of 2).

QCD, on the other had, suffers from a large coupling constant, α_s, (at least at lower energies) which prevents the calculation of strong interactions characterized by energies smaller than several GeV in terms of a series expansion in α_s. This prevents the calculation of the masses of the lighter hadrons, such as the proton and neutron and proves to be one of the most difficult outstanding problems of physics. At higher momentum transfer due to the running of the coupling constant and asymptotic freedom, α_s becomes smaller allowing for the successful treatment using perturbative QCD (pQCD).

Six types (or flavors) of quarks have been identified and can be found in Table 1.1. The lightest quarks, up (u) and down (d), comprise the two nucleons, the proton and neutron, which can be modeled as being made up of three quarks in the combinations uud and udd. It is important to note that these are not the only particles found in the nucleon and it is more appropriate to refer to them as 'valence quarks'.

Due to the large coupling constant of QCD and the non-Abelian nature of the gluon fields, QCD interactions are much more complicated than those of QED. The gluons exchanged by the quarks will frequently split into quark-antiquark pairs, especially for lower energy gluons. These virtual quark pairs, generally referred to as 'sea quarks', may also interact. Gluons, unlike their QED counterparts, also carry color and may interact with each other. It has been shown that some properties of the nucleon, such as the total nucleon spin, are products more of these interaction by-products than from the valence quarks themselves [1].

		Up	Down	Charm	Strange	Top	Bottom
		u	d	c	s	t	b
Charge		2/3	-1/3	2/3	-1/3	2/3	-1/3
Spin		1/2	1/2	1/2	1/2	1/2	1/2
Isospin	I_z	1/2	-1/2	0	0	0	0
Strangeness	S	0	0	0	-1	0	0
Est. Current-quark Mass		1.5 - 3 MeV	3 - 7 MeV	1.25 GeV	70 - 120 MeV	170 GeV	4.5 GeV

Table 1.1: Properties of quarks.

The structure of the nucleon is therefore very complicated and also difficult to predict from first principles. One of the simplest experimental tests of structure can be done using an electron as a probe. As QED is well understood, tests of the charge and magnetic moment distributions can be done experimentally. The downside to using such a probe is that it is insensitive to a portion of the structure, that of the gluons, because the electron does not interact strongly. However, a great deal of information can be obtained using such a method. We wish to produce a mathematical description of these distributions which can then be obtained from the data.

1.1 Quantum Electrodynamics and Scattering Theory

Quantum electrodynamics provides a relativistic quantum field theory of electromagnetic interactions. One of its most powerful features is the fact that the interactions may be expanded in a perturbative series in terms of the coupling constant, α. This allows practical calculations to be done to an arbitrary degree of accuracy and also gives a very powerful method to describe the processes in terms of Feynman diagrams. It has been very successful in describing observable phenomena and provides a useful tool with which to study other interactions.

While a fully rigorous treatment of this subject is far beyond the scope of this work, we will cover some useful results relevant to our analysis. In particular we will closely follow the description presented by Halzen and Martin [2]. We are mainly interested in the scattering of a point-like spin 1/2 charged particle from an arbitrary target. For such a particle in the absence of any other interaction, the wavefunction is governed by the Dirac equation

$$(i\gamma^\mu \partial_\mu - m)\psi = 0 \tag{1.3}$$

where m is the mass of the particle, ψ is the four component Dirac wavefunction, μ runs from 0..3, and γ^μ are a set of 4×4 matrices which satisfy the relations

$$\gamma^\mu \gamma^\nu + \gamma^\nu \gamma^\mu = 2g^{\mu\nu} \tag{1.4}$$

where $g^{\mu\nu}$ is the metric tensor for Minkowski space. While the choice is not unique, the four matrices may be written

$$\gamma^0 = \begin{pmatrix} I & 0 \\ 0 & -I \end{pmatrix} \tag{1.5}$$

$$\vec{\gamma} = \begin{pmatrix} 0 & \vec{\sigma} \\ -\vec{\sigma} & 0 \end{pmatrix} \tag{1.6}$$

where the components of $\vec{\sigma}$ are the Pauli matrices. Using this equation, a charge-current density, j^μ, can be associated with ψ with

$$j^\mu = -e\bar{\psi}\gamma^\mu\psi \tag{1.7}$$

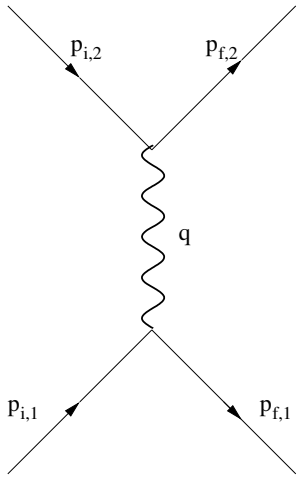

Figure 1.1: Two body scattering diagram.

where

$$\bar{\psi} \equiv \psi^\dagger \gamma^0. \tag{1.8}$$

To describe an interaction, we represent the free wavefunction for a particle of four momentum p as

$$\psi = u(p) e^{-ip\cdot x} \tag{1.9}$$

where u is the four component spinor. Inserting in the Dirac equation, Eq. 1.3, the derivative is associated with the momentum

$$(\gamma^\mu p^\mu - m)\psi = 0. \tag{1.10}$$

For an electron in an electromagnetic field, represented by the 4 potential A^μ, we perform a transformation

$$p^\mu \to p^\mu + eA^\mu \tag{1.11}$$

which then gives us the equations of motion for a particle in a potential. To first order, the transition amplitude of a particle from initial state i to final state f is

$$T_{fi} = ie \int \bar{\psi}_f \gamma_\mu A^\mu \psi_i d^4x = -e \int j_\mu^{fi} A^\mu d^4x \tag{1.12}$$

where we have defined the transition current, j_μ^{fi}. For our purposes we're interested in the scattering of one particle from another, and not a fixed potential, as shown in Fig. 1.1. For simplicity we will assume that they are both spin 1/2. In this case, the four potential, A^μ, associated from a charge-current distribution, j^μ, can be related through Maxwell's equations

$$\Box^2 A^\mu = j^\mu \tag{1.13}$$

For $j_\mu^{fi} = \bar{u}_f \gamma_\mu u_i e^{i(p_f - p_i)\cdot x}$, it is easy to check that the solution for A^μ is

$$A^\mu = -\frac{j_\mu^{fi}}{(p_i - p_f)^2} = -\frac{j_\mu^{fi}}{q^2} \tag{1.14}$$

where we have defined the four momentum transfer $q = p_i - p_f$. Using this formalism, the transition amplitude for scattering between two currents j_1^μ and j_2^μ is

$$T_{fi} = -i \int j_1^\mu \frac{1}{q^2} j_{\mu 2} d^4x = -ie^2 \int \bar{\psi}_{f,1} \gamma_\mu \psi_{i,1} \frac{1}{q^2} \bar{\psi}_{f,2} \gamma^\mu \psi_{i,2} d^4x. \tag{1.15}$$

This transition amplitude can then be related to a differential cross section which contains the information about our scattering probability into particular final states. The transition rate per unit volume, W_{fi}, is

$$W_{fi} = \frac{|T_{fi}|^2}{TV} \tag{1.16}$$

where T is the time interval for the interaction and V is the interaction volume. The differential cross section, $d\sigma$, is then

$$d\sigma = \frac{W_{fi}}{\Phi} dQ \tag{1.17}$$

where dQ is the Lorentz invariant phase space, Φ is the initial flux of particles. The results for many processes, at least to leading order, are quite well known, so we will avoid repeating the calculations here. For the scattering of two (distinguishable) spin 1/2 point particles in the lab frame, the differential cross section (including target recoil) is

$$\frac{d\sigma}{d\Omega} = \left.\frac{d\sigma}{d\Omega}\right|_{\text{Mott}} \frac{E'}{E}\left(1 - \frac{q^2}{2M^2}\tan^2\frac{\theta}{2}\right) \tag{1.18}$$

where the Mott cross section which describes scattering of an electron from a structureless, spinless target

$$\left.\frac{d\sigma}{d\Omega}\right|_{\text{Mott}} = \frac{\alpha^2\cos^2\frac{\theta}{2}}{4E^2\sin^4\frac{\theta}{2}} \tag{1.19}$$

and θ is the scattering angle of the electron, M is the mass of the target, E is the initial energy of the electron, and E' is the final energy of the electron.

1.2 Particles with Structure

We now have a start on modeling the scattering of an electron from a target. This model must be extended to include targets with arbitrary structure so that we may parametrize the cross section of the nucleons. We start with Eq. 1.15, which describes the transition amplitude for two interacting currents

$$T_{fi} = -i\int j^\mu \frac{1}{q^2} J_\mu d^4x. \tag{1.20}$$

We will take j^μ to be the current for our electron and J_μ to be the current for our nucleon. We are interested in the most general form for J_μ, which is a Lorentz 4-vector, so we must come up with an exhaustive list of linearly independent 4-vector quantities which can describe the interaction. We have already seen γ^μ, p^μ, and p'^μ, but combinations with the contracted quantities $p^\mu\gamma_\mu p^\nu$, etc. must also be considered. All possible 4×4 matrices can be constructed from the 16 linearly independent matrices

$$\mathbb{I}, \gamma^\mu, \gamma^5, \sigma^{\mu\nu}, \gamma^\mu\gamma^5 \tag{1.21}$$

where we have introduced two new objects

$$\gamma^5 = i\gamma^0\gamma^1\gamma^2\gamma^3 \tag{1.22}$$

$$\sigma^{\mu\nu} = \frac{i}{2}\left(\gamma^\mu\gamma^\nu - \gamma^\nu\gamma^\mu\right). \tag{1.23}$$

γ^5 has the property of anticommuting with the parity operator and is therefore a pseudoscalar. The only remaining available 4-vectors are the incoming momentum, p, and the outgoing momentum, p'. We can quickly eliminate terms involving γ^5, as the electromagnetic interaction conserves parity. Any coefficients must be functions of Lorentz scalars, however q^2 is the only independent scalar

(scalars involving combinations with p and p' can be reduced in terms of m and q). Taking these into account, the most general form for the hadronic current, J^ν, is

$$\begin{aligned} J^\nu &= e\bar{u}(p')\big[K_1(q^2)\gamma^\nu + (p^\nu + p'^\nu)K_2(q^2) + (p^\nu - p'^\nu)K_3(q^2) \\ &\quad + i\sigma^{\nu\mu}(p_\mu - p'_\mu)K_4(q^2) + i\sigma^{\nu\mu}(p_\mu + p'_\mu)K_5(q^2)\big]u(p)e^{i(p-p')\cdot x}. \end{aligned} \tag{1.24}$$

From the Gordon decomposition identity, we can equate

$$\bar{u}\gamma^\mu u = \frac{1}{2M}\bar{u}\left(p^\mu + p'^\mu + i\sigma^{\mu\nu}\left(p'_\nu - p_\nu\right)\right)u \tag{1.25}$$

so any $(p+p')^\mu$ terms can be put into other terms. Enforcing current conservation, $\partial_\mu J^\mu = 0$ (or $q_\mu J^\mu = 0$ in our case), any terms which do not vanish for an arbitrary K must have $K = 0$. For the K_1 term,

$$\gamma^\mu q_\mu = \gamma^\mu(p^\mu - p'^\mu) = (m - m) = 0 \tag{1.26}$$

where we have utilized the Dirac equation, Eq. 1.3. For the K_4 term, because the tensor $\sigma^{\mu\nu}$ is antisymmetric (Eq. 1.23)

$$q_\mu\sigma^{\mu\nu}q_\nu = -q_\mu\sigma^{\nu\mu}q_\nu = 0. \tag{1.27}$$

The K_3 term does not vanish, as we have q^2K_3, so to have current conservation for J^ν there can be no $(p^\nu - p'^\nu)$ term. Rewriting the remaining K functions in different terms, this leaves

$$J^\nu = e\bar{u}(p')\big[F_1(q^2)\gamma^\nu + \frac{\kappa}{2M}q_\mu\sigma^{\nu\mu}F_2(q^2)\big] \tag{1.28}$$

where κ is the anomalous magnetic moment of the target. There are two independent functions of q^2 which parametrize the structure of our nucleon, F_1 and F_2, also called the Dirac and Pauli form factors, respectively. The differential cross section for electron nucleon scattering can then be written

$$\frac{d\sigma}{d\Omega} = \frac{\alpha^2}{4E^2\sin^4\frac{\theta}{2}}\frac{E'}{E}\left[\left(F_1^2 - \frac{\kappa^2q^2}{4M^2}F_2^2\right)\cos^2\frac{\theta}{2} - \frac{q^2}{2M^2}\left(F_1 + \kappa F_2\right)^2\sin^2\frac{\theta}{2}\right]. \tag{1.29}$$

This is also known as the Rosenbluth formula. In the limit of $q^2 \to 0$ we are not sensitive to the structure of the nucleon and only see a particle having the total charge and having magnetic moment expected for that particle plus κ. This puts the limiting values on F_1 and F_2 for the proton and neutron

$$F_1^p(0) = 1, \qquad F_2^p(0) = 1 \tag{1.30}$$

$$F_1^n(0) = 0, \qquad F_2^n(0) = 1. \tag{1.31}$$

In the case of $\kappa = 0$ and unit charge, we recover Eq. 1.18 as expected.

Eq. 1.29 parametrizes our observations of the differential cross section for a general spin 1/2 particle with structure. In Chapter 2 we will provide interpretations of the form factors in terms of the electric charge and magnetic moment distribution. Modeling and measurements of these form factors will be discussed. In Chapter 3, a discussion of experiment E02-013 will be given and the experimental technique and setup used will be presented. In Chapter 4, results from the calibrations of our newly constructed detector set for that experiment will be presented. In Chapters 5 and 6 methods for analysis and results for two of four kinematic points will be given.

Chapter 2

Electromagnetic Form Factors and G_E^n

In the last chapter we discussed how to parametrize electron scattering off a general spin-1/2 particle with structure. We arrived at Eq. 1.29 which contained two independent functions, the Dirac and Pauli form factors, for four-momentum transfer, q^2. In this chapter we will discuss how these form factors are related to the electric charge and magnetic moment distributions in the nucleon, examine techniques that the electric form factor of the neutron is measured, and compare previous measurements of this form factor to theoretical predictions and fits.

2.1 Sachs Form Factors

Sachs first suggested rewriting the form factors in two linear combinations such that they were related to the electric charge and current distributions inside the nucleon [3]. Hand, Miller, and Wilson showed that two functions, G_E and G_M, could be related to the Fourier transforms of the charge and magnetic moment distributions [4]. These functions are also known as the electric and magnetic form factors

$$G_E = F_1 + \frac{\kappa q^2}{4M^2} F_2 \tag{2.1}$$

$$G_M = F_1 + \kappa F_2. \tag{2.2}$$

Rewriting Eq. 1.29, this gives the differential cross section

$$\frac{d\sigma}{d\Omega} = \left.\frac{d\sigma}{d\Omega}\right|_{\text{Mott}} \frac{E'}{E}\left(\frac{G_E^2 + \tau G_M^2}{1+\tau} + 2\tau G_M^2 \tan^2\frac{\theta}{2}\right) = \frac{\alpha^2 \cos^2\frac{\theta}{2}}{4E^2 \sin^4\frac{\theta}{2}} \frac{E'}{E}\left(\frac{G_E^2 + \tau G_M^2}{1+\tau} + 2\tau G_M^2 \tan^2\frac{\theta}{2}\right). \tag{2.3}$$

G_E and G_M can be physically interpreted best in the the frame of zero energy transfer, also known as the Breit frame. Here, they are closely related to the Fourier transforms of their respective distributions [5], [2]. This leads to difficulties in producing three dimensional representations of the distributions because the definition of the Breit frame is different for each q^2.

However, in the non-relativistic limit of $q^2 \to 0$, it simply is the Fourier transform in the nucleon rest frame. In this case, we may perform an expansion of the charge distribution transform in terms of $\vec{x}$

$$G_E = \int d^3x e^{i\vec{q}\cdot\vec{x}}\rho(\vec{x}) = \int d^3x\rho(\vec{x})\left(1 + i\vec{q}\cdot\vec{x} - \frac{(\vec{q}\cdot\vec{x})^2}{2} + ...\right) = \left(\int d^3x\rho(\vec{x})\right) - \frac{1}{6}|\vec{q}|^2\langle r^2_{\text{charge}}\rangle + ... \tag{2.4}$$

The first term in the expansion is simply the total charge of the particle. Performing an expansion of G_E in terms of q^2 and matching terms of q^2, the mean-square charge radius is related to the first derivative of G_E in the limit as $q^2 \to 0$.

$$\langle r^2_{\text{charge}}\rangle = -6\frac{dG_E}{dQ^2}\bigg|_{Q^2=0}. \tag{2.5}$$

This provides a useful method to define a gross structure property of the nucleons.

2.2 Previous G_E^n Measurements

For this experiment we are interested in measuring G_E^n, the electric form factor of the neutron. Of the four nucleon form factors, it has traditionally been the most difficult to measure, as the neutron is an overall neutral particle and there are no free neutron targets. We will now review previous measurements and measurement techniques for G_E^n.

2.2.1 Rosenbluth Separation

The first measurements for G_E^n were done through measurement of elastic electron-deuteron cross section. For the cross section for a spin 1 particle, the form of which is given by Gourdin [6] in terms of three form factors

$$\frac{d\sigma}{d\Omega} = \frac{d\sigma}{d\Omega}\bigg|_{\text{Mott}}\left[A(Q^2) + B(Q^2)\tan^2\left(\frac{\theta}{2}\right)\right] \tag{2.6}$$

where $A(Q^2) = G_C^2(Q^2) + \frac{8}{9}\eta^2 G_Q^2(Q^2) + \frac{2}{3}\eta(1+\eta)G_M^2(Q^2)$, $B(Q^2) = \frac{3}{4}\eta(1+\eta)^2 G_M^2(Q^2)$, and $\eta = Q^2/(4M_d^2)$. These three form factors can then be related to the isoscalar electric and magnetic form factors of the nucleon, G_{ES} and G_{MS}

$$G_C = 2G_{ES}C_E \tag{2.7}$$
$$G_Q = 2G_{ES}C_Q \tag{2.8}$$
$$G_M = \frac{M_D}{M_p}(2G_{MS}C_S + G_{ES}C_L) \tag{2.9}$$

where

$$G_{ES} = \frac{1}{2}\left(G_E^p + G_E^n\right) \tag{2.10}$$
$$G_{EM} = \frac{1}{2}\left(G_M^p + G_M^n\right) \tag{2.11}$$

and C_E, C_Q, C_S, and C_L are related to the deuteron wavefunction. The determination of G_E^n is done by measuring the deuteron elastic cross section and using the Rosenbluth separation technique by varying the electron scattering angle, θ, for a fixed Q^2 to separate the functions $A(Q^2)$ and $B(Q^2)$. G_E^n is then isolated using calculations for the four C functions and previous electromagnetic form factor data. This type of analysis is very dependent on the choice of wavefunction and requires a number of corrections for relativistic effects, meson exchange currents, delta isobar contributions, and final state interactions. One of the earliest measurements of this type was performed at DESY in 1971 by Galster et. al [7] and measured G_E^n up to $Q^2 = 0.6$ GeV^2 with good accuracy.

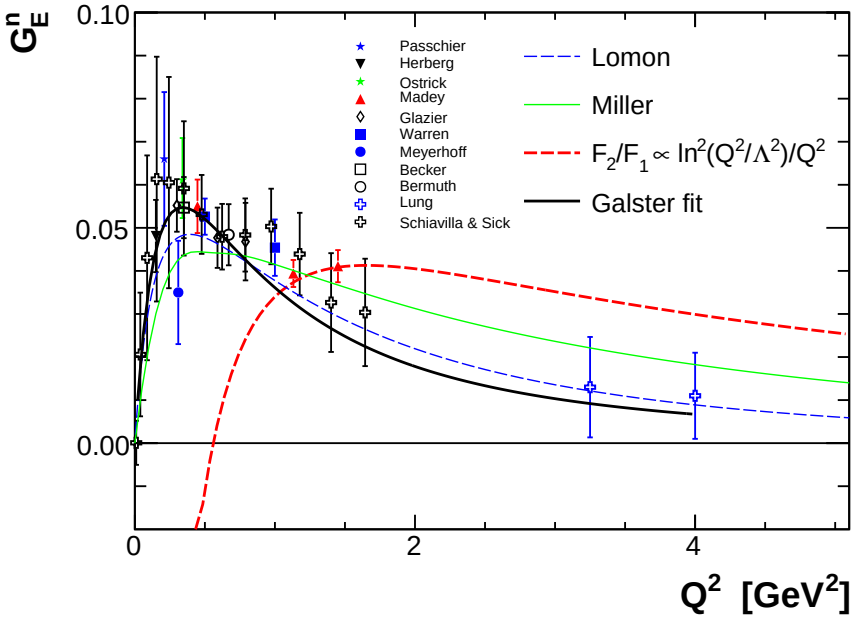

Figure 2.1: Selected world data and theory curves. The F_2/F_1 ratio curve has been scaled to the Madey $Q^2 = 1.45$ GeV^2 point.

2.2.2 Polarization Observables

Separation using the Rosenbluth method is inherently difficult due to the small values of G_E^n and is further complicated by corrections from higher order effects. However, longitudinally polarized electron beams with ^{2}H and ^{3}He targets have proven to provide more accurate measurements by measuring either the polarization transfer or cross section asymmetry using quasi-free kinematics. These types of methods were proposed shortly after the discovery of structure in the proton [8],[9],[10]. The advantage of such methods is the lack of sensitivity to the choice of nuclear wavefunctions and the suppression of higher order effects, such as final state interactions, for low missing momenta.

To relate these quantities to the form factors, modifications to the formalism presented in Chapter 1 must be done. There, in the calculation of the cross section in terms of the structure functions, sums were taken over the spin states producing the spin-independent cross sections. To relate polarization observables to the form factors, this sum does not take place to account for specific polarizations.

For longitudinally polarized electrons on an unpolarized nucleon target, the polarization components for the nucleon after scattering are [11]

$$I_0 P_x = -2\sqrt{\tau(1+\tau)} G_E G_M \tan\frac{\theta}{2} \tag{2.12}$$

$$I_0 P_z = \frac{E_{\text{beam}} + E_{e'}}{M} \sqrt{\tau(1+\tau)} G_M^2 \tan^2\frac{\theta}{2} \tag{2.13}$$

$$I_0 = G_E^2(Q^2) + \frac{\tau}{\epsilon} G_M^2(Q^2) \tag{2.14}$$

where P_x is the polarization component perpendicular to the momentum transfer in the scattering plane, P_z is the polarization component along the momentum transfer, $\tau = \frac{Q^2}{4M^2}$, M is the mass of the nucleon, ϵ is the longitudinal polarization of the exchanged virtual photon, θ is the scattering

angle of the electron, E_{beam} is the initial energy of the beam, and $E_{e'}$ is the energy of the scattered electron. The ratio of G_E/G_M can then be obtained directly

$$\frac{G_E}{G_M} = -\frac{P_x}{P_z}\frac{E_{\text{beam}} + E_{e'}}{2M}\tan\frac{\theta}{2}. \tag{2.15}$$

This technique was employed for a number of measurements at MIT-Bates [12], MAMI [13] [14], [15], and JLab [16] and provided data up to $Q^2 = 1.45$ GeV^2.

The reaction $^2\vec{\text{H}}(\vec{e}, e'n)p$ can be measured in quasielastic kinematics for access to G_E^n through the spin-correlation parameters A_{ed}^V, as done by Passchier [17] and in experiment E93-026 at JLab [18]. This yielded points at $Q^2 = 0.21, 0.5$, and 1.0 Gev^2.

Double polarization experiments using a polarized target and polarized beam can be used to extract G_E when G_M is known through measuring the cross section asymmetry from the two lepton helicity states [19]. In 1984 Blankleider and Woloshyn proposed using a polarized ^{3}He target as the effective polarized neutron target, which would then allow this technique to extract G_E^n [20]. Several experiments successfully utilized this method starting in the early 1990s at MAMI through the reaction $^3\vec{\text{He}}(\vec{e}, e'n)pp$ [21], [22], [23], [24]. This provided data for a range of $Q^2 = 0.31$ to 0.67 GeV^2. This is also the technique chosen for our measurement [25] and a more detailed description can be found in Chapter 3.

2.2.3 Deuteron Quadrupole Form Factor

Due to a lack of higher Q^2 G_E^n data, Schiavilla and Sick calculated this form factor utilizing the world data of the deuteron quadrupole form factor, $F_{C2}(q)$ [26]. Using theoretical predictions for this form factor in conjunction with the data, a set of G_E^n data points up to about 1.6 GeV^2 was obtained. These points showed rough agreement with the Galster parametrization, shown in Fig. 2.1.

2.3 Nucleon Models and Parametrizations

Many models and parametrizations of the nucleon form factors have been developed to fit and predict the measured data. These models have not had any influence from G_E^n at high Q^2 due to the dearth of data. With this analysis, it is then interesting to see how well the predictions from these models agree with new measurements.

2.3.1 pQCD

Due to the size of the coupling constant of the strong force at $Q^2 < \Lambda_{\text{QCD}} \sim 1$ GeV, $\alpha_s \sim 1 - 10$, perturbative techniques are not applicable in this regime. However, at higher energies α_s becomes smaller through the running of the coupling constant and pQCD starts to become applicable. For this experiment we are near energies where the transition to pQCD starts to become relevant, so it is interesting to examine some predictions.

For many years, the behavior of the ratio of the Dirac and Pauli form factor was expected to scale as $F_2/F_1 \sim Q^2$ at large Q^2. However, the measurements in Hall A of G_E^p showed a strong drop off in this ratio contradicting the previously observed behavior [27]. More recent calculations showed that when including one unit of quark orbital angular momentum, pQCD predicts [28]

$$\frac{F_2(Q^2)}{F_1(Q^2)} \propto \frac{\log^2\left(\frac{Q^2}{\Lambda^2}\right)}{Q^2} \tag{2.16}$$

where $\Lambda \approx 300$ MeV. This can be related to the Sachs form factors using Eq. 2.1 and Eq. 2.2

$$\frac{G_E}{G_M} = \frac{Q^2 - \kappa\tau\alpha\log^2\left(Q^2/\Lambda^2\right)}{Q^2 + \kappa\alpha\log^2\left(Q^2/\Lambda^2\right)} \tag{2.17}$$

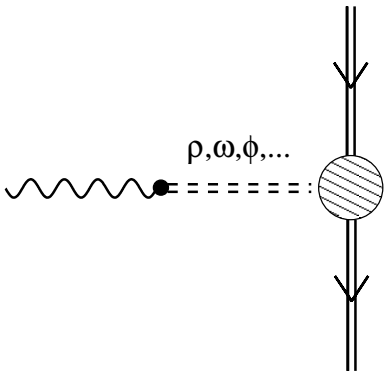

Figure 2.2: The VMD model describes an electromagnetic interaction through the intermediate coupling with vector mesons.

where α is a constant. This type of behavior was confirmed in the available proton data for $Q^2 > 3$ GeV.

2.3.2 Vector Meson Dominance

The vector meson dominance model (VMD) was first hypothesized to explain electromagnetic interactions with hadrons through coupling with intermediate vector mesons. In this model, a virtual photon will transform into a lower-lying vector meson, such as the $\rho(770)$, $\omega(782)$, and $\phi(1020)$, which have the same quantum numbers as the photon, and then interact with the target hadron, Fig. 2.2. The motivation for such a model is through the process $e^-e^+ \rightarrow$ hadrons where these mesons show up as as prominent resonances. The contributions due to these resonances (poles) to the space-like diagrams for eN scattering processes can then be evaluated and predictions can be made.

In these models the strength of the couplings, which are left as free parameters, are fit to existing form factor data. Early VMD fits were developed by Iachello et al. [29] and then improved upon by Gari and Krümpelmanm [30] which included pQCD effects at higher Q^2. More recently, the Gari-Krümpelmanm model has been extended to include more mesons in a fit by Lomon [31], which also included the $\rho'(1450)$ and $\omega'(1420)$. A phenomenological addition including the quark structure of the hadron was added by Bijker and Iachello [32]. Such models have had great success in fitting data as it is measured, but have not had great predictive power [33].

2.3.3 Constituent Quark Model

Constituent quark models take the structure of the nucleon to be comprised of the three valence quarks. In this model, the quarks are taken to have masses of about $m_N/3 \approx 300$ MeV and are placed in a confining potential. The ground state of such a system is then taken to describe the nucleon. Relativistic effects are taken into account such that these models can be used to describe scattering at Q^2 on the order of the constituent quark masses. These types of models have had general success in the description of the form factors at higher Q^2, but the lower Q^2 data includes additional degrees of freedom, such as in the form of pion clouds or local structure of the constituent quarks.

Recently, calculations by Miller were performed using light front dynamics and a model called the light front cloudy bag model (LFCBM) was developed [34]. In this model, an additional cloud of pions was added which then allows for a virtual photon to interact with these pions as well as the

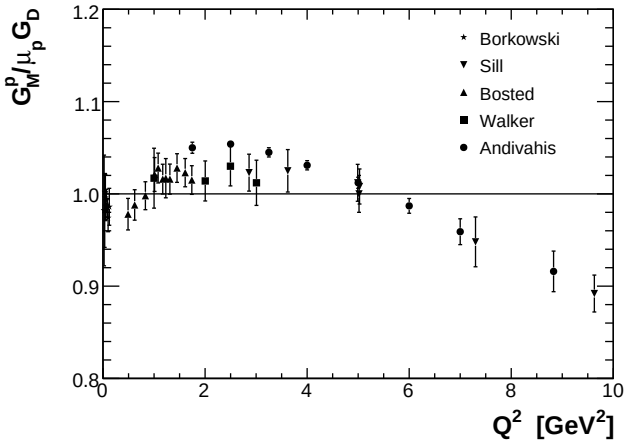

Figure 2.3: Selected data for G_M^p divided by the dipole parametrization.

bare constituent quarks. This model has had success in describing all of the electromagnetic form factors, with the exception of G_M^n at low Q^2.

2.3.4 Dipole

The scaled dipole parametrization has enjoyed considerable success in describing the magnetic Sachs form factors G_M^p, and G_M^n. In this parametrization the form factors take the form

$$\frac{G_M^p(Q^2)}{\mu_p} = \frac{G_M^n(Q^2)}{\mu_n} = G_D(Q^2) = \left(1 + \frac{Q^2}{0.71 \text{ GeV}^2}\right)^{-2} \tag{2.18}$$

where $G_D(Q^2)$ is the dipole form factor, $\mu_p = 2.79$, the magnetic moment of the proton, and $\mu_n = -1.91$, the magnetic moment of the neutron. These all demonstrate the appropriate $Q^2 \to 0$ behavior since $\lim_{Q^2 \to 0} G_D(Q^2) = 1$. Form factor data relative to these fits can be found in Figs. 2.3 and 2.4. Traditionally, this form had also been used for the form factor G_E^p, though with the recent Hall A G_E^p measurement [27] which shows the form factor dropping at a faster rate than previously observed, this fit is no longer good. This is seen in Fig. 2.5, where the ratio G_E^p/G_M^p is not constant in Q^2.

In the low Q^2 Fourier transform interpretation, the dipole form corresponds to a charge or magnetic moment distribution that is exponentially decaying. Using this parametrization to determine the RMS radius through Eq. 2.5, $\sqrt{\langle r^2_{\text{dipole}} \rangle} = 0.81$ fm, which is near the measured nucleon size.

2.3.5 Galster

The dipole parametrization is inappropriate for G_E^n, since $\lim_{Q^2 \to 0} G_E^n(Q^2) = 0$. However, a similar parametrization by Galster [7] has been quite successful in describing the data. This takes the form

$$G_E^n(Q^2) = -\frac{\mu_n \tau}{1 + 5.6\tau} G_D(Q^2) \tag{2.19}$$

where $G_D(Q^2)$ is given by Eq. 2.18, $\mu_n = -1.91$ is the magnetic moment of the neutron, and $\tau = \frac{Q^2}{4m_n^2}$. Despite having been proposed over three decades ago, this form continues to be remarkably successful in describing the data, shown in Fig. 2.1. This parametrization corresponds to a charge

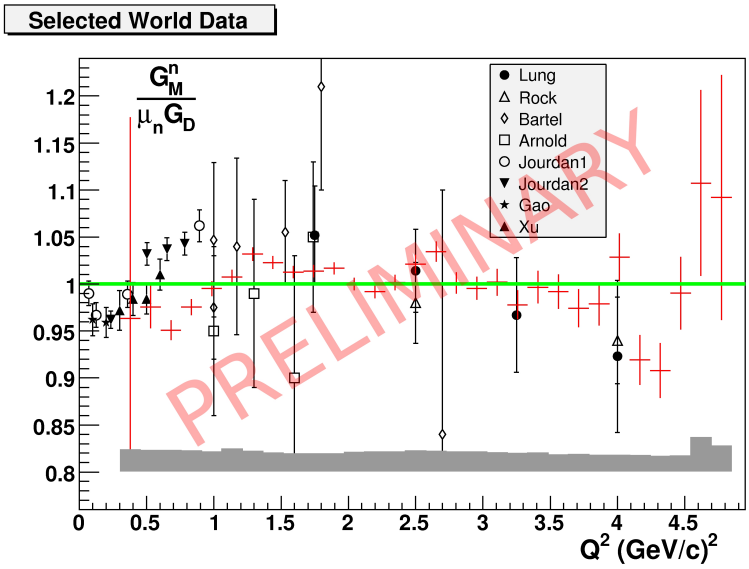

Figure 2.4: Selected G_M^n world data divided by the dipole (from [35]). Red + are from a recent measurement by CLAS [35] and statistical uncertainty. Systematic uncertainty for that analysis is in the grey band. The green line represents the dipole parametrization.

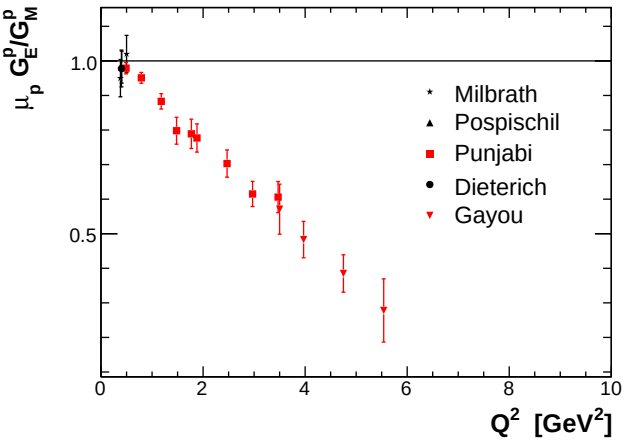

Figure 2.5: Ratio of the electric and magnetic form factors for the proton. G_E^p does not exhibit a dipole form, unlike G_M^p.

radius $\langle r_n^2 \rangle = -0.112$ fm^2. The minus sign indicates the charge distribution is more positively charged near the neutron center and negatively charged at larger radii. This type of distribution would coincide with the simple model of the neutron as a proton with a π^- cloud.

2.3.6 Kelly

A recent phenomenological fit by Kelly [36] attempts to parametrize the form factors using current data. This model is useful in producing continuous values of the form factors and their uncertainties with a greater accuracy than that of the dipole. The Sachs form factors, except for G_E^n, are assumed to have the form

$$G(Q^2) \propto \frac{\sum_{k=0}^{n} a_k \tau^k}{1 + \sum_{k=1}^{n+2} b_k \tau^k}. \tag{2.20}$$

The limiting behavior as $Q^2 \to 0$ for G is taken to be 1 for G_E^p and the respective magnetic moments for the magnetic form factors, fixing a_0. For G_E^n, he continued to use the Galster parametrization form, which has two free parameters

$$G_E^n(Q^2) = \frac{A\tau}{1 + B\tau} G_D(Q^2). \tag{2.21}$$

A fit was performed using a wide set of world data for $n = 1$. For each of these fits he achieved a χ^2/N of approximately 1 except for G_M^n, which was about 0.5.

Chapter 3

Hall A Experiment E02-013

The E02-013 experiment ran at Jefferson Lab in experimental Hall A from February to May 2006. Its goal was to measure the electric form factor of the neutron at momentum transfers, Q^2, of 1.2, 1.7, 2.7, and 3.5 GeV^2 by measuring cross section asymmetries using alternating beam helicities on a polarized ^{3}He target, the so-called "double polarization technique" measuring the reaction $^3\overrightarrow{\text{He}}(\vec{e}, e'\text{n})pp$. To allow for the accumulation of sufficient statistics, a large angular and momentum acceptance spectrometer, named 'BigBite', was employed to measure the momentum of the scattered electron. Since it is also necessary to identify the charge of the scattered nucleon from the ^{3}He nucleus, as well as help identify quasielastic scattering events, a large wall of scintillator, called the 'neutron arm' was constructed to match the acceptance of BigBite. Furthermore, as the sensitivity of the measurement is dependent upon the degree of polarization in the target, a new type of ^{3}He target was constructed for this experiment which allows for higher degrees of polarization than previously realized.

In this chapter we will cover how our experiment was performed and give an overview of the analysis considerations in the design of the experiment. We will also describe the equipment, detectors, and software that were necessary for our measurement.

3.1 Experimental Technique

Shown in Chapter 2, the differential cross section for an unpolarized electron scattering off of an arbitrary spin 1/2 target with structure in the lab frame using the one photon exchange approximation and accounting for recoil of the nucleus can be parametrized as 2.3

$$\left.\frac{d\sigma}{d\Omega}\right|_{\text{LAB}} = \left.\frac{d\sigma}{d\Omega}\right|_{\text{Mott}} \frac{E'}{E}\left(\frac{G_E^2+\tau G_M^2}{1+\tau}+2\tau G_M^2\tan^2\frac{\theta}{2}\right) = \frac{\alpha^2\cos^2\frac{\theta}{2}}{4E^2\sin^4\frac{\theta}{2}}\frac{E'}{E}\left(\frac{G_E^2+\tau G_M^2}{1+\tau}+2\tau G_M^2\tan^2\frac{\theta}{2}\right) \tag{3.1}$$

where $\left.\frac{d\sigma}{d\Omega}\right|_{\text{Mott}}$ is the Mott cross section, which describes scattering off of a structureless target, α is the electromagnetic coupling constant ($\approx 1/137$), E is the incoming electron energy, E' is the scattered electron energy, θ is the scattering angle of the electron, $\tau = -\frac{q^2}{4m^2}$, q^2 is the absolute value of the square of the 4-momentum transfer, m is the mass of the target nucleon, and G_E and G_M are the electric and magnetic form factors as described in Chapter 2. The four momentum transfer, q, is

$$q = p_{e,\text{i}} - p_{e,\text{f}} \tag{3.2}$$

where $p_{e,\text{i}}$ is the initial four-momentum of the electron and $p_{e,\text{f}}$ is the final momentum of the electron.

We can also define the differential cross section in terms of the beam helicity

$$\sigma_h = \Sigma + h\Delta \tag{3.3}$$

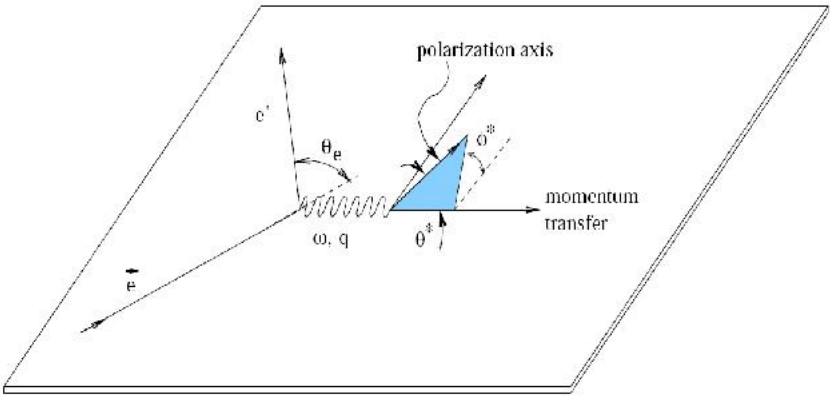

Figure 3.1: Quasielastic scattering kinematics

where h is the sign of the helicity represented as $+1$ or -1. We will refer to Σ as the unpolarized part and Δ as the polarized part. The asymmetry of this cross section, assuming a 100% polarized target and 100% polarized electron, is taken to be

$$A_{\text{phys}} = \frac{\sigma_+ - \sigma_-}{\sigma_+ + \sigma_-} = \frac{\Delta}{\Sigma}. \tag{3.4}$$

Using the definition of the Mott cross section (Eq. 1.19), the unpolarized part can simply be represented by

$$\Sigma = \left.\frac{d\sigma}{d\Omega}\right|_{\text{Mott}} \left(\frac{G_E^2 + \tau G_M^2}{1+\tau} + 2\tau G_M^2 \tan^2 \frac{\theta}{2} \right). \tag{3.5}$$

It should be noted that Eq. 3.5 is calculated by summing over all electron and nucleon spins. By repeating the calculation for a specific target polarization, the difference between the differential cross section for each helicity can be described as [37]

$$\Delta = -2 \left.\frac{d\sigma}{d\Omega}\right|_{\text{Mott}} \sqrt{\frac{\tau}{1+\tau}} \tan \frac{\theta}{2} \left[\sqrt{\tau(1 + (1+\tau)\tan^2(\theta/2))}(\hat{q} \cdot \hat{T}) G_M^2 + \hat{n} \cdot (\hat{q} \times \hat{T}) G_M G_E \right] \tag{3.6}$$

where $\hat{q}$ is the direction of the three momentum transfer, $\vec{q}$, $\hat{T}$ is the direction of the target polarization, and $\hat{n}$ is the vector normal to the scattering plane (defined as $\vec{e} \times \vec{e}'$). See Fig. 3.1.

Using equation (3.4) and taking the ratio of equations (3.6) and (3.5), we find the expression for our asymmetry

$$\begin{aligned} A_{\text{phys}} &= -\frac{2\sqrt{\tau(\tau+1)}\tan(\theta/2)\Lambda \hat{n} \cdot (\hat{q} \times \hat{T})}{\Lambda^2 + (\tau + 2\tau(1+\tau)\tan^2(\theta/2))} \\ &\quad -\frac{2\tau\sqrt{1+\tau+(1+\tau)^2\tan^2(\theta/2)}\tan(\theta/2)(\hat{q} \cdot \hat{T})}{\Lambda^2 + (\tau + 2\tau(1+\tau)\tan^2(\theta/2))} \end{aligned} \tag{3.7}$$

where $\Lambda = G_E/G_M$, the ratio of the electric and magnetic form factors. From this expression it is easy to see that given the scattering angle of the electron, θ, the four momentum transfer, q, and the target polarization, the only remaining unknown quantities are the asymmetry, A and the

Kin	Q^2 (GeV^2)	$E_{\rm beam}$ (GeV)	$\theta_{\rm BigBite}$ (deg)	$\theta_{\rm NA}$ (deg)	$d_{\rm NA}$ (m)	Run Time (days)
1	1.3	1.519	-56.3	35.74	8.23	8
2	2.4	2.642	-51.6	30.25	10.94	19
3	3.5	3.291	-51.6	25.63	10.97	33
4	1.7	2.097	-51.6	35.74	8.23	9

Table 3.1: Settings for the four measured kinematic points for E02-013.

ratio Λ. Since the first term contains a factor of Λ in the numerator, we wish to maximize it with kinematics for which the target polarization is close to perpendicular to the momentum transfer. If G_M is known for the value of q^2, then measuring the asymmetry can yield a value of G_E. We also note that the asymmetry is also frequently written in terms of a transverse and longitudinal part

$$A_{\rm perp} = -\frac{2\sqrt{\tau(\tau+1)}\tan(\theta/2)\Lambda}{\Lambda^2+(\tau+2\tau(1+\tau)\tan^2(\theta/2))} \tag{3.8}$$

$$A_{\rm long} = -\frac{2\tau\sqrt{1+\tau+(1+\tau)^2\tan^2(\theta/2)}\tan(\theta/2)}{\Lambda^2+(\tau+2\tau(1+\tau)\tan^2(\theta/2))}. \tag{3.9}$$

These equations apply for a 100% polarized neutron target and a 100% polarized beam. Of course, these conditions are not present in our laboratory and corrections must be made. Furthermore, the quasielastic sample of events identified as scattering from a neutron will not be wholly comprised of neutrons and other effects such as accidental background and misidentification of protons and neutrons will occur. False asymmetries may be introduced from supplying asymmetric beam charges across the two helicities and also from the electronics and analysis code by biasing towards events of one helicity. All of these factors must be taken into account to accurately reconstruct the "physical asymmetry" from the "raw asymmetry" produced in the data.

It is clear that a strongly polarized neutron source is required to measure G_E^n. Although there are no free neutron targets due to the short half-life of the neutron ($\lambda = 14.8$ minutes), ^{3}He has properties that make it a suitable replacement. Using spin-exchange optical pumping (SEOP) techniques, E02-013 was able to achieve a polarized ^{3}He target with polarization of up to 50% and calculations using a variety of techniques find that the neutron carries about 86% of this polarization as a target ([38], [39], [40], [41], [42], [43], [44]).

Using a target where the neutron is bound in a nucleus introduces several complications in interpreting the results of scattering. These effects include Fermi motion, the possibility of scattering off of meson-exchange currents (MEC), and other off-shell effects. Furthermore, contributions from delta-isobar states and final-state interactions may also affect the final results. By carefully choosing kinematics that emphasize quasielastic events one can attempt to minimize many of these effects.

3.2 Measurements

E02-013 was originally proposed to measure three kinematic points, however, due to circumstances during the experiment, four points were measured. The kinematic settings, the positions of the detectors, and the amount of time for each setting can be found in Table 3.1.

3.3 Experimental Setup

Experiment E02-013 took place at Thomas Jefferson National Accelerator Facility inside experimental Hall A, one of three experimental halls. Much of the equipment used for the experiment involving production and measurement of the incoming beam was developed for use during previous

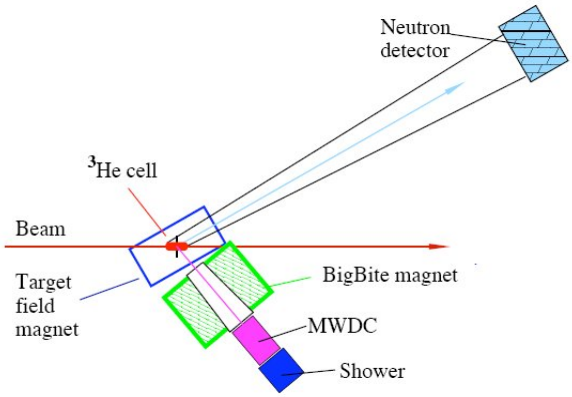

Figure 3.2: E02-013 Experimental Setup

experiments. However, due to the nature of producing a double coincidence experiment requiring large acceptance detectors, new equipment was necessary for this experiment. Furthermore, a target capable of the sustainably high polarizations was also developed.

Two major detectors were used to perform E02-013 (Fig. 3.2). BigBite, a large angular and momentum acceptance spectrometer with a newly constructed detector array, was assembled to detect scattered electrons and the neutron arm, a large wall of scintillator was constructed to detect the recoiling nucleon in coincidence.

BigBite measures the magnitude and direction of the momentum of the scattered electron. This spectrometer was chosen as it would provide adequate statistics through its large momentum bite and angular acceptance. Obtained from NIKHEF, the BigBite magnet is capable of providing a maximum field of 1.2 T with a field integral of approximately 1.0 T $\cdot$ m. Combined with a newly developed detector package for this experiment, BigBite was able to provide an RMS resolution of approximately $\sigma_{\frac{\delta p}{p}} = 1\%$. This portion of the experiment presented the challenge of providing accurate and efficient tracking in a high luminosity environment.

For the neutron arm, the chance of detecting neutrons by a hadronic shower is greatly increased by including lead and iron plates in between the planes of scintillator. An additional two layers of scintillator are placed at the front of the detector without these plates, known as the "veto layers". One may identify the charge of the nucleon from the target through the signals produced in these layers. Ideally, a proton will produce a signal while a neutron will not. More advanced schemes for charge identification will covered in Chapter 5.

3.3.1 CEBAF

The continuous electron beam accelerator facility (CEBAF, [45], [46]) is a medium energy electron accelerator capable of delivering continuous beams of electrons at energies up to about 5.7 GeV at currents up to about 150 μA. This energy provides the opportunity to study the properties of matter in the regime where hadronic and quark degrees of freedom overlap. By using the electron as an electromagnetic probe, an interaction that is well understood through perturbation theory due to the small electromagnetic coupling between charges, we can study the properties of hadrons through the interaction with the charged quarks.

The accelerator features a pair of superconducting radio frequency linacs which utilize recirculation to achieve the necessary energies. Each linac contains 160 superconductor accelerating cavities housed in 20 cryomodules, that resonate near 1497 MHz and have field gradients of 5 MV/m. Each

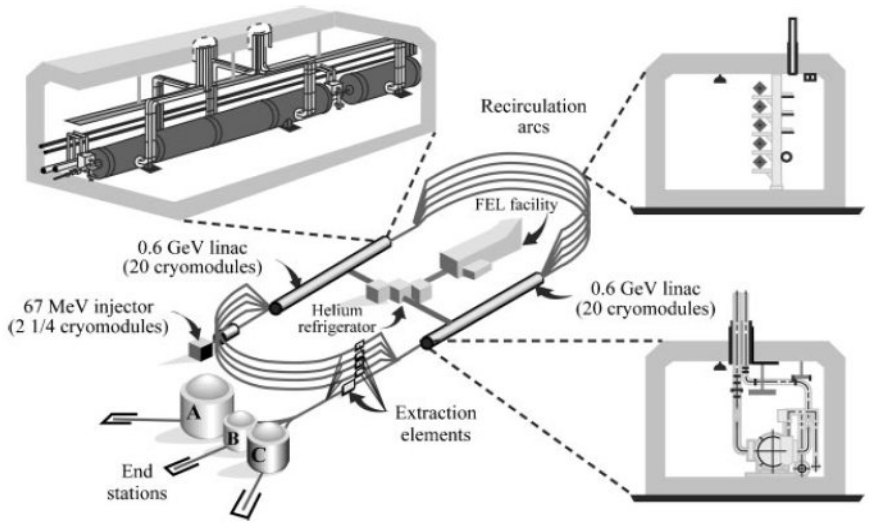

Figure 3.3: Schematic of the CEBAF accelerator

linac produces an energy gain of about 600 MeV in each pass and can recirculate up to 5 passes.

Electrons are initially created at the injector using three RF-gain-switched lasers focused on a single photocathode to produce 100 keV electrons through a process analogous to the photoelectric effect and an electric field gradient. The injector is capable of providing separate beams for the three experimental halls by interlacing light from three diode lasers pulsed at 499 MHz onto a strained GaAs photocathode at a wavelength of 780 nm such that it produces a 1497 MHz train of electrons. The spin direction of the electrons is determined by the polarization of the light on the photocathode, which is controlled by a Pockels cell. The injector is capable of routinely producing polarizations greater than 80%.

A Mott polarimeter is employed at the injector to measure the polarization of the beam as it is produced. This polarimeter measures the asymmetry of counting rates in elastic Mott scattering (electrons on nuclei). This asymmetry is proportional to the beam polarization.

The electrons then are sent to a cryounit (a two-superconducting-cavity module) where they are accelerated to just over 5 MeV and then accelerated in two cryomodules to 45 MeV. These then enter the main accelerator system where they recirculate to the desired energy.

To provide beam to each of the three halls, the three 499 MHz bunches, created by each injector pulse, can be pulled out using RF separators after any linac pass. This beam is approximately 80 μm RMS in the transverse direction and has an RMS relative energy spread of 2.5×10^{-5} when it enters the hall.

Information about the beam, such as the measured energy, is available through the EPICS data system. Furthermore, a phase-locked clock generates a signal in time with the production of each electron bunch produced by the accelerator at a frequency of 499 Hz and is sent to the CODA system for each event. This signal can then be used to associate events in the detectors with a specific bundle.

Helicity Determination

The helicity of the beam is produced according to a known pseudo-random algorithm and is changed at a rate of 30 Hz. This produces a series of beam pulses of a specific helicity that last for 33.3 ms.

These individual states are generated in patterns of four, known as *quads*, and may follow the pattern of either $+--+$ or $-++-$. For each state transition, an inverted "master pulse signal" (MPS) at the same rate is sent to the hall electronics. These signals are put into the CODA data stream and a copy of the transition signal is sent to the E02-013 trigger supervisor. These events are then synchronized in software to determine which helicity state was present for a given event. The absolute sign of the helicity must be independently determined, such as from the Hall A Møller polarimeter. This style of running is referred to as "G^0" mode, after the Hall C experiment which designed it.

Due to the fact that the helicity signal sent from the accelerator is delayed by some fixed amount of time, 8 quads, there are two options to determine the helicity when decoding an event. First, one may try to "read ahead" in the data stream to try and find the signal corresponding to the event of interest, which may be problematic depending on how one records the data. The other solution is to use a predictable pattern. By examining some number of events, typically on the order of 1000, it is possible to then determine where in the sequence of helicities one is at and all knowledge of helicity states at all times is then known.

To check for possibly lost MPS signals, an additional 105 kHz clock signal fed into a scaler is implemented into the system. This scaler provides a time-stamp for each event which then provides a method to check when events occurred relative to each other, such as the time difference from the last MPS. For example, if this time difference becomes too large, attempts to reconstruct the helicity when a lost MPS occurred can be made. This signal is also sent to the E02-013 trigger supervisor. A description of this process is in Fig. 3.4.

For each transition, there is a 500 μs transition period during which the Pockels cell used to determine the photon helicity may be in an undetermined state. The 30 Hz MPS is logically '0' for the duration of this transition period and is used to gate the helicity readout. When an event occurs in this period the helicity is undefined and is rejected for use in determining asymmetries.

Using the pseudo-random method is useful in controlling systematic uncertainties in the determination of the asymmetry. By using this method it is much easier to control the relative amounts of beam charge for each helicity state (which to this point we have assumed to be equal) as well as analyzing portions of the experiment which may drift over time, such as the target polarization.

3.3.2 Hall A Beamline

The Hall A Beamline contains the necessary magnetic, electronics, and instruments to transport the beam onto the target as well as measure various properties of the beam. For E02-013, the properties of particular interest are the beam position, direction, current, and polarization.

Beam Current Equipment

Two beam current monitors (BCMs) are employed to determine the current and integrated charge over a period of time. They consist of two RF cavities, tuned to a frequency of 1497 MHz, which produce an RF signal which is then demodulated to produce a voltage output proportional to the beam current and an Unser monitor [47]. In addition, instrumentation at the injector section of the accelerator provides a reference for calibration. The Unser monitor itself only acts as an absolute reference for calibration and cannot be used for extended periods of time due to signal drift over the period of several minutes.

The RF cavity outputs are sent to both a high precision voltmeter and several copies to a voltage to frequency converter (VTOF). The voltmeter provides an updated signal every 1-2 s which is recorded in the EPICS data stream. The signals to VTOF are sent through a set of amplifiers providing gains of 1,3, and 10 for both of the cavities, such that a total of six signals are present for both BCMs. Each of these six signals is sent to 200 MHz VME scalers, which also provide helicity-gated information, and the accumulated output gives a number proportional to the

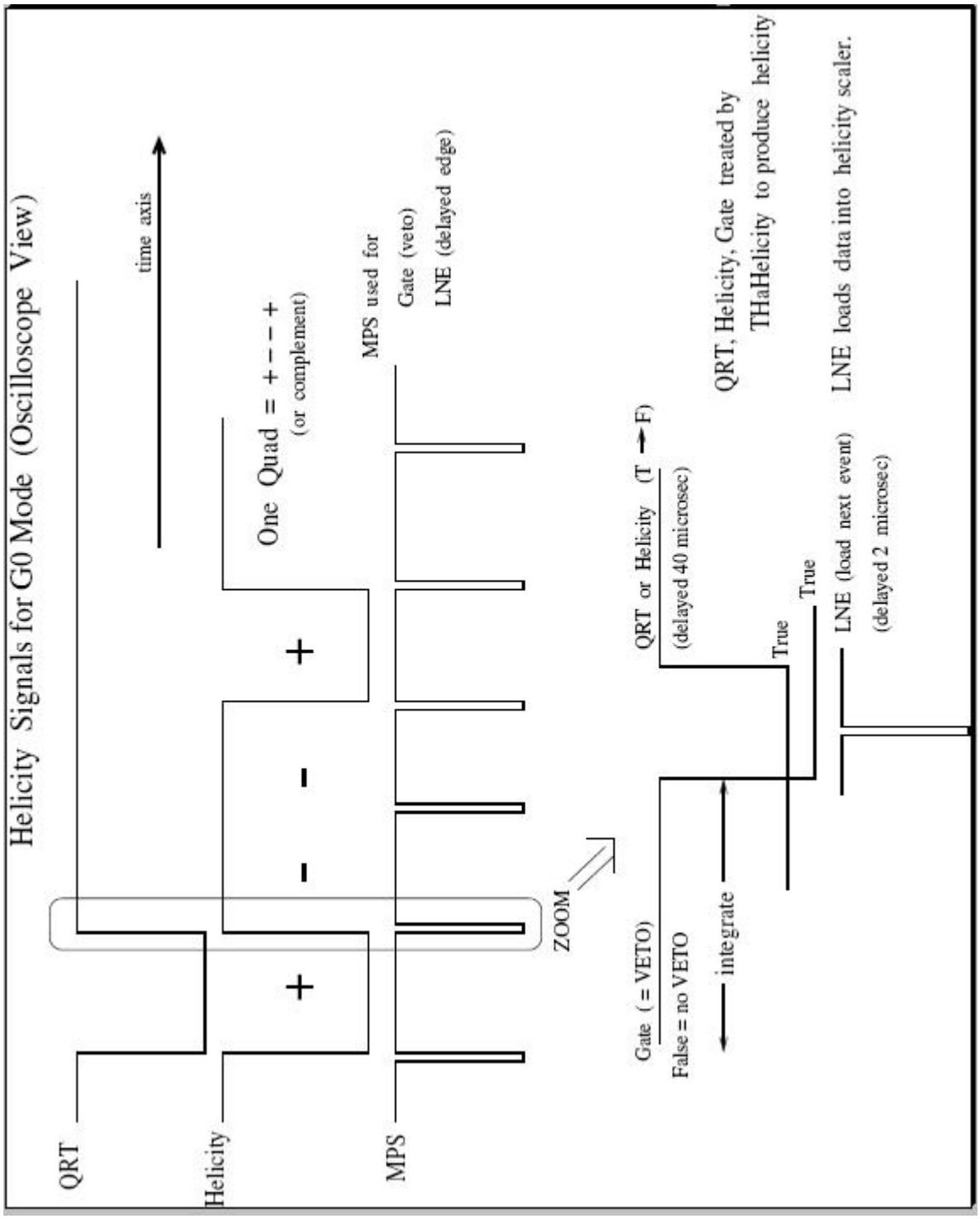

Figure 3.4: Helicity Timing Diagram

integrated charge. Calibrations of the BCMs using the Unser monitor and a Faraday cup at the injector are done through separate runs and are performed every 2-3 months.

Beam Position Equipment

Two beam position monitors are employed to determine the position and direction of the beam. These are each composed of a four-wire strip-line antenna system and are located 7.52 m and 1.29 m upsteam of the target. They provide an accuracy of about 100 μm through ADC readout of the monitors. Their absolute positions are calibrated by using a set of wire scanners known as harps, which are surveyed relative to the hall regularly to provide known positions. By moving the harp wires through the beam at a known rate, the absolute positions provided by BPMs can be determined. The average position recorded by the BPMs over 0.3 s is logged into EPICS at 1 Hz and the position for each event is stored into the CODA data stream.

Polarimetry

The Hall A beamline also provides two beam polarimeters to determine beam polarization through two different methods, one using Møller scattering and another using Compton scattering. The Møller polarimeter consists of a magnetized ferromagnetic foil, providing a target of polarized atomic electrons, a magnetic spectrometer, and two lead-glass calorimeters [48]. Longitudinal beam polarization is determined by measuring the scattering cross sections for two different orientations of the foil. The asymmetry of these measurements depends on the beam polarization in a known way. This method provides a statistical accuracy of about 0.2% for about one hour of data taking, and about 3% systematic uncertainty. This type of measurement is invasive and must be performed separately from an experiment.

The Compton polarimeter works on the principle of scattering electrons off of polarized photons. By measuring the cross section asymmetry between the two beam helicity states, the overall beam polarization can be determined. The Hall A Compton polarimeter consists of a magnetic chicane, a photon source, an electromagnetic calorimeter, and an electron detector [46]. The entire beam is deflected into the chicane where it interacts with a photon beam in a Fabry-Pérot cavity, used to enhance the photon density. To maximize the luminosity, the photons and electrons intersect at the smallest possible angle while the cavity mirrors do not interfere directly with the beam. For the Hall A polarimeter, this is at an angle of 23 mrad. The scattered electrons and photons are detected in coincidence and their energy is reconstructed from the electron detector and calorimeter for calibration. For normal polarization measurements the polarimeter runs in "single arm" independent of the electron arm. This method is non-invasive and provides a statistical accuracy of about 1% for 30 minutes of running.

Raster

The Hall A beamline also incorporates a set of fast rastering field coils located 23 m upstream to produce small deviations in the beam position at the target. This technique is often useful to prevent significant amounts of heating on small areas on the target which can reduce usable lifetimes, cause permanent damage, or rupture a target.

This system operates by producing small transverse magnetic fields for the beam to pass through. These fields produce deviations of several millimeters in both directions at the target locations. It is able to sweep across the range at a rate of 17 to 24 kHz. The current supplied to the raster is read into the CODA data stream for each event for use in calculation of the beam position.

Foil	Type	Position v_z (m)
1	C	-0.133
2	C	-0.067
3	BeO	0.000
4	C	0.067
5	C	0.133

Table 3.2: Types and positions of (visible) foils for the carbon foil target.

3.3.3 Target

The hybrid ^{3}He target and associated equipment were newly developed by Alan Gavalya and the polarized ^{3}He target groups at the University of Virginia, College of William and Mary, University of Kentucky, and Jefferson Lab Hall A. This target used the spin-exchange optical pumping method of polarizing the target with the novel use of combining two alkaline vapors (instead of one) in the optical pumping scheme to provide high, sustained polarizations. Associated equipment built for the experiment included an iron target box, target ladder system for switching between different types of targets, a set of Helmholtz coils, lasers to be used for optical pumping, an oven to maintain fixed temperatures of the pumping chamber, and various readout electronics. Both nuclear magnetic resonance (NMR) and electron paramagnetic resonance (EPR) techniques were employed to measure and monitor the polarization of the target during the running of the experiment.

For this experiment, two additional target types were employed for use in calibration of the experiment. These were a carbon foil target, which consists of a set of four carbon foils and a BeO foil at known positions along the beam line. Table 3.2 describes the type and position of the foils visible for this target.

The other additional target was a glass reference cell, which could be filled either with H_2 or N_2 to pressures of about 150 psig, or evacuated. The length of the reference cell was approximately 40 cm.

Polarized ^{3}He as a Polarized Neutron Target

Because there are no free neutron targets of sufficient density due to the relatively short lifetime of a neutron outside of a bound nucleus, a substitute must be employed to act as an effective neutron target. Using the double polarization technique in E02-013, an experiment where the measurement is sensitive to the degree of the polarization of the neutron, a target that provides the highest practical polarization is desired. ^{3}He is a natural candidate, as about 86% of the nuclear spin is carried by the neutron. The degree of this polarization, as well as any residual spin carried by the two protons is well understood and has been accurately calculated using a variety of techniques ([38], [39], [40], [41], [42], [43], [44]).

The contributions of various states are represented in Fig. 3.5. A majority of the time, the nucleus is in a configuration where the two proton spins oppose each other. However, there is a small contribution of the protons of roughly 3% which must be taken into account when considering the contamination of protons in the asymmetry of a quasielastic neutron sample.

Polarized ^{3}He Target Principles

The method of spin-exchange optical pumping [49] was used to put the ^{3}He gas into a polarized state. In the past, this technique involved exposing circularly polarized light on a single alkali metal vapor, such as ^{85}Rb, contained within a magnetic field. For this discussion we will take the projected spin direction to be in the direction of the angular momentum carried by the photon.

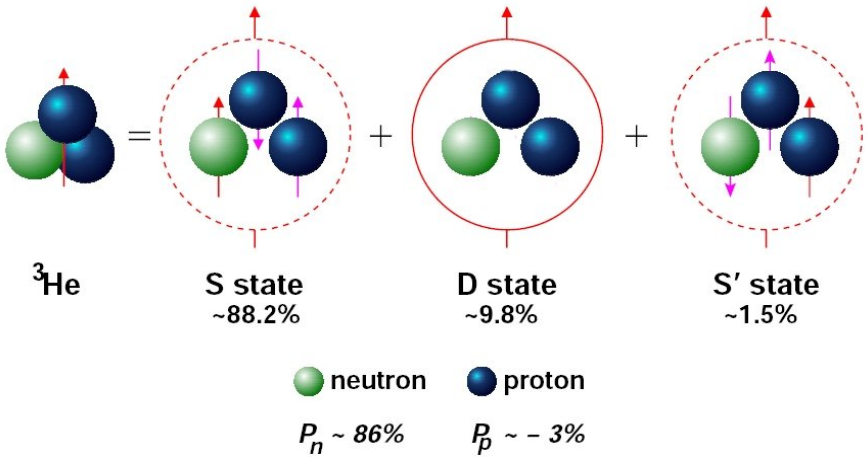

Figure 3.5: Contribution of different states to the spin of the ^{3}He nucleus.

The alkali vapor and ^{3}He gas are placed together in magnetic holding field in the same direction. This produces an energy level splitting in the valence electron of the alkali vapor, separating the $m_s = -1/2$ and $m_s = 1/2$ levels. The circularly polarized light is tuned to the transition of the valence electron in a spin down S state ($m_s = m_j = -1/2$) to a spin up sublevel in a P state ($m_j = 1/2$) (Fig. 3.6). This transition follows from the conservation of angular momentum when the photon is absorbed, i.e. $\Delta j = 1$ and $\Delta m_j = 1$.

This new excited state will either decay by some path back down into a spin up S sublevel ($m_s = 1/2$), or through collisional mixing with other atoms move to spin down P sublevel $m_j = -1/2$ and then decay. The probability of ending in either S state after the final decay is about 50%, which results in a net gain of angular momentum for the target. Angular momentum is then transferred from the polarized alkali valence electron to the ^{3}He nucleus via a hyperfine interaction between the polarized alkali vapor valence electron and the ^{3}He nucleus [50], resulting in a polarized ^{3}He nucleus.

In these decays, the radiation released is generally unpolarized which may cause the problematic effect of depolarizing neighboring atoms. In high pressure systems, as is often desirable for polarized target experiments, a single photon may be absorbed and reradiated several times before it escapes the system causing the depolarization of many atoms. This effect can be quenched by the inclusion of nitrogen gas into the system. The effect of the gas is to radiationlessly quench the excited electrons back to the ground state, such as through transfer of energy through kinetic collisions. Introducing sufficient quantities of nitrogen, typically of densities on the order of 2% relative to the number of ^{3}He, decreases the amount of depolarizing photons.

The target cells used in E02-013 are known as hybrid target cells, meaning they contained two alkali metal vapors, in our case Rb and K. This creates a slightly different scenario when polarizing our nuclei. The purpose of having two different vapors is to decrease the amount of time necessary to polarize a cell by exploiting how angular momentum is transferred to different components in the target.

The mechanism for this is understood to be the exploitation of the relaxation cross section of K, which is a factor of 15 smaller than that of Rb [51]. The spin exchange between K and Rb atoms transfers the Rb polarization to K very efficiently [52], such that their polarizations are practically equal for the time scales of the other angular momentum transfer processes.

Using only Rb, the "spin up time" or amount of time required to polarize the cell to certain polarization, is typically on the order of 15 hours whereas a hybrid cell will have a spin up time close to 8 hours. This not only decreases the amount of time necessary to have a cell attain a useful

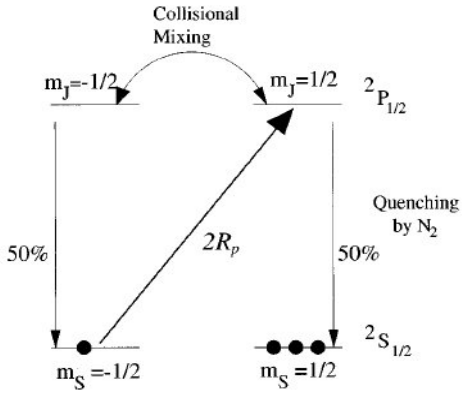

Figure 3.6: The process of optically pumping an alkali gas. Circularly polarized photons cause the transition between the $m_s = m_j = -1/2$ level to the $m_j = 1/2$ level. This excited state then decays by some path (possibly involving interactions with other atoms) back down to the S level. The final state will be roughly equally distributed between the $m_s = -1/2$ and $m_s = 1/2$ level, resulting in a net gain of half a unit of angular momentum for each absorbed photon.

polarization, but also allows for higher polarizations to be achieved and for those polarizations to remain more stable during depolarizing beam effects and polarimetry measurements.

K, however is difficult to polarize by itself due to the frequency of the $5S_{1/2} \rightarrow 5P_{1/2}$ transition near a depolarizing frequency. Using a mixture of Rb and K, one is able to quickly polarize the K using the Rb as a proxy, and take advantage of the enhanced spin exchange of K. With a much larger density of K compared to the Rb, ^{3}He should polarize much more efficiently than through Rb alone.

Polarization Measurement Techniques

Two separate methods were used to measure the polarization of the target. One using nuclear magnetic resonance (NMR) and the other using electron paramagnetic resonance (EPR). Both of these methods provide complementary ways to access the polarization.

NMR and AFP

An NMR measurement is done by taking a set of nuclei and placing them in a magnetic field and then applying a radio frequency field. When resonance conditions are met, a signal can then be measured that is proportional to the polarization of the target. To find the proper resonance conditions in E02-013, we looked for this resonance through adiabatic fast passage (AFP) [53].

AFP is the method of reversing the spins of the ^{3}He nuclei by changing the magnetic holding field while applying a radio frequency magnetic field. If the field change is slow enough, the spins of the nuclei will change to the opposite direction. However, it must be fast enough such that the spins do not have time to relax. The reversal will sweep through a resonance, which produces an EMF signal that is proportional to the polarization of the target in a separate set of coils known as the pickup coils.

Looking at the problem classically, placing the polarized nuclei in a holding field, $\vec{H}_0$, with which the spins are aligned, and then applying a perpendicular rotating field, $\vec{H}_1$, of frequency ω, the nuclei

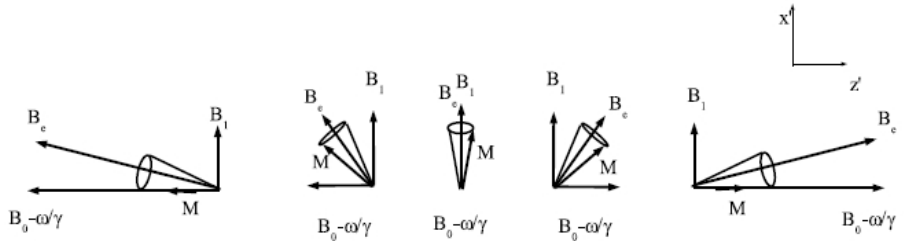

Figure 3.7: AFP of the nuclei magnetic moments in the rotating frame as the holding field is swept through the resonance condition (resonance occurs at the center figure).

will begin to precess. This is given by the formula [53]

$$\frac{d\vec{M}}{dt} = \gamma\vec{M} \times (\vec{H}_0 + \vec{H}_1) = \gamma\vec{M} \times \vec{H}_e \tag{3.10}$$

where $\vec{M}$ and γ are the magnetic moment and gyromagnetic ratio of the nucleus, respectively, and $\vec{H}_e$ is the total effective field. For convenience, we take $\vec{H}_0$ to be in the $\hat{z}$ direction and transform to a rotating frame of frequency $-\omega_0$ about the z axis. The effective field becomes

$$\vec{H}_e = \left(H_0 - \frac{\omega_0}{\gamma}\right)\hat{z} + \vec{H}_1. \tag{3.11}$$

It is this effective field that the polarization of the spins follow under AFP conditions, Fig. 3.7. Applying adiabatic fast passage, the angle between the effective field and the holding field in the rotating frame, θ, is given by

$$\tan\theta = \frac{H_1}{H_0 - (\omega/\gamma)}. \tag{3.12}$$

Using this method, the resonance condition can be met by either sweeping the holding field or the frequency of the RF field. In E02-013, the holding field is linearly swept from about 25 to 32 G using an RF frequency of 91 kHz and RF field of about 90 mG.

The strength of the signal from the induction in the pickup coils due to the rotating spins is dependent on several factors

$$S_{\mathrm{NMR}} = P \cdot n_{^3\mathrm{He}} \cdot \Phi \cdot \mu_{^3\mathrm{He}} \cdot C_{\mathrm{electric}} \tag{3.13}$$

where P is the polarization of the target, $n_{^3\mathrm{He}}$ is the density in the ^{3}He cell, Φ is the flux of the signal through the coils, $\mu_{^3\mathrm{He}}$ is the magnetic moment of the ^{3}He nuclei, and C_{electric} is a constant dependent upon the electronics and coils used to measure the signal.

Due to the fact that the spins will change direction with the field, a sweep of the holding field is done by moving past the resonance and then back again, moving to the original holding field position (a "double sweep"). In the case that it is desired to have the spins of the ^{3}He nuclei flipped to the opposite direction, a single sweep may be performed (that is, leaving the holding field on the "other side" of the resonance), as was done periodically during the experiment. This change also required a change in the direction of polarization of the laser light to maintain the pumping process. To completely destroy the polarization, the holding field may be left at the resonance condition.

When performing an NMR measurement small depolarizations will occur. These were measured to be on the order of 1%, but are considered to be minimally invasive.

EPR

EPR, electron paramagnetic resonance, measures the shift in electron energy levels when in a magnetic field (the Zeeman effect). For E02-013 this was measured in the electrons of the K atoms. While there are several magnetic contributions to the energy levels, such as the holding field and a shift due to the spin exchange mechanism, a small and measurable contribution will result from the polarization of the ^{3}He nuclei.

By performing a measurement of the shifts with opposite target polarizations, we can isolate the shift due to the nuclei polarization away from other contributions. AFP provides a useful method to change the direction of the spin of the nuclei while causing only small amounts of depolarization. In the EPR measurement however, the frequency of the applied field is varied to achieve the flip while the holding field is kept constant (in NMR we sweep the holding field using a constant applied field frequency). This is due to the fact that holding field, which contribute the splitting in the EPR measurements must be kept constant to successfully isolate the small shift due to the field from our nuclei.

By sweeping through an electromagnetic frequency range near the energy splitting of about 58 kHz, a resonance can be detected when this frequency is exactly the splitting. By determining the shift when the spins are aligned or anti-aligned with the holding field, the shift due to ^{3}He polarization can be isolated:

$$\begin{aligned} \Delta\nu_+ &= \Delta\nu_{^3\mathrm{He}} + \Delta\nu_{B_0} + \Delta\nu_{\mathrm{other}} && (3.14)\\ \Delta\nu_- &= -\Delta\nu_{^3\mathrm{He}} + \Delta\nu_{B_0} + \Delta\nu_{\mathrm{other}} && (3.15)\\ 2\Delta\nu_{^3\mathrm{He}} &= \Delta\nu_+ - \Delta\nu_- && (3.16) \end{aligned}$$

where $\Delta\nu_{^3\mathrm{He}}$ is the splitting contribution from the polarization of ^{3}He, $\Delta\nu_{B_0}$ is the contribution from the holding field, and $\Delta\nu_{\mathrm{other}}$ is the sum of contributions from all other effects. The frequency splitting can then be related to the polarization by [54]

$$\Delta\nu_{^3\mathrm{He}} = \frac{d\nu_{\mathrm{EPR}}(F,M)}{dB} C n_{^3\mathrm{He}} \mu_{^3\mathrm{He}} P \tag{3.17}$$

where $\Delta\nu_{^3\mathrm{He}}$ is the signal shift, $\frac{d\nu_{\mathrm{EPR}}(F,M)}{dB}$ is obtained by other experiments and is available in the literature, and C is a dimensionless quantity that depends on the shape of the sample. For a spherical cell

$$\Delta\nu_{^3\mathrm{He}} = \frac{8\pi}{3} \frac{d\nu_{\mathrm{EPR}}(F,M)}{dB} \kappa_0 \mu_{^3\mathrm{He}} P \tag{3.18}$$

where κ_0 is a constant that must be determined experimentally and is dependent on temperature [55]. As it only varies in the EPR signal, it can be mapped out by performing repeated NMR and EPR measurements at various pumping chamber temperatures. $\Delta\nu_{^3\mathrm{He}}$ for a polarization of 52% corresponds to about 16 MHz.

As a side note, the holding field (assuming other effects are small), can also be determined by the sum

$$\Delta\nu_{B_0} = \frac{\Delta\nu_+ + \Delta\nu_-}{2} \tag{3.19}$$

where

$$B_0 = -\frac{h\Delta\nu_{B_0}}{\mu_B} \tag{3.20}$$

h is Planck's constant, and μ_B is the Bohr magneton.

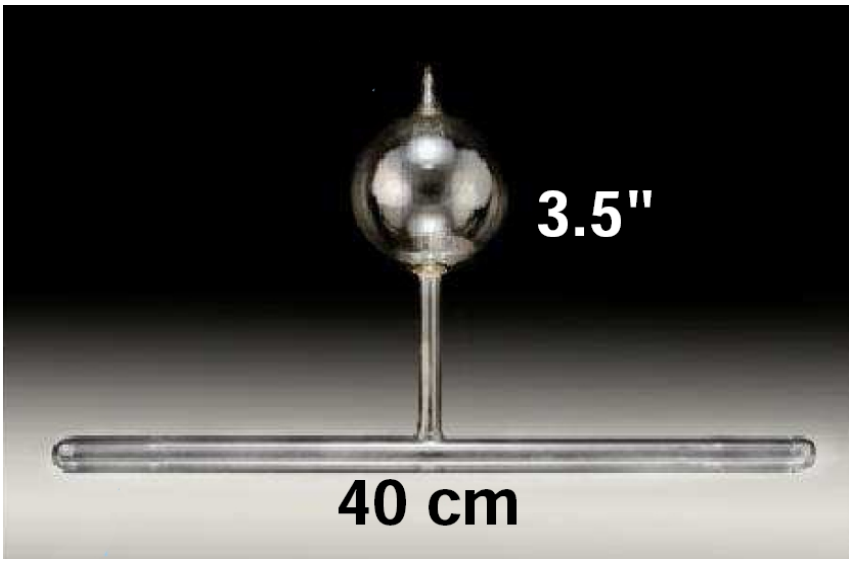

Figure 3.8: ^{3}He target for E02-013 [56].

Target Setup

The target for E02-013 was housed in an iron box which featured all the necessary equipment to provide a holding field, measure the polarization through EPR and NMR techniques, polarize the target, and provide other targets relevant to the experiment.

The target itself was constructed from hand-blown glass and featured two chambers (Fig. 3.8). The upper, spherical chamber, known as the pumping chamber, is the region where the circularly polarized laser light is focused and polarization occurs. It has a diameter of approximately 3.5 in. This chamber must be kept at a temperature of approximately 240°C to maintain a gaseous state of the alkali metals which was achieved by placing the pumping chamber inside an oven. The lower chamber is roughly cylindrical and is approximately 40 cm long. This is the target chamber where the beam passes and scattering occurs.

Several sets of coils were present around the target, (Fig. 3.10). The first set provides a holding field of approximately 25 G. A second set was introduced to drive an RF signal transverse to the holding field for NMR and EPR measurements. The two remaining sets of coils, called pickup coils, were used to measure the NMR signals (Fig. 3.9) and to excite the EPR transition.

All of these components are housed within an iron target box with a remotely controllable mechanical target ladder which allows for different targets to be put into the beamline. These include the empty glass reference cell, which can be filled with nitrogen, hydrogen gas, or evacuated and the carbon foil target of six carbon foils and one BeO foil, separated at known intervals.

3.3.4 Neutron Arm

The neutron arm is a relatively simple detector in concept. To detect recoiling nucleons resulting from a quasielastic collision between the electron beam and our ^{3}He target, a large wall of scintillator is employed. This acts as a crude sort of hadronic calorimeter. Placing lead and iron plates (known as converter plates) in between many layers of scintillator enhances the possibility of measuring a hadronic shower caused by nucleons regardless of charge (Fig. 3.11). The desired information we wish to extract from this detector is to identify if the particle is charged associated with the

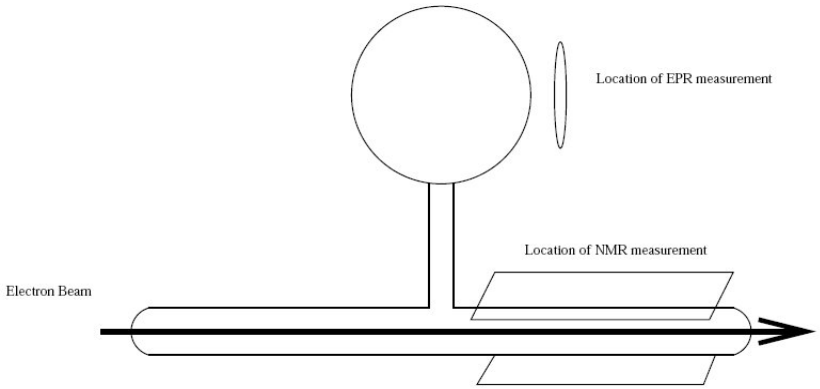

Figure 3.9: Position of the pickup coils relative to the target [57].

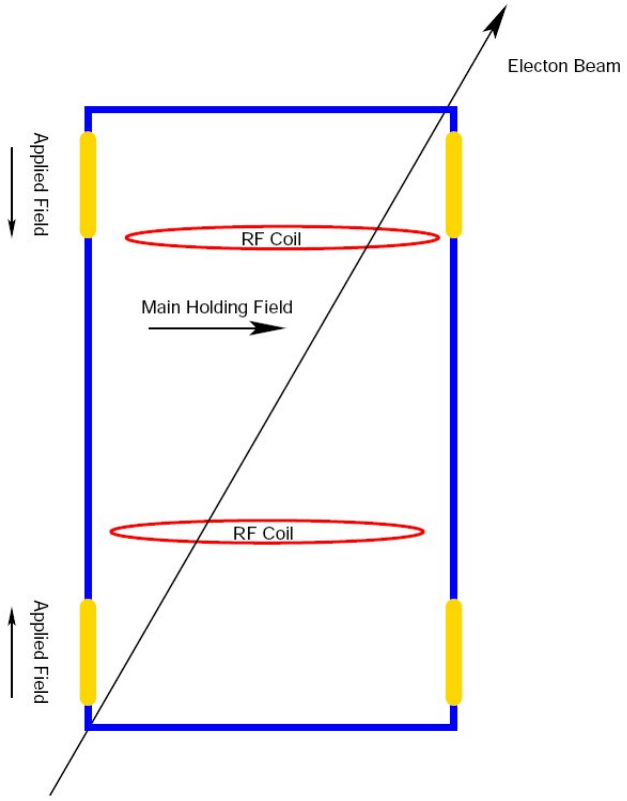

Figure 3.10: Conceptual position of holding field relative to target and beam [58]. Top down view.

cluster, the direction of the momentum, determined by the position of the hit, and magnitude of the momentum through time of flight.

The charge may be determined by measuring a scintillator signal before any type of nuclear interaction can take place (or at least in an attempt at minimal interaction), Fig. 3.12. To achieve this, two layers of scintillator, called the veto layers, are placed before any of the converter plates. Any signals in these planes are associated with signals behind the converter layers to identify charge. If there is a signal, we say that the particle was charged, otherwise a neutral particle is assumed. Care must be taken in the analysis to account for dead times and efficiencies of the detectors. For example, some veto signals may be masked by dead times producing false neutron identifications.

There were two main considerations taken in the design of this detector. As the electronics for the neutron arm are of finite timing resolution and the momentum is determined through time of flight, the distance between the target and neutron arm determines the overall resolution of the momentum, as given in the equation

$$\delta p = \left| \frac{mc\beta^2}{l} \left[\frac{1}{(1-\beta^2)^{3/2}} \right] \right| \delta t \tag{3.21}$$

where δp is the neutron momentum resolution, δt is the time of flight resolution, c is the speed of light, l is the flight distance, m is the mass of the particle, and $\beta = l/(ct)$. Clearly, maximizing the distance is crucial for a given β, which is determined by the kinematics. However, the overall active area of the detector must match that of the electron spectrometer to ensure coincidence. For larger areas, this can become prohibitive in both structural design and cost. By choosing $l \approx 10$ m and the active area of approximately 8 m^2, we achieve a good balance between the two. For the most restrictive kinematic of 3.5 GeV^2, we have a $\beta = 0.95$. Given a RMS timing resolution of 300 ps defined by the timing resolution of the electronics and the quality of timing calibration between scintillator bars, we expect to have a momentum resolution of approximately 200 MeV/c.

The neutron arm has dimensions of width, depth, and height of $4.2 \times 2.0 \times 6.2$ m^3, which has an aspect ratio designed to match that of the BigBite spectrometer. When placed 8 m from the target it subtends approximately 100 msr. Each scintillator bar is connected to at least one photomultiplier tube (PMT), which is in turn connected to an analog-to-digital converter (ADC) to provide information about the amplitude of the signal present in the scintillator. A copy of the signal is also sent to a discriminator and then a time-to-digital converter (TDC) to provide timing information. When a PMT is connected to each end of the scintillator, the difference between the two times recorded can provide information of where along the bar the signal originated.

Structurally, the neutron arm is composed of two veto layers and seven scintillator layers. The veto layers consist of two scintillator bars per horizontal row, each with a photomultiplier tube on the end. Each bar on one side has dimensions $11.0 \times 70.0 \times 2.0$ cm^3 (veto short) and $11.0 \times 110.0 \times 2.0$ cm^3 (veto long) on the other. Each veto plane consists of 48 rows which are offset between each other by 5.1 cm. Because each row is physically separated into left and right segments, the time difference between the left and right PMT cannot be used to reconstruct the position along the bar of the hit, as is done with the other neutron arm layers.

Planes 1-4 of the neutron arm are comprised mainly of "CMU" scintillator bars (as they were provided by Carnegie Mellon University). Each bar has dimension $15.0 \times 180.0 \times 5.0$ cm^3. Planes 1 and 3 also contain four and five "Glasgow" bars of dimension $20.0 \times 180.0 \times 10.0$ cm^3 located at the top of the planes. Planes 5-7 contain 40 "UVA" bars of dimension $10.0 \times 180.0 \times 10.0$ cm^3 with 5 Glasgow bars at the top.

Additionally, four vertical "marker counters" were also employed to aid in calibration of the horizontal positions of each bar. Each counter consisted of plastic scintillator of dimension $2.54 \times 2.54 \times 304.8$ cm^3. These ran vertically from the top to bottom of the neutron arm, perpendicular to the direction of the other scintillator bars, spanning the entire height.

The readout signal for the neutron arm electronics is formed using the sum of the amplitudes of bars reaching some threshold value which is then generated by the trigger supervisor. These sums

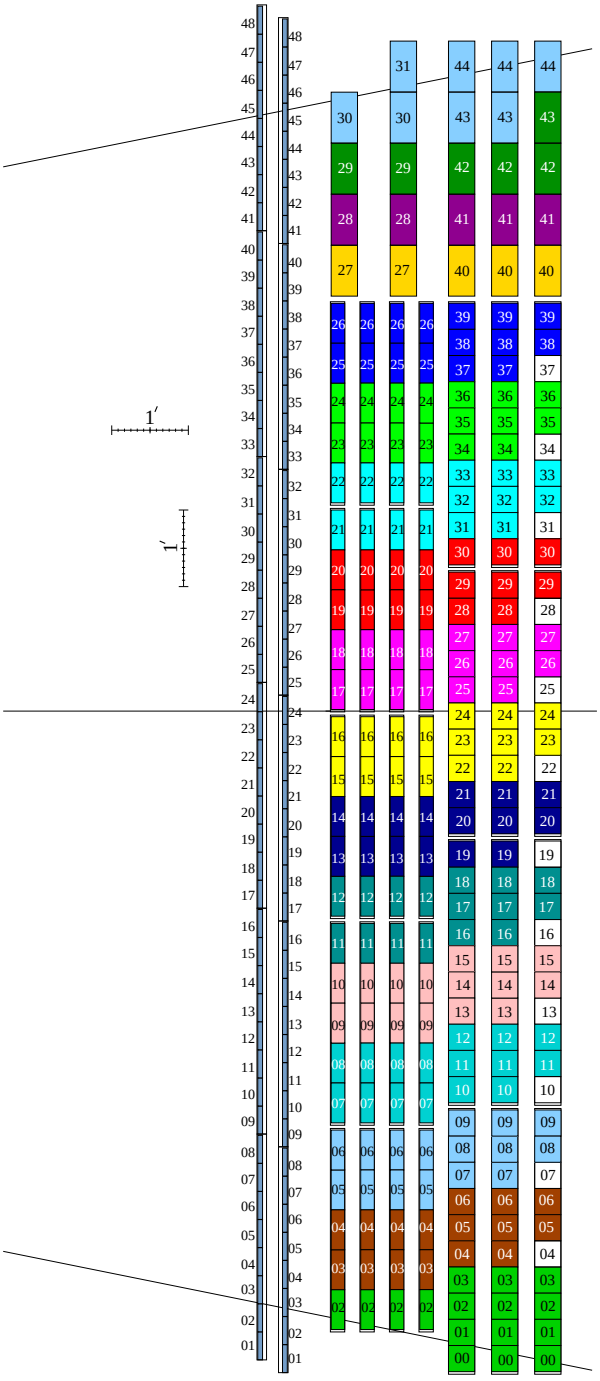

Figure 3.11: Cross section of the neutron arm, showing the layers of scintillator, converter plates, and veto layers. Bars of the same color are included in the same sum to form the neutron arm trigger [59]. White bars are not connected to any sum.

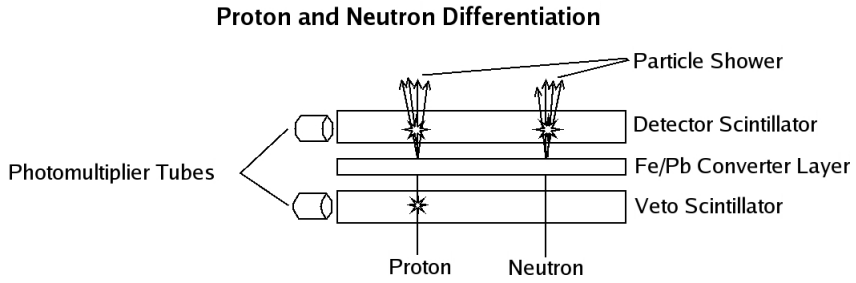

Figure 3.12: Interaction of charged and uncharged particles in the neutron arm.

are generated by a sum over either left or right PMTs across a group of bars. These groups are shown by bars of the same color in Fig. 3.11. A diagram of the electronics for these sums can be found in Fig. 3.13.

Calibration of the timing of all the scintillators is done by using the known time of flights from the elastic scattering of protons in a H_2 target and from quasielastic scattering from the ^{3}He target.

3.3.5 BigBite Spectrometer

The BigBite spectrometer represents the electron arm of the coincidence measurement. It is designed as a high-resolution spectrometer with a field integral using high-resolution drift chambers to provide electron track reconstruction. Its goal is to measure the direction and momentum of the electron as it leaves the target. This is done by having the electron first pass through a magnetic field where it will deflect some amount based upon its momentum, the depth of the field, and the strength of the field. After deflection the path of the electron is measured by a set of multiple wire drift chambers which provide high-resolution hit-based tracking. Once the path is known, the momentum and direction of the electron as it left the target can be inferred.

BigBite itself is a large angular-and momentum-acceptance spectrometer, subtending for this experiment approximately 76 msr and accepting electrons of momenta from 0.6-1.8 GeV. It is capable of reconstructing momenta with a resolution of approximately $\sigma_{\delta p/p} = 1\%$. It consists of a large iron dipole magnet capable of field integrals of about to 1.0 T $\cdot$ m. The opening at the front face of this magnet is 0.95 m $\times$ 0.25 m and sits approximately 1.15 m from the target.

The detector package for this experiment was newly constructed. It consists of three multiple wire drift chambers, a layer of scintillator, and two lead-glass calorimeters, known as the shower and preshower, Fig. 3.14.

Coordinate Systems

There are three different coordinate systems used in reference to the BigBite spectrometer. The standard lab coordinate system, the target coordinate system, and the detector coordinate system.

The lab coordinate system or hall coordinate system has an origin at the center of the target, y goes against gravity ("up"), z is in the nominal direction of the beam, and x is to the left when looking down the beam.

The target coordinate system has the origin at the intersection of the BigBite central ray with the lab z axis, x goes with gravity ("down"), z is parallel to the ground to point along the BigBite central ray, and y forms a right handed coordinate system.

The detector coordinate system origin is specified by the center of the first plane of the drift chambers. The x axis is perpendicular to the direction of the wires in the X wire plane and resides in that plane. Positive x is in the magnetic dispersion direction. z is in the nominal direction of

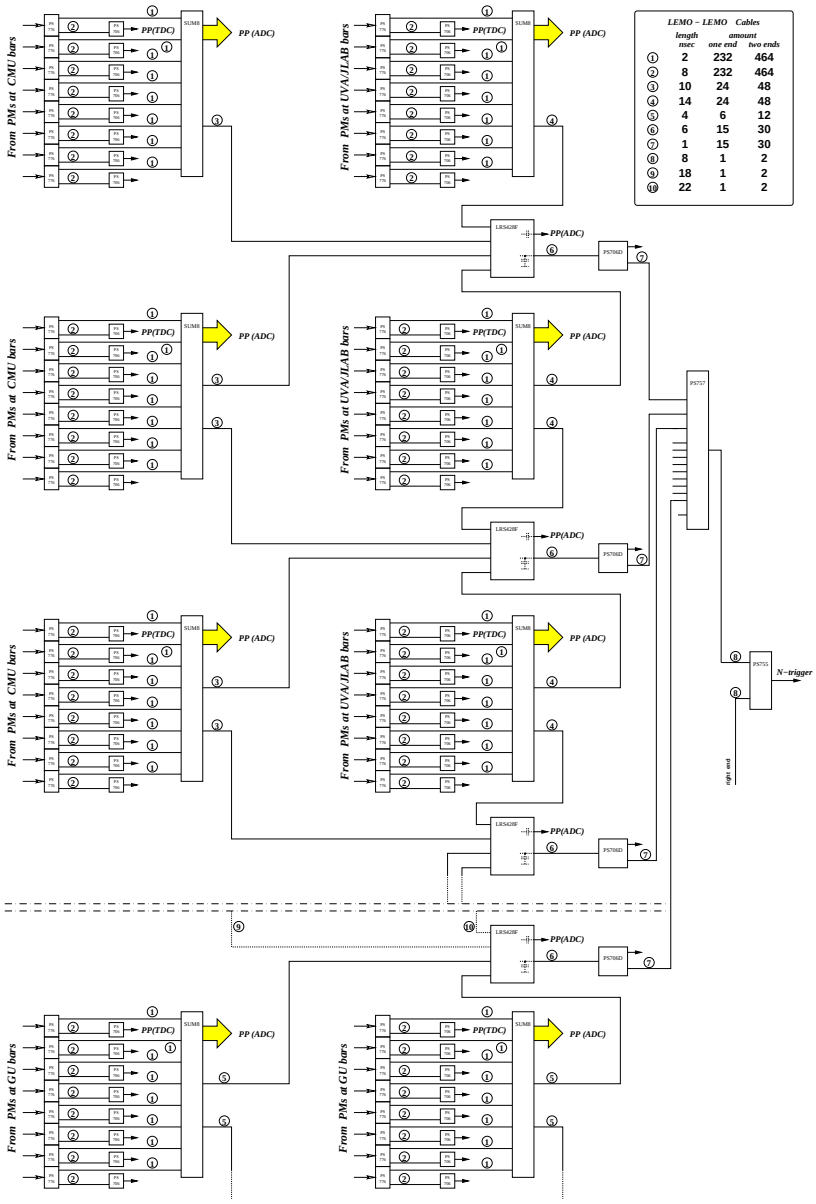

Figure 3.13: Diagram of the electronics used for neutron arm sums that form the trigger [60].

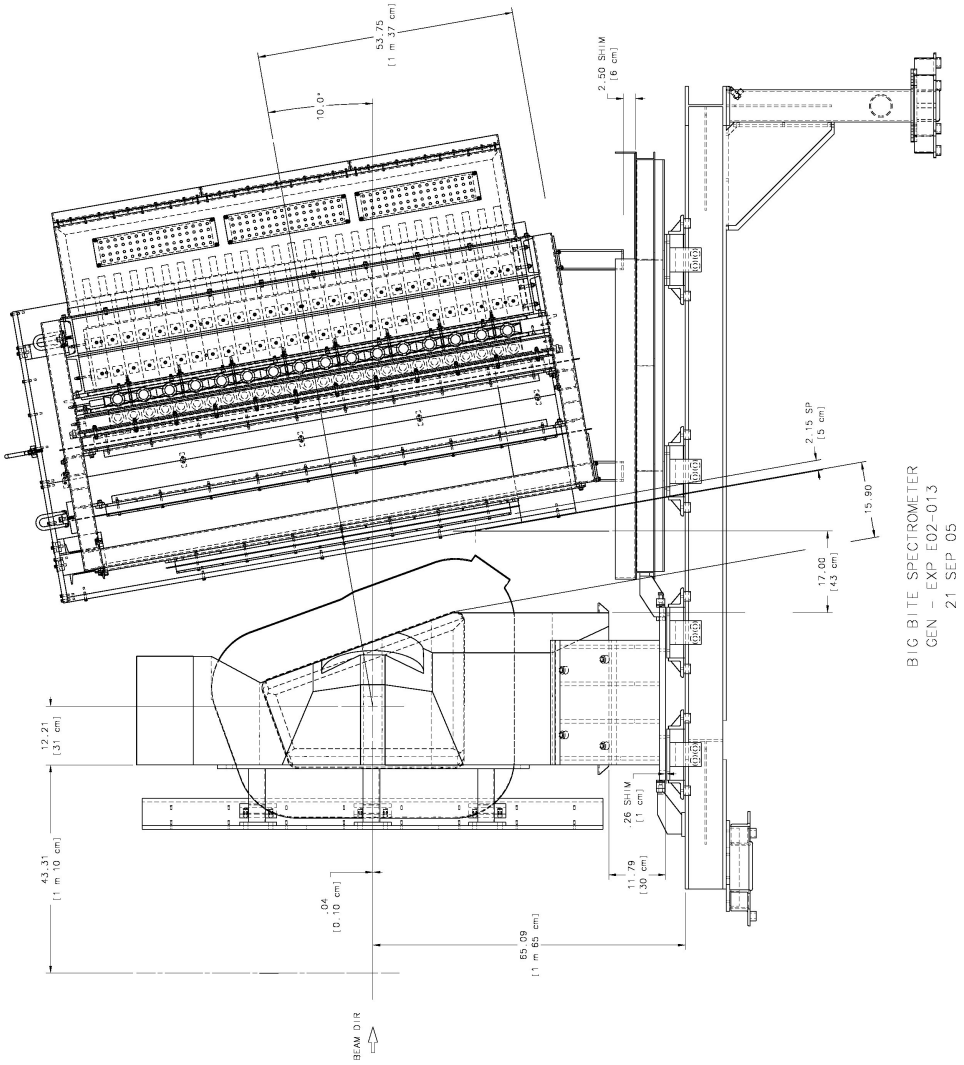

Figure 3.14: The BigBite Spectrometer [61].

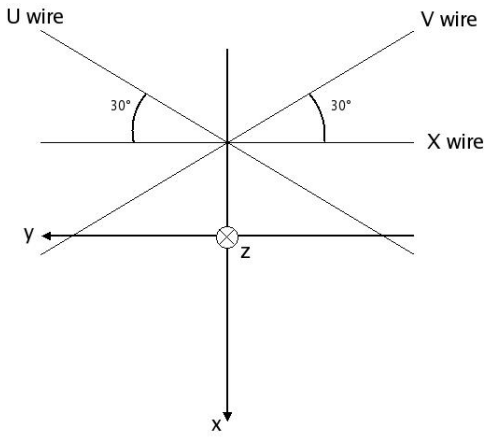

Figure 3.15: Wire orientation relative to detector coordinate axes.

particles perpendicular to the first drift chamber plane. It is therefore at an angle with the lab $x-z$ plane equal to the pitch of the drift chamber stack (approximately 10°). The projection of $z_{\rm det}$ into the lab $x-z$ plane is at an angle with the $z_{\rm LAB}$ axis equal to the central angle of the spectrometer. y is defined such that a right-handed coordinate system is formed. This is described in Fig. 3.15, looking down z.

Optics

The purpose of the spectrometer is to measure the momentum of a charged particle scattered from the target. To do this, one must have an understanding of how the particle trajectory depends on the magnetic field and how that trajectory relates to what is measured in the drift chambers. In this section we will discuss the method of determining the momentum assuming that tracks have already been found.

Given a track in the chambers, we assume an effective bend plane model, represented in Fig. 3.16, where all interaction in the magnet is treated as occurring at the magnetic mid-plane. The track reconstructed in the chambers, or "back track" is taken to be the track after deflection. Making the assumption that there is no dispersion in the $y_{\rm det}$ direction and that the particle originated along the electron beam, we can reconstruct the "front track" or the track before it entered the magnet as it was leaving the target.

This is done by first interpolating the back track to the bend plane, which uniquely defines a point on the plane. With our assumptions that dispersion only occurs in the $x_{\rm det}$ direction, the family of potential front tracks defines a plane. The intersection of this plane with the beam then defines a unique point on the beam which we take to be our naive vertex reconstruction. Corrections, discussed below, are made to the vertex based on the reconstructed back track parameters. The front track is then defined to be the vector from the corrected vertex to the point on the effective bend plane where the back track made an intersection.

Several coordinates are defined which are useful in making corrections and calculations from the optics. The track reconstructed in the drift chambers can be defined by four parameters in the detector coordinate system: x and y, the $x_{\rm det}$ and $y_{\rm det}$ coordinates at the intersection of the track with the plane $z_{\rm det}=0$. The two coordinates which describe the direction of the back track are x'

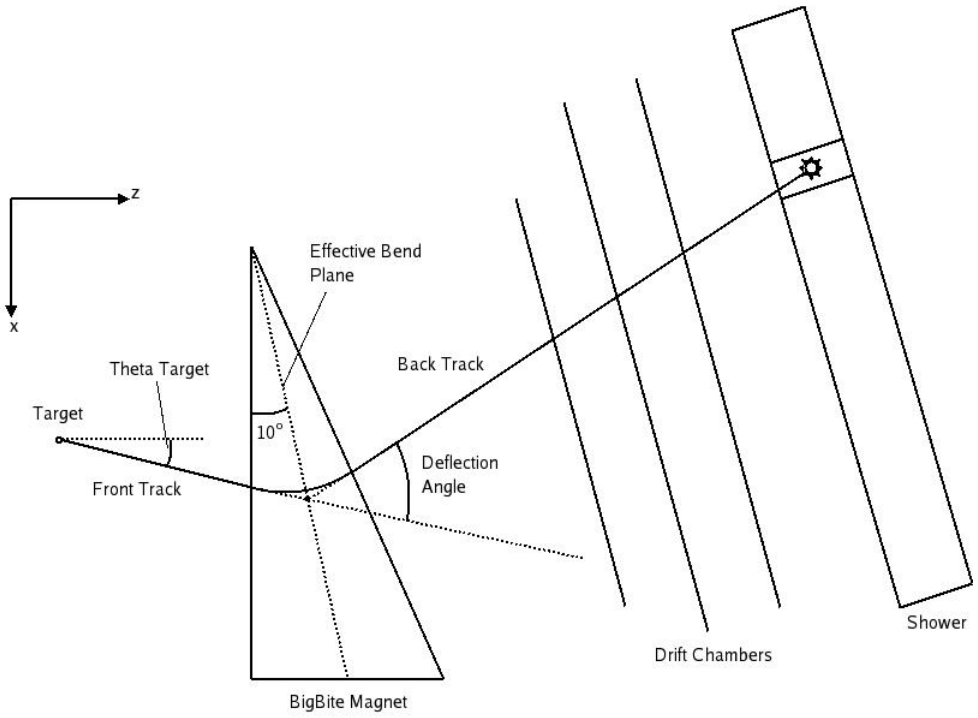

Figure 3.16: The effective bending plane model (side view, not to scale). Axes are in target coordinates.

and y' (occasionally referred to as $\theta_{\rm targ}$ and $\phi_{\rm targ}$, respectively) are defined as:

$$x' = \frac{dx_{\rm det}}{dz_{\rm det}} \tag{3.22}$$

$$y' = \frac{dy_{\rm det}}{dz_{\rm det}}. \tag{3.23}$$

Two other useful coordinates are $x_{\rm bend}$ and $y_{\rm bend}$, the $x_{\rm det}$ and $y_{\rm det}$ coordinates where the track intersects the effective bend plane.

The corrections applied to the vertex position take the form

$$v_{z,\rm LAB} = c_0 v_0 + c_x x + c_{x'} x' + c_y y + c_{y'} y' + a(x_{\rm bend}, y_{\rm bend}) \tag{3.24}$$

where $v_{z,LAB}$ is our z coordinate of the vertex in the lab coordinate system, v_0 is the naive vertex position determined as above. In the extreme vertical positions of the magnet, or the highest and lowest $x_{\rm bend}$, corrections must be made which deviate from outside of this model. The a term in Eq. 3.24 is introduced to account for these corrections. These corrections are found by fitting to data taken on carbon foils of a known position.

The model used to reconstruct momentum gets its leading term from a small-angle approximation of a charged particle moving through a uniform magnetic field. Empirical first order corrections are made based on various track variables. The formula currently used is

$$p = \frac{c_0(x_{\rm bend}, y_{\rm bend}) + c_x x_{\rm bend}}{\vartheta_{\rm def}} + c_\vartheta \vartheta_{\rm targ} + c_y y_{\rm det} + c_\varphi y'_{\rm det} + a \tag{3.25}$$

where $x_{\rm bend}$ is the x coordinate of the intersection of the bending plane in detector coordinates, $\vartheta_{\rm targ}$ is the out of plane angle ("theta target" in Fig. 3.16), and $y_{\rm det}$ and $y'_{\rm det}$ are the two respective track coordinates in the detector coordinate system. $\vartheta_{\rm def}$ is the deflection angle made by the particle in the field defined as:

$$\vartheta_{\rm def} = \cos^{-1}\left(\frac{\vec{x}_{\rm front}\cdot\vec{x}_{\rm back}}{|\vec{x}_{\rm front}||\vec{x}_{\rm back}|}\right) \tag{3.26}$$

where $\vec{x}_{\rm front}$ is the vector representing the track as it leaves the target and $\vec{x}_{\rm back}$ is the vector representing the track as it passes through the drift chambers. The leading term is based upon the relationship of momenta and deflection angles for small angle scattering

$$p \propto \frac{\int B_\perp dl}{\theta} \tag{3.27}$$

where $\int B_\perp dl$ is the field integral for the path of the electron and θ is the deflection angle.

The purpose of the $x_{\rm bend}$ term is primarily to correct for the differing field integral in the magnetic field volume due to the trapezoidal shape. The remaining detector plane variables are first order corrections to this model. Due to deviations from this model in the extreme vertical positions of the magnet, c_0 is allowed to vary over $x_{\rm bend}$ and $y_{\rm bend}$ in these regions.

To provide a consistent model over a wide range of momenta, the a term in Eq. 3.25 gives a degree of freedom to allow for a linear transformation in p. This transformation is necessary to develop a model that provides accurate reconstruction for all of our kinematics at a single spectrometer angle. (See Section 4.4.5)

All calibrations of these coefficients are determined by selecting elastic events on H_2, where the momentum of the particle can be determined solely from the scattering angle, $\theta_{e'}$, defined as the polar angle of the front track with the beam.

Multiple Wire Drift Chambers

The drift chambers of the spectrometer consist of three separate horizontal drift chambers spaced approximately 35 cm apart. The drift chambers are the first set of detectors after the magnet and are the highest-spacial-resolution detectors in the detector stack. The approximate configuration of the three chambers is found in Table 3.3. These chambers were newly constructed for this experiment by the University of Virginia [62].

To achieve the ability to resolve tracks in three dimensions, three different types of planes are used, called U, X, and V. All three plane types are designed to reside in a plane of constant $z_{\rm det}$. X wires run parallel to the $y_{\rm det}$ axis and U and V wires are $\mp 30^\circ$ to that axis (Fig. 3.15). In each plane, the sense wires are spaced 1 cm apart, with a field-shaping wire in between each pair. Planes of the same type, when next to each other, are staggered 0.5 cm relative to one another. Cathode planes (held at the same voltage as the field wires) are located 3 mm above and below each wire plane. This configuration provides a roughly symmetric potential around the sense wires (Fig. 3.17). The chambers are filled with a 50% argon-50% ethane gas mixture bubbled through 0° C ethyl alcohol and are kept slightly above atmospheric pressure.

The sense wires detect the electrons released when a charged particle ionizes the gas as it passes through the chamber. Since the wires are held at some potential difference, the liberated charges drift towards the wires, eventually causing ionization themselves and forming a small cascade, generating an electrical signal which is then sent to an amplifier/discriminator and a pulse is sent to a time-to-digital converter. The amount of time it takes to drift from the track to the wire can then be converted into a distance.

During the experiment different voltages were used for each of the planes, shown in Table 3.4. These voltages were chosen such that the per-plane efficiencies were at approximately 85%, a trade off between maximizing the number of reconstructing tracks and extending the usable lifetime of the drift chambers. Voltages on the chambers were different due to different amplifier cards placed on

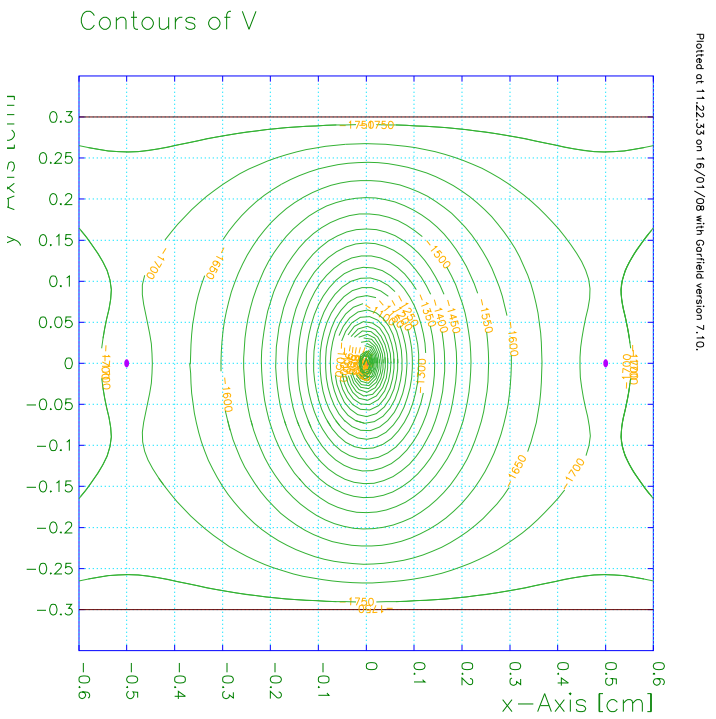

Figure 3.17: Drift chamber equipotential lines around a sense wire generated with GARFIELD.

the chambers. Chamber 1 used a newer set of cards, which were more senstive [63]. Furthermore, these voltages may not reflect the effective voltage inside the chamber due to current drain effects. Efficiencies were measured from tracking results by determining how frequently a wire was not used in a reconstruction in the case a track passed through the cell containing the wire.

BigBite Scintillator

A set of 13 scintillator paddles resides between the preshower and shower providing timing information. Each paddle is connected to two photomultiplier tubes, one on each end. The signal from each photomultiplier tube is sent to a an amplifier and copy of the signal is sent to an ADC, which integrates the amplitude of the signal over time, and a discriminator which sends a logical pulse to a TDC to provide timing information. This timing, with a resolution of about 300 ps, when associated with a track can then be used to reconstruct the time of the electron at a drift chamber plane. Since the scintillator plane resides about 1.0 m from the first plane, timing corrections (assuming a particle traveling at the speed of light) to the drift times can be up to a few nanoseconds, which can be seen in tracking.

Furthermore, this timing is used in reference to the neutron arm. By calculating the difference

Chamber	Plane Pattern	Number of Wires Per Plane	Wire Spacing (cm)	Height (m)	Width (m)	$z_{\rm det}$ (m)
1	UUXXVV	142	1.0	1.40	0.35	0.00
2	UXV	200	1.0	2.00	0.50	0.36
3	UUXXVV	200	1.0	2.00	0.50	0.71

Table 3.3: BigBite drift chamber configuration.

Chamber	Voltage (V)
1	-1630
2	-1770
3	-1785

Table 3.4: BigBite drift chamber voltages.

between the time of a hit in the scintillator and the time of the corresponding hit in the neutron arm, given the path length of the electron, one can calculate the time of flight for the recoiling nucleon.

Preshower and Shower

The front face shower and preshower are located behind the drift chambers at approximately $z_{\rm det}$ =1.0 m and $z_{\rm det}$ =0.85 m, respectively. The preshower consists of 54 lead glass blocks which are 35 cm wide and 8.5 cm tall set in 2 columns and 27 rows. The shower consists of lead glass blocks 189 8.5 cm $\times$ 8.5 cm set in 7 columns and 27 rows (Fig. 3.18). A charged particle entering a block will produce an electromagnetic shower where the Cerenkov light from the shower is collected by a photomultiplier tube. The PMT signal is sent to an amplifier and one copy is sent to an ADC to integrate the signal amplitude and another copy is sent to a set of summing modules. A copy of the summed signals is sent to an ADC and another to a discriminator which produces a logical pulse sent to a TDC. The sum of the amplitudes generated by the shower is approximately linearly dependent upon the energy of the particle. The combination of the shower and preshower gives reconstructed energy with resolution $\sigma_{dE/E} \approx$10%.

The shower and preshower system together acts as a calorimeter and also as a robust method to identify particle types. We can restrict ourselves to specific signatures in the preshower which are likely to identify an electron event. $x_{\rm det}$ and $y_{\rm det}$ position information is also obtained from the block that produced a signal in the shower. While this position resolution is quite poor (8.5 cm in both directions) this can be used to straightforwardly fix a point of our track. Exploiting the fact that there is a known target image for a range of momentum, we can then narrow the volume in which it is necessary to search for an electron track in the chambers by a factor of 10.

3.3.6 Data Acquisition

Data acquisition for E02-013 involves several systems. They include the EPICS system, which generally provides slow, real-time information about the accelerator and the target, the trigger supervisor and read-out controllers (ROCs), which handle the event-by-event retrieval of data recorded from the detectors, and the scalers, which provide information such as rates, as well as information on current and charge accumulation.

CODA, the CEBAF on-line data acquisition system, is the standard data acquisition system designed for use at Jefferson Lab [65]. It provides software tools for monitoring, accumulating, recording, and decoding data taken during experiments. This is done by providing a common

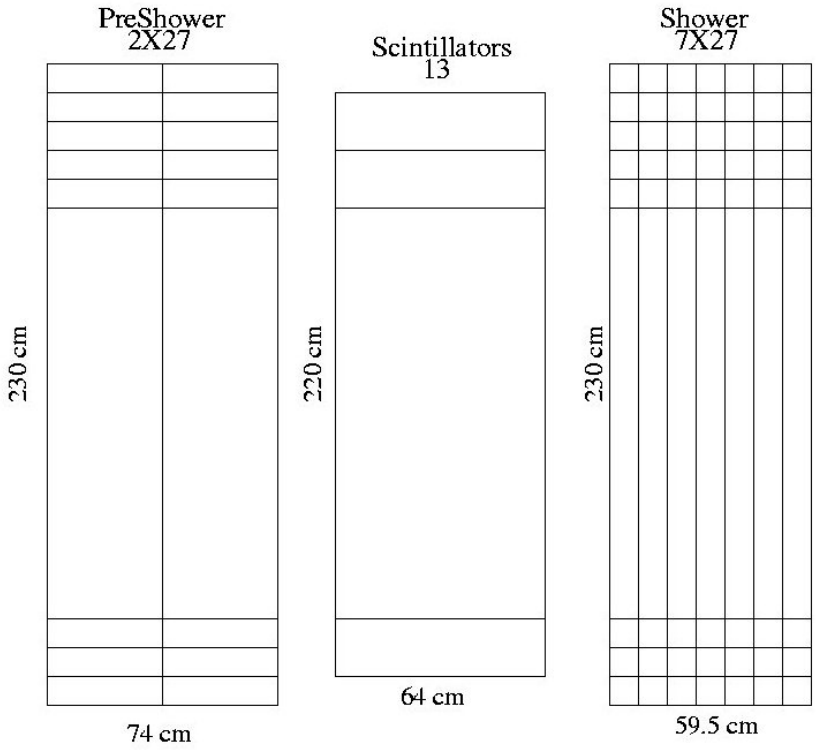

Figure 3.18: The shower and preshower configuration [64].

interface to manage a set of read-out controllers, which store and retrieve data from individual modules, such as TDCs and ADCs.

CODA for E02-013 was used to accumulate data for most aspects of the experiment, except for some target information, such as the polarization, which was recorded separately. This includes all data from the detectors through read-out controllers, scaler data, and EPICS data.

EPICS

The Experimental Physics and Industrial Control System (EPICS) provides information about the accelerator and the hall conditions. It is a set of software tools and applications designed to control and operate large devices, such as particle accelerators and telescopes. It provides a method to gather information from a large variety of subsystems, often varying greatly in design, in a concise and standardized way.

For E02-013, EPICS provides information about the beam current, beam energy, beam position, and the state of a half wave plate at the injector, which affects our beam helicity. This information is stored in the CODA data stream. Its design is to provide "soft" real time information, that is, information which is real time data but is generally recorded over time-points on the order of seconds. While this provides information over "slow" variables that do not change frequently, such as the beam energy, other means must be used to gather information that is specific to individual events.

BigBite

BigBite has several components providing data. TDC information is recorded from each wire on the three multiple wire drift chambers and TDC and ADC information are recorded from the scintillators, preshower sums, and shower sums, and ADC information alone from the individual shower and preshower PMTs.

Each drift chamber wire is connected to an amplifier/discriminator card which is in turn connected to a set of LeCroy 1877 multihit time-to-digital converters running in common-stop mode. These 96-channel TDCs feature a timing resolution of 500 ps and a multiple event buffer of 7 events. Each TDC records approximately 1.5 μs of time information for each event.

These TDCs are located in a set of FASTBUS crates. Their readout is controlled by the overall BigBite trigger. Data recording is handled by CODA.

The scintillator signal is sent to a channel of a LeCroy 1881 ADC and to a discriminator. The discriminator output is then sent to a CAEN 775 TDC. The 1881 is located in a FASTBUS crate while the TDC is located in a separate VME crate. The shower and preshower individual PMT amplitudes and sums of the amplitudes are sent to the same 1881 ADC as the scintillator. A copy of each of the sums is also sent to a discriminator and then to a LeCroy 1877 TDC located in the same FASTBUS crate as the 1881 ADC.

The signal for BigBite arm trigger is formed by the amplitude sums over a set of overlapping blocks of both the shower and preshower set at some predefined threshold. A diagram of the electronics can be found in Fig. 3.19.

Neutron Arm

The neutron arm electronics record information collected by PMTs attached to the large array of scintillators. Each of these PMTs has a signal that is sent to an amplifier and a copy is sent to an ADC and another is sent to a discriminator which produces a logic pulse which is sent to a TDC. Furthermore, a set of summed signals is produced that is used in the trigger logic.

Several varieties of TDC were used for this apparatus. For the veto detectors and sums, LeCroy 1877 TDCs, identical to those used for the BigBite drift chambers, were employed. For the main scintillator planes F1 multihit TDCs were used.

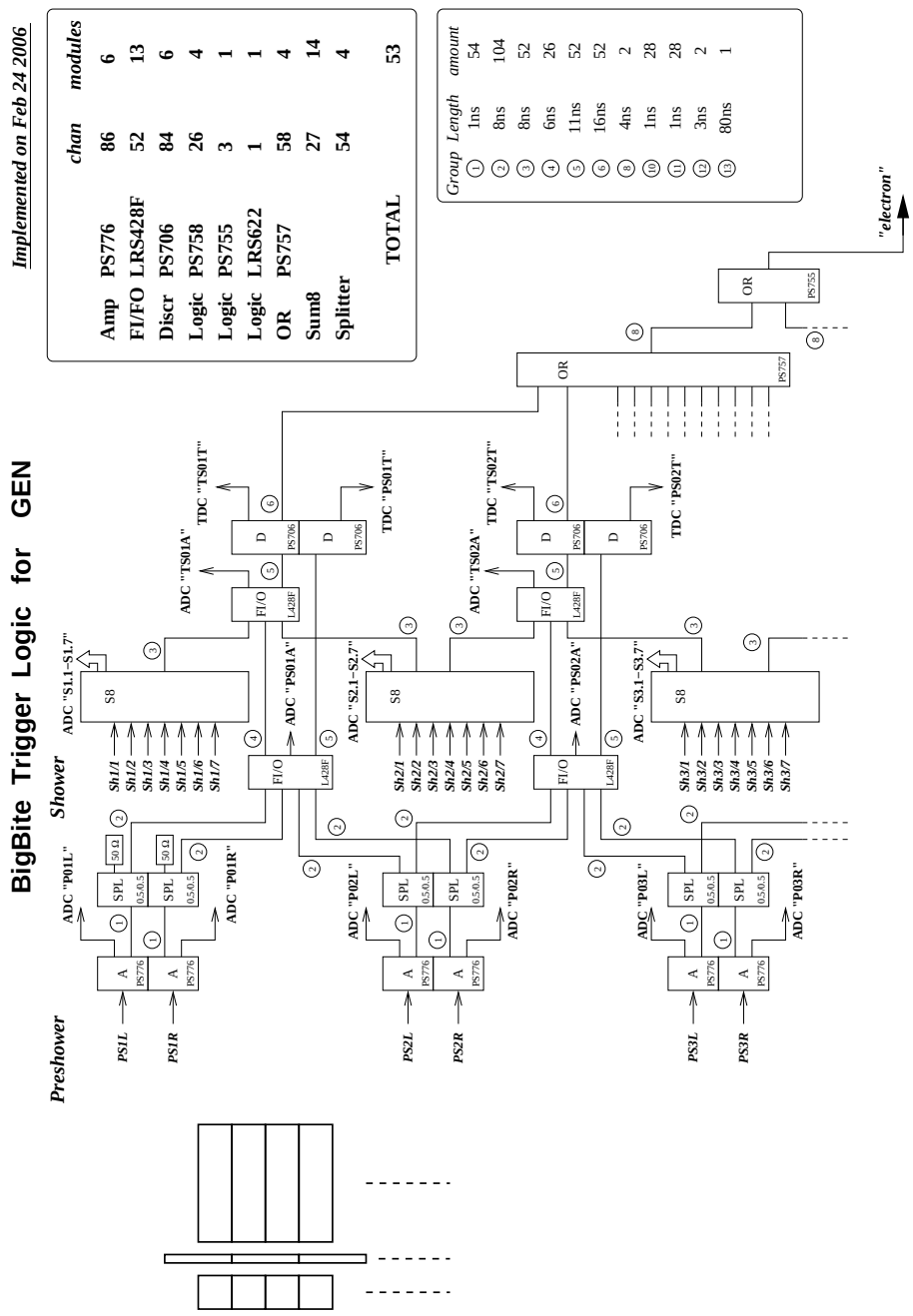

Figure 3.19: Diagram of the BigBite shower and preshower summing modules [66].

Trigger Type	Description
1	Neutron Arm Trigger
2	BigBite Trigger
3	Neutron Arm/BigBite Coincidence
7	8.5 Hz Pulser
8	105 kHz Helicity Synchronization Signal
9	30 Hz Helicity Quad Duration Signal

Table 3.5: E02-013 trigger types.

The F1 TDC is a common-stop multihit TDC developed by the Jefferson Lab electronics group. It features a timing resolution of approximately 120 ps. This higher resolution TDC was chosen due to the necessity of determining the neutron momentum accurately from time of flight.

LeCroy 1881 ADCs were used for measuring amplitudes produced by the PMTs. The 1881 features 64 channels per module, has a short conversion time of 12 μs, and can store up to 64 events in its event buffer.

Triggers

Given a set of detector signals, the "trigger supervisor" determines if a readout of event data should occur from the detector electronics. A number of different trigger conditions were used in E02-013, given in Table 3.5.

A copy of each trigger signal is also sent to a set of general scalers and helicity gated scalers. The trigger supervisor is also set with a prescale factor for each trigger type, which determines how frequently to initiate a readout for each trigger signal. For example, for a trigger with a prescale factor of 1000, only 1 of 1000 of these triggers will actually cause a readout and store the raw data. This is useful for events that occur very frequently, but are not desirable to record in every instance due to storage space and readout time concerns, such as the neutron arm triggers in the absence of a BigBite trigger.

A trigger based on the coincidence between BigBite and the neutron arm requires some mechanism to determine if the triggers from the two arms overlap sufficiently to be a coincidence event. This mechanism must take three considerations into account for this experiment. First, the times between the BigBite and neutron arm signals may vary due to differences in time of flight in both arms and the window for coincidence must be sufficiently wide. Second, the window must not be too large as false coincidences will be recorded when caused by random background. Third, a background event may cause an early trigger in the neutron arm, but a coincidence may still occur in the overlapping timing window. A diagram of the electronics to generate a trigger and readout signals is shown in Fig. 3.20.

To form the T3 coincidence signal, the T1 (neutron arm) trigger is approximately 40 ns long and the T2 (BigBite) trigger is approximately 100 ns long, as shown in Fig. 3.21. The leading edge of the logical AND between these two signals defines the start of the T3 (coincidence) signal, which is approximately 40 ns long. The electronics are designed such that nominally, the T1 signal arrives approximately 40 ns after the T2 signal. This is achieved by making signal timing adjustments for the T1 signal for each kinematic to account for different nominal times of flight.

At the start of the T3 signal, a signal called level 1 accept (L1A) is also generated. This signal is sent to a LeCroy 1875 TDC, which has a common stop given by the BigBite readout signal (the signal fed to the TDC common stops and ADC gates). The time produced by this TDC channel is then the difference between the BigBite readout and the L1A, referred to in the experiment as ctimeL1A. The L1A is also given to the neutron arm electronics as the readout signal. A separate module, called the retiming module, handles the generation of the BigBite readout signal. This

module produces a signal a fixed amount of time after the T2 trigger. However, in the case where no T2 trigger is present (such as with a single-arm T1 event), a signal is generated a fixed amount of time after the L1A signal. See Fig. 3.21.

To determine if a T2 signal is present for coincidence, a BigBite signal is required within some time window smaller than the 100 ns window. This presents the possibility of a real coincidence event occurring, but the T2 signal retiming failing as the edge is outside the smaller retiming window. While the electronics have been set up such that under normal circumstances the T1 signal arrives nominally 40 ns after the T2 signal, the presence of background events may trigger the neutron arm early. This may result in a L1A signal matched to the leading edge of the T2 signal (Fig. 3.22).

Time of Flight Determination

A simplified timing diagram is presented in Fig. 3.23. We are most interested in calculating the time of flight, $t_{\rm tof}$, using the TDC electronics readouts values. We have several such variables read out from TDCs for any given event. Those of interest for the time of flight calculation are, $t^{\rm TDC}_{\rm BB,hit,L}$ and $t^{\rm TDC}_{\rm BB,hit,R}$, the left and right PMT TDC value of the scintillator hit time, $t^{\rm TDC}_{\rm clus,L}$ and $t^{\rm TDC}_{\rm clus,R}$, the left and right PMT TDC value of the neutron arm bar containing a hit, and $t^{\rm TDC}_{\rm L1A}$, the TDC value of the difference between the BigBite readout signal and the L1A trigger.

Each TDC time read out is the time difference measured between the signal fed into the TDC, such as from the discriminator attached to a PMT connected to an end of a scintillator bar, and some stop signal. For the BigBite scintillator, the stop is generated from the retiming modules and for the neutron arm, from the level 1 accept, or L1A signal from the trigger supervisor. So,

$$t^{\rm TDC} = t^{\rm read} - t^{\rm stop}. \tag{3.28}$$

The left and right values for the PMT times are generated by the light propagation from a single hit through the scintillator reaching each end, shown in Fig. 3.24. The signal at each end then produces a voltage signal from the PMT, which is sent to a discriminator. If the signal is above threshold, then a logic signal is sent out to the TDC. The discriminator may produce a small time delay, which varies on the order of hundreds of ps and as a function of the signal amplitude. This is due to the shape of the pulse (in time) reaching the threshold value at different points of the pulse. It is referred to as a "time-walk" effect and is denoted in the figure as $t_{\rm tw}$.

For the BigBite scintillator hit and neutron arm cluster, we can reconstruct the time of the scintillator interaction, up to a constant, by taking the average of the left and right signals. This removes any dependence on horizontal hit position, or y, as shown in the figure. We define this averaged time, $t^{\rm TDC,avg}$ as

$$\begin{aligned} t^{\rm TDC,avg} &= \frac{t^{\rm TDC}_{\rm L} + t^{\rm TDC}_{\rm R}}{2} = \frac{t^{\rm read}_{\rm L} + t^{\rm read}_{\rm R}}{2} - t^{\rm stop} \\ &= t_{\rm hit} + \frac{t_{\rm L,tw} + t_{\rm R,tw} + t_{\rm L,0} + t_{\rm R,0}}{2} + \frac{d}{2c_s} - t^{\rm stop} \\ &= t_{\rm hit} + \frac{t_{\rm L,tw} + t_{\rm R,tw}}{2} + t_{0,\rm bar} - t^{\rm stop} \end{aligned} \tag{3.29}$$

where the $t_{\rm L,0}$ and $t_{\rm R,0}$ are values are related to the cable lengths from the PMT to the TDC input, which are in general different for each PMT. $t^{\rm stop}$ is the time of the stop signal input to the TDC. We have also defined a bar-dependent constant, $t_{0,\rm bar}$

$$t_{0,\rm bar} = \frac{t_{\rm L,0} + t_{\rm R,0}}{2} + \frac{d}{2c_s}. \tag{3.30}$$

For the neutron arm the stop is $t_{\rm L1A} + a$, the level 1 accept time plus a constant for cable length propagation. For the BigBite scintillator this is $t_{\rm RT}$, the time the retiming module issues a signal

calculated on the inputs of the level 1 accept and the BigBite trigger. All of the constants, which are bar dependent and do not vary on any other parameters, are summed into the constant $t_{0,\mathrm{bar}}$ which must ultimately be calculated in our calibration process. The hit time in the scintillator is then

$$t_{\mathrm{hit}} = t^{\mathrm{TDC,avg}} - \frac{t_{\mathrm{L,tw}} + t_{\mathrm{R,tw}}}{2} - t_{0,\mathrm{bar}} + t^{\mathrm{stop}}. \tag{3.31}$$

To find the time of flight of the nucleon from the target, t_{tof}, from the hits in the BigBite scintillator and the neutron arm cluster, we relate them to the TDC read values

$$t_{\mathrm{tof}} = t_{\mathrm{clus}} - t_{\mathrm{evt}} \tag{3.32}$$

$$t_{\mathrm{BB,hit}} = t_e + t_{\mathrm{evt}} \tag{3.33}$$

$$t^{\mathrm{TDC}}_{\mathrm{L1A}} = t_{\mathrm{L1A}} - t_{\mathrm{RT}} + a \tag{3.34}$$

where t_{evt} is the time of the scattering event, t_e is the time of flight of the electron from the target to the BigBite scintillator.

Taking the sum of Eq. 3.33 and Eq. 3.32, substituting in Eq. 3.31 for $t_{\mathrm{BB,hit}}$ and t_{clus}, and solving for t_{tof} we have

$$\begin{aligned} t_{\mathrm{tof}} = & \left(t^{\mathrm{TDC,avg}}_{\mathrm{clus}} - \frac{t_{\mathrm{clus,L,tw}} + t_{\mathrm{clus,R,tw}}}{2} - t_{0,\mathrm{clus,bar}} + t_{\mathrm{L1A}}\right) \\ & - \left(t^{\mathrm{TDC,avg}}_{\mathrm{BB,hit}} - \frac{t_{\mathrm{BB,hit,L,tw}} + t_{\mathrm{BB,hit,R,tw}}}{2} - t_{0,\mathrm{BB,hit,bar}} + t_{\mathrm{RT}}\right) + t_e. \end{aligned} \tag{3.35}$$

Using Eq. 3.34 to relate t^{RT} and t^{L1A}, we finally get

$$\begin{aligned} t_{\mathrm{tof}} = & \left(t^{\mathrm{TDC,avg}}_{\mathrm{clus}} - \frac{t_{\mathrm{clus,L,tw}} + t_{\mathrm{clus,R,tw}}}{2} - t_{0,\mathrm{clus,bar}}\right) \\ & - \left(t^{\mathrm{TDC,avg}}_{\mathrm{BB,hit}} - \frac{t_{\mathrm{BB,hit,L,tw}} + t_{\mathrm{BB,hit,R,tw}}}{2} - t_{0,\mathrm{BB,hit,bar}}\right) + t_e + t^{\mathrm{TDC}}_{\mathrm{L1A}} - a. \end{aligned} \tag{3.36}$$

For convenience, we rewrite this using a corrected TDC time, $t^{\mathrm{TDC,corr}}$,

$$t^{\mathrm{TDC,corr}} = t^{\mathrm{TDC,avg}} - \frac{t_{\mathrm{L,tw}} + t_{\mathrm{R,tw}}}{2} - t_{0,\mathrm{bar}}. \tag{3.37}$$

The time of flight is then simply

$$t_{\mathrm{tof}} = t^{\mathrm{TDC,corr}}_{\mathrm{clus}} - t^{\mathrm{TDC,corr}}_{\mathrm{BB,hit}} + t^{\mathrm{TDC}}_{\mathrm{L1A}} + t_e - a. \tag{3.38}$$

From this it is apparent that the time of flight is dependent on the three TDC times, a set of constants (which are bar dependent), the timewalk effects for each PMT, and the time of flight of the scattered electron from the target to scintillator planes. It is worth noting that regardless of how the L1A time is determined and with which signal the retiming is done, there is no effect on the time of flight, provided that the electronics chosen are capable of recording the more extreme time differences presented in this case.

For future notation, we will use t_{clus} and $t_{\mathrm{BB,s}}$ for the the TDC corrected times, $t^{\mathrm{TDC,corr}}$.

Scalers

Scalers were employed to monitor several portions of the experiment. For each scaler signal, an additional helicity-gated scaler was employed to monitor asymmetries.

Along with trigger rates, each of the six BCMs, three different gains on two different monitors, were also employed. A voltage to frequency converter was used to change each signal generated by the BCMs into a scaler input.

3.4 Analysis Software

Due to the scope of the data involved, a large amount of software is required to analyze the raw data produced by the detectors. While most of the detectors produced a relatively simple signal, such as an amplitude or hit time, certain detectors require a significant amount of analysis. For E02-013, the most effort was placed in producing high-resolution tracks from a set of hits in the multiple wire drift chambers in BigBite and analyzing clusters of hits in the neutron arm.

3.4.1 ROOT/Hall A Analyzer

ROOT is a software package developed by CERN designed to aid in the organization, analysis, and representation of data [67]. It is distributed freely under the GNU lesser general public license (LGPL) and GPL. Among its features, it includes well documented facilities to quickly store, retrieve, and manipulate large arrays of data, produce histograms and graphs, and provide a number of analysis facilities such as fitting data to curves. It also provides methods to store and retrieve abstract data types to and from files allowing for simplified development in complex data situations.

ROOT is built around CINT, a C programming language interpreter that also allows for dynamic library loading. This facility allows for rapid development of software around the C++ classes included with ROOT and gives the opportunity to include outside code away from the slower interpreted environment.

The Hall A collaboration has developed an extension of ROOT called the Hall A ROOT/analyzer [68]. This package takes advantage of the features offered by ROOT and provides abstraction for describing various detector models as well as facilities for decoding raw data produced by CODA and producing ROOT trees. Originally designed to provide an analysis framework for the Hall A high-resolution spectrometers (HRS), this package was modified for use in E02-013 in a package called the AGen library.

There were two software development efforts which are important to E02-013. These were the development of software to analyze and organize data produced by the neutron arm and the tracking and optics code in the BigBite drift chambers.

3.4.2 Neutron Arm

The neutron arm consists of over 600 photomultiplier tubes, each connected to a block of scintillator. For each event, scattering of incoming hadrons can cause shower induced signals which may then span across several other scintillator blocks, leading to somewhat complex event types. Additional concerns arise from interactions from accidental background events, which are indistinguishable from other events.

To handle this detector, software had to be developed to take the individual signals in each photomultiplier tube and combine them appropriately to attempt to reconstruct each individual interaction. These interactions are intended to span across several layers, so some type of clustering of hits together must be used.

Coordinates are defined as the x axis running against gravity, z normal to each scintillator plane in the nominal direction of recoiling nucleons, and y such that it forms a right handed coordinate system. The x position of each hit is determined solely by the central vertical position of the scintillator log. z is defined by the plane that the log resides in. Both of these must be found by surveying relative to the experimental hall.

Raw Analysis

As described in Section 3.3.6, for each PMT signal one time is recorded in a TDC. This time is subject to timewalk effects, which must be corrected for, similar to the corrections discussed in the previous section. Furthermore, the amplitude measured by the PMTs are sent to a set of ADCs.

The ADC value is assumed to be proportional to the amount of light collected, offset by a pedestal value, $A_{\rm ped}$, which is constant for a given ADC channel. The pedestal-subtracted signal which we say is proportional to the amount of light, A, can be written

$$A = A_{\rm ADC} - A_{\rm ped} \tag{3.39}$$

The value of the pedestal can be determined by examining sets of data where no amplitude is expected. We will assume that all amplitudes have had the pedestal already subtracted.

Continuing the notation presented in Section 3.3.6, the left or right PMT time in the TDC is given by

$$t^{\rm TDC} = t_{\rm hit} + t_{\rm prop} - CA^P + t_0 - t^{\rm L1A} \tag{3.40}$$

where $t_{\rm hit}$ is the time the hit occurred, with corrections for signal propagation time and timewalk effects, $t_{\rm prop}$ is the propagation time of light through the scintillator from the cluster to the PMT, t_0 is a constant related to the signal propagation time from the PMT to the TDC, A is the sum produced by the ADCs, which is proportional to the integrated amplitude of the signal, and C and P are constants calibrated for each PMT. $t^{\rm L1A}$ is the time of the stop signal for the TDC electronics. The amplitude term, CA^P, is a model used to handle the time-walk effects.

By using the left and right PMT TDC time differences, the position along the bar where the signal originated can be reconstructed. The propagation times for the left and right PMTs are $t_{\rm prop,L} = \frac{d/2-y}{c_s}$ and $t_{\rm prop,R} = \frac{d/2+y}{c_s}$, where y is the position along the scintillator log as was shown in Fig. 3.24, d is the total length of the scintillator log, and c_s is the effective speed of light in the scintillator.

Ignoring time-walk effects, the horizontal, or y, position as measured by the scintillator log relative to the equidistant point between the PMTs can be reconstructed by taking the difference between the two times

$$y = \frac{t_{\rm L}^{\rm TDC} - t_{\rm R}^{\rm TDC}}{2c_s} - \frac{t_{\rm L,0} + t_{\rm R,0}}{2c_s}. \tag{3.41}$$

This measurement requires knowledge of the effective speed of the light in the scintillator, c_s, and a constant related to the difference in the cable lengths from the PMTs to the TDC. For E02-013, this was determined by using marker scintillators running parallel to the x axis at known positions, described in Section 4.3.1.

The amplitude for each signal is subject to attenuation through the scintillator medium. This attenuation can be modeled as an exponential decay dependent upon the y position of the hit

$$\begin{aligned} A_{\rm L} &= A_{\rm L,0} e^{\frac{d/2-y}{\Gamma}} \\ A_{\rm R} &= A_{\rm R,0} e^{\frac{d/2+y}{\Gamma}} \end{aligned} \tag{3.42}$$

where $A_{\rm L,0}$ and $A_{R,0}$ are the raw amplitudes measured in the ADCs, Γ is the attenuation constant for the scintillator, which has units of length and A_L and A_R are the amplitudes measured at the PMTs.

For each event, several measurements from the PMTs are required to reconstruct a hit. However, there is the possibility for the generated signals to be below threshold of the discriminators for the PMTs, resulting in hits that are not recorded. These events are discarded and are not used in analysis. In all events, ADC information is recorded as the gate for the ADCs is given by the neutron arm trigger.

Cluster Finding

The interactions of the nucleons in the neutron arm frequently provide reconstructed hits across several layers. Given a set of individual hits for an event, the analysis software attempts to find hits

that were likely caused by a single particle and to combine them into a single object known as a "cluster". These clusters will then be used to identify coincidence events using BigBite.

The software first takes all combinations of left and right hits on a scintillator, and places a cut upon the reconstructed horizontal y position, such that

$$|y_{\text{hit}}| < \frac{d}{2} \tag{3.43}$$

where $\frac{d}{2}$ is half the length of the scintillator bar. This ensures that the two hits used for this reconstruction were likely from a particle passing through position y. Reconstructed hits that have neighboring hits on adjacent scintillators in the same plane that are matched in time (within 10 ns) are combined. Hits in neighboring scintillator planes of similar x positions (within 1.5 bar spacings) and within 10 ns are also considered to be in the same cluster.

The time of flight and position for this cluster are determined by the hit closest to the front (smallest z value) of the neutron arm. An amplitude-weighted position is used in the case of adjacent multiple hits on the same plane by

$$x_{\text{weighted}} = \frac{\sum_{\text{hits}} A_{\text{hit}} x_{\text{hit}}}{A_{\text{cluster}}}. \tag{3.44}$$

3.4.3 Veto Matching

Matching clusters to veto hits is used to determine the charge of the particle which caused the cluster. To determine a match between a veto hit and a given cluster, all veto hits are considered and are compared by examining the difference in position and time. First, a veto hit on each plane is sought to fit the requirement

$$|x_{\text{clus}} - x_{\text{veto}} - x_0| < \Delta x \tag{3.45}$$

where x_{clus} is the reconstructed x position of the cluster and x_{veto} is the x position of the veto bar that fired. x_0 is a constant alignment offset that must be determined from the data. Δx is on the order of 30 cm.

The time of each veto hit is subject to propagation distortion due to the fact that we cannot compare "left" and "right" hits on the same bar. However, attempts to correct this can be made using knowledge from the y position of the cluster. The time difference between a veto hit and a neutron arm hit is given by

$$\Delta t = t_{\text{veto}} - t_{\text{clus}} + \frac{|y_{\text{clus}} - y_0|}{c_s} + t_0 \tag{3.46}$$

where t_{veto} is the TDC time read for the veto, t_{clus} is the reconstructed, corrected cluster time, given in Section 3.3.6, y_{clus} is the reconstructed y position of the cluster. c_s, y_0, and t_0 are constants to be determined from the data.

There are three distinct possibilities to consider. If Δt is within some reasonable time window (the charged window), we consider that to be a charged hit. If there is a hit on the veto in a given window before the start of the charged window and that hit is within the dead time for the electronics, we consider the time to be unrecordable and we are blind to the charge. These events must be discarded. If we find no hits in either of these regions then we consider the particle to have been neutral. The size and placement of these windows must be determined from the data. See Fig. 3.25.

If both planes are considered blind in the cluster timing region, the cluster is discarded. Otherwise, if a veto hit is then found to match these criteria in either plane, a charged particle is assumed. Finally, all other clusters are assigned a neutral charge.

3.4.4 BigBite Tracking

The BigBite tracking code works mainly with the wire hits in the MWDCs, using the rest of the detector set to help reduce noise and computation time. Noise becomes a significant factor in doing tracking as additional hits that must be considered when fitting tracks contribute to the computation time. The noise to signal ratio can be determined by examining the number of hits above a background that is flat in time. It has been observed to be on the order of 10 for a production environment. This presents a significant challenge to perform sufficiently efficient and fast tracking.

The purpose of the tracking code is to find straight lines by using signals from the BigBite detector stack. Primarily, these signals come from the drift chambers, but information from the shower, preshower, and scintillator is also used. By exploiting how the electron trajectories depend on the magnetic field of BigBite and using the position given by the shower to fix one point of the track, we can narrow volumes of interest in the spectrometer detectors down considerably. Then, using a reduced set of hits in the drift chambers, we can then apply some algorithm to find the best straight line representing the trajectory of our particle that caused the trigger.

The ultimate challenges of the tracking code are to:

1. Identify the subset of hits that represent our signal, eliminating noise as well as possible.
2. Identify the combination of hits which represents the trajectory of the track.
3. Identify which left/right configuration of the hits is the most likely configuration.

Once a track is found, using the knowledge that it originated from the electron beam and how it travels through the magnetic field, we can then measure the momentum of the electron to an accuracy of $\sigma_{\frac{\delta p}{p}} \approx 1\%$.

General Algorithm

The general algorithm to find tracks is as follows:

- Decode
  1. Identify hits in the drift chamber
  2. Remove hits that are outside of a specific time window
- Coarse Process
  1. Identify a cluster in the shower
  2. Remove hits that are outside a volume between the magnetic target image and the shower block
  3. Find all valid combinations of wires across all active planes
  4. Fit for straight trajectories for each hit combination using a minimum χ^2 fit using only the wire positions for each combination and save a subset which are potentially real tracks

BigBite Configuration for G_E^n	
Distance from target to magnet face	1.09 m
Distance z_{targ} from target to drift chamber 1 center	2.25 m
Height difference (y_{LAB}) from target to drift chamber 1 center	0.17 m
Detector stack pitch	10°

Table 3.6: Nominal geometrical configuration of BigBite for E02-013.

5. Tracks that are sufficiently similar are identified as the same track and the poor χ^2 combinations are removed

- Fine Process

1. Find the associated scintillator hit from the coarse tracking and correct the drift time
2. For our coarse tracks, find the drift distance from each wire from the drift time
3. From the best combinations sorted by χ^2 identify the proper left/right differentiation, and refit the tracks using the drift distances
4. Tracks that are sufficiently similar are identified as the same track and the poor χ^2 combinations are discarded

A set of timing window cuts are performed on all hits recorded in the TDCs to remove hits that cannot be associated with the trigger. The width of these cuts are defined by the maximum drift time, about 200 ns. In theory, the window is variable for each plane due to differing voltages across chambers and thus different maximum drift times. However, examination of the drift time spectrum proved the distributions widths were practically identical. Typically, this type of cut reduces the number of hits to consider by about a factor of 10 for a production run.

Shower clusters are currently determined by identifying the shower block with the largest signal. A more sophisticated method involving the weighted sums of the block positions will likely be implemented in the future, but was not performed for this analysis. The block face normal to the electron tracks is 8.5 cm $\times$ 8.5 cm, which is then the accuracy of the position reconstruction. After the shower clusters are determined, a window around the cluster position and the target image is used to define two ends of a volume. The target image is the result of track deflection in the magnet and is spread out in the dispersive direction due to the range of possible momenta of the tracks (Fig. 3.26 and Fig. 3.27). The projection of rectangular slices of the volume onto each plane defines the area of valid wires to be considered in tracking, Fig. 3.28. If any portion of a wire with a recorded hit enters in this area, that hit is considered valid and available to the tracking algorithm.

In effect, these cuts place a very coarse momentum cut on the data. To determine the proper parameters for these cuts, rough analysis must be done on real or Monte Carlo data to look at the wire distributions around some line drawn between the center of the target image and the cluster center.

Valid Wire Combinations and χ^2 Fitting

The determination of wire combinations that form a valid, straight track through the chambers and then fitting them is one of the more difficult tasks for tracking. The tracking code developed approaches the problem by finding all reasonable combinations and then finding the most likely combinations based on the χ^2 values from the fit. While this approach lacks any elegance, it has the desirable feature of a high efficiency of finding a track.

A set of matrices is generated to be used to produce the four parameters necessary to describe a track, x_0, y_0, x', and y'. The goal of fitting is to find r_λ, a column representation of the four track variables and represents the minimum χ^2 fit based upon the points d_i. We wish to find a matrix $F_{\lambda i}$ such that

$$r_\lambda = F_{\lambda i} d_i. \tag{3.47}$$

where d_i is the position in the coordinate system measured by the ith plane. For each plane, this is the axis running perpendicular to the wires, e.g. for the X planes, this is directly the $x_{\rm det}$ coordinate. These were originally defined in Section 3.3.5 and are x, y, x', and y', the (x, y) detector coordinate at the first drift chamber plane and the two slopes. We adopt the convention that Greek indices run

from 0 .. 4 and Roman indices run from 1 .. N where N is the number of planes to fit. Summation over Greek indices is implied. χ^2 is then

$$\chi^2 = \sum_i \frac{1}{\sigma_i^2}(d_i - f_i)^2 \tag{3.48}$$

where σ_i is the resolution of the ith plane and f_i is the intercept of the track described by r_λ in the plane coordinate system of the ith plane. There is just a linear relationship between f_i and r_λ, so we can define a matrix, $M_{i\lambda}$

$$f_i = M_{i\lambda} r_\lambda \tag{3.49}$$

where a summation over λ is implied. We wish to minimize χ^2 with respect to the four track variables

$$\frac{\partial \chi^2}{\partial r_\eta} = 2 \sum_i \frac{1}{\sigma_i^2}(d_i - M_{i\lambda} r_\lambda) M_{i\eta} = 0 \tag{3.50}$$

Let

$$\alpha_{\lambda\eta} = \sum_i \frac{1}{\sigma_i^2} M_{i\lambda} M_{i\eta}. \tag{3.51}$$

Then, multiplying both sides by r_η and implicitly summing over η and γ

$$\alpha_{\lambda\eta} r_\eta = \sum_i \frac{1}{\sigma_i^2} M_{i\lambda} M_{i\gamma} r_\gamma. \tag{3.52}$$

Using Eq. 3.50,

$$\alpha_{\lambda\eta} r_\eta = \sum_i \frac{d_i}{\sigma_i} \frac{M_{i\lambda}}{\sigma_i} = \sum_i \frac{M^T_{\lambda i}}{\sigma_i} \frac{d_i}{\sigma_i}. \tag{3.53}$$

Since α is a square matrix, if its determinant is non-zero, we can invert it

$$r_\eta = \alpha^{-1}_{\eta\gamma} \sum_i \frac{M^T_{\gamma i}}{\sigma_i} \frac{d_i}{\sigma_i}. \tag{3.54}$$

We now have a matrix that, when multiplied by the column vector, d_i, gives us our minimum χ^2 track, so

$$F_{\eta i} = \alpha^{-1}_{\eta\gamma} \frac{M^T_{\gamma i}}{\sigma_i^2}. \tag{3.55}$$

Since the drift distance, d_i, is measured in our drift chambers, this gives a simple way to quickly calculate a track given a set of points across several planes. There are a few interesting things to note: first, the matrix M is easy to calculate, as it is just a rotation given x and y projected onto a plane (for example, for an X plane this is trivially $f_X = x_0 + x' z_X$).

All of these fitting matrices for each potential plane combination are calculated each time the code is initiated (typically once for a given replay). The amount of time necessary for the calculation is on the order of one second on modern computers and is not a concern. The calculation of the intermediate matrix, α, allows us to identify which plane combinations can be used to fit a track.

If the number of planes to fit to is less than 4, α is singular. Therefore, it is necessary (but not sufficient) to have at least four planes to reconstruct a track. If the matrix α is singular, we cannot invert it and therefore we cannot fit a track. For example, this occurs in the cases where the planes used do not constrain the problem appropriately to find a unique track. For example, if a fit is attempted using only X planes, we do not have any information on the y positions and therefore cannot generate a track with y information. In the generation of the these matrices we immediately find which combinations of planes can be used in reconstruction and which combinations cannot.

Left/Right Differentiation

The need for left-right differentiation comes from our ignorance on the direction of drift. Since the drift time just provides a magnitude, a method is necessary to determine which side of the wire the track passed on for each hit used in the fit. There are several methods that were considered for this code.

The simplest method is to first fit using just the wire positions themselves and then look at which sides of the wires the fit track fell on. This method works well with a large number of planes, since the spacial resolution achieved will becomes better. However, if this coarse track passes sufficiently near a wire position, the left/right resolution becomes difficult to determine and may choose the wrong side.

In the other extreme, a brute force method can be used to test all possible left/right combinations and choose the one that produces the best χ^2. This method uses all available information, can be considered to be fairly accurate, and works well with a small number of planes. However, as the number of planes in the fit increases, it quickly becomes bogged down in combinatorics, as the number of combinations it must try is 2^N where N is the number of planes.

A variation of the second method is used, where the minimum χ^2 is chosen but for subsets of the hits. The natural way to divide the problem is across planes of the same type, so all left/right combinations of the U planes will be done separately from the V and X planes. In the cases where there are not sufficient degrees of freedom to compare χ^2s (i.e. two or fewer planes), the other plane types are calculated first. Then all combinations of planes that have not been fixed left/right are combined with the fixed planes, and the differentiation is chosen by the minimum χ^2.

Similar Tracks and Geometry Checks

The tracking algorithm is designed to check all combinations of hits that can be considered a possible signature for a track. However, the criteria for determining what is likely a real track and what is simply fitted noise is not trivial. For the most part, χ^2 and physical considerations give a useful guide to determining these criteria.

χ^2 is the first thing calculated when a set of hits is fit and while placing a tight cut on χ^2 would cause inefficiencies in the tracking, a loose cut appears to be reasonable. Therefore, any combinations that give a χ^2 above some minimum value are immediately discarded. This minimum value is on the order of 50 independent of the number of degrees of freedom.

Geometrical considerations are also taken into account. Any track must stay within the active area of all planes whether or not that plane was used in the fit. This removes tracks that did not originate from the electron beam and false combinations we do not wish to consider.

Any track must stay near the wires it was fit with, so a track is required to have all wires within some fixed distance. The intention of the design of the drift chambers was to have a single wire firing due to a track. It is unlikely that more than a pair of wires in the same plane will fire due to the same track.

Finally, considerations must be made regarding subgroups of the hits used for a track. For a track fully described by hits across 15 planes, there are many subgroups of these hits that will also yield a valid (and identical) track, but at a reduced resolution. In this light, we would with to maximize the number of hits used to describe a track. However, with the addition of noise, care must be taken to exclude it from fitting. To do this, we identify all similar tracks as tracks that share a similar intercept across a minimum number of planes. They are then sorted by χ^2 per degree of freedom and the best track is chosen. All other tracks that were similar to the one with the minimum χ^2 per degree of freedom are discarded.

Processing Time

The time it takes to process an event appears to go linearly with the number of calls to a specific function used to build all groups to be fit. The amount of time spent in tracking can be represented by

$$t_{\text{tracking}} \approx (10\ \mu s) \times \sum_{c \in \{\text{plane combinations}\}} \sum_{n=0}^{\text{nplanes}(c)} \prod_{m=0}^{n} \text{nhits}(\text{plane}_m). \tag{3.56}$$

There are several checks that are done to not spend unreasonable amounts of time on individual events. First, we compute a number that roughly represents a measure of the processing time for a given event, as represented by the Eq. 3.56. A cut is placed on this number and events that do not pass this cut are identified as "too busy" and are skipped.

There is also a soft and hard maximum on the number of groupings to consider as the code searches for them. When the soft maximum is reached, the code finishes up looking for groups with that number of planes to be considered and stops. As the groups are considered in descending order of number of planes, this halts looking for any smaller subgroups. The hard maximum halts looking for groups as soon as it is reached. The values for these cuts are determined from the data given desired constraints on processing times.

3.4.5 Dead Time and False Asymmetries

For this experiment it is important to be able to determine the number of events lost to dead time in our electronics and data acquisition, as well as determine if these effects, or any other portion of the analysis, introduce false asymmetries into our data. These false asymmetries can occur due to helicity-dependent inefficiencies or background and ultimately bias our calculation of G_E^n.

Electronic dead time deals with the masking of signals in the front-end electronics, such as PMTs and discriminators, due to the recovery times. This effect with regard to the trigger electronics can be measured to determine the number of events lost to this effect. It should be noted that other dead times still remain in the data, such as in the readout of individual PMTs. To evaluate the fraction of events lost to these effects, a pulser signal of 8.5 Hz was sent to the BigBite and neutron arm trigger electronics as an artificial T3 event. This signal was also recorded by the trigger supervisor as a T7 event.

By examining the number of T7 events that do not have a corresponding T3, the quantity $r_{\text{dead,elec}} = 1 - N_{\text{T7\&T3}}/N_{\text{T7}}$ is a measure of the fraction of events lost to electronic dead time of the trigger, where $N_{\text{T7\&T3}}$ is the number of events with a T3 and T7 and N_{T7} is the number of events with a T7 but no T3.

The data acquisition (DAQ) dead time correction, is the fraction of events lost due to data acquisition electronics, the readout controllers, being in a "busy" state. In this state these electronics are in the process of reading the data from the TDC and ADC modules at the request of the trigger supervisor and all other requests by the trigger supervisor for readout are discarded, resulting in a lost event. The length of these periods is around 300-500 μs.

To determine this dead time, the number of T3 events written to the data file is compared to a scaler connected to the T3 signal. This scaler provides the "true" number of T3 events. If the number of T3 events is prescaled, this must also be taken into account. The dead time is then

$$r_{\text{DAQ,dead}} = 1 - \frac{c_{\text{prescale}} N_{\text{T3,data}}}{N_{\text{T3,scaler}}} \tag{3.57}$$

where c_{prescale} is the prescale factor for T3 events. False asymmetries can be introduced through dead times affecting one helicity state more than the other. In such a case the number of events for one state becomes skewed, producing incorrect raw asymmetries, and ultimately affecting the value for G_E^n.

For the case of dead time asymmetries, dead time is calculated for each helicity state. By then correcting the number of events in each state for the dead time, artificial asymmetries by the dead time are then removed. Corrections are done by dividing the counts for a given helicity, h, by the efficiency for that helicity, $1 - r_{\text{dead},h}$, to be discussed in Section 5.8.

Two other potential sources for false asymmetries come from the beam charge asymmetry and from the BigBite tracking code. The beam charge asymmetry is determined by examining the helicity-gated totals from the BCM scalers, which keep helicity-gated totals of the beam charge. Beam charge, while examined post-running, was also carefully and continually monitored during the experiment. To correct for beam charge asymmetries, an artificial efficiency, ϵ for each helicity, h, is constructed, where

$$\epsilon_{Q,h} = \frac{2Q_h}{Q} \tag{3.58}$$

where Q_h is the accumulated charge for helicity state h and Q is the accumulated charge for both helicity states.

Tracking asymmetries are introduced by the tracking code having different efficiencies on reconstruction of one helicity over the other. Such an effect could occur due to an asymmetry in the rate dependent tracking efficiency. This number is more difficult to evaluate because of natural asymmetries in the data, so the naive attempt to identify one helicity state more frequently reconstructed than another is incorrect. However, by examining how frequently events are skipped due to being "too busy" in proportion to the number reconstructed for a given helicity state, h, a number analogous to dead time can be determined

$$r_{\text{track},h} = \frac{N_{\text{skip,hel}}}{N_{\text{recon,hel}} + N_{\text{skip,hel}}}. \tag{3.59}$$

A total correction can be determined by taking the product of the live times and effective live times.

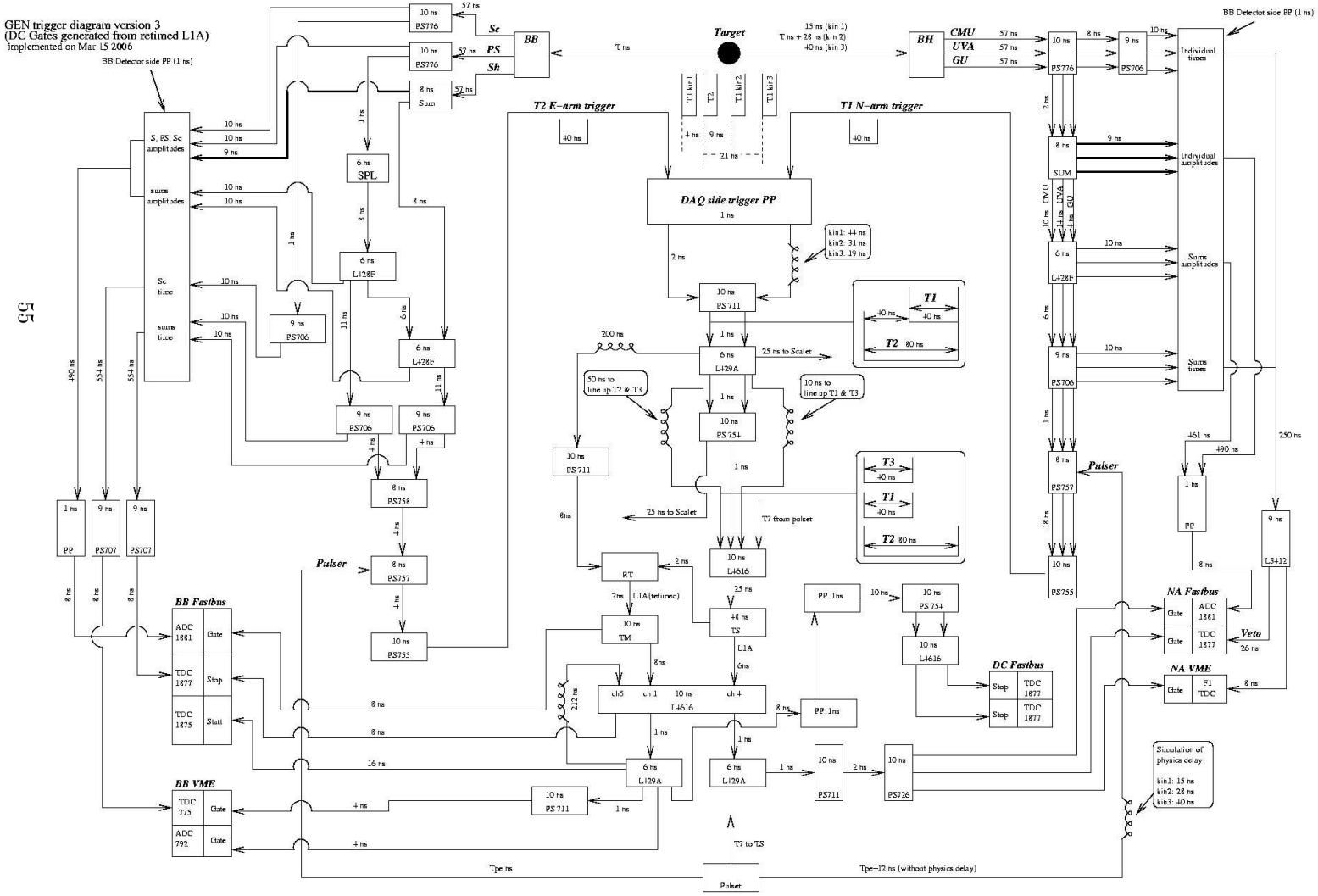
GEN trigger diagram version 3
(DC Gates generated from retimed L1A)
Implemented on Mar 15 2006
BB Detector side PP (1 ns)
Target
BB
BH
Sc
PS
Sh
CMU
UVA
GU
T2 E–arm trigger
T1 N–arm trigger
DAQ side trigger PP
T1
T2
T3
Pulser
BB Fastbus
BB VME
DC Fastbus
NA Fastbus
NA VME
Veto
Individual times
Individual amplitudes
Sums amplitudes
Sums times
Simulation of physics delay
kin1: 15 ns
kin2: 28 ns
kin3: 40 ns
T7 from pulser
T7 to TS
Tpe ns
Tpe−12 ns (without physics delay)

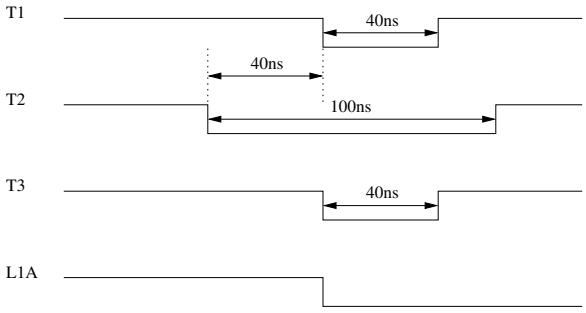

Figure 3.21: Neutron Arm/BigBite coincidence trigger timing schematic for a typical event.

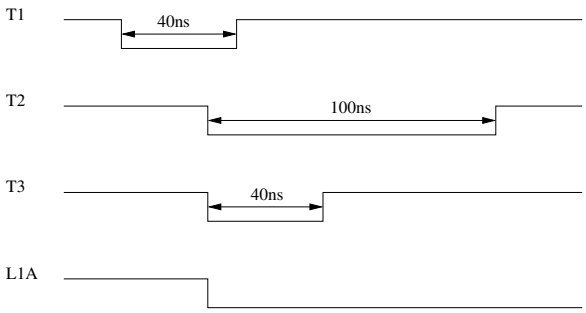

Figure 3.22: Neutron arm/BigBite coincidence timing schematic. T1 signal arrives before T2 signal causing L1A aligned with T2.

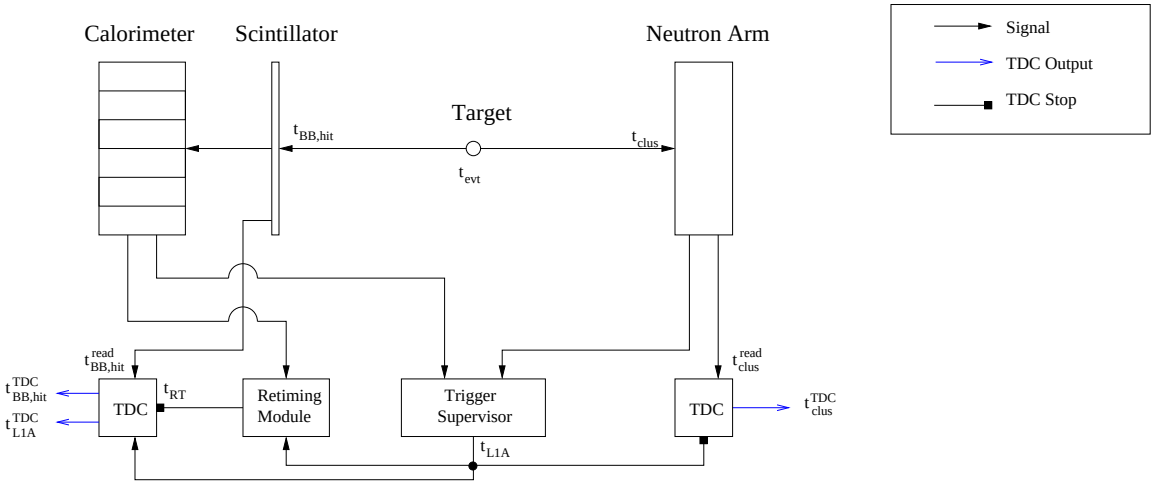

Figure 3.23: Simplified Trigger/Electronics Diagram as described in Section 3.3.6.

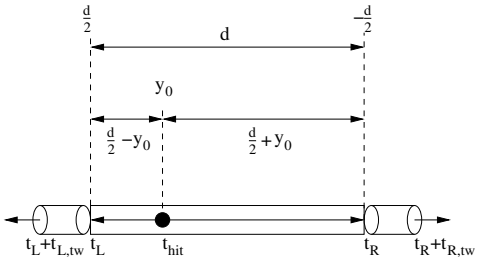

Figure 3.24: Propagation of the signal from a hit to the left and right PMTs.

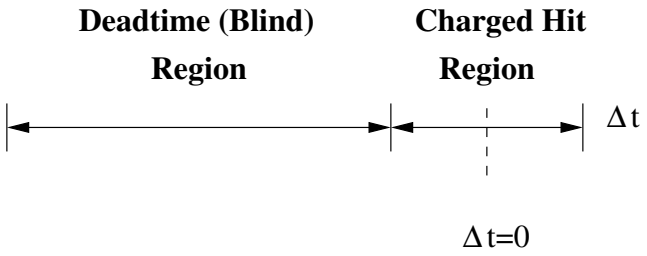

Figure 3.25: Veto timing regions

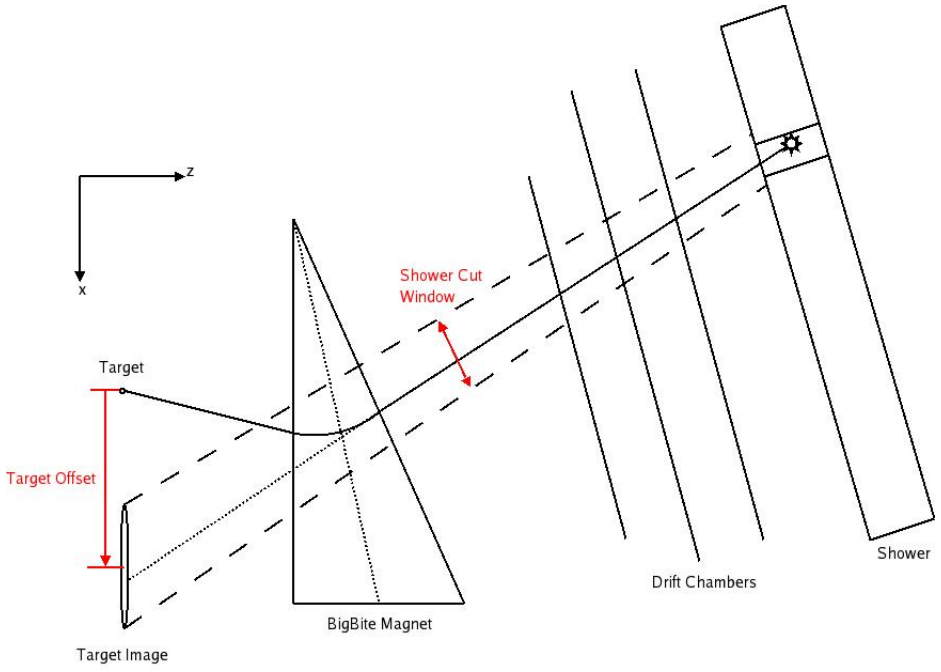

Figure 3.26: Diagram of how shower cuts are formed (side view, not to scale). Axes are in target coordinates.

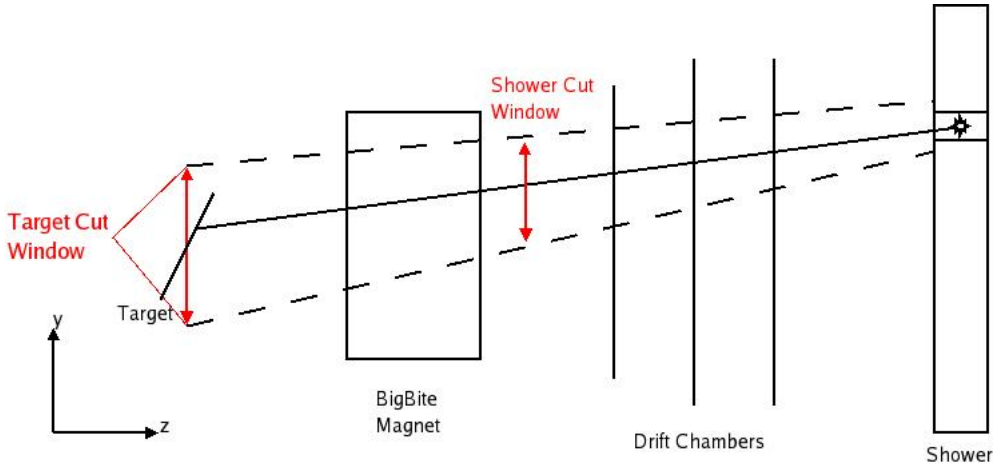

Figure 3.27: Diagram of how shower cuts are formed (top view, not to scale). Axes are in target coordinates.

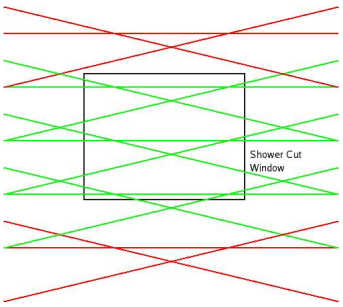

Figure 3.28: Shower Cut wire selection. Green wires are selected to be used in tracking. Red are not.

Chapter 4

Detector and Target Calibrations

As with any experiment, a careful calibration of all detectors must be performed to ensure the accuracy of our measurements. For E02-013, this is especially important due to the fact that almost all of the detectors in the experiment were newly built and untested in a production environment. In this chapter we will cover the calibrations for the beamline, target, neutron arm, and BigBite spectrometer. We will also examine the performance of the track reconstruction for the BigBite spectrometer software.

Considerable effort was employed to measure the target polarization magnitude, which will be shown to be a larger contribution to the systematic uncertainty of our measurement. Also, measurements of the target polarization direction, calibration the neutron arm timing, and calibrations of the BigBite tracking, optics, and detector subsystems were performed. Furthermore, the identification and calibration of detector positions relative to each other to provide reliable coincidence data was also a strong focus.

4.1 Beam

4.1.1 Polarization

Beam polarization was measured using both Mott polarimeter (Section 3.3.1) and the Hall A Møller polarimeter (Section 3.3.2). Data from the Compton polarimeter was not analyzed for this work, though it was available through most of the experiment, with the exception of kinematic 4, where high background rates prevented reliable data taking.

Two Mott measurements were taken during E02-013. One on March 30, 2006 and April 13, 2006. These results can be found in Table 4.1. The Møller polarimeter was employed during several periods through E02-013. The results of these measurements are in Table 4.2. Taking the uncertainty-weighted average of these two polarization measurements, a beam polarization of 83.5

Date	Time	Polarization (%)	Stat Err	Sys Err
March 30, 2006	18:44	83.32	1.45	1.00
March 30, 2006	18:50	81.62	1.45	0.98
April 13, 2006	09:43	84.12	1.11	1.01
April 13, 2006	09:49	83.25	1.11	1.00
Average		83.08	0.65	1.00

Table 4.1: Mott polarimeter measurement results.

Date	Time	Polarization (%)	Stat Err	Sys Err
February 28, 2006	18:03	88.8	0.2	3.0
February 28, 2006	18:03	86.8	0.2	3.0
March 4, 2006	22:42	88.2	0.14	3.0
March 9, 2006	20:15	86.5	0.15	3.0
March 25, 2006	21:37	82.2	0.3	3.0
Average		86.5	0.09	3.0

Table 4.2: Møller polarimeter measurement results.

$\pm$ 1.1% is obtained. For this analysis the beam polzarization is assumed to remain constant.

4.1.2 Energy

Beam energies were supplied from the accelerator group using the Tiefenbach method. This method is a variation of the ARC method by measuring the bend of the beam through known magnetic fields. The principle method of measurement for the ARC method is through measuring the bend of the electron beam through a known magnetic field and relating the field integral, $\int B_\perp dl$ and deflection angle, θ to the momentum

$$p = e\frac{\int B_\perp dl}{\theta}. \tag{4.1}$$

The Tiefenbach energy is the result of such a calibration and is performed separately by the CEBAF accelerator group.

4.1.3 Position

Beam position monitors were calibrated by using a set of HARP measurements, which are surveyed relative to the experimental hall. However, the readout for the BPMs is bandwidth limited which leads to measurements producing delayed values when the raster is active. To find the position of the beam when the beam is rastered a separate method must be used to calculate the beam position for a specific event. The beam raster currents are recorded and can then be mapped to the beam position to provide an accurate reconstruction.

An analysis of the BPM and raster current data was performed by University of Virginia graduate student Brandon Craver [69]. In this section we will present the results of this calibration.

The BPMs are connected to an ADC readout, which can then be related to position assuming a linear transformation from ADC channels to position. To perform this transformation, several numbers must be determined to convert this to a position measurement:

- The physical z positions of the BPMs
- Gain coefficients giving conversion of ADC channels to position.
- x and y offsets to correct the central value of the measured positions to known points
- Pedestal values to be subtracted from each ADC readout

The z positions of the BPMs are provided from the survey group while, the remaining constant must be determined from data. The results are found in Table 4.3.

To determined the position for a given event, a calibration involving the readout of the raster magnet current after the BPMs have been well calibrated must be done. The beam position at the

BPM A				
Offsets	X	Y	Z	
(m)	0.00110	0.00086	-7.517	
Pedestal	1	2	3	4
(chan)	691	719	693	729
BPM B				
Offsets	X	Y	Z	
(m)	-0.00030	0.00240	-2.378	
Pedestal	1	2	3	4
(chan)	668	650	670	661

Table 4.3: BPM calibration results.

target, assuming a linear conversion between the raster current and position, can be given by the formula

$$r_i = \langle r_i \rangle + m_i \cdot (I_i - \langle I_i \rangle) \tag{4.2}$$

where r_i is true the beam position, i an index representing the x or y position, $\langle r_i \rangle$ is the time-averaged beam position, m_i is a constant that relates raster current to position, I_i is the measured raster current, and $\langle I_i \rangle$ is the time-averaged raster current.

The value of $\langle r_i \rangle$ can be determined from BPM data as the time average is insensitive to the readout delay. For the calibration for a given event, the last 1000 values were used in the average. This number is sufficient given a raster frequency of 25 kHz and a trigger frequency of the order of 1 kHz.

The determination of m_i is calculated in different ways for the x and y calculations. For the x (horizontal) component, the deviation of the horizontal position from average position of the tracks found in the spectrometer can be observed. By using a thin BeO foil target, a fixed point along the beam line is chosen. This correlation can be fit to the formula

$$m_x = \frac{dy_{\text{targ}}(z_{\text{targ}} = 0)}{I_x} \frac{1}{\cos\theta} \tag{4.3}$$

where $dy_{\text{targ}}(z_{\text{targ}} = 0)$ is the deviation of the average y coordinate at $z = 0$ in target coordinates, I_x is the x direction raster current, and θ is the angle of the target coordinate system z axis with the lab z axis (Fig. 4.1. This dependency and fit can be seen in Fig. 4.2.

The value of m_y is more difficult to measure due to this direction being the dispersive direction of the spectrometer. To work around this, the measured width given by the BPM is compared to the width of the raster current, such that

$$m_y \approx \frac{\sigma_y(\text{BPM})}{\sigma_y(\text{Raster})}. \tag{4.4}$$

Given two BPMs spaced along the beamline, the direction, dr_i may be determined using a small angle approximation, from the formula

$$dr_i = \langle dr_i \rangle + \frac{m_i(I_i - \langle I_i \rangle)}{z_{\text{targ}} - z_{\text{raster}}} \tag{4.5}$$

where $\langle dr_i \rangle$ is the average direction measured by the BPMs, z_{targ} is the z_{LAB} position of the target, and z_{raster} is the z_{LAB} position of the raster magnet. The results for these calibrations for the x direction are $\langle I_i \rangle = 2400$ and $m = -3.36 \times 10^{-6}$(m/chan).

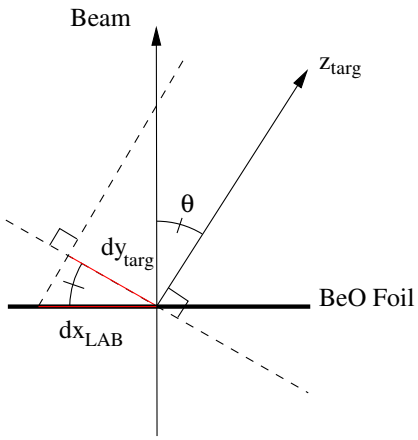

Figure 4.1: Horizontal raster contribution.

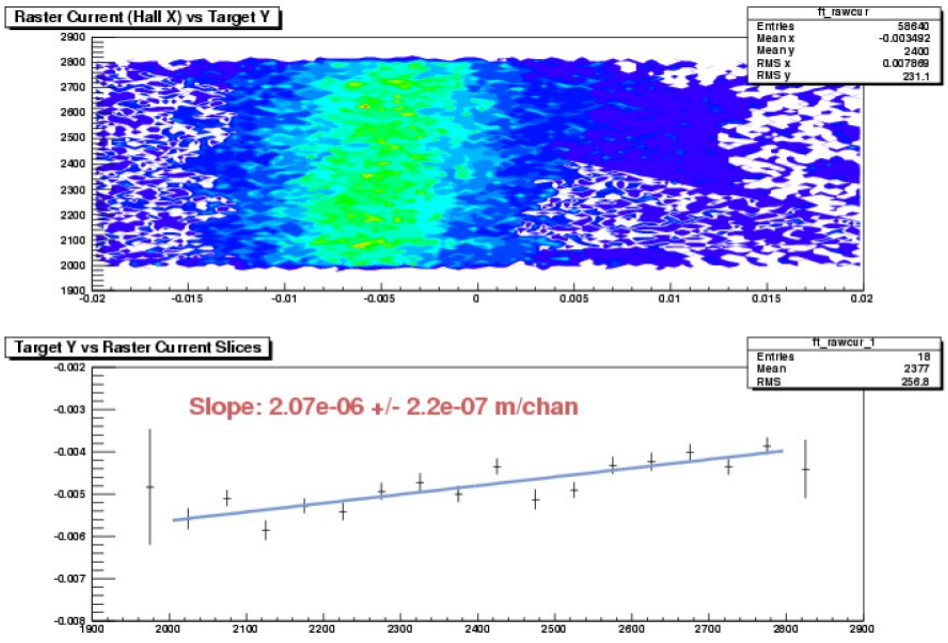

Figure 4.2: y deviation dependence on raster current [69].

4.2 ^{3}He Target

The ^{3}He target has several parameters that must be determined for the experiment. The magnitude of the polarization must be determined as well as the direction of the polarization (through the holding field). Both of these quantities are directly incorporated into the calculation of G_E^n (Eq. 3.7).

Several other parameters involved with the cell are important as well. The thicknesses of the glass of the cell itself is needed for radiative correction calculations. Also, there is a small presence of N_2 gas in the cell which contributes some amount in the quasielastic cross sections which must be determined.

4.2.1 Polarization Magnitude

To determine the polarization magnitude a number of measurements must be made to calibrate the measurement technique [57]. Most of these measurements are required to relate the absolute EPR measurement to the more frequently done and less invasive NMR measurement. However, as these two measurements are taken at two physically different locations in the cell, polarizations measured using the EPR technique do not directly reflect the polarization given by the NMR signal. However, by taking into account phenomena such as polarization gradients and varying temperatures, a reliable technique can be constructed.

Target Density and Temperature

Target density and temperature become important when determining the target polarization in Eq. 3.13 and in the comparisons to absolute cross sections. While the total number of atoms in the cell (i.e. the total volume) remains constant, the density in portions of the cell change due to localized heating by the lasers in the pumping chamber.

Several resistive temperature devices are employed to measure the temperature on the outside of the cell, but they do not provide information about localized temperatures inside of the cell. By performing a set of NMR measurements under different conditions, changes in density can be determined and then temperatures can be extracted.

The NMR signal can be expressed as a product of several factors given in Eq. 3.13. By performing signal measurements at various temperatures the density can be determined. The density in the target chamber can be expressed

$$n_t = \frac{n_0}{1 + \frac{V_p}{V_0}(\frac{T_t}{T_p} - 1)} \tag{4.6}$$

where n_t is the density of particles in the lower target chamber, n_0 is the overall average density, V_p is the volume of the upper pumping chamber, V_0 is the total volume inside of the cell, T_t is the temperature in the target chamber, and T_p is the temperature in the pumping chamber.

To determine the density when the lasers are on, a measurement of the ratio of the NMR signal strengths when the lasers are on to when they are off is performed. The temperature in the target chamber remains constant under different laser conditions. We then have

$$\frac{S_{\text{on}}}{S_{\text{off}}} = \frac{n_{\text{on}}}{n_{\text{off}}} = \frac{1 + \frac{V_p}{V_0}(\frac{T_t}{T_{p,\text{on}}} - 1)}{1 + \frac{V_p}{V_0}(\frac{T_t}{T_{p,\text{off}}} - 1)} \tag{4.7}$$

where S_{on} is the measured NMR signal when the lasers are on and S_{off} is the signal when the lasers are off. However, special consideration must be paid due to depolarization of the target from repeated NMR measurements, also known as adiabatic fast passage loss. To account for this, tests at constant temperature can be done and then fit to a decaying exponential curve, Fig. 4.3. The polarization losses were determined to be 1.24% for a field "up sweep" and 1.27% for a "down sweep".

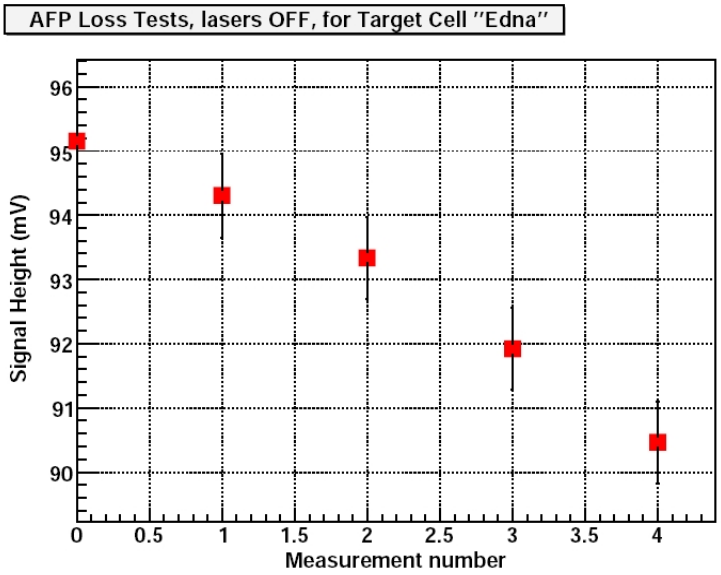

Figure 4.3: AFP loss due to repeated NMR measurements [57].

Parameter	Value
T_t	35.62°C
$T_{p,\text{off}}$	234.23°C
$T_{p,\text{on}}$	242.96°C
V_0	377.73 mL
V_p	292 mL
S_{on}	122.67 mV
S_{off}	115.45 mV

Table 4.4: Cell parameters for determining the pumping chamber temperature.

The change in relative density is determined to be 1.0625 between the laser on and off states, Fig. 4.4. This corresponds to a temperature change of about 40°C.

Polarization Gradient

The calibrating EPR signal measures the polarization in the pumping chamber while the frequently measured NMR signal measures the polarization in the target chamber. To compare the two measurements, the polarization gradient in the connecting tube between the two must be determined. This gradient arises from the fact that depolarization occurs in the target chamber due to the fact that there is no alkali metal vapor to spin-exchange with (the temperature is too low to maintain the gaseous state) and the presence of depolarizing beam exposure.

The relation between the two polarizations was calculated by the polarized ^{3}He target group at UVA and William and Mary [70].

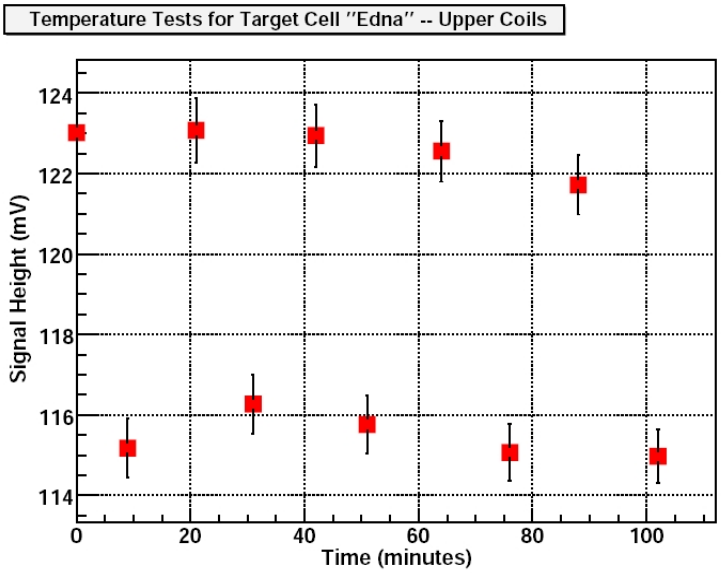

Figure 4.4: NMR signal changes due to temperature differences when the lasers are on or off. AFP loss has been corrected for this plot. [57]

Polarization

The relation between the polarization measured by the EPR method, P_{EPR}, and the NMR signal can be determined by using the NMR measurements to fix the constant c in the relation

$$c = \frac{S_{\mathrm{NMR}}}{P_{\mathrm{EPR}}(n_{\mathrm{p}}\Phi_{\mathrm{p}} + n_{\mathrm{t}}\Phi_{\mathrm{t}} + n_{\mathrm{tt}}\Phi_{\mathrm{tt}})} \tag{4.8}$$

where S_{NMR} is the signal measured from the pickup coils during an NMR measurement, P_{EPR} is the polarization measured by an absolute EPR measurement, n_{p}, n_{t}, and n_{tt} are the number of particles in the pumping chamber, target chamber, and transfer tube, respectively, and Φ are the corresponding fluxes of the NMR signal (which do not change for a given cell). Once c is fixed, NMR measurements can then be performed to identify the polarization in the pumping chamber. Correcting for the polarization gradient then gives the polarization in the target chamber, the quantity of interest.

Contributions of uncertainty to the target polarization are in Table 4.5. κ_0 is a constant measured experimentally, as introduced in Eq. 3.18. The EPR measurement uncertainty is an estimation of systematic uncertainties through repeated measurements. The flux and density uncertainties are due to uncertainty of the temperature (through density measurements) as described in Section 4.2.1. NMR fit uncertainty is the uncertainty of the resonance location from the Breit-Wigner fit. Other density uncertainty is in the uncertainty from the density in its contribution in Eq. 3.17.

Polarizations between 45% and 50% were routinely observed throughout the experiment as shown in Fig. 4.5.

4.2.2 Magnetic Field Measurement

For E02-013 it is necessary to determine the the magnetic holding field direction to better than 0.1° such that the uncertainty contributions from the angle between the three-momentum transfer

Source	Relative Error
κ_0	4.11%
EPR Measurement	1.32%
Flux and Density	1.00%
NMR Fit	0.6%
Other Density	0.25%
Overall	4.47%

Table 4.5: Relative uncertainty contributions to polarization calculations.

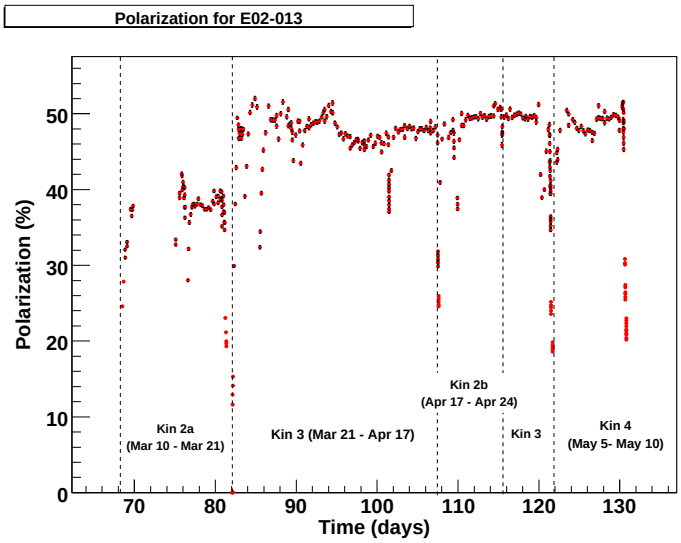

Figure 4.5: Polarizations of the target for final three kinematics [57].

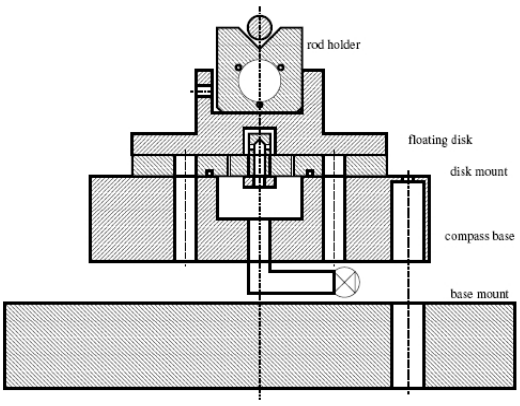

Figure 4.6: Schematic of the compass used for field direction measurements [58].

and target polarization are small. As shown in Section 3.1, we wish to maximize the perpendicular asymmetry, A_{perp}, Eq. 3.8, which contributes with a factor $\sin\theta$, θ being the angle between the target polarization and the three-momentum transfer. The central angle of the neutron arm is approximately 30° from the beamline, so the field is then chosen to be at approximately 120° in the scattering plane.

A measurement of the field inside the target box was carried out and analyzed by Vladimir Nelyubin, et. al [58]. A precision magnetic compass was used to measure the deviations of the field from the nominal direction. It consists of an iron rod on a disk mounted on a base which floats on flowing pressurized nitrogen under the base, as in Fig. 4.6.

An aluminum reference bar was installed on the outside of the target box and the compass was placed at the target center. A small mirror was affixed to the bar and a laser was set up outside of the box such that the laser light, reference bar mirror, and compass mirror were collinear (though the mirrors not necessarily parallel, Fig. 4.7). By measuring the spot reflected by the reference bar and compass on a transparency at a known position, the relative angles between the two can be determined. By then surveying the reference bar relative to the hall, an absolute measurement is then obtained.

Relative measurements were then performed by doing 1 in. shifts along the beam line using several "spacers". These 3 in., 4 in., and 5 in. wide bars were placed flush against a guide bar to provide a fixed distance and keep the 1 in. shifts running in the same direction. For each position of the compass, the position of reflected laser light was measured on a cardboard screen (Fig. 4.8). This method then maps out the direction of the magnetic field on a grid around the target area.

Fitting the direction measurements to a second order polynomial in the beamline vertex position v_z, Fig. 4.9, the angle of the field along the target can be expressed by

$$\theta_{\text{field}} = 117.8^\circ + ((1.78 \times 10^{-5})^\circ/\text{mm}^2) \cdot (v_z + 7.0\ \text{mm})^2 \tag{4.9}$$

where v_z is the z position in lab coordinates along the nominal beam axis. These measurements were performed before, during and after the experiment and analyzed by Vladimir Nelyubin [58]. The holding field was found to be stable for each measurement.

An out-of-plane angle measurement was done using a separate compass setup and that angle was found to be less than 1 mrad. This deviation is of much less importance, as it only contributes to the asymmetry on the order of $\delta\phi^2$.

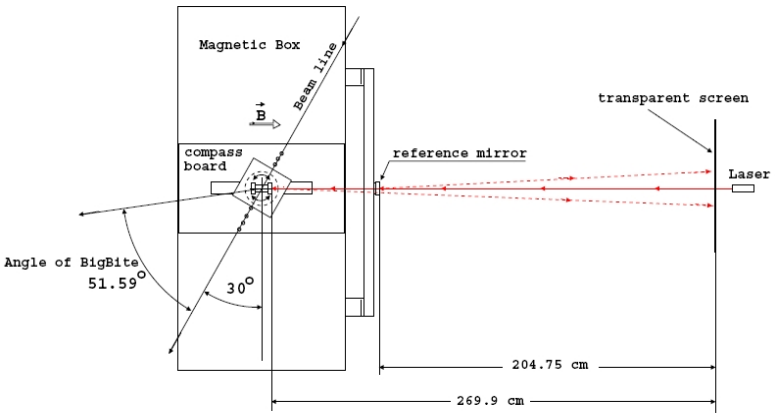

Figure 4.7: Absolute compass measurement relative to the hall [58].

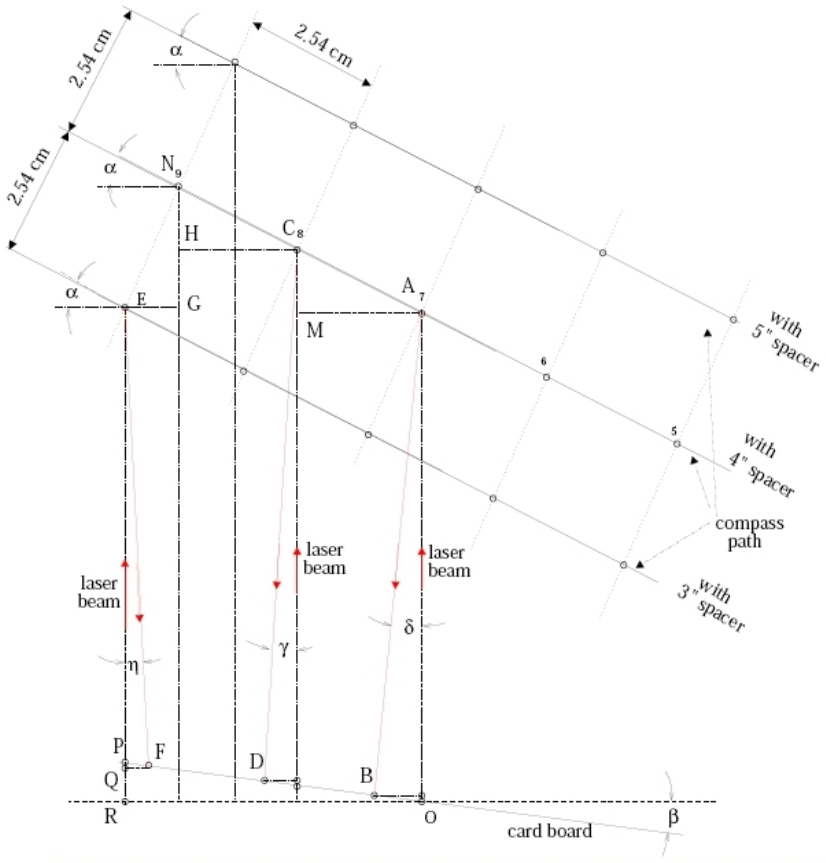

Figure 4.8: Relative compass measurements scanned across the region where the target resides [58].

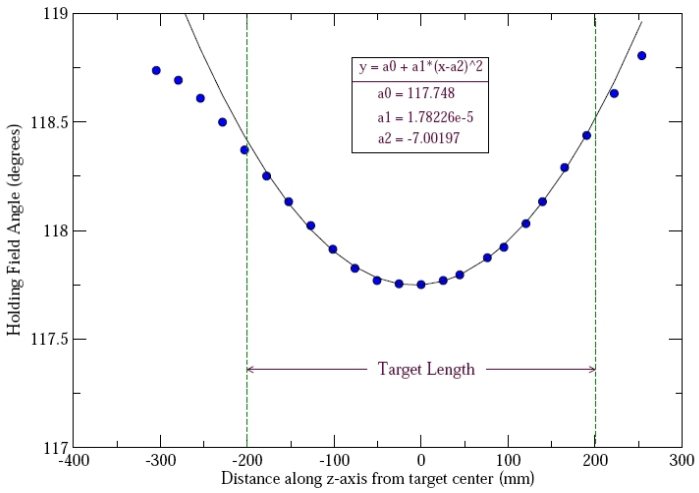

Figure 4.9: Field angle vs. position along the beamline [58].

4.2.3 Geometry and Construction Parameters

The hybrid target cells are constructed of hand-blown glass, which is prone to variations in thickness in the target wall size. Knowledge of these thicknesses is necessary to perform calculations such as contributions of radiative effects. Measurements of these thicknesses were done using laser interferometry at 12 places along the cell: each of the two end caps and five points along each side. Results of these measurements can be found in Table 4.6, Table 4.7, and Table 4.8 [57].

4.3 Neutron Arm Timing and Position

The neutron arm requires careful analysis to determine the position and relative timing offsets of each bar and PMT. To do this, careful surveying was performed such that each position of the neutron arm throughout the experiment was well known and timing calibration was done using both elastic H_2 data and quasielastic ^{3}He data [71].

4.3.1 Survey Analysis

Two survey reports were produced containing the position of several markers on the outside of the neutron arm relative to the experimental hall and target.

The neutron arm itself was placed on a set of rails allowing it to change positions to match the acceptance of BigBite for various kinematic settings. These rails were surveyed such that resurveying of the neutron arm was not necessary for each kinematic change. A summary of the positions during the experiment is given in Table 4.9.

The y position along each scintillator bar can be determined by the left and right PMT time difference given by Eq. 3.41. This equation, however, has an additional bar-dependent constant based on the differences between the two timing offsets, $t_{L,0} - t_{R,0}$. To accurately determine the y position and identify the value of this constant, vertical marker scintillators were placed at known positions on the face of the neutron arm. These bars ran such that when a hit occurred on the marker bars, the horizontal position of the successive hits behind it was determined.

The shift of the central value of the reconstructed y positions from the known position of the

Right/Left	From	Distance(cm)	Thickness (mm)
n/a	Upstream	0	0.1278
Left	Upstream	2.8	0.708
		11.5	0.815
		18.7	0.852
	Downstream	13.3	0.859
		3.5	0.944
		Average	0.8356
Right Upstream	4.1	1.10	
		12.2	0.84
		19.4	0.812
	Downstream	10.9	0.784
		4.3	0.8766
		Average	0.8766
n/a	Downstream	0	0.122

Table 4.6: Cell wall thicknesses for reference cell.

Right/Left	From	Distance(cm)	Thickness (mm)
n/a	Upstream	0	0.121
Left	Upstream	3.5	1.65
		12.11	1.71
		19.3	1.72
	Downstream	12.2	1.62
		4.2	1.54
		Average	1.648
Right Upstream	4.0	1.49	
		11.3	1.60
	Downstream	19.6	1.56
		13.4	1.66
		3.7	1.61
		Average	1.584
n/a	Downstream	0	0.152

Table 4.7: Cell wall thicknesses for target Dolly.

Right/Left	From	Distance(cm)	Thickness (mm)
n/a	Upstream	0	0.1263
Left	Upstream	3.6	1.64
		11	1.60
		20	1.60
		27.3	1.62
	Upstream	3.0	1.59
		Average	1.610
Right	Upstream	3.8	1.55
	Downstream	27.0	1.64
		19.5	1.65
		12.3	1.64
		3.9	1.59
		Average	1.610
n/a	Downstream	0	0.1378

Table 4.8: Cell wall thicknesses for target Edna.

Kinematic	Start Date	End Date	Distance (m)	Angle (deg)
1	03/05/06	03/08/06	8.23	35.74
2a	03/09/06	03/21/06	10.94	30.25
3a	03/24/06	04/17/06	10.97	25.63
2b	04/17/06	04/24/06	10.94	30.25
3b	04/24/06	05/03/06	10.97	25.63
4	05/03/06	05/12/06	8.23	35.74

Table 4.9: Position of the neutron arm for E02-013. Distance is measured from the target center to the center of the neutron arm. Angle is measured by the polar angle of the neutron arm z_{targ} axis with respect to the nominal beam direction.

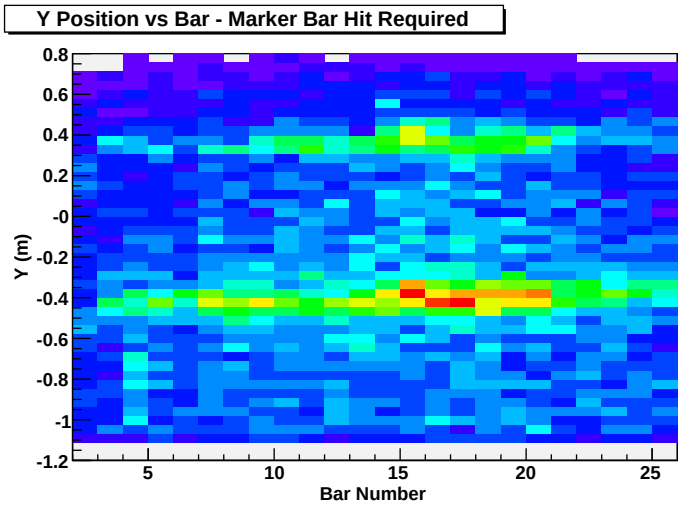

Figure 4.10: Vertical marker bars were used to calibrate the y positions of the horizontal scintillator bars. With a hit on the marker bar, the reconstructed y distribution for each horizontal bar then has a known central value.

marker bars is determined and subtracted, removing any artificial offset due to PMT timing differences as well as any spatial position offsets. When well calibrated, events where the marker bar was hit will yield a narrow y distribution centered on identical y values on the scintillators responding to the same particle. The markers near the top of the neutron arm were offset slightly in y from the bottom markers, producing a small difference in the y position measured by the marker bar. This calibrated state is represented in Fig. 4.10.

4.3.2 Attenuation

For calibration of attenuation, events were selected such that five or more consecutive bars were triggered in a single event and both left and right PMTs had a signal. Amplitudes were corrected for attenuation as given in Section 3.4.2. By taking the log of the ratios of the two amplitudes in Eq. 3.42 we get

$$\ln \frac{A_{\mathrm{R}}}{A_{\mathrm{L}}} = -\frac{2y}{\Gamma}. \tag{4.10}$$

By taking a fit of this quantity, Γ can be obtained as in Fig. 4.11.

4.3.3 Timing Calibration

Timing calibration of all PMTs in the neutron arm is critical to the accurate reconstruction of nucleon momentum from the time of flight. This analysis was carried out by University of Maryland graduate student Jon Miller and College of William and Mary postdoctoral associate Robert Feuerbach [59]. To achieve a resolutions on the order of 100 MeV, a timing resolution of better than a few hundred ps is required, as given by Eq. 3.21.

To perform this calibration, elastic scattering on H_2 as well as quasielastic events on ^{3}He are used. While using elastic protons would be ideal, these events do not sufficiently cover the entire acceptance of the detector. Quasielastic scattering from the ^{3}He target is used to supplement the data as the nominal time of flight will be the same as in the elastic case. Furthermore, H_2 is used

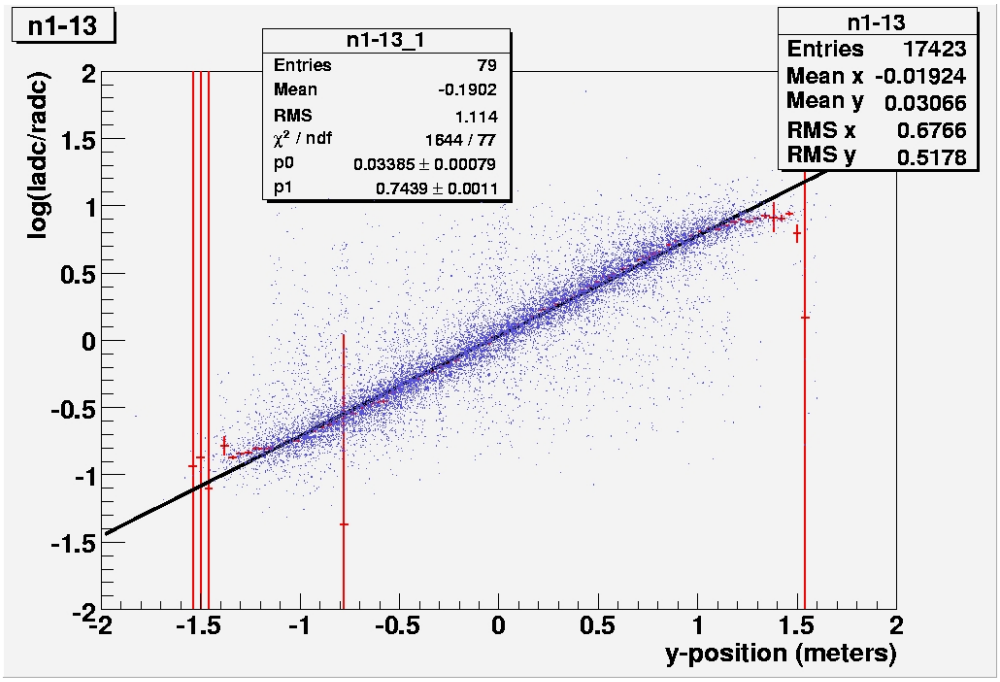

Figure 4.11: Fitting for the attenuation constant Γ [71].

only to calibrate the first scintillator plane, while ^{3}He data is used to calibrate timings between planes to provide sufficient statistics.

To calibrate the first layer of scintillator, elastic events are selected from a H_2 run. These are events identified as electrons by BigBite, which are within the elastic peak in the invariant-mass spectrum ($|W - 0.94$ GeV$| < 0.05$ GeV, shown in Fig. 4.12), and have a corresponding coincidence hit in the neutron arm near the expected position. Assuming elastic kinematics, the time of flight of the proton or neutron may then be determined by the three-momentum transfer, $\vec{q}$, and the distance from the reconstructed vertex to the cluster position, d, from the formula

$$t_{\text{tof}} = \frac{d}{c}\sqrt{1 + \left(\frac{m}{|\vec{q}|}\right)^2} \tag{4.11}$$

where m is the mass of the nucleon.

The neutron arm measures the time difference between the BigBite trigger and neutron arm trigger as detailed in Section 3.3.6. Assuming the BigBite scintillator calibrations have been completed, which are independent of the neutron arm, the remaining calibrations for time of flight are apparent from Eq. 3.38

$$t_{\text{tof}} = t_{\text{clus}}^{\text{TDC,corr}} - t_{\text{BB,hit}}^{\text{TDC,corr}} + t_{\text{L1A}}^{\text{TDC}} + t_e + a$$

and, $t_{\text{clus}}^{\text{TDC,corr}}$, t_e, and a, remain to be determined.

For now, we will assume we do not care about the overall constant a, which will be determined later in Section 5.4. Determination of the path-length correction, t_e, is discussed in Section 4.5. This leaves the time $t_{\text{clus}}^{\text{TDC,corr}}$, described by Eq. 3.37

$$t^{\text{TDC,corr}} = t^{\text{TDC,avg}} - \frac{t_{\text{L,tw}} + t_{\text{R,tw}}}{2} - t_{0,\text{bar}}.$$

Time walk effects can be determined by using the model presented in Eq. 3.40

$$t^{\text{TDC}} = t_{\text{hit}} + t_{\text{prop}} - CA^P + t_0 - t^{\text{L1A}}.$$

For this experiment, only a crude calculation for time walk effects was performed by observing amplitude dependent deviations in time of flight from that predicted by $\vec{q}$ after a calibration ignoring these effects. This was performed for the detector as a whole and not for individual bars and provided corrections up to a few hundred ps.

The bar-dependent term $t_{0,\text{bar}}$, comes from different propagation times from the PMTs to the TDC inputs for each scintillator bar. By removing the bar dependence (that is, by adjusting $t_{0,\text{bar}}$ such that any overall offset is independent of the bar producing a signal), we can then calculate the time of flight up to an overall constant. This is done by solving Eq. 3.38 for $t_{0,bar}$ for each bar using elastic scattering kinematics and then determining the central value of the time distribution. This central value is then to be subtracted from future time of flight calculations for that particular bar.

Intra-plane calibrations are done using the abundant ^{3}He data. Events are selected such that the particle is identified as charged by the vetos, is within 30 ns of the coincidence region expected for an elastic event (which acts as a sanity cut), and is found within 0.08 m of the expected position on the neutron arm from as an elastic event. A hits in each plane of the neutron arm is required. The time expected for each plane is determined by assuming the momentum is constant as it traverses through the neutron arm. A plot showing the stability of these calibrations is shown in Fig. 4.13.

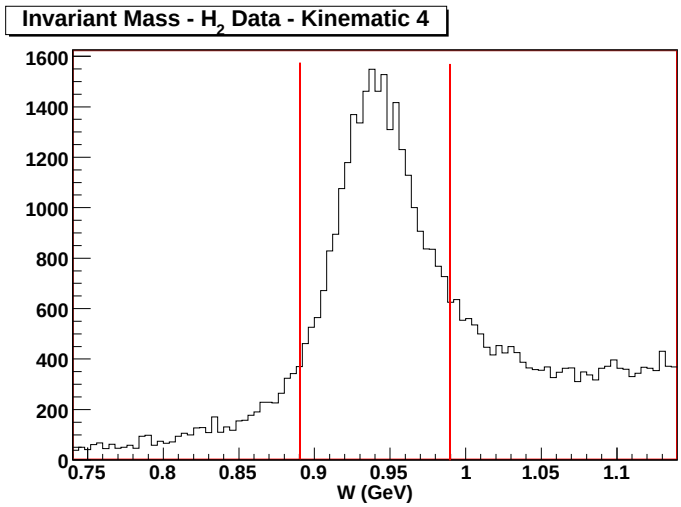

Figure 4.12: The invariant mass spectrum for a H_2 target run. The cuts used to select on the elastic peak, found at the nucleon mass, for scintillator time of flight calibration is shown by red lines.

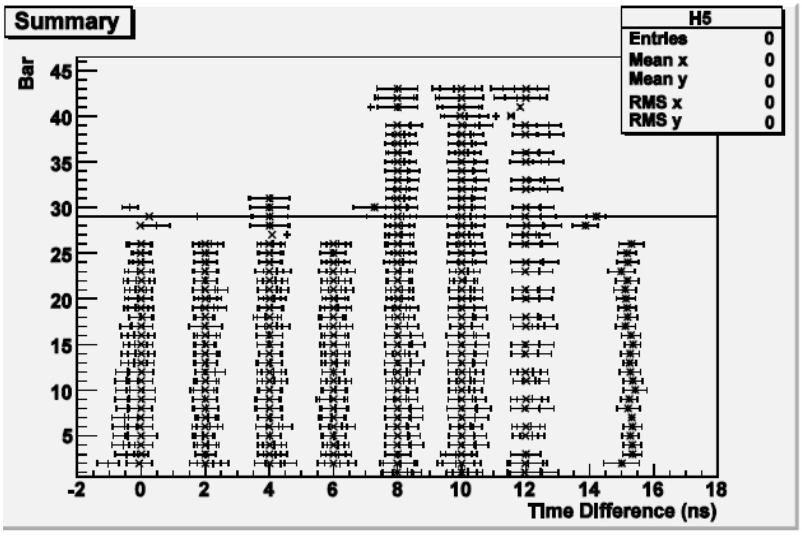

Figure 4.13: Results of neutron arm timing calibrations applied to later runs [59]. An artificial 2 ns $\times n$ offset is added to each plane to produce separation for each plane in the plot. '$\times$' represents the position of the timing offset for each bar, which ideally would be centered around 0 nsbetween (apart from any offset).

4.4 BigBite Spectrometer

The BigBite spectrometer provides measurements of the direction and momentum of the scattered electron by measuring the trajectory of the electron after it passed through a magnetic field. BigBite is designed to have properties close to those of an ideal dipole magnet, that is, to have a uniform magnetic field throughout the volume of the magnet. However, it does contains measurable deviations which can be observed in the data. While the field of the magnet is not measured directly throughout the volume, by exploiting properties of the magnet and applying empirical corrections to deviations from the effective bend plane model, a sufficiently accurate reconstruction of the electron deflection and momentum can be obtained.

To perform this measurement, several subsystems of the spectrometer must be accurately calibrated. These subsystems include the set of multiple wire drift chambers, the lead glass calorimeter, and a layer of scintillator paddles.

4.4.1 Shower and Preshower

The BigBite lead glass shower and preshower is an electromagnetic calorimeter that also provides some facility for particle identification. The sum of the amplitudes over the PMTs in both detectors is roughly proportional to the total energy carried by the incident particle. This sum can then be calibrated using particles of known energies. For E02-013, elastic events from a H_2 target were used for this calibration.

The energy deposited in a calorimeter block is assumed to be linear in the integrated charge measured by the ADCs connected to the shower and preshower block PMTs

$$E_{\text{block}} = C_{\text{g}}(A^{\text{PMT}}_{\text{block}} - A^{\text{ped}}_{\text{block}}) = C_{\text{g}}A_{\text{block}} \tag{4.12}$$

where E_{block} is the energy deposited in the block, C_{g} is the gain coefficient, having units of energy per channel, $A^{\text{PMT}}_{\text{block}}$ is proportional to the integrated amplitude from the ADC for the block, and $A^{\text{ped}}_{\text{block}}$ is the pedestal value for that block, a constant offset which can be measured by taking data with no signal. We will use A_{block} as the pedestal-subtracted amplitude.

The high voltages on the photomultiplier tubes for both the shower and preshower have been selected to provide similar gain coefficients by selecting high voltages that yield similar pedestal-subtracted ADC spectra. (Although the overall gain coefficients for portions of the calorimeter are in theory different, and this has not been taken into account for this analysis and a single gain coefficient is used for all blocks.) To obtain the overall gain coefficients, a minimum-χ^2 fit is done for a sum of linear contributions from the pedestal-subtracted shower and preshower amplitudes using cosmic ray events. The total energy is then determined to be

$$E = (3.57^{-4}\text{GeV/channel})A_{\text{ps}} + (5.10^{-4}\text{GeV/channel})A_{\text{sh}} \tag{4.13}$$

where A_{ps} is the sum of pedestal-subtracted preshower amplitudes over all preshower blocks and A_{sh} is the sum of pedestal-subtracted amplitudes for the shower (both in units of channels). By fitting a Gaussian to the energy difference between the calorimeter and the energy given by the optics, a resolution of $\sigma_{\frac{dE}{E}} = 8.5\%$ can be determined (Fig. 4.14).

Position reconstruction of the track can be performed by taking an amplitude weighted sum of block positions. This technique was not used for this analysis and instead the position of the block that had the largest amplitude was used.

Basic electron/pion differentiation can be done by examining the preshower signal. Lower energy-depositions are identified as pions while the higher energy-depositions are electrons. This electron distribution becomes more pronounced as one selects on the elastic peak in momentum, while if one looks in the spectrometer for purely positively charged particles (which are identified to be bending in an opposite direction), the pion peak becomes enhanced (Fig. 4.15 and Fig. 4.16).

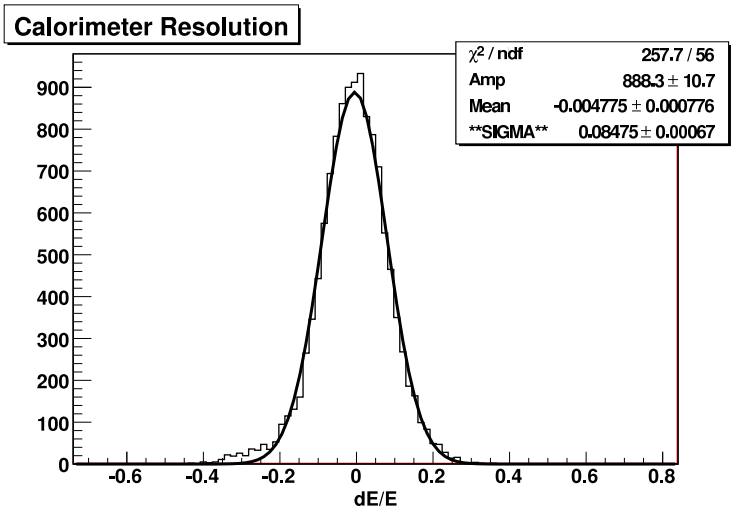

Figure 4.14: Energy difference of the energy measured by the calorimeter and the energy of the electron as measured by the deflection angle of the electron for electron events divided by energy. Fitting this to a Gaussian yields an energy resolution of about $\sigma = 8.5\%$.

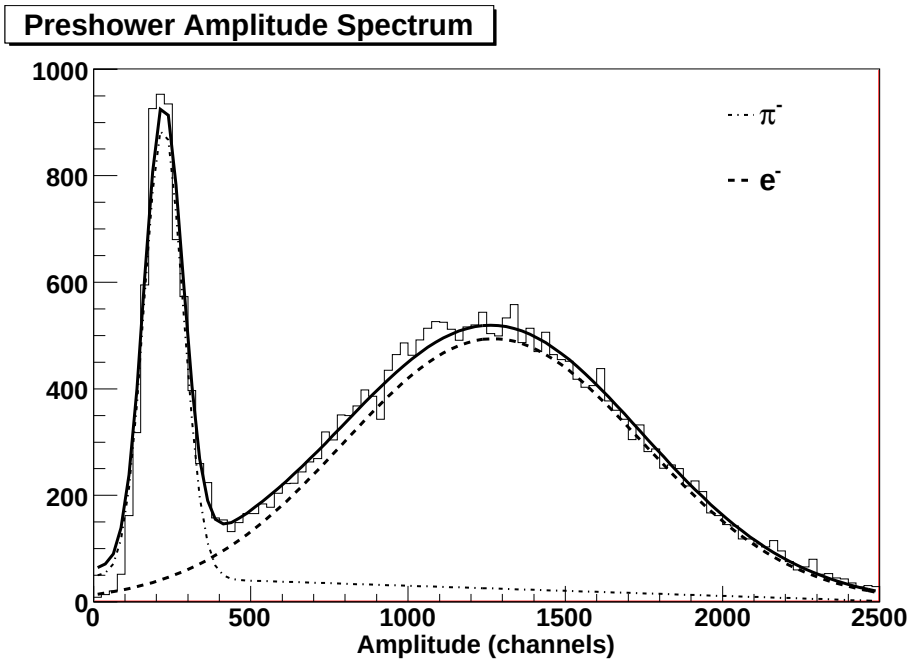

Figure 4.15: Two distributions are identified in the preshower energy spectrum associated with pions and electrons. Curves were reproduced by fitting plots similar to those found in Fig. 4.16.

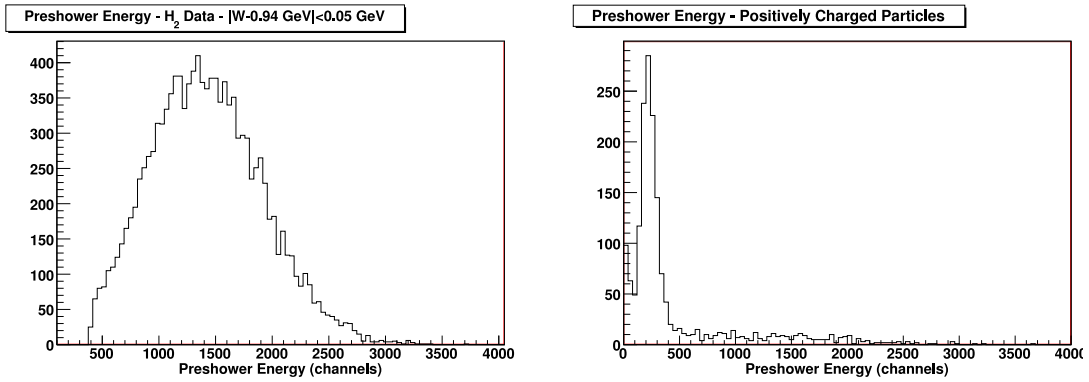

(a) (b)

Figure 4.16: Preshower energy spectrum distributions separate when a) selecting on elastic scattering events with H_2 data and $|W - 0.94 \text{ GeV}| < 0.05$ GeV, electron enhancement and b) selecting on positively charged particles, pion distribution enhancement.

Selecting preshower energy deposition greater than 500 channels will eliminate most of the pions in the data and this cut is used as an electron selection. This causes a loss of approximately 7% of the electron data.

4.4.2 Drift Chambers

The multiple wire drift chambers are the most crucial portion of the BigBite spectrometer in regards to providing accurate reconstructions of the electron track after it has passed through the magnetic field. At the lowest level, the drift chambers provide a time of a hit relative to a trigger which can then be interpreted as some function of the distance of the track to the wire. These hits over all chambers can then be reconstructed into a single track (as described in Section 3.4.4).

However, there are sets of calibrations that must be done to determine parameters that will provide accurate reconstructions in software. These include individual timing offsets of each of the drift chamber wires, accurate knowledge of all drift chamber wire positions and orientations relative to one another, and determination of the functional dependence of drift time on drift distance.

t_0 Offsets

Each wire of each drift chamber is connected to a channel in a common-stop TDC whose readout is controlled by the BigBite trigger (as described in Section 3.3.6). The readout time for a wire, i, can be described as

$$t_{\text{TDC}} = t_{\text{drift}} + t_{\text{delay},i} - t_{\text{path}} - t_{\text{trig}} \approx t_{\text{drift}} + t_{0,i} \tag{4.14}$$

where t_{drift} is the drift time, $t_{delay,i}$ is an offset particular to the wire which is the propagation time of the signal to the TDC, t_{path} is the amount of time the electron takes to propagate to the trigger detectors, and t_{trig} is the time it takes for the trigger to occur and be sent to the TDC as

the common stop signal. The last three terms modifying the drift time are taken into a single offset, $t_{0,i}$.

The value of $t_{0,i}$ for each wire must be determined such that t_{drift} can be extracted from the measured quantity, t_{TDC}. We take this to be a constant for any given event as t_{trig} is not expected to vary between events and the variation of the path lengths is sufficiently small. Given a distance between the front drift chamber plane and trigger calorimeter plane of about 1 m, an active area of the drift chamber plane of 1.40 m×0.35 m, and an active area of the calorimeter of 2.30 m×0.60 m, a maximum track length variation of 1.16 m is found. This implies into a 3.9 ns difference in t_{path} between the most extreme events. With an average drift distance resolution of $\sigma_{d_{\text{drift}}} = 350$ μm and a drift velocity on the order of 5×10^{-5}m/ns, the drift time resolution is effectively $\sigma_{t_{\text{drift}}} = 7$ ns. This track variation effect is small compared to a nominal drift time resolution and is not taken into account.

To measure and build a set of databases containing the values of $t_{0,i}$ for each wire, a time spectrum for each wire is produced. To minimize the amount of background signal for the time spectra, data from cosmic trigger events are used (which are collected at rates on the order of Hz). The use of cosmic events is not necessary, as a flat background can be assumed and the rate determined by looking at times before the true spectrum begins given sufficient statistics, and the background can then be subtracted.

For each time spectrum two points are determined: the earliest times when the (background subtracted) spectrum is 80% of the maximum and 20% of the maximum. These two points then define a line for which the offset is given by time at which the line intersects the axis defining no signal. See Fig. 4.17.

Offsets are generally determined to be similar (within 5 ns) for each 16 channel discriminator card. To help enhance statistics and simplify the calibration, offsets for individual cards were determined using the same technique as described above rather than for each individual wire. An example of the values of these offsets for a single plane is shown in Fig. 4.18.

Survey Analysis

Two surveys were performed of the BigBite spectrometer magnet and three drift chambers relative to the experimental-Hall center, before and after the experiment. These will be referred to as the Kin. 1 survey and the Kin. 2-4 survey, the interpretation of which will be the focus of this section. In addition an independent survey was performed by Eugene Chudakov before and after the experiment [72]. These measured the spectrometer at the two central angles, $-56.26°$ and $-51.59°$. These providing confirmation of the alignment done in Section 4.4.2 as well as provide information about the normal vectors for each plane relative to one another and about rotations of the chambers about the z_{det} axis. Raw values from the BigBite surveys can be found in Appendix A.

Given the positions of the four corners and the center of each drift chamber, cross products can be taken to find the normal vector for each chamber. Since only three coordinates are necessary to define a plane, there is an amount of redundant data provided. By taking the cross product of vectors from the drift chamber center to points lying on a common edge (calling these cross products top, bottom, left, and right), the survey should provide four identical vectors. Tables 4.10 and 4.11 list the angles between these redundant vectors from the surveys and show they are in good agreement.

The spectrometer central angle was found by minimizing the angle between the unit vector along the z_{det} axis and the unit chamber normal. Since we have not yet calculated the pitch, $-10.0°$ was assumed. The points to minimize are shown in Figs. 4.19 and 4.20. Results for the final angles of -56.26° and -51.59° for the kin. 1 and kin. 2-4 survey respectively are shown in Tables 4.12 and 4.13. These results were deemed to be in agreement with the surveys performed by Eugene Chudakov [72].

Using the central angle found, we then adjust the pitch to, once again, minimize the arc cosine of the dot product between the unit vector along the z_{det} axis and the unit chamber normal. The points to minimize are shown in Figs. 4.21 and 4.22.

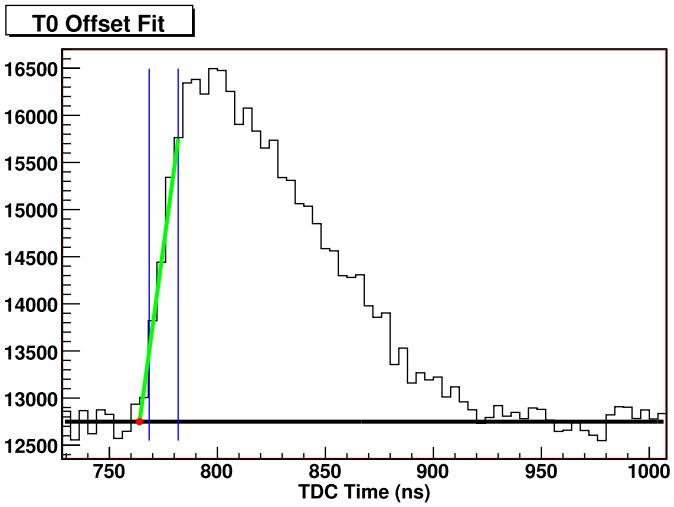

Figure 4.17: t_0 offsets are determined by extrapolating the leading edge of the time distribution to the background level. Plotted is an example of this fit using ^{3}He data, which has a considerable background. The black line represents the background level, the blue lines are the 20% and 80% signal strength marks, and the green line represents our fit to the leading edge of the signal. The red dot indicates the position of the offset.

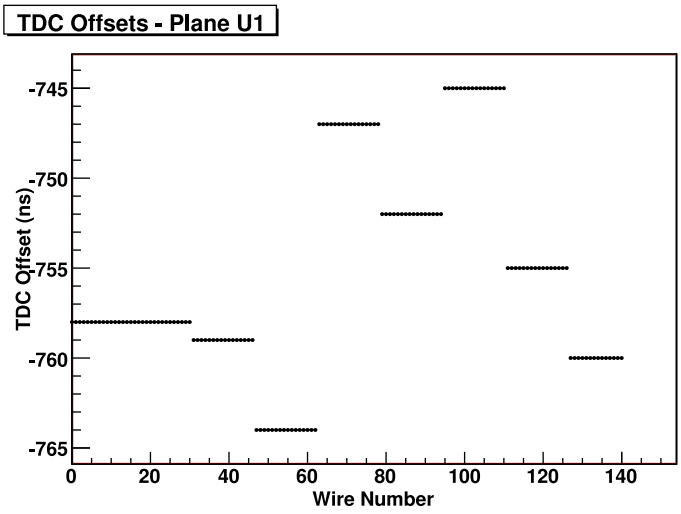

Figure 4.18: t_0 offsets calculated for each wire in a plane.

Chamber 1 (mrad)				
	Top	Right	Bottom	Left
Top	—	0.000	0.050	0.050
Right	0.000	—	0.050	0.050
Bottom	0.050	0.050	—	0.000
Left	0.050	0.050	0.000	—
Chamber 2 (mrad)				
	Top	Right	Bottom	Left
Top	—	0.136	0.099	0.117
Right	0.136	—	0.117	0.234
Bottom	0.099	0.117	—	0.136
Left	0.117	0.234	0.136	—
Chamber 3 (mrad)				
	Top	Right	Bottom	Left
Top	—	0.005	0.043	0.046
Right	0.005	—	0.046	0.049
Bottom	0.043	0.046	—	0.005
Left	0.046	0.049	0.005	—

Table 4.10: Angular difference between cross products generated by adjacent corners on a common side (identified by the side) for the kin. 1 survey.

Chamber 1 (mrad)				
	Top	Right	Bottom	Left
Top	—	0.079	0.177	0.115
Right	0.079	—	0.115	0.086
Bottom	0.177	0.115	—	0.079
Left	0.115	0.086	0.079	—
Chamber 2 (mrad)				
	Top	Right	Bottom	Left
Top	—	0.033	0.077	0.050
Right	0.033	—	0.050	0.035
Bottom	0.077	0.050	—	0.033
Left	0.050	0.035	0.033	—
Chamber 3 (mrad)				
	Top	Right	Bottom	Left
Top	—	0.267	0.501	0.277
Right	0.267	—	0.277	0.209
Bottom	0.501	0.277	—	0.266
Left	0.277	0.209	0.266	—

Table 4.11: Angular difference between cross products generated by adjacent corners on a common side (identified by the side) for the kin. 2-4 survey.

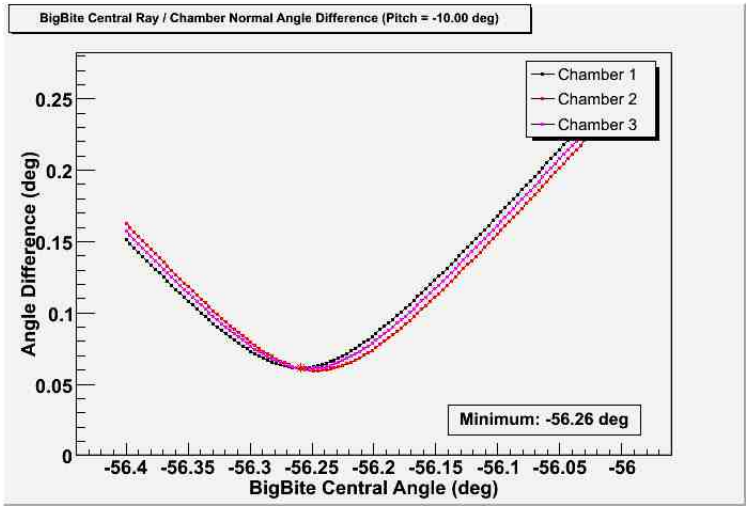

Figure 4.19: Angular difference for several assumed central angles for the three chambers for the kin. 1 survey. The minimum of chamber 1 is taken as the true central angle.

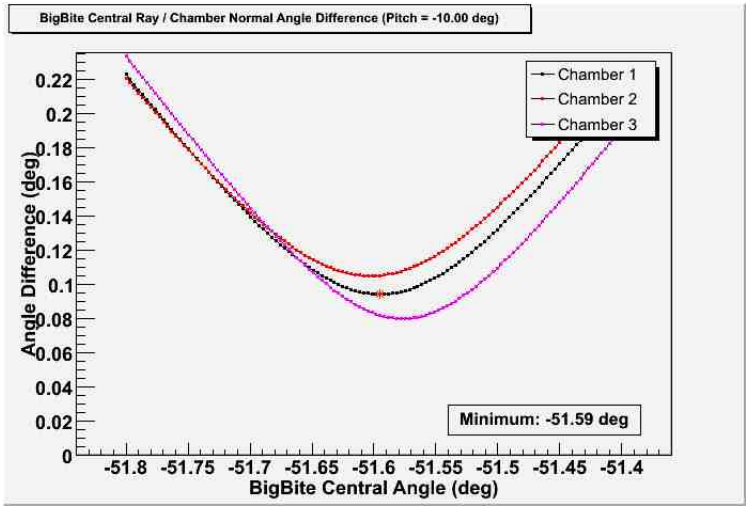

Figure 4.20: Angular difference for several assumed central angles for the three chambers for the kin. 2-4 survey. The minimum of chamber 1 is taken as the true central angle.

BigBite Central Angle: -56.26°	
Chamber	Angular Difference (mrad)
1	1.073
2	1.064
3	1.073

Table 4.12: Angular difference between chamber normal vectors and central ray for the best central angle of $-56.26°$ for the kin. 1 survey . A pitch of -10.0° was assumed.

BigBite Central Angle: -51.59°	
Chamber	Angular Difference (mrad)
1	1.649
2	1.840
3	1.432

Table 4.13: Angular difference between chamber normal vectors and central ray for the best central angle of $-51.59°$ for the kin. 2-4 survey. A pitch of -10.0° was assumed.

BigBite Pitch: -10.06°	
Chamber	Angular Difference (mrad)
1	0.007
2	0.222
3	0.112

Table 4.14: Angular difference between chamber normal vectors and central ray for the best pitch from the kin. 1 survey. A central angle of -56.26° was used.

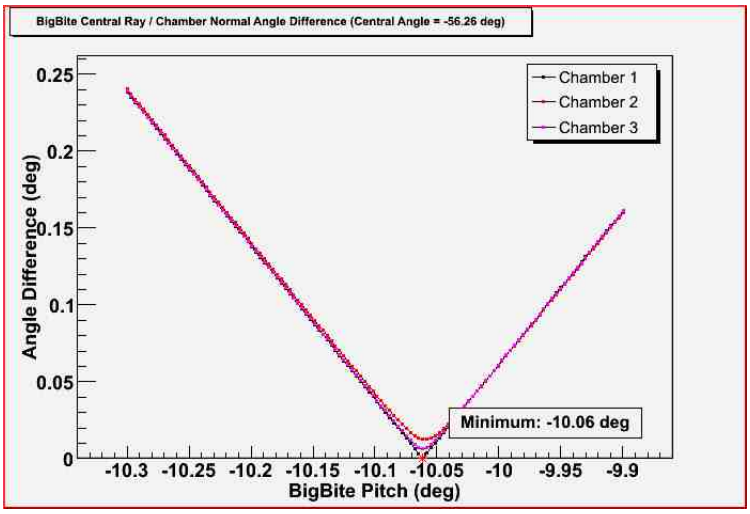

Figure 4.21: Angular difference for several pitches for the three chambers for the kin. 1 survey. The minimum of chamber 1 is taken as the true pitch.

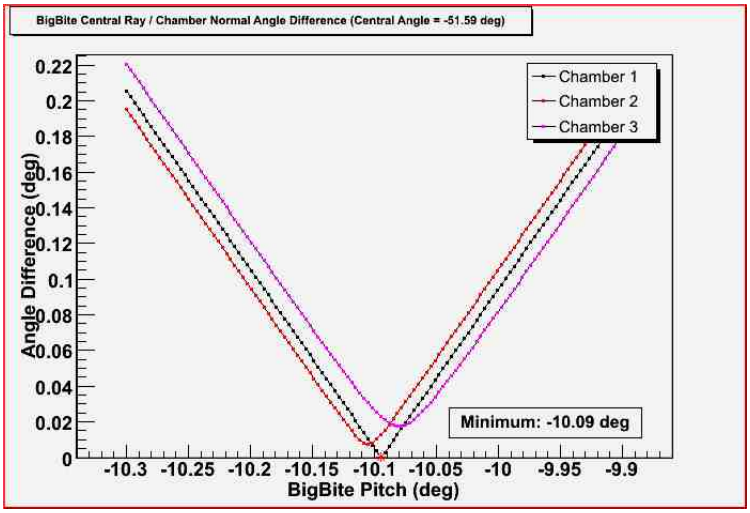

Figure 4.22: Angular difference for several pitches for the three chambers for the kin. 2-4 survey. The minimum of chamber 1 is taken as the true pitch.

BigBite Pitch: -10.09°	
Chamber	Angular Difference (mrad)
1	0.009
2	0.223
3	0.404

Table 4.15: Angular difference between chamber normal vectors and central ray for the best pitch from the kin. 2-4 survey. A central angle of -51.59° was used.

Chamber	Top	Left	Bottom	Right	Average
1	0.039	0.049	0.042	0.041	0.043
2	-0.050	-0.050	-0.050	-0.047	-0.049
3	-0.162	-0.139	-0.163	-0.150	-0.153

Table 4.16: Necessary angular adjustments to wire orientation from the kin. 1 survey. Units are degrees.

Chamber	Top	Left	Bottom	Right	Average
1	0.040	0.043	0.041	0.046	0.042
2	-0.064	-0.064	-0.064	-0.064	-0.064
3	-0.18	-0.196	-0.181	-0.197	-0.189

Table 4.17: Necessary angular adjustments to wire orientation from the kin. 2-4 survey. Units are degrees.

The roll of each chamber is determined by calculating the central point of each side of the chamber. These points were found by averaging adjacent vectors defined by the center of the chamber to a corner, and looking at the deviation of the azimuthal angle ϕ from the ideal orientation. Results are in Tables 4.16 and 4.17. Applying these corrections produced systematically smaller χ^2 in all fit tracks.

The center of the BigBite magnet relative to the hall was measured once at the beginning of the experiment (Appendix A). Although we have now calculated the central angle of the spectrometer, we can determine the distance center of the magnet from the target center in the target reference frame. We are only interested in the $z_{\rm targ}$ position for the effective bend plane model we use. This was determined to be 1.415 m. The distance from the front face to the magnetic mid-plane along the median line was taken to be 0.325 m (Fig. 3.14).

Drift Chamber Positions

The positioning of the drift chambers relative to the first chamber can be checked using reconstructed tracks from any data set and examining the central values of the residuals. The $z_{\rm det}$ positions of the second and third plane can be check by looking for dependencies of residuals on the track angle orthogonal to the wire direction (for example, the x' coordinate for X planes) (Fig. 4.23). The relation between the deviation of the coordinate measured by the plane, Δr, and the deviation of the assumed plane position from reality Δz, is simply:

$$\Delta z = \langle \frac{\Delta r}{r'} \rangle \tag{4.15}$$

where $r' = \frac{dr}{dz}$.

To minimize convolution of uncertainties between chambers, determination of deviations in chamber 3 is done without using hit information from chamber 2 (as chamber 2 gives the least tracking information as it only has 3 planes). Chamber 2 deviations can then be determined from examining hits near the tracks and adjusting positions until they agree. This technique was used before survey information was available and was based purely on data and course measurements with a tape measure. The results of the survey when compared to this calibration agreed extremely well, within 10^{-4} m.

Adjustments to positions of the second and third chamber relative to the first were done by making adjustments such that residual peaks became centered and had no dependence on track

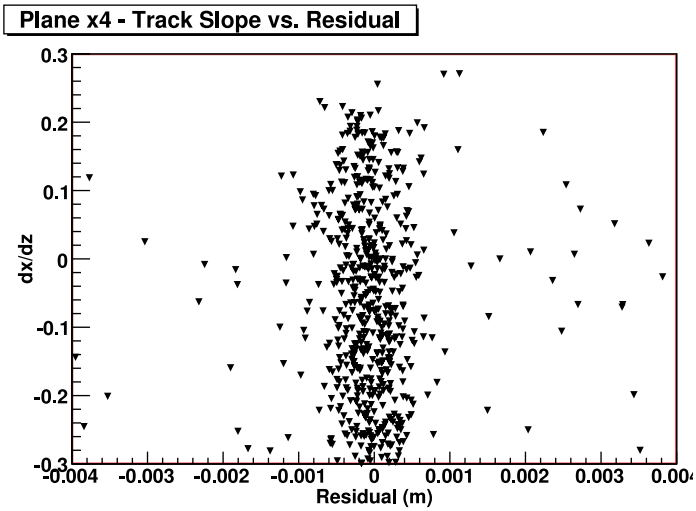

Figure 4.23: Track residuals vs. out of plane angle.

Chamber	Plane	x_1 Position (m)	$z_{\rm det}$ (m)
1	U1	-0.7025	0.0000
1	U2	-0.6975	0.0064
1	X1	-0.7025	0.0128
1	X2	-0.7075	0.0224
1	V1	-0.7025	0.0288
1	V2	-0.6975	0.0352
2	U3	-0.9927	0.3598
2	X3	-0.9975	0.3662
2	V3	-0.9939	0.3825
3	U4	-1.0023	0.7444
3	U5	-0.9973	0.7385
3	X4	-1.0136	0.7316
3	X5	-1.0085	0.7178
3	V4	-1.0031	0.7109
3	V5	-0.9981	0.7050

Table 4.18: A list of plane z positions and starting wire positions.

angle. These values cannot be obtained by the survey, as they are dependent on the positions of the wires inside the chamber housing themselves. These corrections were produced by minimizing the track residuals. A list of plane $z_{\rm det}$ and first wire positions, taken to be the radial distance from ($x_{\rm det}$, $y_{\rm det}$) = (0,0) in the plane, can be found in Table 4.18.

Corrections can be made to the $z_{\rm targ}$ origin using carbon foils data by adjusting $z_{\rm targ}$ such that the center foil reconstructs to $z_{\rm LAB} = 0$. This has been done for the final three kinematics and the origin for the target detector system in lab coordinates determined to be $z_{\rm targ} = 0.005$ m.

Overall shifts of the vertical position of the BigBite spectrometer were made by comparing coincidence data with the known position of the neutron arm. An adjustment of the vertical position of the detector stack was made such that the out of plane angles of the electron and proton were in agreement for elastic H_2 data (Fig. 4.24). The lab y coordinate of the origin of the target detector system was set to $y_{\rm targ}$=1.8 cm compared to 0 cm from the survey. This was the only deviation from the survey data found.

Drift Time to Distance Conversion

To determine drift distances, the (background-subtracted) drift time distribution was mapped to drift distances such that the resulting drift distance spectrum was flat. Drift-time to distance conversion is then handled by using an empirical formula which fits the data. To generate the flat mapping, we use the condition that sampling some number of events in the time spectrum in a window Δt will map proportionally to some drift distance range, Δd

$$f(t)\Delta t = \Delta d \tag{4.16}$$

where $f(t)$ is a function that describes the drift time spectrum. Taking this to the continuum limit, recognizing that $t = 0$ should correspond to a drift distance of 0, and integrating from $t = 0$ to some time t, we have

$$\int_0^t f(t')dt' = d(t) \tag{4.17}$$

where c is some constant and $d(t)$ is the drift distance for drift time t. To find c we recognize that the maximum drift time $t_{\rm max}$ must correspond to the maximum drift distance $d_{\rm max}$. Solving for c

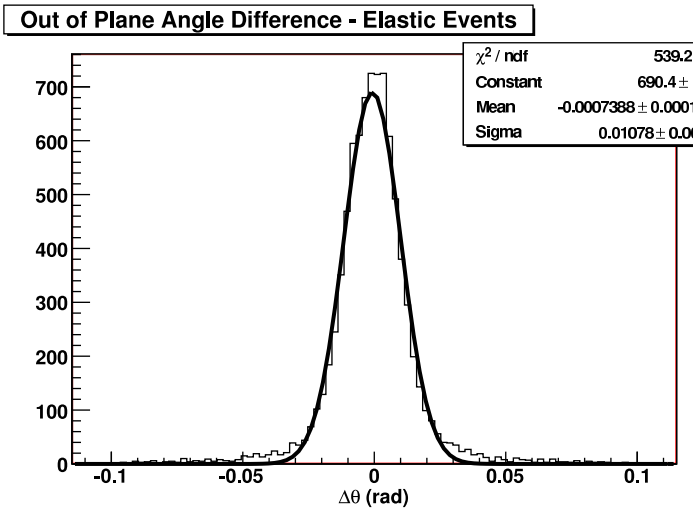

Figure 4.24: Coplanarity check for the scattered electron and recoiling nucleon for H_2 data.

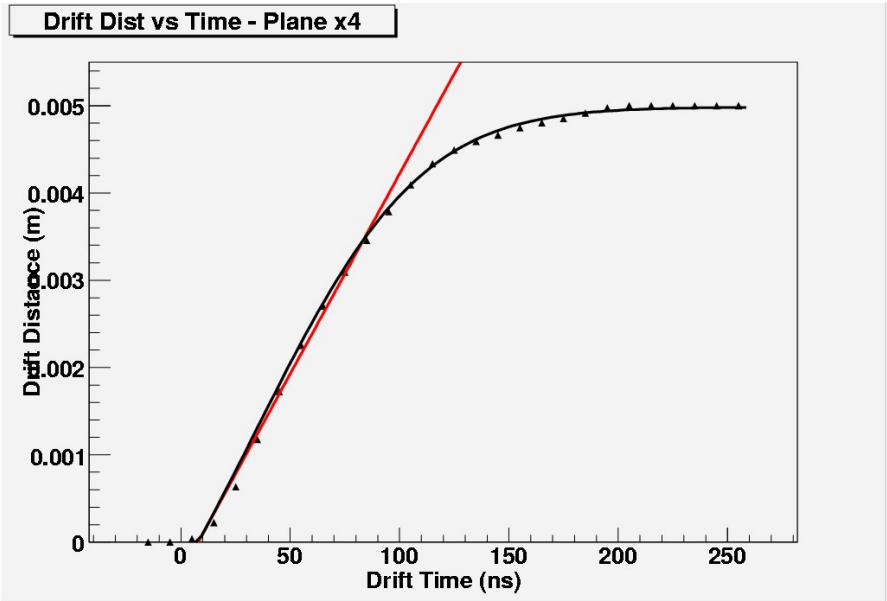

Figure 4.25: Drift distance vs. drift time relation and two methods fit to them.

in this case the drift distance for a given drift time is then

$$d(t) = d_{\max} \frac{\int_0^t f(t')dt'}{\int_0^{t_{\max}} f(t')dt'}. \tag{4.18}$$

In our case, $d_{\max}$ is half the cell width for each plane, which is 0.5 cm. The maximum drift time we consider is taken to be 250 ns, sufficiently beyond the nominal 200 ns range as shown in Fig. 4.18. The results of the calculation for $d(t)$ are in Fig. 4.25.

Using a constant drift velocity appears to be a good approximation up to a certain point where the average drift velocity begins to slow down (at roughly 4.0 mm). This approximation is shown in Fig. 4.25 as the dashed red line.

A more accurate method is to fit the time vs. distance relation to some function or polynomial. The function

$$d_{\text{drift}} = c_0 \tanh\left(\frac{v(t_{\text{drift}} - t_0) + c_2(t_{\text{drift}} - t_0)^2}{c_0}\right) \tag{4.19}$$

fits to longer drift times better than assuming a constant drift velocity. This is shown in Fig. 4.25 as the solid black line. This function has the two features that a) the function is linear at low drift times and b) the function asymptotically reaches a specified maximum drift distance.

Calibration can be performed on any set of data, as a uniform distribution of tracks across individual cells is expected. Separate calibrations are done for each individual plane and are not expected to be identical for different chambers due to differences in supplied voltages. Typical values used in the experiment are found in Table 4.19.

A typical reconstructed drift distance spectrum is shown in Fig. 4.26. The distribution is expected to be flat if the function fits the data exactly, but contains some apparent deviations at smaller drift

c_0	0.005 m
v	5.02×10^{-5} m/ns
t_0	6.1 ns
c_2	1.95×10^{-7} m/s^2

Table 4.19: Drift time to distance conversion parameters used for track reconstruction.

distances. The peak at 0.005 m is due to "asymptotic build-up" due to the model at drift times greater than 200 ns.

Crosstalk

Crosstalk between wires occurs when a sense wire acquires a signal and another signal is induced in the adjacent wire in the associated electronics. Fortunately, the signal appears to be induced consistently at about 7±2 ns after the original signal (Fig. 4.27). In theory, the second signal can be removed from the data, though this has not been implemented. The first chamber appears to be more sensitive to this effect (due to different amplifier/discriminator cards). Roughly 12% of the hits in the first chamber are a crosstalk signal compared to 5% of the other two chambers.

4.4.3 Scintillator Calibrations

The BigBite scintillator plane requires the same type of calibration necessary for that of the neutron arm timing described in Section 4.3.3. Individual offsets for each of the scintillator paddles, as given in Eq. 3.37 must be determined. Furthermore, the time walk corrections must be determined for the PMTs.

To determine the offsets, events are used for which the electron tracks are determined to be near an edge of two adjacent paddles, for which both paddles fire, and both paddles have an energy deposition above the mean. Energy-dependent timing effects should be minimized by requiring high energy deposition in both paddles. Light propagation path length differences should be minimized as the propagation should be approximately symmetric by choosing tracks near the edges and these events should have PMT signals that occur at the same time. By determining the offset differences between all paddles, offsets relative to one paddle can be determined.

To determine energy-dependent effects (time walk corrections), these effects can be isolated to a single paddle when the signal in the adjacent paddle is large, minimizing the effect in the adjacent paddle. By examining the time difference between the two paddles versus energy deposition, these corrections can be determined and removed. In Fig. 4.28 these corrections seem to be linear in inverse energy deposition.

4.4.4 Tracking Results

Basic results from tracking provide information on the performance of the spectrometer in the areas of resolution and reconstruction efficiency, but is also an invaluable aid in examining the performance of related detectors in determination of their efficiencies.

Plane and Tracking Efficiency

Individual plane and wire efficiency can be determined from reconstructed track data. As the tracking algorithm does not require each plane to have a hit, instances in which a track is determined to pass near a wire, but does not cause a hit, indicate inefficiency. Optimizing the efficiency of drift chamber planes by adjusting the high voltages of the field wire and cathode planes is important to

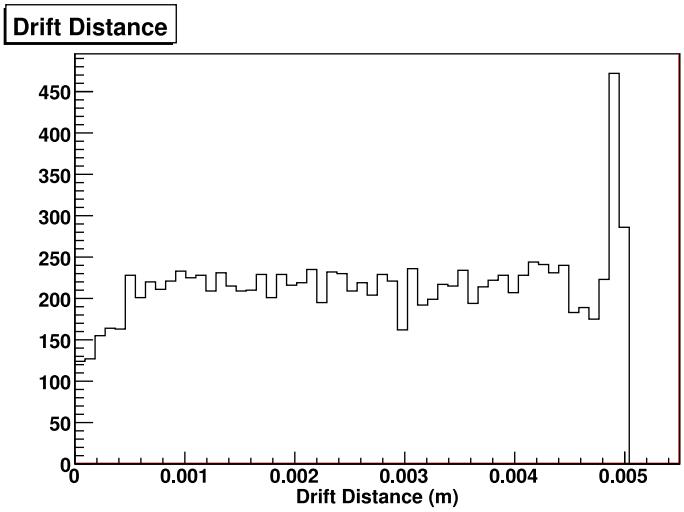

Figure 4.26: Drift distance spectrum using phenomenological model.

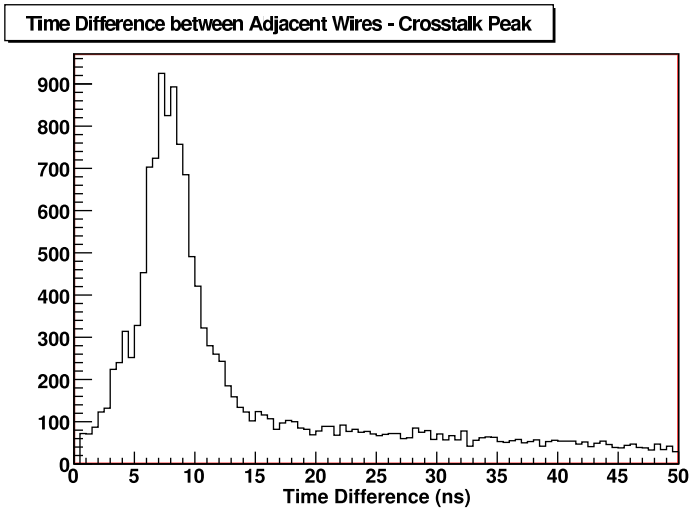

Figure 4.27: Crosstalk peak shown by the hit time differences on adjacent wires.

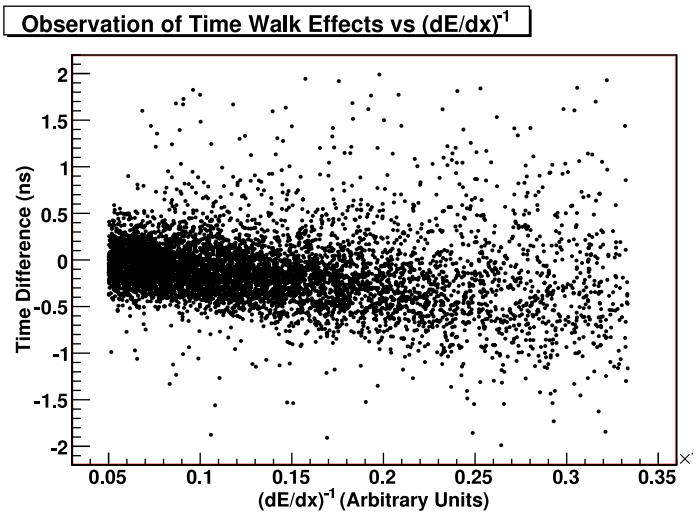

Figure 4.28: Determination of timewalk effects by examining time difference dependence against inverse energy deposition.

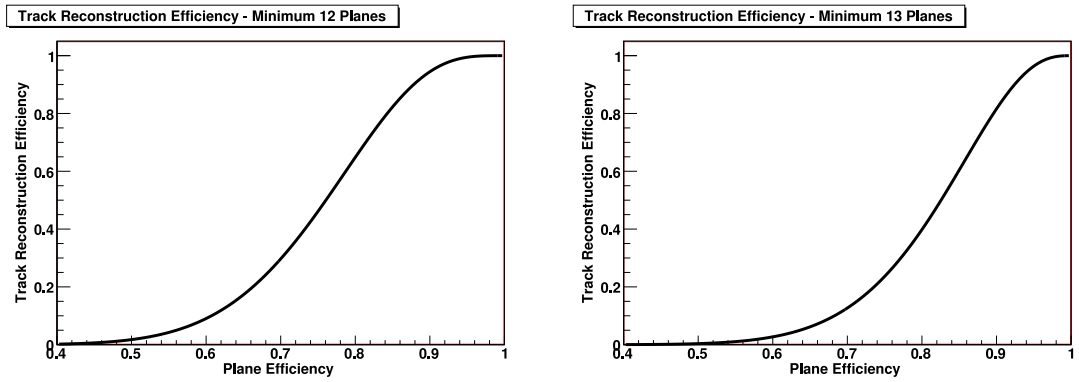

(a) (b)

Figure 4.29: Track reconstruction efficiencies as a function of plane efficiency for a minimum of a) 12 and b) 13 planes required in reconstruction.

provide sufficient information to reconstruct high resolution tracks, but also to help maximize the lifetime of the chambers by running at less damaging lower voltages.

The distribution of the number of planes firing for each event can be described using a binomial distribution given the efficiency of the planes. Given n planes, the probability of k planes firing when all planes have efficiency ϵ is

$$P(k,n) = \binom{n}{k}\epsilon^k(1-\epsilon)^{n-k}. \tag{4.20}$$

The fraction of the tracks which are reconstructed, P_{track}, given the chamber inefficiencies can be described by the formula

$$P_{\text{track}} = \sum_{i=n}^{n_{\min}} P(i,n) \tag{4.21}$$

where $n_{\min}$ is the minimum number of planes required to reconstruct a track. This is chosen based on considerations of reconstruction speed and, for E02-013, is generally either 12 or 13 of 15. Plots of the track reconstruction efficiency as a function of plane-efficiency are shown in Fig. 4.29. For production runs, plane efficiency was tuned by adjusting chamber high voltages to a value measured to give a plane efficiency of about 85%. This gives reconstruction efficiencies of 0.88 for a minimum of 12 planes in the reconstruction and 0.60 for 13 planes. It should be noted that for the lower beam-current H_2 runs, identical voltages produce efficiencies consistant with 100% efficiency due to the lower rates of incident particles on the chambers.

Tracking and Spectrometer Resolution

Tracking resolution for the four measured parameters that describe the position and slope of a track as it passes through the first drift chamber plane, x, y, x', and y', can be immediately obtained

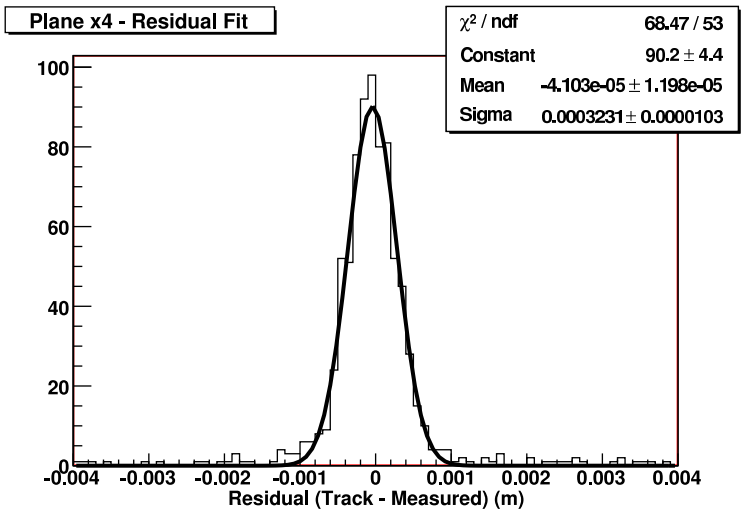

Figure 4.30: Typical residual for a plane, fit to a Gaussian defining resolution. The residual is found by measuring the difference in position of the fit track and the predicted position from the drift time to distance (assuming accurate L/R differentiation). Planes are required be used in the fit when calculating residual. No restrictions on planes used in the entire fit are placed. The average resolution is $\sigma = 350\mu$m.

from the reconstruction matrix described in Section 3.4.4 and Appendix B. As each of the four parameters is simply a linear combination of the measuring positions on each plane, the resolution for parameter r is then

$$\delta r = \sqrt{\sum_{i \in \text{planes}} (c_{r,i}\sigma_i)^2} \tag{4.22}$$

where $c_{r,i}$ is the matrix element for parameter r and σ_i is the spacial resolution for plane i. The spacial resolution for each plane can be found by fitting the residual distribution for each plane, as shown in Fig. 4.30. This is found to be about $\sigma \approx 350$ μm. The matrix used for a 15 plane reconstruction can be found in Appendix B. Following Eq. 4.22 we arrive at the resolutions in Table 4.21.

Estimates of the momentum, track direction, and vertex position can then be made using the track resolutions given in Table 4.21. We use only a few parameters to describe the spectrometer, the four track variables describing the position and slope of the track at the first drift chamber in detector coordinates:

- θ_{def}, the deflection angle of the track after it passes through the magnetic field
- x_0, the distance between the point of intersection of a track described by the line $x = 0$ and

Number/Type	U	X	V
1	385	289	338
2	353	358	299
3	483	375	388
4	324	323	348
5	356	348	335

Table 4.20: Resolutions, σ, for each plane. Units are μm.

Param.	Resolution (σ)
x	150 μm
x'	0.303 mrad
y	346 μm
y'	0.688 mrad

Table 4.21: Resolutions of the four track parameters.

$x' = 0$ with the magnetic mid-plane and the point of intersection of the line $x'_{\rm targ} = 0$ (parallel to the ground) from the center of the target to the magnetic mid-plane

- $d_{\rm pc}$, the distance between the origin of the detector coordinate system and the intersection of the line $x = 0$ and $x' = 0$ with the magnetic mid-plane
- $d_{\rm tp}$, the distance between the center of the target and the intersection of the line $x'_{\rm targ} = 0$ with the magnetic mid-plane
- $\theta_{\rm BB}$, the central angle of the BigBite spectrometer
- θ_0, the pitch of the BigBite spectrometer detector stack

The values of the distances and angles are given in Table 4.22 and shown in Fig. 4.31. Nominal values used in uncertainty estimations are given in Table 4.23.

The out-of-plane (parallel to the ground) angle in the target coordinate system, $\theta_{\rm targ}$, from the target can be described as

$$\theta_{\rm targ} = \tan^{-1}\left(\frac{\cos\theta_0}{\frac{d_{tp}}{x_0 - x + d_{pc}x'} - \sin(\theta_0)}\right) \equiv \tan^{-1}(\mathcal{X}). \tag{4.23}$$

The uncertainty for this is then

$$\delta\theta_{\rm targ} = \frac{\mathcal{X}^{\rm nom}}{1 + \mathcal{X}^{nom\,2}} \frac{1}{\frac{d_{\rm tp}}{x_0} - \sin\theta_0} \frac{d_{\rm tp}}{x_0^2}(\delta x^2 + d_{\rm pc}^2 \delta x'^2)^{1/2}. \tag{4.24}$$

Param.	Value
d_{tp}	1.45m
d_{pc}	0.81m
x_0	0.05m
θ_0	10°
$\theta_{\rm BB}$	51.6°

Table 4.22: Distances and angles used to determine resolutions.

Param.	Value
x	0.0m
y	0.0m
x'	0.0rad
y'	0.0rad
$\mathcal{X}$	0.034
θ_{def}	0.264 rad
p	1.1 GeV

Table 4.23: Nominal values used to determine resolutions.

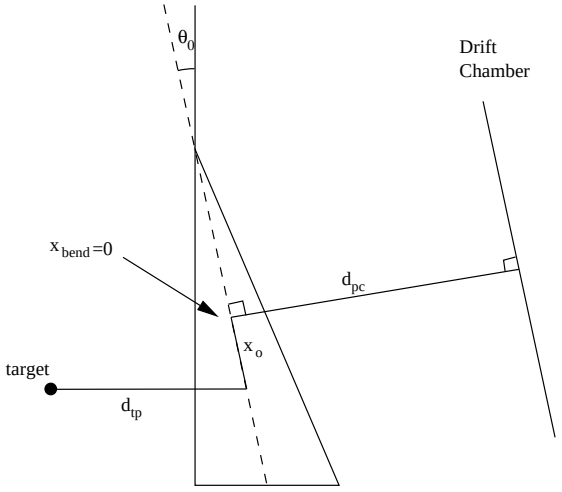

Figure 4.31: Approximate distances and positions for the BigBite spectrometer. Not to scale.

Variable	Resolution (σ)
$\delta\theta_{\rm targ}$	0.358 mrad
$\delta\phi_{\rm targ}$	0.688 mrad
δv_z	0.002 m
$\delta p/p$	0.2%

Table 4.24: Expected resolutions for the BigBite spectrometer.

Deflection angle can be described as

$$\theta_{\rm def} = \theta_{\rm targ} - \tan^{-1}(x') + \theta_0 \tag{4.25}$$

and

$$\delta\theta_{\rm def} = (\delta\theta_{\rm targ}^2 + \delta x'^2)^{1/2}. \tag{4.26}$$

In-plane angle in the target coordinate system, $\phi_{\rm targ}$, is approximately

$$\phi_{\rm targ} = -\tan^{-1}(y') + \theta_{\rm BB} \tag{4.27}$$

so,

$$\delta\phi_{\rm targ} = \delta y'. \tag{4.28}$$

The vertex position along the beamline, v_z, is approximately

$$v_z = \frac{y + (d_{tp} + d_{pc})y'}{\sin\theta_{\rm BB}} \tag{4.29}$$

and

$$\delta v_z = \frac{(\delta y^2 + (d_{tp} + d_{\rm pc})^2\delta y'^2)^{1/2}}{\sin\theta_{\rm BB}}. \tag{4.30}$$

The scattered electron momentum, p, is approximately

$$p = \frac{(0.29\ ({\rm GeV/c})/{\rm rad}) + (0.1\ ({\rm GeV/c})/({\rm rad}\cdot{\rm m}))x}{\theta_{\rm def}} \tag{4.31}$$

and

$$\delta p = \left(\frac{((0.29\ ({\rm GeV/c})/{\rm rad})\delta\theta_{\rm def})^2}{\theta_{\rm def}^{\rm nom\,4}} + \frac{((0.1({\rm GeV/c})/({\rm rad}\cdot{\rm m}))\delta x)^2}{\theta_{\rm def}^{\rm nom}}\right)^{1/2}. \tag{4.32}$$

Solving for the uncertainty given by these equations, the expected resolutions are then given in Table 4.24.

4.4.5 Optics Calibration

Optics calibration involves determining the most accurate vertex and momentum reconstruction by examining known scattering processes on different targets. This also involves allowing for deviations in the magnetic field that vary over the face of the magnet.

Target Image

Identification of the target image is done by examining data at each given kinematic setting to determine the central position of the image and width of the volume to search for drift chamber hits. This is done empirically by examining the wire chamber hit distribution on the X wire chamber planes about some central path line defined by the straight line between the central position of the

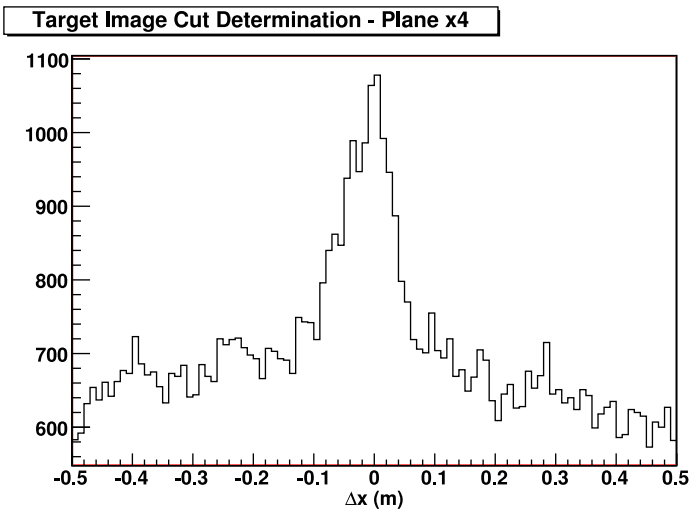

Figure 4.32: Distribution of the differences in drift chamber hit position and the line defining the center of the shower cut region.

target image and the hit found in the shower. By varying the image central position such that the distributions become centered about the projected point of the line, the image position can be determined.

Working in detector coordinates, the projected position of the central path line is

$$x_{\mathrm{path}} = \frac{x_{\mathrm{BB,sh}} - (x_{\mathrm{beam}} - x_{\mathrm{img}})}{z_{\mathrm{BB,sh}} - z_{\mathrm{beam}}} z_i \tag{4.33}$$

where x_{path} is the projected point of the central path line on plane i, $x_{\mathrm{BB,sh}}$ is the x position of the BigBite shower cluster, x_{beam} is the x position of the beam at $y_{\mathrm{det}} = 0$, x_{img} is the central position of the target image relative to the beam, $z_{\mathrm{BB,sh}}$ is the z position of the BigBite shower, z_{beam} is the z position of the beam at $y_{\mathrm{det}} = 0$, and z_i is the z position for drift chamber plane i.

We define the difference between the projected point of the central line x_{path} and the drift chamber hit, $x_{\mathrm{d.c.hit}}$ to be Δx

$$\Delta x = x_{\mathrm{d.c.hit}} - x_{\mathrm{path}}. \tag{4.34}$$

x_{img} is adjusted until the distributions of Δx for each X drift chamber plane is roughly centered. The volume around the central line used to accept hits is chosen to grossly overestimate the width of the distribution of Δx, such as to minimize the number of good hits excluded in tracking. An example of the distribution can be seen in Fig. 4.32. Typical values of the path width are ± 20 cm.

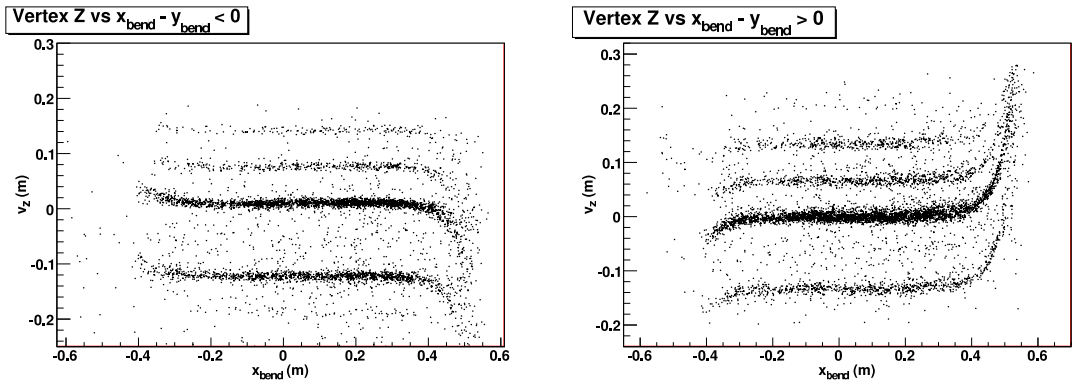

(a) (b)

Figure 4.33: Vertex reconstruction, v_z vs. magnet vertical position, $x_{\rm bend}$ for a) $y_{\rm bend} < 0$ and b) $y_{\rm bend} > 0$. Antisymmetric, nonlinear deviations in $x_{\rm bend}$ are observed in the reconstruction in the extreme vertical regions of the acceptance which are also antisymmetric $y_{\rm bend}$.

Vertex

Vertex reconstruction was calibrated using a set of carbon and BeO foils at known positions. For kinematics 1 through 3, a target with foil pattern of 3 carbon foils, a BeO foil, and 3 more carbon foils 0.067 m apart were placed in the beamline with the BeO foil placed near the lab origin. For kinematic 4, the carbon foil at $v_z = -0.067$ m was damaged and removed. The first and last foil cannot be seen in any data sets due to collimators blocking scattered electrons in those regions. The resulting peaks can be observed in the data using a naive model and then corrections can be determined by examining the vertex dependencies on several track parameters. These can be described by the model given in Section 3.3.5.

A single set of parameters for Eq. 3.24 is not sufficient, as is readily apparent in Fig. 4.33. The vertex reconstruction has very dramatic non-linear behavior in $x_{\rm bend}$, corresponding to the extreme vertical regions of the acceptance, $x_{\rm bend} < -0.2$ m and 0.3 m $< x_{\rm bend}$. These regions account for roughly 40% of the acceptance with more than one third of the statistics falling into a problematic region. These deviations follow a pattern where they are roughly antisymmetric in both $x_{\rm bend}$ and $y_{\rm bend}$ and is consistent with deviations created by the vertical portions of the coils of the magnet, shown in Figs. 4.34 and 4.35.

To account for this, the constant term, a, in Eq. 3.24 is allowed to vary over the acceptance of the magnet. This is then fit by binning the reconstructed vertex of the central foil in equal sized rectangular acceptance regions in the magnetic mid-plane. For simplicity, we do not allow a to vary over the momentum of the electron, though some dependence is likely present. This method is only valid when the variation is linear over the acceptance region and therefore fails for the most extreme vertical regions where the deviations are rapidly changing.

The value of the peak location of this distribution is then taken as the correction to be applied, creating a discrete grid of values $A_{i,j}$, where i, j are indices corresponding to the acceptance bin.

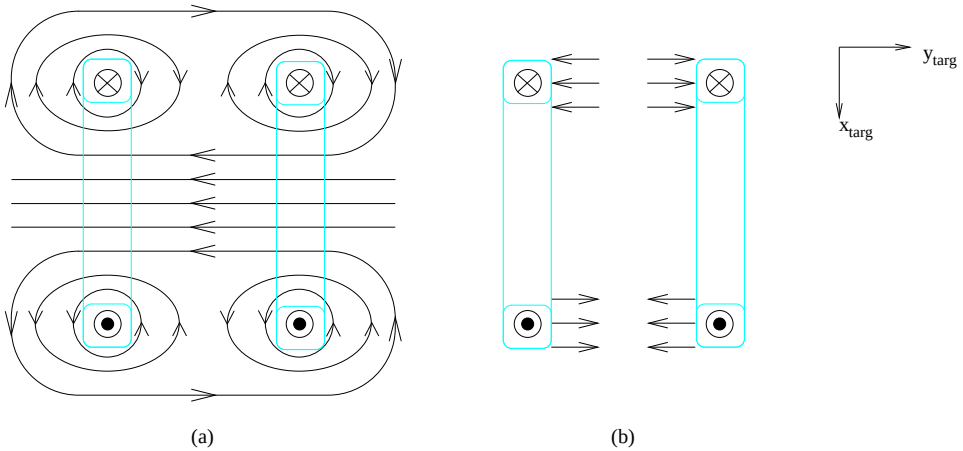

Figure 4.34: a) Magnetic field lines caused by BigBite magnet coils as viewed looking up $z_{\rm targ}$ axis (from chambers to target). b) Expected deflection pattern for negatively charged particles. Not to scale.

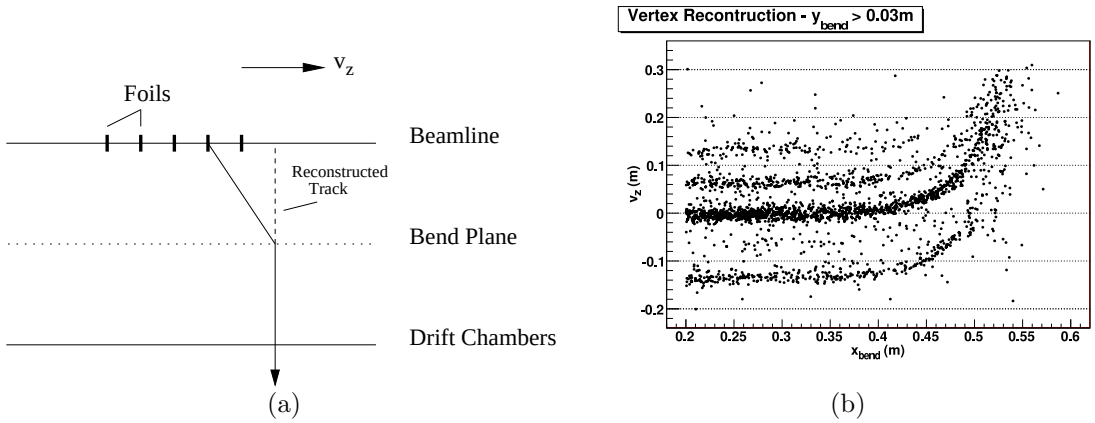

Figure 4.35: Deflections caused by field deviations for high $x_{\rm bend}$, high $y_{\rm bend}$. a) For this region it is predicted to have a reconstructed image at higher v_z. b) This type of deflection is observed in the data. Not to scale.

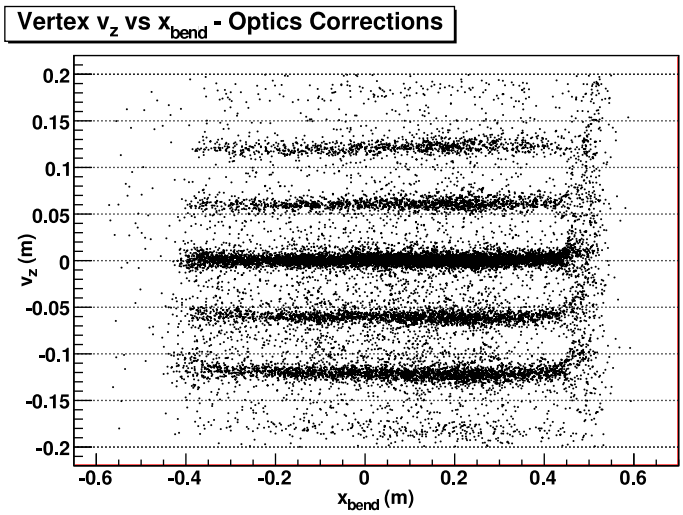

Figure 4.36: Corrected reconstructed vertex vs. vertical track position at the bend plane. All but the most extreme regions have no dependence on v_z.

To allow for smooth variations over acceptance of the magnet, a bilinear interpolation scheme is employed, where the value for a at coordinates $(x_{\rm bend}, y_{\rm bend})$ is found using

$$\begin{aligned} a(x_{\rm bend}, y_{\rm bend}) &= A_{i,j}\frac{(x_{i+1}-x_{\rm bend})}{\Delta x_{\rm bend}}\frac{(y_{j+1}-y_{\rm bend})}{\Delta y_{\rm bend}} + A_{i+1,j}\frac{(x_{\rm bend}-x_i)}{\Delta x_{\rm bend}}\frac{(y_{j+1}-y_{\rm bend})}{\Delta y_{\rm bend}} \\ & A_{i,j+1}\frac{(x_{i+1}-x_{\rm bend})}{\Delta x_{\rm bend}}\frac{(y_{\rm bend}-y_j)}{\Delta y_{\rm bend}} + A_{i+1,j+1}\frac{(x_{\rm bend}-x_i)}{\Delta x_{\rm bend}}\frac{(y_{\rm bend}-y_j)}{\Delta y_{\rm bend}} \end{aligned} \quad (4.35)$$

where x_i and y_j are the ($x_{\rm bend}$, $y_{\rm bend}$) coordinate of the center of acceptance bin (i, j), and Δx and Δy are the spacings between the grid points.

After these corrections are applied the dependence on $x_{\rm bend}$ is removed except in the most extreme regions and no dependence is observed for $y_{\rm bend}$, shown in Figs. 4.36, 4.37, and 4.38. The reconstruction appears to be valid for -0.35 m $< x_{\rm bend} <$ 0.45 m, or about 90% of the total acceptance.

Fitting the vertex z-position for the central foil to a Gaussian, a resolution along the beamline of $\sigma_{v_z} = 0.0046$ m is found. This is a factor of two worse than the predicted value of 2 mm from the drift chamber resolutions.

Momentum

Momentum reconstruction follows a similar procedure to the vertex reconstruction discussed above. Calibration of momentum is done using a H_2 target and selecting on elastic events. These events

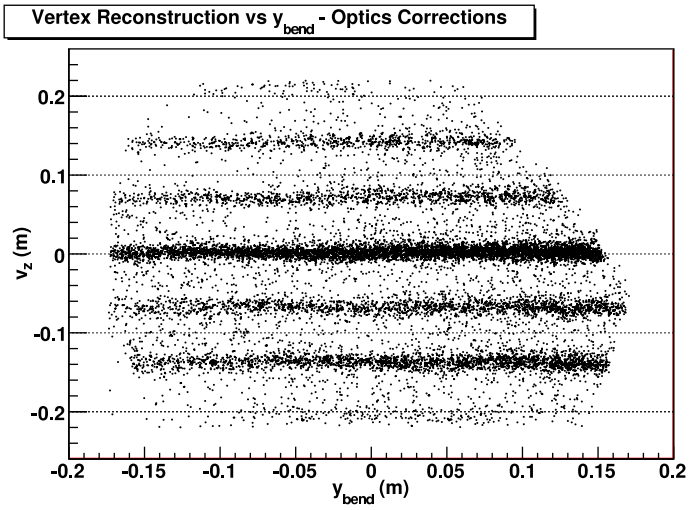

Figure 4.37: Corrected reconstructed vertex, v_z, vs. horizontal track position at the bend plane, $y_{\rm bend}$.

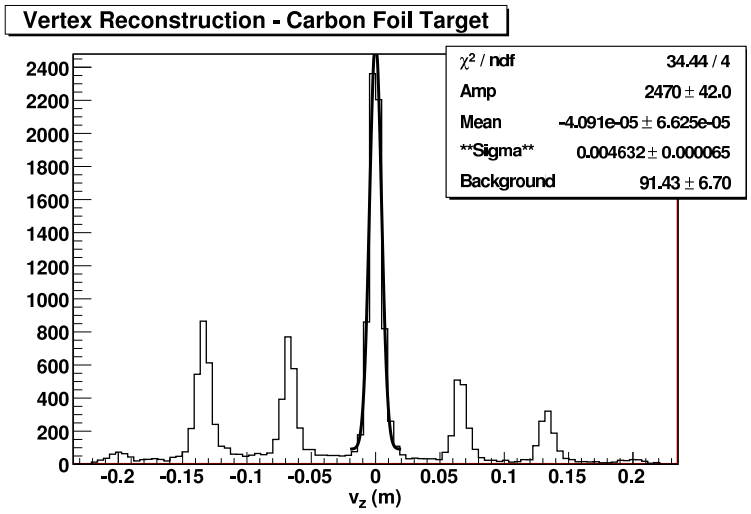

Figure 4.38: Corrected carbon foil beamline vertex reconstruction. The central foil is physically placed to have a position of 0.0m. Resolution of about $\sigma_{v_z} = 4.6$mm is observed.

have a well defined momentum that is only dependent on scattering angle, given by the formula

$$E_{\text{elas}} = \frac{m_p E_b}{m_p + E_b(1 - \cos\theta_e)} \tag{4.36}$$

where m_p is the mass of the proton, E_b is the energy of the beam, and θ_e is the scattering angle of the electron. Once the vertex has been well calibrated, the scattering angle of the electron can be reliably reconstructed and the momentum can then be calibrated. If there are deviations in the vertex reconstruction, these will translate directly into changes in the scattering angle (seen in Fig. 4.35 (a)), so it is imperative to perform the vertex calibration first.

Elastic events are chosen in the H_2 data by first requiring rough coincidence between a hit in the neutron arm and an electron track in the spectrometer. Electron tracks are selected by requiring preshower signals greater than 500 channels and by selecting on vertices that originate within the target chamber, $-0.17\text{m} < v_z < 0.17\text{m}$. For coincidence, it is useful to define

$$\Delta_{\text{coplane}} = \frac{p_y^{\text{NA}}}{p_x^{\text{NA}}} - \frac{p_y^e}{p_x^e} \tag{4.37}$$

where $\vec{p}^{\text{NA}}$ is the momentum vector of the proton measured by the neutron arm and $\vec{p}^{e}$ is the momentum vector of the electron measured by BigBite and components are evaluated in the Hall coordinates. This gives a measure of the "coplanarity" of the event, as the electron and neutron should be in a single scattering plane by conservation of momentum. It should be noted, that since we are just interested in ratios of momenta, they are simply functions of the direction of the track and momentum does not have to be well calibrated.

For timing coincidence, a pseudo-time of flight is examined

$$t_{\text{coinc}} = t_{\text{clus}}^{\text{TDC,corr}} - t_{\text{BB,hit}}^{\text{TDC,corr}} + t_{\text{L1A}}^{\text{TDC}} \tag{4.38}$$

where $t_{\text{clus}}^{\text{TDC,corr}}$ is the corrected reconstructed time of a neutron arm cluster, $t_{\text{BB,hit}}^{\text{TDC,corr}}$ is the corrected reconstructed time of a BigBite scintillator hit, and $t_{\text{L1A}}^{\text{TDC}}$ is the TDC time of the level 1 accept, given in Eq. 3.38. This provides a flight time up to a constant, neglecting electron path length differences, which is acceptable when placing a cut on the order of several ns. Even with such a wide cut, a significant amount of accidental background and other events can be removed, greatly improving the elastic signal.

The values of the cuts vary between kinematics (especially the timing cut), and are chosen through examination of the data. An example for kinematic 4 is given in Figs. 4.39 and 4.40.

The quantity of interest when doing a momentum calibration is the difference between the momentum provided by the optics model, p_{fit}, (the value we are calibrating) and the reference momentum, p_{elas} obtained using the scattering angle and the assumption that it is an elastic event, which we call δp

$$\delta p = p_{\text{fit}} - p_{\text{elas}}. \tag{4.39}$$

Ideally when calibrated, this quantity will be zero. However, due to the finite resolution of the spectrometer and radiative effects, there will be some spread about $\delta p = 0$ once the optics model is correctly calibrated.

The formula described in Eq. 3.25 is used and is fit to p_{elas}. However, problems similar to those of the vertex reconstruction become apparent when the fit is extended into the same extreme vertical regions of the magnet. In these regions, deviations are slightly more complicated as shown in Fig. 4.41. Similar antisymmetric effects that were present in the vertex reconstruction appear not to be as well defined in the momentum distributions.

Furthermore, when examining the central region of the acceptance, $-0.25\text{ m} < x_{\text{bend}} < 0.35\text{ m}$, it is apparent that a single set of parameters are insufficient to describe the optics. When calibrating for a single kinematic (and allowing for the constant a term in Eq. 3.25 to be taken as 0), applying

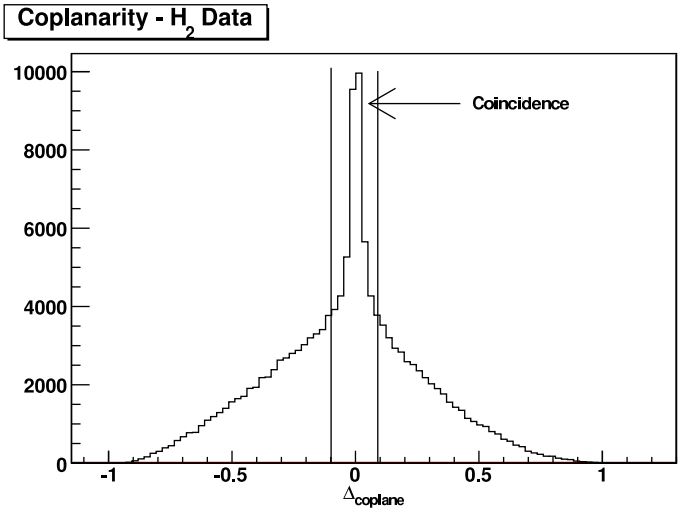

Figure 4.39: Coplanarity selection for elastic events.

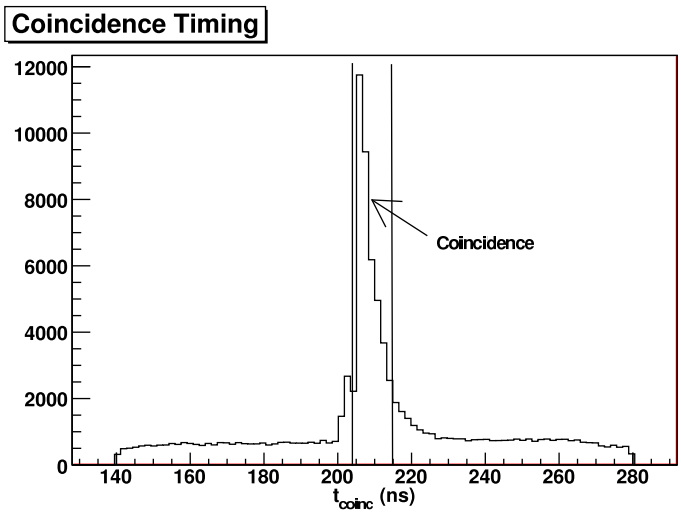

Figure 4.40: Pseudo-time of flight selection for elastic events.

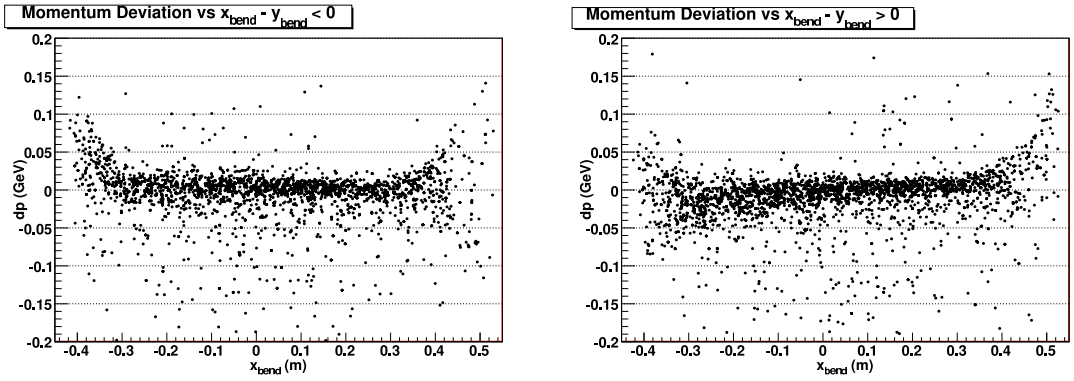

(a) (b)

Figure 4.41: δp vs. $x_{\rm bend}$ for a) $y_{\rm bend} < 0$ and b) $y_{\rm bend} > 0$ using a constant set of parameters.

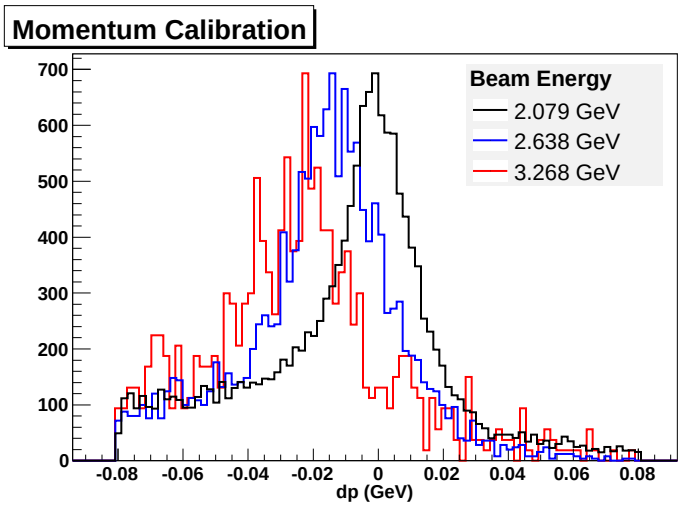

Figure 4.42: Difference of momentum calibration to p_{elas} when using identical coefficients over several kinematics. Ideally all distributions would be centered about 0.

those parameters to other kinematics yields δp distributions that are not centered around 0, as in Fig. 4.42.

A corrected value of the momentum, p', is obtained from the uncorrected value, p, by assuming a correction of the form

$$p' = cp + b \tag{4.40}$$

where the parameters c and a are determined by the following approach:

1. One kinematic has a set of optics parameters fit with the constant term, a taken to be 0.
2. This set of parameters is then applied to all kinematics and the shift in δp is determined.
3. A linear transformation is determined such that the central value of δp for all kinematics is centered around 0. That is,
$$p' = cp + b.$$
4. The in-plane dependent coefficients of the momentum function, y and y', are refit to optimize resolution

The refitting of the in-plane dependent coefficients is included to correct for resolution degradation due to the linear transformation. There will be little initial dependence on p for the first set of parameters and additional dependencies will be introduced when the linear transformation is taken since p is highly correlated with the in-plane parameters y and y'. Adjusting the associated coefficients will remove these dependencies.

To resolve discrepancies in the extreme vertical region, an approach similar to the vertex corrections is taken. The leading coefficient in Eq. 3.25, c_0, is allowed to vary over coordinate (x_{bend}, y_{bend}). The remaining parameters are fit in the central region, -0.25 m $< x_{\text{bend}} < 0.35$ m where a constant set of parameters is sufficient. We note that for simplicity we do not allow this constant to have any p dependence, though it is likely that some would be present. To determine the values, the acceptance is broken into 10×6 identically sized rectangles on the effective bend plane. For all elastic events in each bin, c_0 is determined

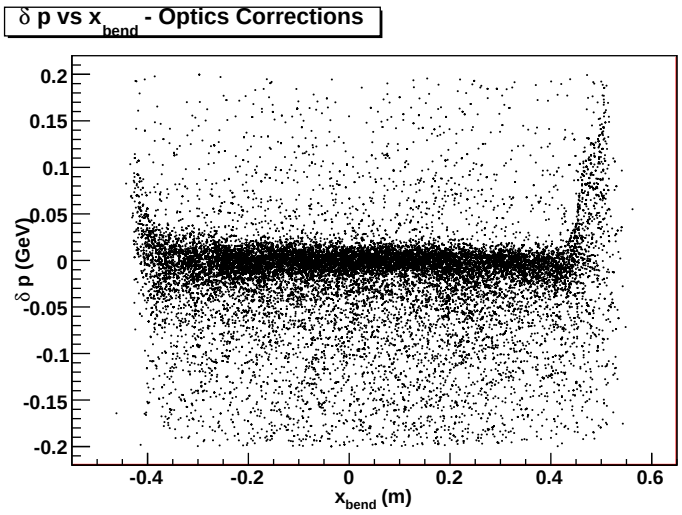

Figure 4.43: δp vs $x_{\rm bend}$ after c_0 is allowed to vary over the acceptance. This scheme fails for the most extreme regions of the magnet and we restrict ourselves to $-0.35 < x_{\rm bend} < 0.45$ m.

$$c_0 = (p_{\rm elas} - c_\vartheta \vartheta_{\rm targ} - c_y y_{\rm det} - c_\varphi y'_{\rm det} - a)\vartheta_{\rm def} - c_x x_{\rm bend}. \tag{4.41}$$

The central value of the resulting c_0 distribution is then identified with a grid value, $C_{i,j}$ at position (x_i, y_j), the $x_{\rm bend}$ and $y_{\rm bend}$ coordinates for the center of the acceptance bin. A bilinear interpolation scheme is then used to provide a smooth variation of c_0 over the acceptance. As with the vertex procedure, this method is only valid when the variation of c_0 over the acceptance bin is small and therefore fails for the most extreme regions, namely $x_{\rm bend} < -0.35$ m and 0.45 m $< x_{\rm bend}$, the same regions where the vertex reconstruction fails, shown in Fig. 4.43.

These deviations have been seen before in BigBite analysis during experiments when the magnet was at NIKEF. While the magnet was run with smaller fields, similar deviations occurred in the same manner as observed in our data. Previous corrections were applied in a manner similar to ours by performing an interpolation of the momentum deviation along the vertical angle [73].

Once these parameters are determined, they can then be applied to all other kinematics. By examining the central values of δp distributions, a linear transformation can be done and the collective in-plane terms refit. The results are a set of parameters that are then consistent across all kinematics. Fig. 4.44.

Resolution can be determined by fitting the δp distribution to a Gaussian and first order polynomial. The polynomial is necessary to help account the asymmetric radiative tail of the distribution. A resolution of about $\sigma_p = 10$ MeV is found, or about 0.9% (Fig. 4.45). This is about a factor of 5 worse than the predicted value of 2 MeV based on the plane resolutions.

4.4.6 Field Simulation Results

To obtain insight to the behavior of charged particles passing through the BigBite magnetic field, a TOSCA simulated magnetic field model was developed for a 12 kG field. This simulation was done before the experiment and the software has since become unavailable due to monetary restrictions. While results from this simulation do not prove to be useful in accurately determining the optics coefficients in our model, the simulation does provide some qualitative insight into some features of the data as well as provide confirmation that our optics model accurately reconstructs track vertices

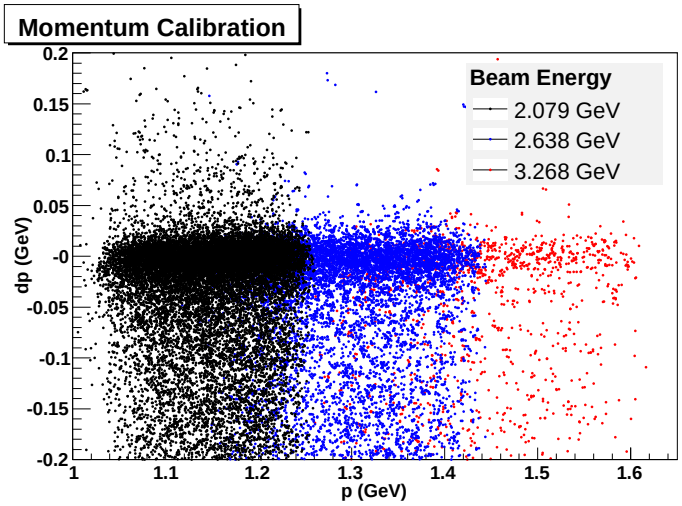

Figure 4.44: δp vs p for all kinematics using a single set of optics parameters.

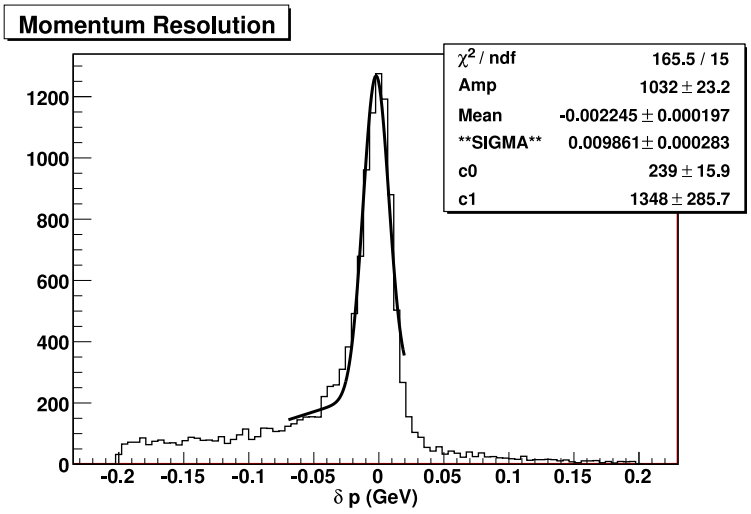

Figure 4.45: Momentum resolution fit. A resolution of about 10 MeV is found.

and momenta. The field map produced covered a volume of $y_{\rm targ} = -5.5$ cm to 5.5 cm, $x_{\rm targ} =$ -70cm to 80 cm, and from 40 cm in front of the face of the magnet to 130 cm behind the face of the magnet. A 3-vector of the magnetic field is given on a 2 cm $\times$ 2 cm $\times$ 2 cm spaced grid.

Using this model, simulated tracks were propagated numerically through the field and the deflected track that would be measured in the drift chambers was recorded. By using such a model, comparisons can then be made directly to the data.

A fourth order Runge-Kutta method was employed to provide iterative numerical propagation of the scattered electron track through the magnetic field. This provides numerical solutions to the Lorentz force

$$\frac{d\vec{p}}{dt} = q\vec{v} \times \vec{B} + q\vec{E} \tag{4.42}$$

For each position, $\vec{x}_i$, and momentum, $\vec{p}_i$, at a given iteration in time, t_i,

$$\vec{p}_{i+1} = \vec{p}_i + \frac{\Delta t}{6}(\vec{k}_1 + 2\vec{k}_2 + 2\vec{k}_3 + \vec{k}_4) \tag{4.43}$$

$$\vec{x}_{i+1} = \vec{x}_i + \Delta t \frac{\vec{p}_i c}{\sqrt{|\vec{p}_i|^2 + m_e^2}} \tag{4.44}$$

$$t_{i+1} = t_i + \Delta t \tag{4.45}$$

where

$$\vec{k}_1 = \frac{d\vec{p}(\vec{x}_i, \vec{p}_i)}{dt} \tag{4.46}$$

$$\vec{k}_2 = \frac{d\vec{p}(\vec{x}_i + \frac{\Delta t}{2}\frac{\vec{p}_i c}{\sqrt{|\vec{p}_i|^2+m_e^2}}, \vec{p}_i + \frac{\Delta t}{2}\vec{k}_1)}{dt} \tag{4.47}$$

$$\vec{k}_3 = \frac{d\vec{p}(\vec{x}_i + \frac{\Delta t}{2}\frac{\vec{p}_i c}{\sqrt{|\vec{p}_i|^2+m_e^2}}, \vec{p}_i + \frac{\Delta t}{2}\vec{k}_2)}{dt} \tag{4.48}$$

$$\vec{k}_4 = \frac{d\vec{p}(\vec{x}_i + \Delta t\frac{\vec{p}_i c}{\sqrt{|\vec{p}_i|^2+m_e^2}}, \vec{p}_i + \Delta t\vec{k}_3)}{dt}. \tag{4.49}$$

Tracks were generated using the Born approximation on a proton target using the dipole approximation (introduced in Section 2.3.4) for the electric and magnetic form factors. This gives a differential cross section, the same in Eq. 3.1, equal to

$$\frac{d\sigma}{d\Omega} = \frac{\alpha^2}{4E^2 \sin^4\frac{\theta}{2}} \frac{1}{1 + \frac{E}{M}(1 - \cos\theta)} \left(\frac{G_E^2 + \tau G_M^2}{1+\tau} \cos^2\frac{\theta}{2} + 2\tau G_M^2 \sin^2\frac{\theta}{2} \right) \tag{4.50}$$

where

$$G_E(Q^2) = \left(1 + \frac{Q^2}{0.71\text{GeV}^2}\right)^{-2}, \tag{4.51}$$

$$G_M(Q^2) = \mu_p \left(1 + \frac{Q^2}{0.71\text{GeV}^2}\right)^{-2}, \tag{4.52}$$

E is the initial beam energy, θ is the scattering angle of the electron, M is the mass of the proton, $\tau = \frac{Q^2}{4M^2}$, $q^2 = -Q^2$ is the 4-momentum transfer, and μ_p is the magnetic moment of the proton, approximately 2.792.

Tracks are generated according to this distribution by using the "acceptance-rejection method" [74] using a fixed beam energy. Furthermore, the track vertex along the beamline was uniformly distributed along a "target" of some length. After generation, if the tracks are determined to enter the opening of the magnet, the they are propagated through the field and are otherwise thrown away.

Parameter	Value
Magnet face from target	1.1 m
Magnet opening width	0.11 m
Magnet opening height	0.9 m
Magnet central angle	-51.59°
Target Length	0.4 m
Detector stack pitch	10°
Detector from target z_{targ}	2.25 m
Detector from target x_{targ}	-0.17 m
Detector height	1.4 m
Detector width	0.35 m
Beam Energy	2.079 GeV
Time Step	5×10^{-12} s
σ_x	150 μm
$\sigma_{x'}$	0.30 mrad
σ_y	340 μm
$\sigma_{y'}$	0.69 mrad

Table 4.25: Field simulation parameters.

Param.	Simulation	Data
c_0	0.225	0.272
c_x	0.125	0.130
c_θ	0.0	0.0
c_y	1.05	0.17
c_ϕ	-0.35	-0.12

Table 4.26: Fit momentum parameters for simulated field and kinematic 4 data. These fits assumed the a term was 0 and the fit was only done for the central region.

After propagation the deflected track at the position of the drift chambers is calculated. Gaussian smearing of x, x', y, and y' can be specified to simulate finite drift chamber resolution. The same optics method as done for BigBite is then applied and the track before scattering is reconstructed.

Tracks were generated using the parameters given in Table 4.25. Of note is the field volume generated is smaller than the actual size of the magnet, which may be the cause of deviations from reality.

Unfortunately, serious deviations from the data were immediately discovered using the provided field map. Notably, the optics coefficients after performing a fit for the momentum in the central region using a perfect vertex reconstruction was significantly different compared to performing the same analysis on real data, as shown in Table 4.26. The most significant difference is in the leading coefficient, suggesting that the field integral for a track is smaller in the simulation than in reality. Resolution for the simulation of about $\sigma_p = 10$ MeV was comparable to real data (Fig. 4.46).

This suggests that the field provided differs from the field used for the experiment, but lends strong credence to the optics model chosen. Also, several qualitative results were found from the simulation that compare well to the data. Namely, the extreme region deviations in the vertex and momentum reconstruction are also seen in the simulation.

For the vertex reconstruction, deviations in the extreme vertical regions manifest themselves in similar regions in x_{bend} with identical behavior in relation to $y_{\text{bend}} > 0$, Fig. 4.47. However, the $y_{\text{bend}} < 0$ behavior is not present, suggesting the field simulation is not complete and only

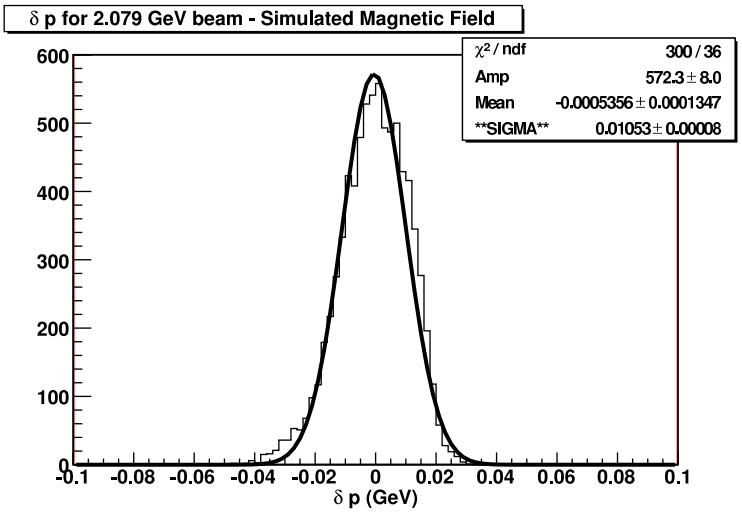

Figure 4.46: Simulation momentum resolution is about $\sigma_p = 10$ MeV.

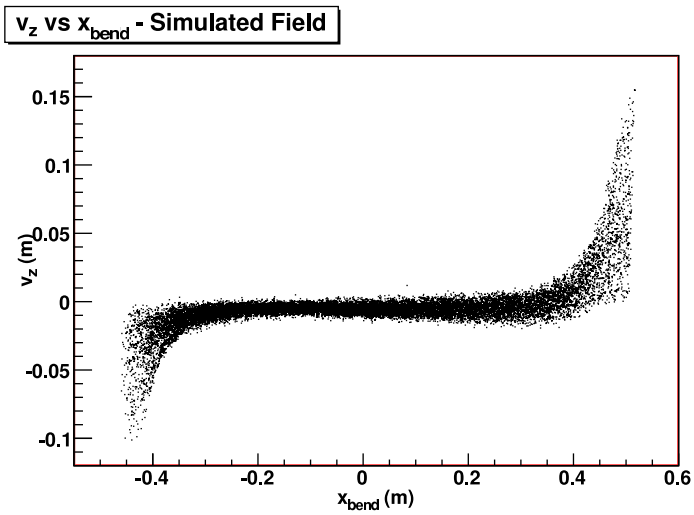

Figure 4.47: v_z vs $x_{\rm bend}$ for simulated field with no cuts on $y_{\rm bend}$. Only the $y_{\rm bend} > 0$-type behavior that is seen in the data appears to be present in the simulation.

represents one side of the magnet (compare to Fig. 4.33). (As a side note, this can be taken into account by symmetry considerations but was not done.) For the momentum reconstruction, using a perfect vertex reconstruction (forcing the vertex to be the true vertex to simulate an already corrected vertex position), once again deviations in the same regions are found, Fig. 4.48. Compare to Fig. 4.41. Both of these results show qualitative agreement with the data and provide confirmation that the deviations in the vertical regions seen in the data are expected from the design of the magnet.

4.4.7 Carbon Foil Reconstruction Amplitudes

The reconstructed counts as a function of vertex position for the foil targets should be predictable given the acceptance of the spectrometer as a function of beamline vertex, the material of the foils, and the thicknesses of the foils. As we have two different materials, C and BeO, the ratio of amplitudes can be calculated without calculation of the absolute cross section.

We expect this ratio to be

$$R = \frac{\rho_{\rm BeO} w_{\rm BeO}}{\rho_{\rm C} w_{\rm C}} \tag{4.53}$$

where ρ is the density of the material, and w is the thickness, as traversed by the beam. Given the densities and widths provided in Table 4.27, we predict a ratio of 3.28.

To determine the relative amplitudes in the data, a histogram of the vertex reconstruction is produced. For each foil an integral over a set of bins for the region ± 2 cm around the foil central value is used to measure the reconstructed amplitude. To account for acceptance variations over v_z, the

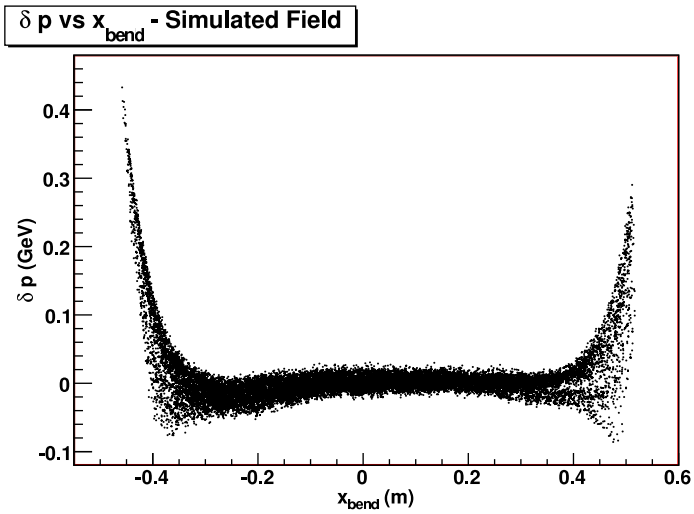

Figure 4.48: δp vs x_{bend} for a simulated field. Strong deviations in the extreme regions are present similar to those in the data.

Material	Density (g/cm^3)	Width (cm)	Thickness (mg/cm^3)
C	2.2	0.025	55.0
BeO	3.01	0.060	180.6

Table 4.27: Thicknesses and densities of foil target.

Foil	Integral		N_{H_2}	Normalized Integral	
	Kin 3	Kin 4		Kin 3	Kin 4
1	2.039	3.434	1202	1.764	2.971
2	2.032	-	1288	1.641	-
4	0.976	1.829	772	1.315	2.464
5	0.613	1.121	450	1.417	2.591
Average				1.534	2.675
BeO	5.140	8.295	1050	5.140	8.295
Ratio				3.350	3.100
Predicted				3.284	3.284
Frac. Error				0.02	0.06

Table 4.28: Analysis of foil target reconstruction amplitude ratios.

empirical variation of the vertex reconstruction due to acceptance for a H_2 target is used to normalize the counts since this distribution without acceptance effects should be flat. This distribution is shown in Fig. 4.49. By measuring the relative number of counts in the H_2 distribution at the foil position relative to the value at $v_z = 0$, a normalization constant is obtained. The corrected amplitude for each foil is then

$$N_i^{\text{norm}} = \frac{\sum_{v_{z,i} \pm 2 \text{ cm}} N_i^{\text{foil}} N^{H_2}(v_z = 0)}{N^{H_2}(v_{z,i})} \tag{4.54}$$

where N_i^{norm} is the normalized number of counts for foil i, $v_{z,i}$ is the position of foil i, $N^{H_2}(v_z = 0)$ is the number of counts in the H_2 spectrum for the histogram bin at $v_z = 0$, and $N^{H_2}(v_{z,i})$ is the number of counts in the H_2 spectrum for the histogram bin at $v_{z,i}$. Integrals of the foils are presented in Table 4.28.

The ratios are within a few percent of the predicted values for kinematic 3 and kinematic 4. This acts as a check of reconstruction along the vertex for the new tracking code.

4.4.8 Radiative Effects

Radiative effects can have a significant effect on the elastic momentum distribution. These effects arise from electron interaction with the target cell wall before or after scattering via the emission of a real photons and also from internal radiative effects where the electron will emit a photon while interacting with the target nucleus. These effects are of great importance in the calculation of absolute cross sections, but for E02-013 they are mostly only of passing interest. Given the δp distribution given by Eq. 4.39, the number of particles having radiated a photon in addition to scattering can be measured and then compared to theory. This is not critical to the determining the asymmetry.

Ultimately, we wish to calculate the change in the measured cross section due to these effects. We can write this as

$$\sigma^{\text{meas}}(\Delta E) = K^{\text{int}}(\Delta E) K^{\text{ext}}(\Delta E) \sigma \tag{4.55}$$

where we take ΔE to be the half-width of the elastic peak, $K^{\text{int}}(\Delta E)$ and $K^{\text{ext}}(\Delta E)$ are the internal and external correction factors such that the fraction K of scattering events reside in the measured peak between initial energy E_i and $E_i - \Delta E$. That is to say, the fraction $1 - K(\Delta E)$ electrons lose an amount of energy more than ΔE.

The internal radiative corrections were first calculated by J. Schwinger [75] for potential scattering. Here it was found that, for highly relativistic electrons, the fraction of events losing energy

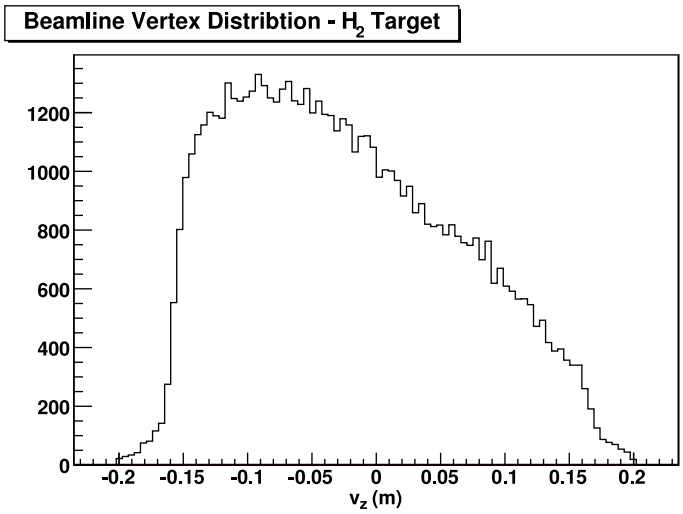

Figure 4.49: Vertex distribution for H_2 target. Varying spectrometer acceptance along the beamline produces a non-uniform distribution.

greater than ΔE is [76]

$$\delta^{\text{int}} \approx -\frac{2\alpha}{\pi}\left[\left(\log\frac{E_i}{\Delta E}-\frac{13}{12}\right)\left(\log\frac{Q^2}{m^2}-1\right)+\frac{17}{36}\right]. \tag{4.56}$$

One problem associated with this calculation is in the limit as $\Delta E \to 0$, δ diverges logarithmically. This problem is associated with neglecting processes where more than one low frequency photon is emitted and is corrected by replacing $1-\delta$ with $e^{-\delta}$ as was explicitly proven by Yennie and Suura [77]. However, in cases where δ is small, such corrections are unnecessary.

External radiation can be modeled using the formalism presented by J. Friedrich [78]. The probability of an electron with initial energy, E_i, and final energy, E_f, radiating a single photon of energy $\Delta E = E_i - E_f$, after distance t in a material with radiation length X_0, can be described by the formula

$$f^{\text{rad}} = \frac{t}{X_0}\frac{1}{\Delta E}\left[1-\eta\frac{E_f}{E_i}+\left(\frac{E_f}{E_i}\right)^2\right] \tag{4.57}$$

where

$$\eta = \frac{2}{3}-\frac{1}{9}\left(\log 183\ \mathrm{Z}^{-1/3}\right)^{-1} \tag{4.58}$$

and Z is the atomic number of the nuclei in the material.

This leads to a fractional loss in the cross section of

$$\delta^{\text{ext}} = \frac{t}{X_0}\left[-\left(\frac{3}{2}-\eta\right)+(2-\eta)\log\left(\frac{E_i}{\Delta E}\right)+(2-\eta)\left(\frac{\Delta E}{E_i}\right)-\frac{1}{2}\left(\frac{\Delta E}{E_i}\right)^2\right]. \tag{4.59}$$

However, this also leads to unphysical results as $\Delta E \to 0$ as the model does not account for multiple low photon emission. For simplicity, the same replacement of $1-\delta \to e^{-\delta}$ made by Schwinger is done once again. We note that in our case, δ will be small because of our intrinsic resolution and these substitutions will make little difference on the final result. To relate Eq. 4.56 and Eq. 4.59 to Eq. 4.55,

$$K = e^{-\delta}. \tag{4.60}$$

To compare to our data, an examination of a portion of the radiative tail relative to the elastic peak is of interest. To determine the size of the radiative tail, successive corrections to the cross section and radiative tail are calculated for

1. External radiation from entering the target.
2. Internal radiation from elastic scattering.
3. External radiation from leaving the target.

Furthermore, we expect some contribution from non-Gaussian tails seen in the superelastic region ($\delta p > 0$) of the δp spectrum. We assume these to be symmetric about $\delta p = 0$ and subtract them from the radiative tail. This produces three regions in the δp spectrum we are interested in, shown in Fig. 4.50.

We expect the number we find in the elastic peak, N_0, and radiative tail, R, region to be

$$N_0 = K^{\text{ext,in}}K^{\text{ext,out}}K^{\text{int}}N \tag{4.61}$$

$$R = \left[\delta_{\text{R}}^{\text{ext,in}}K_{\text{tail}}^{\text{int}}K_{\text{tail}}^{\text{ext,out}}+\delta_{\text{R}}^{\text{int}}K^{\text{ext,in}}K_{\text{tail}}^{\text{ext,out}}+\delta_{\text{R}}^{\text{ext,out}}K^{\text{ext,in}}K^{\text{int}}\right]N \tag{4.62}$$

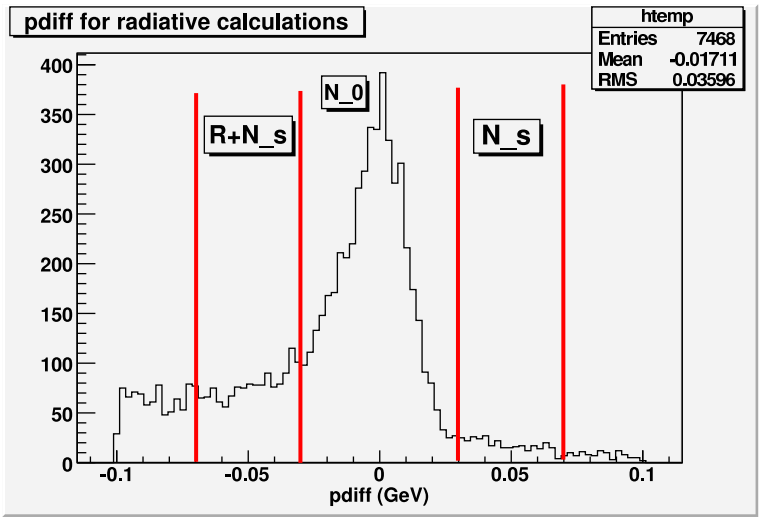

Figure 4.50: Three regions in H_2 elastic scattering to consider radiative corrections, the radiative tail region, elastic region, and superelastic region.

where N is the number of elastically scattered particles and the fraction falling into our tail region δ_{R} due to radiative effect x,

$$\delta_{\mathrm{R}}^{x} = K^{x}(\Delta E + 2\Delta E_{\mathrm{tail}}) - K^{x}(\Delta E) \tag{4.63}$$

and the radiative correction for the tail region due to the radiative effect x is K_{tail}^{x},

$$K_{\mathrm{tail}}^{x} = K^{x}(\Delta E_{\mathrm{tail}})). \tag{4.64}$$

For our analysis, we choose the bounds of the radiative tail region to be between -70 MeV and -30 MeV. This gives us $\Delta E = 0.03$ GeV, and $\Delta E_{\mathrm{tail}} = \frac{70\ \mathrm{MeV} - 30\ \mathrm{MeV}}{2} = 0.02$ GeV. Performing this analysis on H_2 data for kinematic 4, we use the parameters given in Table 4.29 to describe our kinematics and target. We then calculate

Parameter	Value
E_i	2.08 GeV
E_f	1.14 GeV
Q^2	1.75 GeV^2
m	511 keV
X_0	12.3 cm
Z_{eff}	10
t_{in}	0.01 cm
t_{out}	0.16 cm
η	0.64

Table 4.29: Parameters used to determine radiative corrections describing our kinematics and target.

$$\begin{aligned}
\delta_{\text{R}}^{\text{ext,in}} &= 1.16 \times 10^{-3} \\
\delta_{\text{R}}^{\text{int}} &= 5.79 \times 10^{-2} \\
\delta_{\text{R}}^{\text{ext,out}} &= 4.18 \times 10^{-3} \\
1 - K^{\text{ext,in}} &= 6.08 \times 10^{-3} \\
1 - K^{\text{int}} &= 2.18 \times 10^{-1} \\
1 - K_{\text{tail}}^{\text{int}} &= 2.45 \times 10^{-1} \\
1 - K^{\text{ext,out}} &= 5.38 \times 10^{-2} \\
1 - K_{\text{tail}}^{\text{ext,out}} &= 6.06 \times 10^{-2}.
\end{aligned}$$

Due to the thinness of our target wall, the radiative corrections are dominated by internal radiation. Using the formula given in Eq. 4.62, this yields a value of $N_0/N = 0.735$ and $R/N = 0.058$. The expected ratio of the number in the radiative tail region to the elastic region is then 0.079.

Selecting on elastics, we find $N_0 = 5349$ events in the elastic peak, $R + N_s = 775$ in the radiative tail region, and $N_s = 372$ in the superelastic region. This gives a ratio of $R/N_0 = 0.075$, within 5% of the predicted value of 0.079.

4.4.9 Comparison to Absolute Cross Section

While the measurement of the absolute cross section for of H_2 is not necessary for the analysis of E02-013, it is of interest when evaluating the performance of the spectrometer in the reconstruction of elastic and quasielastic events.

The number of scattered electrons in solid angle $\Delta\Omega$ for a total beam charge Q is

$$N_{\text{elas}} \approx Q \frac{n_{\text{H}} l \frac{d\sigma}{d\Omega} \Delta\Omega}{e} \tag{4.65}$$

where $\frac{d\sigma}{d\Omega}$ is given by Eq. 3.1 using the central angle of BigBite, θ_{BB}; n_{H} is the number of protons per volume; l is the length of the target; and $\Delta\Omega$ is the solid angle subtended by the spectrometer. For G_E and G_M, the dipole approximation is used (as given in Eqs. 4.51 and 4.52).

The differential cross sections at the central angle of BigBite and the expected yields for kinematic 3 and 4 are given in Table 4.30. To determine the density of protons in the target, the ideal gas law was used

$$\frac{N}{V} = \frac{p}{k_B T}. \tag{4.66}$$

Param.	Kin. 3	Kin. 4
$E_{\rm beam}$ (GeV)	3.29	2.08
$\theta_{\rm BigBite}$ (rad)	-0.90	-0.90
$\Delta\Omega$ (msr)	76	76
E' (GeV)	1.41	1.13
Q^2 (GeV^2	3.52	1.78
G_E^p	0.0282	0.0813
G_M^p	0.0786	0.2269
$\frac{d\sigma(\theta_{\rm BigBite})}{d\Omega}$ (fm^{2}msr^{-1})	1.615×10^{-12}	4.974×10^{-11}
l (m)	0.4	0.4
p_{H_2} (psig)	135	135
T_{H_2} (K)	305	305
N_p/V (m^{-3})	4.91×10^{26}	4.91×10^{26}
$N_{\rm elas}/Q$ (mC^{-1})	150.8	4644.7

Table 4.30: Predicted elastic yields per charge for H_2 targets in kinematics 3 and 4.

To compare to the data, the number found in the elastic peak must be corrected for effects such as dead times, tracking inefficiencies and radiative corrections. Furthermore, due to prescaling of the T2 triggers the number of elastics must be counted properly.

There are two event types we are interested in: T3 triggers, signifying a BigBite - neutron arm coincidence, and T2 triggers where no T3 trigger was present, which are the prescaled BigBite singles. The number of corrected elastics seen in the data is then

$$N_{\rm elas,true} = \frac{N_{\rm T3} + k_{\rm T2,ps} N_{\rm T2,noT3} + N_{\rm tails}}{\epsilon_{\rm DAQ}\epsilon_{\rm elec}\epsilon_{\rm track}\epsilon_{\rm track,skip} K_{\rm rad}} \tag{4.67}$$

where $N_{\rm elas,true}$ is the corrected number of elastics, $N_{\rm T3}$ are the number of elastics for T3 events, $k_{\rm T2,ps}$ is the prescale factor for T2 triggers, and $N_{\rm T2,noT3}$ is the number of elastics with a T2 trigger but no corresponding T3. $N_{\rm tails}$ is the number of elastic events lost into the long non-Gaussian tails from resolution effects, estimated by assuming a distribution symmetric in δp measured by counting the number in the superelastic region (as done for when comparing radiative correction calculations). $\epsilon_{\rm DAQ}$ is the DAQ live time, $\epsilon_{\rm elec}$ is the electronic live time, $\epsilon_{\rm track,skip}$ is the effective tracking live time due to skipping tracks due to excessive combinatorics, $\epsilon_{\rm track}$ is the efficiency of tracking due to plane inefficiencies given by Eq. 4.21, and $K_{\rm rad}$ is the radiative corrections as determined by Eqs. 4.59 and 4.56. For H_2 runs which were generally at a much lower current than production runs (usually by a factor of 10), the drift chamber plane efficiency was generally consistent with 100%, so we will assume no tracks were lost based on minimum number of plane constraints for this portion of the analysis (i.e. an elastic event will always produce hits on at least the minimum number of planes required for tracking).

The comparison between $N_{\rm elas,true}$ and the predicted calculation is in Table 4.31. The corrected numbers appear to be about 10% lower than predicted by the cross section, which suggests the reconstruction of tracks is being performed by the tracking code better than 90%. These numbers are very acceptable given the crudeness in the calculation of the cross section and acceptance of the calculation and the fact the experiment is not designed to measure an absolute cross section.

Furthermore, this analysis also yields an upper limit for the neutron-arm trigger efficiency. This efficiency we define as the ratio of the number of elastic events when the neutron-arm gives a trigger to the number of elastic events measured by BigBite regardless of neutron-arm trigger. This efficiency,

	Kin. 3	Kin. 4
Runs	3368,3369	4427
Q (mC)	7.80	2.71
N_{peak}, T3	149	11327
N_{peak}, T2	73	321
$k_{\text{T2,ps}}$	1	20
N_{tails}	20	2800
ϵ_{DAQ}	0.98	0.93
ϵ_{elec}	0.98	0.92
$\epsilon_{\text{track,skip}}$	0.97	0.93
$\bar{\epsilon}_{\text{plane}}$	0.98	0.99
ϵ_{track}	1.0	1.0
K_{rad}	0.73	0.74
$N_{\text{elas,true}}$	356	34895
$N_{\text{elas,pred}}$	408	36229
$N_{\text{elas,true}}/N_{\text{elas,pred}}$	0.87	0.96

Table 4.31: Comparison of elastic yields from data to predicted yields.

barring any accidental coincidence events is

$$\epsilon_{\text{NA,upper}} = \frac{N_{\text{T3}}}{N_{\text{T3}} + k_{\text{T2,ps}} N_{\text{T2,noT3}}}. \tag{4.68}$$

In light of accidental coincidences, this gives an upper bound, as the number of T3 events will be artificially inflated. For kinematic 3, $\epsilon_{\text{NA,upper}} = 0.67$ and for kinematic 4, $\epsilon_{\text{NA,upper}} = 0.63$.

4.5 Coincidences

A final step must be done to calibrate the timing of the neutron arm relative to BigBite and to correctly calculate the time of flight up to a constant. As shown in Eq. 3.36, the time of flight calculation also requires knowledge of the time of flight of the electron from the target to the BigBite scintillators (up to a constant). To determine this number, we use a 499 MHz signal generated by the accelerator to determine a known time when the electron is at some fixed position relative to the target (modulo a pulse bin).

Following the formalism set in Section 3.3.6, the RF signal measured in an F1 TDC with the L1A signal as a readout, can be described as

$$t_{\text{RF}}^{\text{TDC}} = v_z/c + t_{\text{evt}} - b - t_{\text{L1A}} - a \tag{4.69}$$

where b is a constant. Using Eqs. 3.33, 3.34, 3.31, and 3.37, the time of flight for the electron, t_e can be determined

$$t_e = t_{\text{BB,hit}}^{\text{TDC,corr}} - t_{\text{RF}}^{\text{TDC}} - t_{\text{L1A}}^{\text{TDC}} + v_z/c - a - b. \tag{4.70}$$

This quantity is dependent on the path length, which in the effective bend plane model, is expected to be between 2.0 and 2.2 m. However, $t_{\text{RF}}^{\text{TDC}}$ is only a number modulo 2 ns, so some arbitrary (event independent) constant is still present.

To obtain $t_{\text{RF}}^{\text{TDC}}$ from the data, a reference time (which represents the readout signal) and the TDC resolution must be applied, such that:

$$t_{\text{RF}}^{\text{TDC}} = (c_{\text{RF}}^{\text{read}} - c^{\text{stop}}) \cdot \alpha_{\text{res}} \tag{4.71}$$

where $c_{\mathrm{RF}}^{\mathrm{read}}$ and c^{stop} are the raw channels read from the TDC. To calculate the time width per channel of the F1 TDC, α_{res}, successive pulses in the RF time signal, which have a fixed time difference can be used. Every 79th RF pulse is recorded and pulses are generated at a frequency of $f = 499$ MHz, so

$$\alpha_{\mathrm{res}} = \frac{79}{499\ \mathrm{MHz} \cdot \Delta T}. \tag{4.72}$$

Where ΔT is the number of channels between pulses. The resolution is determined to be about 118.3 ps/channel.

Calculations of t_e modulo 2 ns can also be made by examining dependencies of t_e calculated through the RF timing and track variables such as v_z, x_{det}, and p. After determining such dependencies, t_e modulo 2 ns can be represented as

$$t_{e,\mathrm{data}} = (-1.8(\mathrm{ns/m})x_{\mathrm{bend}} + (2.3\ \mathrm{ns/m})v_z - (0.8\ \mathrm{ns/GeV}) \cdot (p - 1.0\ \mathrm{GeV}). \tag{4.73}$$

Furthermore, it should be noted that the resolution of the F1 TDC measuring the RF time is about a factor of 2 better than that of the TDC measuring the scintillator time, though can only give this time modulo 2 ns. It is possible to then correct the scintillator time, $t_{\mathrm{BB,hit}}^{\mathrm{TDC,corr}}$ using the RF timing correction. The amount to add to $t_{\mathrm{BB,hit}}^{\mathrm{TDC,corr}}$ to correct it, $\Delta t_{\mathrm{BB,hit}}^{\mathrm{TDC,corr}}$, is

$$\Delta t_{\mathrm{BB,hit}}^{\mathrm{TDC,corr}} = \mathrm{fmod}(t_{e,\mathrm{data}} - t_{\mathrm{BB,hit}}^{\mathrm{TDC,corr}} + t_{\mathrm{RF}}^{\mathrm{TDC}} + t_{\mathrm{L1A}}^{\mathrm{TDC}} - v_z/c + a + b, 2\ \mathrm{ns}). \tag{4.74}$$

This is known as the RF correction. This correction can be up to several hundred ps, shown in Fig. 4.51, which can give a substantial improvement in resolution at the higher Q^2 kinematics, as given by Eq. 3.21.

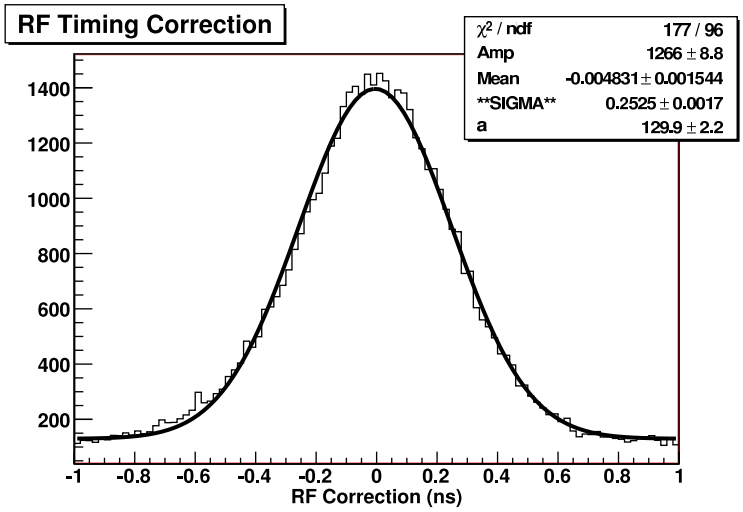

Figure 4.51: RF correction for BigBite scintillator timing.

Chapter 5

Analysis

Ultimately, the goal of E02-013 is to extract the value of G_E^n for the four kinematic points by examining the cross section asymmetry of ^{3}He nuclei for different beam helicities. Once calibrations of our detectors are performed, analysis of quasielastic events can be done.

For this work, two kinematic data sets are analyzed, the highest $Q^2 = 3.5$ GeV^2 point and the $Q^2 = 1.7$ GeV^2 point. To perform this analysis, careful cuts on the ^{3}He target data must be done to select quasielastic events cleanly, modeling of the background must be done, analysis of charge misidentification must be done, and other factors that could ultimately change the asymmetry must be taken into account. Furthermore, some scheme must be developed to take the finite acceptance of the spectrometer into account.

In this chapter, a description of the analysis procedure will be provided as well as some basic results motivating our choices for the analysis. A full presentation and discussion of the results can be found in Chapter 6. In particular, the portions of the analysis which require special attention will be the corrections for final state interactions and the proton contribution to the quasielastic sample identified as neutrons, as they will be some of the largest contribution to the final systematic error. Contributions from accidental background and scattering from N_2 in the target will be shown to play a smaller role.

5.1 Analysis Flow

Analysis for E02-013 is done over several stages to help optimize the amount of time required to perform an analysis. During the course of the experiment, several terabytes of data were accumulated and stored in a raw CODA format. To process all of the data in this form would require on the order of several weeks of processing time given the computing farm resources at Jefferson Lab. This amount of time is prohibitive when several iterations of the processing become necessary as calibrations and the analysis of the data become more refined.

Each stage of the analysis is designed to successively take shorter periods of time to perform an analysis over an entire kinematic set. To optimize analysis time and reduce the number of iterations over the data, calibrations that are not expected to significantly change over the course of a full analysis are placed earlier in the analysis stages.

The conversion of raw data into ROOT trees and basic interpretations of that data are provided by the Hall A ROOT/analyzer facility, which provides a strong framework for detector abstraction as well as useful methods for data interpretation. E02-013 specific contributions to this framework were included in the AGen library, which contains the code necessary to perform analysis specific to our detectors, such as the BigBite tracking and optics and neutron arm cluster reconstruction. Further stages in the analysis, which include more data refinement and the calculation of G_E^n, were

also built using the ROOT package, though are generally in the form of smaller scripts and individual classes.

5.1.1 E02-013 Analysis Flow

Analysis for E02-013 is broken into three stages, first pass, second pass, and final calculations, as depicted in Fig. 5.1. The first pass includes all work done by the Hall A ROOT/analyzer, which performs all the raw event decoding, tracking, cluster finding, and optics. This process is fairly complicated and is discussed by itself in Section 5.1.2.

The second pass involves the calculation of nucleon momentum, coincidence kinematic variables such as $\vec{q}$, and charge identification by the veto layers. While charge identification and neutron momentum could both be done in the first pass, these two calibrations were determined to be "soft" and were left to pass two to allow flexibility in the event that different methods of calibration were chosen. The output of this stage is in the form of ROOT trees similar to the original output. The second pass also has the AGEn library available, so calculations such as the BigBite optics can be re-performed on the data, which may be desirable as more refined optics calculations are made available.

Time of flight can be determined, up to a constant, after the first pass of the data, but there may be cases were this calculation may not be stable across large sets of runs and a set of different offsets may be necessary. These can be determined separately and given as input for the second pass. Time of flight and charge identification are both extremely important calculations with respect to selecting neutral quasielastics, so by allowing these to be flexible, great amounts of time can be saved when examining the effects of varying these methods.

Run characteristics are also calculated during the second pass as gross properties of individual runs. These include calculation of the dead times and effective dead times, veto rates, and accumulated charge.

The final calculation stage involves taking the ROOT trees from the second pass and the run characteristics and then calculating the raw asymmetries, physical asymmetries, and performing the calculation for G_E^n.

5.1.2 Hall A Analyzer/AGen Library Flow

The Hall A analyzer was used as a strong framework for the base E02-013 raw data decoding and basic detector analysis. Several changes were made to enhance or modify this framework specifically for E02-013. This included the development of tracking and optics code, but also changing the hard-coded order in which detectors were analyzed. This was necessary mainly to accommodate the BigBite tracking code so that it could take advantage of other detectors.

The Hall A analyzer is based heavily around object oriented code, which lends itself naturally to data analysis by providing abstraction of physical objects such as a spectrometer composed of several detector systems. Each detector and collection of detectors has three general stages in the analysis:

1. Decoding, where raw data for an event is interpreted as physical values. An example of decoding is taking raw TDC values for drift chamber wires and converting them into drift times or associating an ADC signal with an integrated amplitude.

2. Coarse processing, where the decoded data is processed and refined, usually in a way that is faster and more crude than what is desirable for a final analysis, but may be useful in the later stages of analysis.

3. Fine processing, calculation of final values for a detector in a given event. Here, for example, electron tracks to be used in the rest of the analysis are finalized and neutron arm clusters are combined.

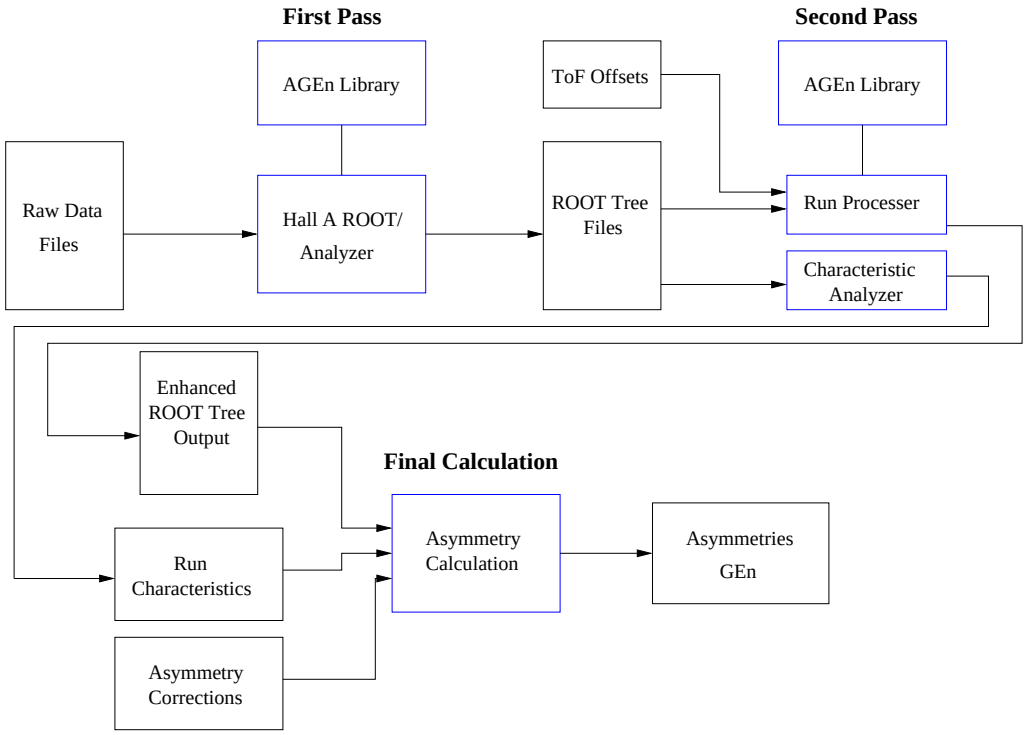

Figure 5.1: Depiction of the stages of E02-013 analysis.

Additionally, arbitrary code can be executed at the end when all detector packages are finished processing to perform additional calculations. These packages, known as physics modules, are useful for determining kinematic parameters such as invariant mass W and three-momentum transfer, $\vec{q}$. Additionally, scaler output is performed in parallel with this analysis and separate ROOT trees are generated with their output.

The standard analyzer performs all analysis in such a way that all detectors and objects would be done in each stage together. For E02-013, this behavior was not desirable, so an abstraction of the ordering was integrated into the AGEn library such that any of the stages listed above for any detector or collection of detectors could be performed in an arbitrary order. Here, five stages of detector processing were defined:

1. Beam Helicity Analysis, where the helicity information is decoded and interpreted. The first 1,000 events in a given run are used to determine the placement in the pseudo-random helicity generation scheme. Here all three detector analysis stages are performed successively.

2. Decoding, where all remaining detector systems pass through the decoding stage.

3. Coarse processing, where all detector systems pass through the coarse processing stage, with exception of the BigBite calorimeter. The calorimeter also goes through the fine processing stage to produce the positions of energy-deposition clusters. The BigBite coarse tracking is performed after the calorimeter to utilize these positions, but is only done using wire positions ignoring drift times.

4. Fine processing, all remaining detector systems pass through the fine processing stage. BigBite tracking is re-performed using drift times.

First Pass
Discard first 1000 events from a run
Discard non-coincidence trigger events
Preshower signal must be above specific threshold (400 channels)

Second Pass
Discard events with no helicity data
Preshower signal must be above specific threshold (500 channels)
Track must be reconstructed in BigBite
Track beamline vertex, v_z, $-0.2 < v_z < 0.2$ m
Track momentum, p, $0 < p < 2.0$ GeV
Invariant mass W, $0.6 < W < 1.8$ GeV

Table 5.1: Base cuts placed on the data for each stage of analysis.

5. Physics analysis, where basic kinematic parameters are calculated using only the BigBite spectrometer and beam information, such as direction and energy.

5.1.3 Event Reduction Cuts

For each stage in processing, very crude and basic cuts are done on the data to cull events from our sample which are clearly not quasielastic. These cuts are left very loose and are chosen so they have little effect on the final analysis. They are in place strictly to reduce the amount of data storage required for output. A table of these cuts can be found in Table 5.1.

For the first pass of the analysis, the first 1000 events are discarded after decoding helicity information as no helicity will be determined for these events. As the typical run size is on the order of hundreds of thousands or millions of events, this is only a small subset. Events in which only one of BigBite or the neutron arm fired are discarded, as no coincidence information can be reconstructed from these events (though for calibration analysis they can be useful, so these are typically kept for H_2 runs). BigBite events where the preshower had an amplitude sum of less than 400 channels are discarded, selecting on electron signatures (discussed in Section 4.4.1). Events where BigBite completed tracking and no track was found are discarded. Events where the tracking was preemptively skipped or terminated early are saved for accounting purposes.

In the second pass of analysis the helicity is required to be well defined. Undefined helicity events correspond to events when the helicity is in a brief transition period where the voltage supplied to the Pockels cell changes. Preshower signal must be above a specific level, determined in Section 4.4.1, strongly selecting on electrons, and a track must be found and must be within the regions where the vertex and momentum are well reconstructed (see Section 4.4.5). Reconstructed momenta must be between 0 and 2 GeV, which is larger than the kinematic region for quasielastic scattering for all of our beam energies. The reconstructed track vertex along the beam line must be within the range of the target, eliminating extraneous events that may have originated elsewhere in the beamline. Coincidence is also required, eliminating other trigger types from the data, such as the MPS for the helicity. Furthermore, a loose cut on invariant mass W is also put in place to reduce the number of events written out. This is generally 0.6 GeV $< W <$ 1.8 GeV, which is much wider than the anticipated quasielastic peak in W on the order of $m_n \pm 200$ GeV due to Fermi motion in the nucleus.

It should be noted that during the second pass analysis, the run characteristics which depend on events in the data that are discarded at this stage are calculated before discarding the data. For example, to determine the helicity-dependent effective efficiency of the drift chamber tracking, the events where tracking was skipped must be counted. These are made available for this purpose at this stage, but the events are not considered for the quasielastic sample at later stages.

Type	Accum. Charge (mC) Kin. 3	Kin. 4
^{3}He	12022	2027
H_2	165	22
N_2	32	4
BeO/C Foils	4	2

Table 5.2: Total usable accumulated charge of the four target types for kinematics 3 and 4 used for this analysis.

5.2 Kinematics and Data Sets

Four types of runs were taken during E02-013 that are relevant to the analysis. The ^{3}He runs from which we measure our quasielastic asymmetry, and the H_2, N_2, and carbon foils targets that we use for calibrations. During the experiment, occasional problems would occur in the data acquisition system resulting in lost information. Furthermore, problems in the detectors would also cause problems in data taking, such as the BigBite drift chamber's current would become too large due to extremely high background rates. This would trip the high voltage supply leaving the chambers unpowered. This caused a number of runs to contain poor data or very little data.

Runs determined to have less than 100 μC of integrated beam are identified and are removed from the data set. Runs where the BigBite drift chambers were inactive for any period of time (determined by examining numbers of hits in all chambers) are kept, but the amount of beam charge accumulated during these periods is subtracted to determine an accurate total usable charge accumulation.

The total amount of charge for each of the four target types for the two kinematic periods 3 and 4 are presented in Table 5.2.

5.3 Charge Identification

The process for charge identification was described in Section 3.4.3. However, there is a choice on where to place limits on the difference between the cluster position and veto hit position and the time difference to associate a veto hit with a neutron arm cluster. To make these choices data is examined to produce not only these limits but also to determine the effective speed of light in the scintillator in Eq. 3.46, c_s. The limits are generally chosen with the intention to reduce the number of misidentified protons in the neutral sample and are thus left intentionally wide.

The spacial association of veto hits to neutron arm clusters is modeled by Eq. 3.45

$$|x_{\text{clus}} - x_{\text{veto}} - x_0| < \Delta x$$

where x_{clus} is the reconstructed x position of the cluster and x_{veto} is the x position of the veto bar that fired. x_0 is an offset that must be determined from the data. By examining this spectrum, a reasonable value of the limit Δx can be deduced and must be repeated for both veto layers. While any data set may be used for this calibration, H_2 data is used as they generally have a lower amount of accidental background due to running at lower beam currents. W cuts of $|W - 0.94 \text{ GeV}| < 0.1$ GeV and a preshower cut of $A_{\text{ps}} > 500$ channels were used to select on elastic events for which have protons, which should leave a strong signal in the veto scintillator. These spacial difference distributions and the limits for hit association for both veto planes are shown in Fig. 5.2.

Time differences between the neutron arm clusters and veto hits are more complicated due to the fact that light propagation times for veto hits must be taken into account. These effects, which are eliminated for the neutron arm clusters, must be corrected for the vetos since veto hits do not

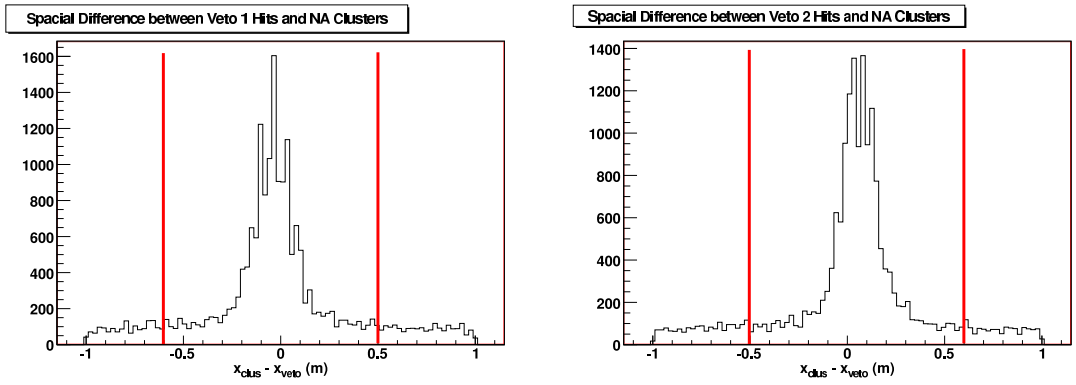

(a) (b)

Figure 5.2: Spacial difference distributions of the vertical positions between hits in the veto layers and neutron arm clusters in a) veto layer 1 and b) veto layer 2. The limits to associate these hits with neutron arm clusters are shown by red lines.

have the benefit of relying on PMTs at each end of the scintillator to reconstruct the position along a scintillator bar. However, by utilizing this reconstructed y position of the cluster and by finding the propagation time of the light in the veto scintillator, the veto time can be corrected and better matched to the cluster time. This effect is clearly shown in Fig. 5.3, where the dependency of the the time difference on the y_{clus} is dramatic.

Taking this effect into account, the corrected time difference can then be modeled by Eq. 3.46

$$\Delta t = t_{\text{veto}} - t_{\text{clus}} + \frac{|y_{\text{clus}} - y_0|}{c_s} + t_0$$

where t_{veto} is the time read by the veto TDC, t_{clus} is the corrected reconstructed time of the cluster defined in Section 3.3.6, and y_{clus} is the reconstructed y position of the cluster. Once again, by examining the data (using the same events for the spatial difference calibration) the offsets y_0 and t_0, as well as the effective speed of light in the scintillator, c_s, can be determined. A plot of the corrected time spectrum and the limits for veto hit association is shown in Fig. 5.4. A list of all values used to associate veto hits to neutron arm clusters can be found in Table 5.3.

Finally, individual electronic dead times of each detector channel must be taken into account for proper charge identification. Due to the fact that a signal from a charged particle can be masked by an earlier signal producing a false neutral identification, individual dead times must be taken into account. To determine these dead times, the time difference between successive hits on each PMT is examined. What is observed is a minimum time gap between the two hits, corresponding to the dead time as shown in Fig. 5.5.

While these numbers can be calculated for each PMT channel, for ease of analysis the dead time is treated to be the maximum of all dead times in the software. This has the side effect of reducing statistics while making the calculation of proton contamination in the quasielastic neutral sample more straightforward (see Section 5.7). While the median dead time for all channels was found to

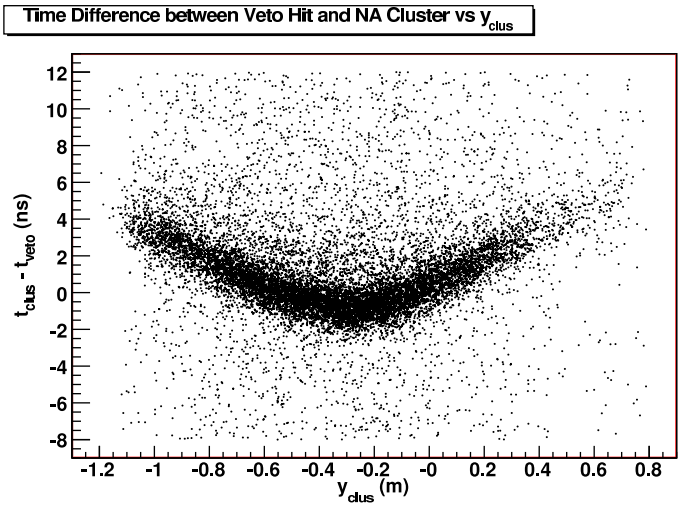

Figure 5.3: Time differences between veto hits and neutron arm clusters vs. the y position of the neutron arm cluster. This dependency is due to the time of the propagation of light in the veto scintillator.

Value	Veto 1	Veto 2
x_0	-0.05 m	0.05 m
Δx	0.55 m	0.55 m
t_0	1.8 ns	1.8 ns
y_0	-0.35 m	-0.35 m
c_s	0.14 m/ns	0.14 m/ns
Δt	10 ns	10 ns

Table 5.3: Values used for veto layers 1 and 2 to associate hits with neutron arm clusters for charge identification.

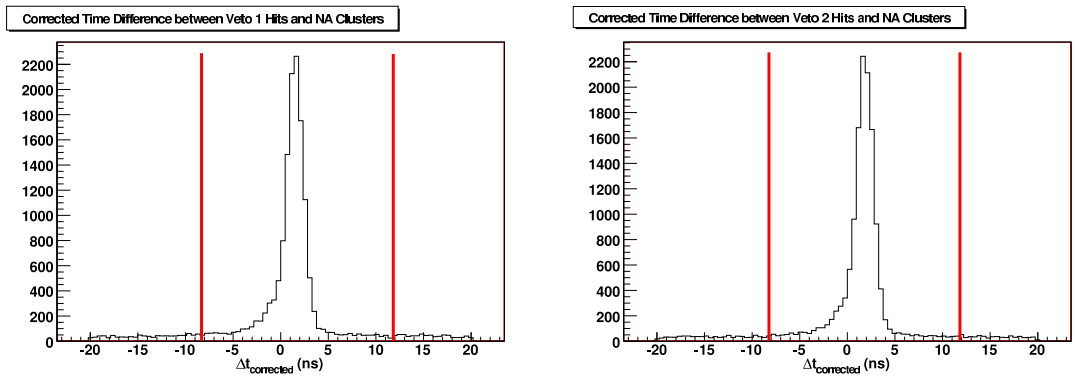

(a) (b)

Figure 5.4: Time differences between veto hits and neutron arm clusters after correction for the propagation of light in the veto scintillator for a) veto layer 1 and b) veto layer 2. Limits for the association of veto hits with neutron arm clusters are shown by red lines.

be about 40 ns, the maximum was roughly 100 ns. For this analysis then, a dead time of 100 ns is enforced for all PMT channels. The number of events lost to dead time increases by roughly a factor of two due to this technique. For kinematic 4, 3.2% of quasielastic events were lost to this dead time. For kinematic 3, 13.1% were lost.

5.4 Absolute Time of Flight Calibration

The calculation of the time of flight of the recoiling nucleon up to a constant was described in Section 3.3.6 and Section 4.5. However, for the nucleon momentum to be calculated, this constant must first be found. There are several ways to calibrate this timing. The first is to use a H_2 run and select upon elastic events where the momentum (and time of flight) of the nucleon is well known from measuring the scattered electron. The second method, which can be done for any given run, is to select upon events in the neutron arm which correspond to $\beta = 1$ from photons.

For elastic events from our H_2 target, the three-momentum transfer $\vec{q}$ corresponds to the nucleon momentum that we are interested in calibrating. The relation between the momentum, $\vec{q}$, and time of flight, $t_{\rm tof}$, is

$$t_{\rm tof} = \frac{d}{c}\sqrt{1 + \left(\frac{m_p}{|\vec{q}|}\right)^2} \tag{5.1}$$

where c is the speed of light, d is the path length from the target vertex to the cluster position, and m_p is the mass of the proton. Using this equation as the true time of flight, any overall offset can then be determined by taking the difference of the time of flight calculated above and the time of flight given in Eq. 3.36.

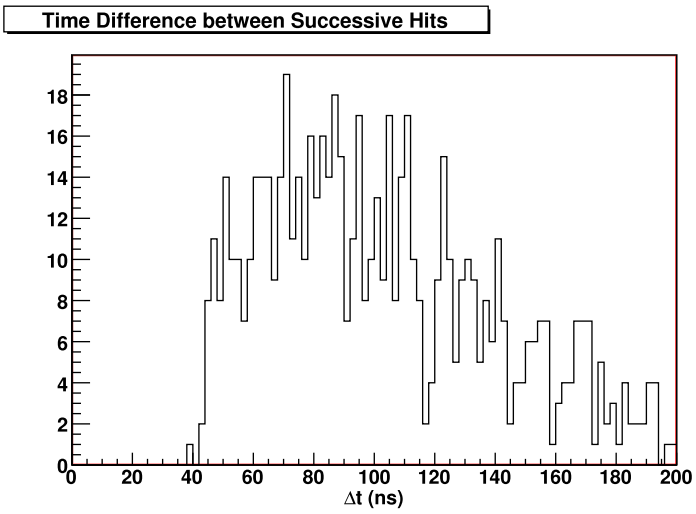

Figure 5.5: The time difference between two successive hits on the same veto scintillator bar. The time gap corresponds to the dead time of the electronics for this channel.

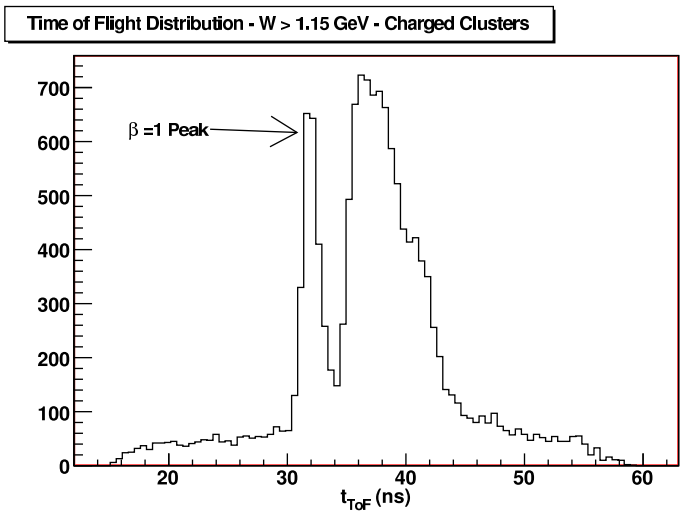

Figure 5.6: The photon peak is found immediately before the quasielastic peak and can be resolved from it by selecting on invariant mass, W, $W > 1.15$ GeV and on neutron arm clusters associated with a veto hit.

An alternate method to determine the time of flight is to select on the photon peak in the time of flight distribution, Fig. 5.6. In this case, the time of flight for a $\beta = 1$ particle is:

$$t_{\rm tof} = \frac{d}{c} \tag{5.2}$$

where d is the distance between the target vertex and the cluster position. This peak is present in all runs and therefore can be immediately determined. It generally requires looking into higher W regions and selecting on charged clusters.

For this analysis, the H_2 method is employed, but shifts in the position of the quasielastic peak over a larger set of runs are taken into account (usually on the order of less than 100 ps). Fitting a Gaussian to the difference of the time of flight spectrum and the time of flight predicted by Eq. 5.1, we arrive at a resolution of about $\sigma_{t,\rm NA} = 500$ ps for both kinematic 3 and kinematic 4. Given Eq. 3.21, this predicts a momentum resolution, $\sigma_{p,\rm NA}$, of 280 MeV for kinematic 3 and 49 MeV for kinematic 4.

5.5 Event Selection

Event selection, beyond the basic cuts described in Section 5.1.3, must be done carefully to maximize the number of quasielastic events while reducing the number of other events that would be present

in the sample. To determine these cuts, the variables missing parallel and perpendicular momentum are useful to define. They are

$$p_{\text{miss},\parallel} = \hat{q} \cdot (\vec{q} - \vec{p}_{\text{NA}}) \tag{5.3}$$

$$p_{\text{miss},\perp} = |\vec{q} - \vec{p}_{\text{NA}} - \hat{q} p_{\text{miss},\parallel}| \tag{5.4}$$

where $\vec{p}_{\text{NA}}$ is the momentum measured by the neutron arm, $\vec{q}$ is the three momentum transfer of the electron measured by BigBite, and $\hat{q}$ is the unit vector of the three momentum transfer. In many respects, the physical interpretation of these two variables is straightforward. $p_{\text{miss},\parallel}$ correlates closely to how well the momentum measured agrees with that predicted by $\vec{q}$, and $p_{\text{miss},\perp}$ represents how far radially the cluster position is from the position predicted by $\vec{q}$.

W, the invariant mass, is used to select quasielastic events. It is defined as

$$W^2 = (p_{i,\text{nucl}} + q)^2 \tag{5.5}$$

where $p_{i,\text{nucl}}$ is the four-momentum of the initial nucleon target and q is the four-momentum transfer. This variable comes with a strong caveat, however. We do not truly know the initial momentum of the nucleon since it is bound in a nucleus. To calculate this variable, $p_{i,\text{nucl}}$ is taken to be $(m_p, \vec{p} = 0)$ where m_p is the mass of the proton and q is the four-momentum transfer. *For the remainder of this analysis, when we refer to invariant mass in regards to* ^{3}He *scattering, we will really be referring to the pseudo-invariant mass where the initial nucleon is assumed to be at rest.*

In the case of elastic scattering, such as the case for our H_2 target, the final momentum of the nucleon is simply $p_{i,\text{nucl}} + q$ and therefore W is the mass of the nucleon (barring any resolution effects).

Using this technique, quasielastic scattering from these nucleons will not produce an invariant mass at the nucleon mass, but will instead have some width. It should also be noted that the mass difference between protons and neutrons, $m_p - m_n \approx 1$ MeV, is small compared to the momentum resolution of the neutron arm and the resolution of BigBite and the two masses are taken to be approximately the same for this analysis.

5.5.1 Inelastic Contribution

To help suppress the inclusion of inelastic events caused by π^0 and $\pi^\pm$ electroproduction, a final cut on missing mass for the reaction $^3\text{He}(\vec{e}, e')X$ is included. Missing mass is defined as

$$m^2_{\text{miss}} = (P_i + q - p_f)^2 \tag{5.6}$$

where P_i is the initial 4 momentum of the ^{3}He nucleus, taken to be at rest in the lab frame, p_f is the measured final four-momentum of the nucleon, and q is the four momentum transfer. This mass represents the mass of the unmeasured final hadronic system. In the case of quasielastic scattering in the impulse approximation, this is simply the mass of the remaining two nucleon system. However, in the case of pion electroproduction, this will also include the contribution from an additional pion. This allows us to define a minimum missing mass necessary for pion production, which is the mass of two nucleons plus the mass of a pion, about 2 GeV. A plot of m_{miss} vs. W can be found in Fig. 5.7. Quasielastic events clearly show up near $W = m_n$ and $m_{\text{miss}} = 2m_n$.

This quantity is highly dependent on the calculation of nucleon momentum through time of flight, so there are some redundancies when placing this cut in addition to our other quantities. However, it provides a useful tool to explicitly suppress inelastic events in our sample.

Due to resolution effects, this distribution will be smeared, so placing a cut at 2 GeV will not fully suppress all pion production. To help determine the contributions of inelastic events to the neutral quasielastic sample, a simple Monte Carlo simulation was developed. The quasielastic cross section for scattering from neutrons is described using elastic scattering, Eq. 3.1, on an neutron using

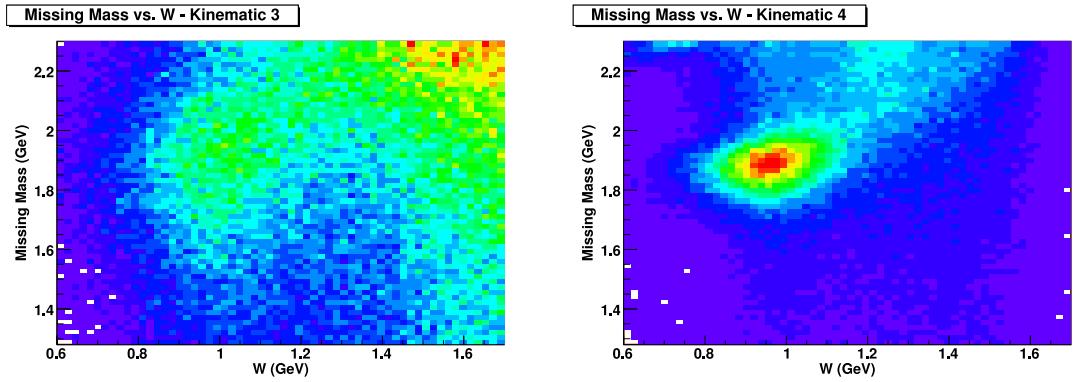

(a) (b)

Figure 5.7: Missing Mass vs. W for kinematics a) 3 and b) 4. Quasielastic events are clearly visible in W around the nucleon mass and m_{miss} around two nucleon masses. A cut is placed selecting on $m_{\text{miss}} < 2.0$ GeV.

a realistic initial momentum state, with the dipole parametrization introduced in Section 2.3.4. To parametrize the cross sections for pion electroproduction from electron scattering on nucleons, data provided by the MAID project from Mainz [79] was used for the production channels

$$\begin{aligned} ep &\rightarrow e'p\pi^0 \\ ep &\rightarrow e'n\pi^+ \\ en &\rightarrow e'n\pi^0 \\ en &\rightarrow e'p\pi^-. \end{aligned}$$

The MAID data consists of fits done to experimental results and is available through a web interface which gives cross sections in terms of various observables in the form of tables. The five-fold differential cross section for each channel was put into a smooth interpolation using fitting software developed by Gregg Franklin and then integrated into the Monte Carlo simulation.

Resolution effects were determined by introducing Gaussian smearing on the momenta of final measured electron and nucleon states. The width of the Gaussian smearing was determined by comparing the data to H_2 scattering data. The initial nucleon momentum distribution was determined by generating a three-dimensional Gaussian momentum distribution. The widths of the Gaussian distributions were determined by the results of a calculation by Rocca Schiavilla [80]. See Section 5.7.4.

It should be noted that this simulation is somewhat crude in that it includes only a simple acceptance test, which was done by testing the polar angle of the electron and nucleon with respect to the beam; if the track for a simulated event was within the nominal acceptance of BigBite and the neutron arm the event was accepted. This simulation does not include any out-of-plane acceptance checks. Furthermore, this simulation does not include additional physics phenomena such as radiative effects or charge exchange.

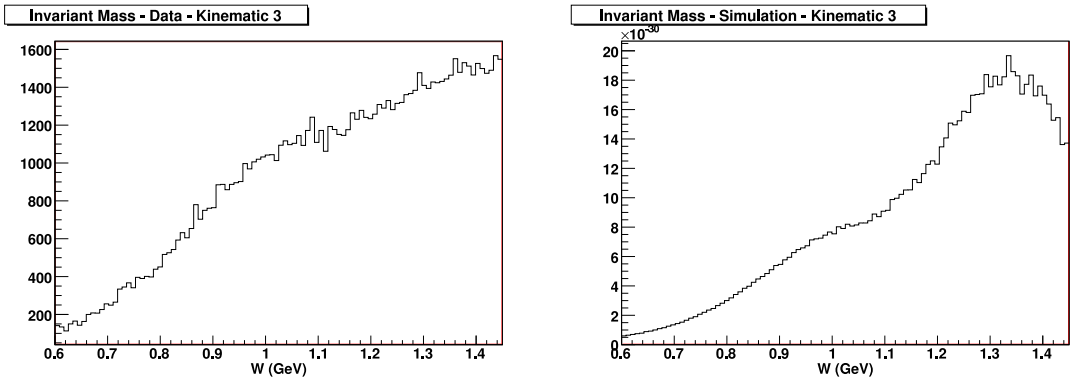

(a) (b)

Figure 5.8: Relative comparison of a) data to b) simulation with pion production for kinematic 3 with cuts of $p_{\mathrm{miss},\perp} < 0.5$ GeV and $|p_{\mathrm{miss},\parallel}| < 0.5$ GeV. Vertical axis units are arbitrary.

Despite these shortcomings, this simple model describes the data qualitatively well for kinematic 4. Comparisons of the simulation to kinematics 3 and 4 data can be found in Figs. 5.8 and 5.9. In the case of kinematic 3 the simulation seems to overpredict the number of pion production events at higher W. In this case it will overestimate the production and provide a result which should be an upper bound. Cuts wider than the quasielastic cuts in $p_{\mathrm{miss},\parallel}$ and $p_{\mathrm{miss},\perp}$ were placed on the data and with identical cuts on the simulation. For both kinematics, the relative amplitude of quasielastics to inelastic events are qualitatively in agreement. For kinematic 4, a minimum between the two peaks occurs at approximately identical W.

5.5.2 Chosen Cuts

We will now choose a set of cuts on the data to select our neutral quasielastic sample using a 2 GeV missing-mass cut (approximately the mass of two nucleons and a pion) to help suppress any pion production. By examining $p_{\mathrm{miss},\parallel}$ and $p_{\mathrm{miss},\perp}$ vs. W, the quasielastic region is clearly seen in Figs. 5.10 and 5.11. For each of the three cuts other than m_{miss}, placing cuts on the remaining two variables results in the distributions seen in Figs. 5.12, 5.13, and 5.14. The $p_{\mathrm{miss},\parallel}$ distribution for kinematic 3 is wider than that for kinematic 4, as expected, due to the degraded momentum resolution. A table of the cuts can be found in Table 5.4.

Placing these same cuts on the pion-production simulation, we see that the contributions from pion production are small in Fig. 5.15. Comparing to Fig. 5.16, we see they are qualitatively in agreement. The W cut upper limit for kinematic 3 is placed lower at 1.05 GeV to help the suppression of leaking from resolution effects. Integrating these histograms between the W values included by our cuts, the contribution is about 2% for kinematic 4 and 3% for kinematic 3. Inspecting the raw asymmetry values against invariant mass for both kinematics, Fig. 5.17, the values for the asymmetry in the regions of $W > 1.1$ GeV are roughly on the same order of magnitude and sign as those where quasielastics are expected to dominate. We infer that any asymmetry contributions

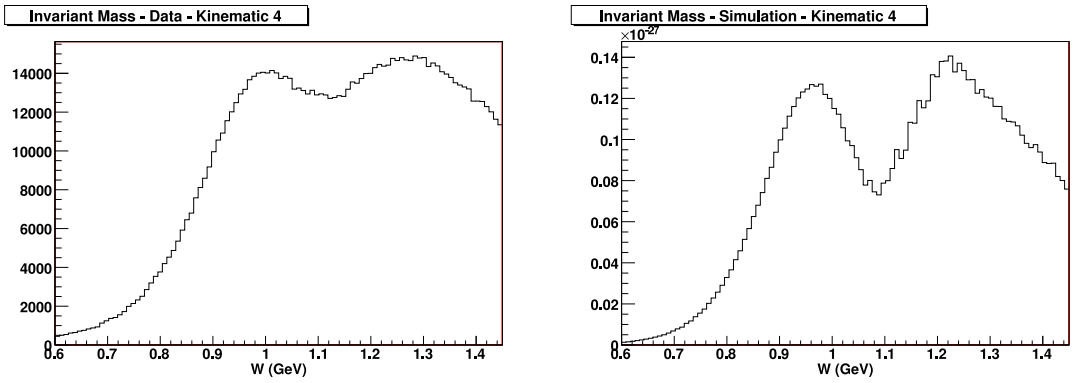

(a) (b)

Figure 5.9: Comparison of a) data to b) simulation with pion production for kinematic 4 with cuts of $p_{\text{miss},\perp} < 0.5$ GeV and $|p_{\text{miss},\parallel}| < 0.5$ GeV.

Cut	Kin. 3	Kin. 4
W	$0.7 < W < 1.05$GeV	$0.7 < W < 1.15$GeV
$p_{\text{miss},\parallel}$	$\lvert p_{\text{miss},\parallel}\rvert < 400$MeV	$\lvert p_{\text{miss},\parallel}\rvert < 250$MeV
$p_{\text{miss},perp}$	$p_{\text{miss},\perp} < 150$MeV	$p_{\text{miss},\perp} < 150$MeV
m_{miss}	$m_{\text{miss}} < 2.0$ GeV	$m_{\text{miss}} < 2.0$ GeV

Table 5.4: Cuts used for the selection of quasielastic events.

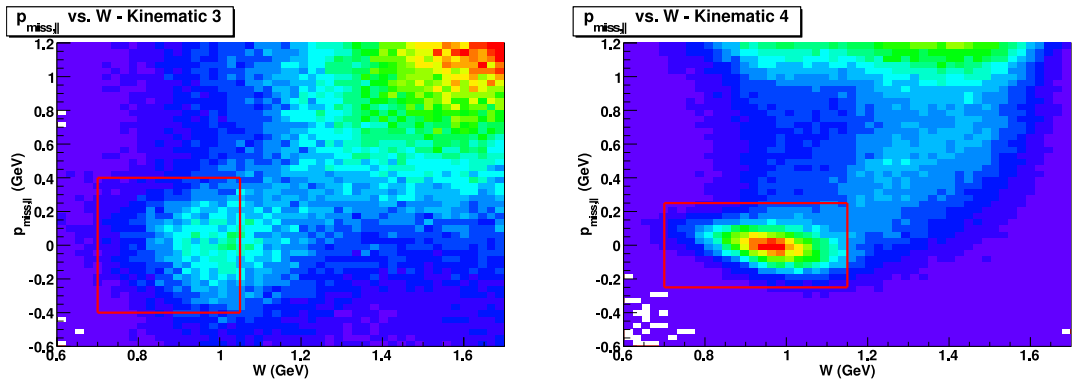

(a) (b)

Figure 5.10: $p_{\mathrm{miss},\parallel}$ vs. W for kinematics a) 3 and b) 4. The chosen cuts are shown in the red boxes. For a) an artificially low upper limit on W is used to suppress pion production events as shown in Section 5.5.1.

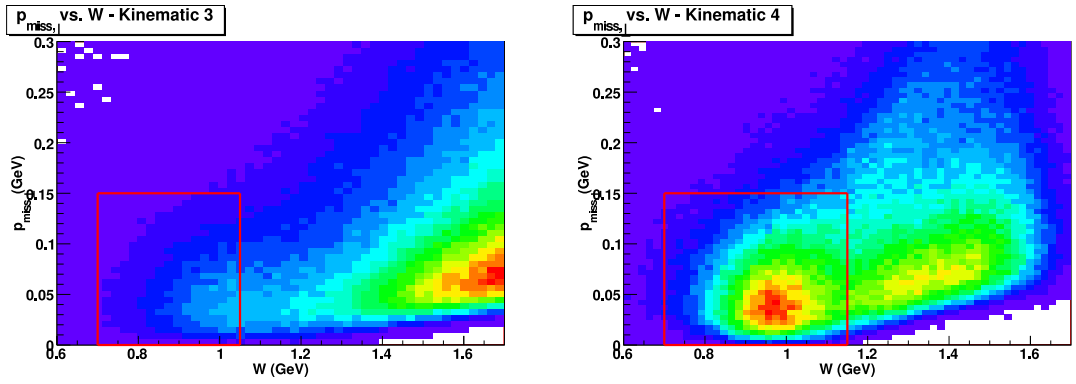

(a) (b)

Figure 5.11: $p_{\mathrm{miss},\perp}$ vs. W for kinematics a) 3 and b) 4. The chosen cuts are shown in the red boxes. For a) an artificially low upper limit on W is used to suppress pion production events as shown in Section 5.5.1.

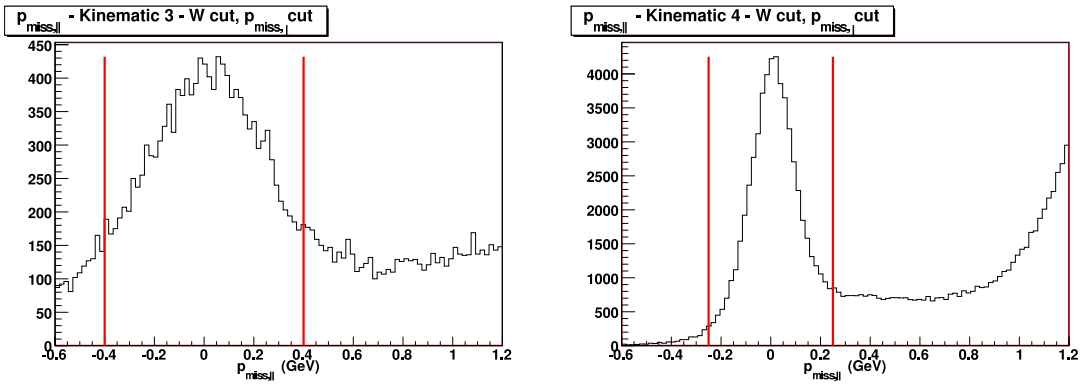

(a) (b)

Figure 5.12: $p_{\mathrm{miss},\parallel}$ for kinematics a) 3 and b) 4. Cuts in $p_{\mathrm{miss},\perp}$ and W have been applied. Chosen cuts are shown by red lines.

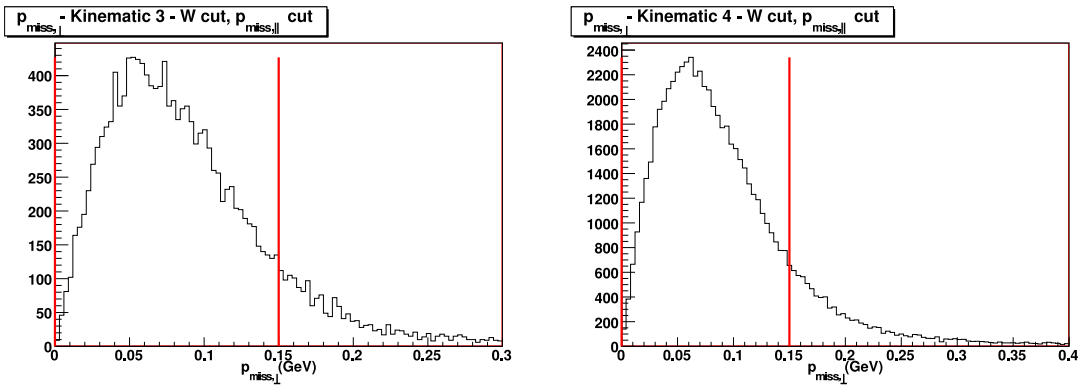

(a) (b)

Figure 5.13: $p_{\mathrm{miss},\perp}$ for kinematics a) 3 and b) 4. Cuts in $p_{\mathrm{miss},\parallel}$ and W have been applied. Chosen cuts are shown by red lines.

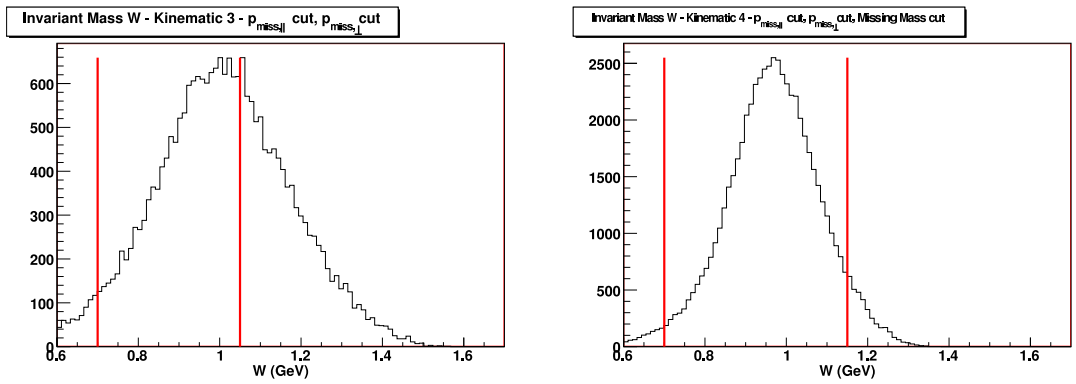

(a) (b)

Figure 5.14: W for kinematics a) 3 and b) 4. Cuts in $p_{\text{miss},\parallel}$ and $p_{\text{miss},\perp}$ have been applied. Chosen cuts are shown by red lines.

for pion production in our sample will then be suppressed and will be subsequently ignored for this analysis. Furthermore, to help confirm the suppression of these events, the value of G_E^n should not vary significantly as cuts are varied, as will be shown in Section 6.3. We make a final note that with these stronger cuts, the data (Fig. 5.16) is still qualitatively described by the Monte Carlo.

5.6 Accidental Background

In our data, accidental background events in the neutron arm can clearly be seen when looking for hits that occur in very early time regions which would reconstruct $\beta > 1$. These are found to occur in the data randomly in time at some measurable mean rate. To determine the contributions of accidental background within the quasielastic cuts, an identical analysis is done on the data after shifting *all* the neutron arm data in β^{-1} *before any quasielastic cuts* such that the new quasielastic region is entirely composed of random background events that were originally in a $\beta > 1$ region. This $\beta > 1$ region represents events that could not have originated from the event of interest by causality and is then populated by events uncorrelated to the scattering process measured by BigBite. By assuming the distribution of events is symmetric under time translation, they make up a "flat accidental background" which has contributions to the quasielastic sample.

By shifting in β^{-1} an equivalent shift in time is achieved. After shifting, the number of background events for any given set of cuts remains identical by invariance under time translation. However, the number of quasielastic events (and all other events that could be associated with the electron scattering process from the electron found in BigBite) is reduced to 0, as there cannot be any true coincidence events related to the BigBite trigger in the region. Performing the same cuts on this shifted data then gives a count of the background events in the quasielastic sample, within some error due to statistics.

Fig. 5.19 shows how events in one region of β^{-1} are then identified as background when shifted

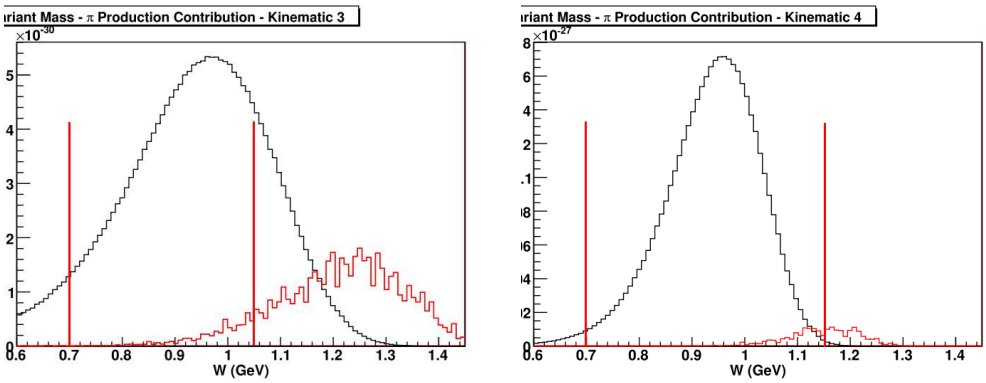

(a) (b)

Figure 5.15: Simulation of elastic in black and pion electroproduction in red for a) kinematic 3 and b) kinematic 4. Cuts in Table 5.4 in $p_{\mathrm{miss},\perp}$ and $p_{\mathrm{miss},\parallel}$ have been applied. Contributions for $W < 1.05$ GeV for kinematic 3 and $W < 1.15$ GeV for kinematic 4 show a suppressed presence of pion production.

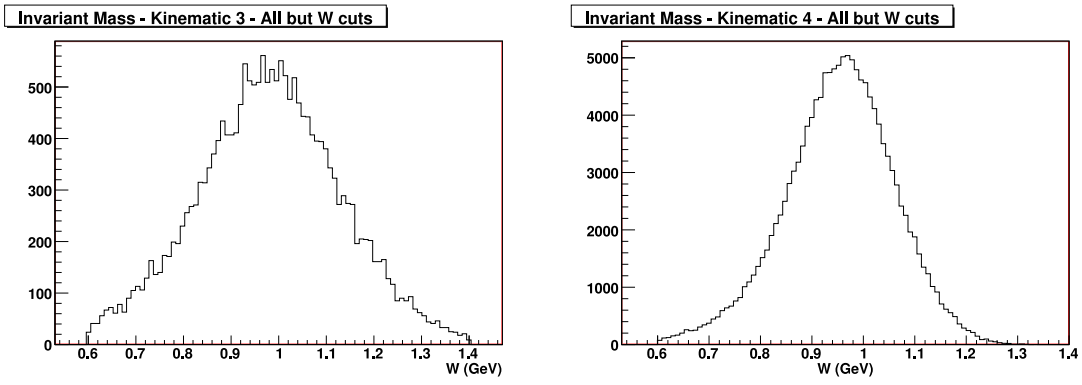

(a) (b)

Figure 5.16: Invariant mass with all cuts described in Table 5.4except for W cut for a) kinematic 3 and b) kinematic 4. Compare to simulation in Fig. 5.15. The peak is slightly shifted towards higher W due to the presence of inelastic events.

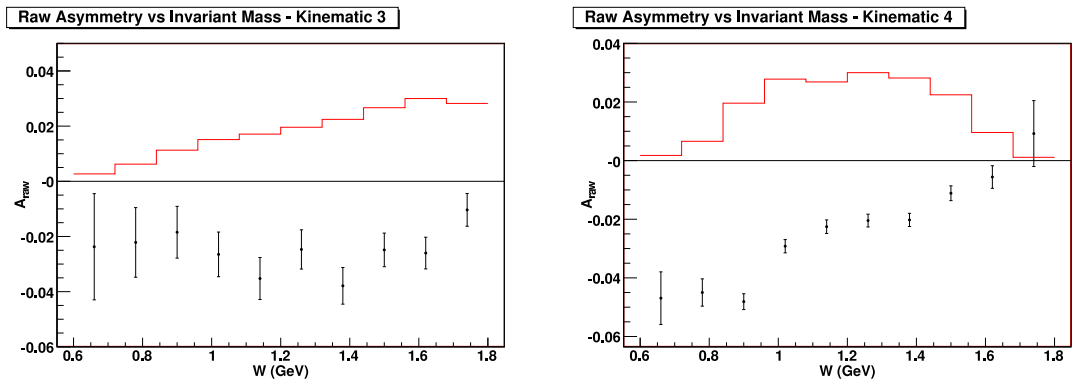

(a) (b)

Figure 5.17: Raw asymmetry vs. W for a) kinematic 3 and b) kinematic 4 with $p_{\text{miss},\perp} < 0.5$ GeV and $|p_{\text{miss},\parallel}| < 0.5$ GeV. The W spectrum is inlaid in red for relative comparison of counts between bins; vertical axis units are arbitrary.

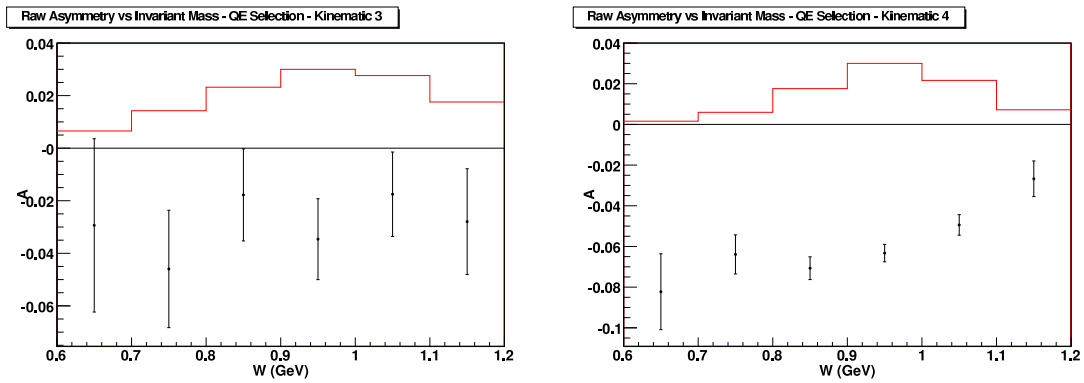

(a) (b)

Figure 5.18: Raw asymmetry vs. W for a) kinematic 3 and b) kinematic 4 with all quasielastic cuts in Table 5.4 applied. Natural variations in the asymmetry from θ_e correlating with W are expected from Eq. 3.7. The W spectrum is inlaid in red for relative comparison of counts between bins; vertical axis units are arbitrary.

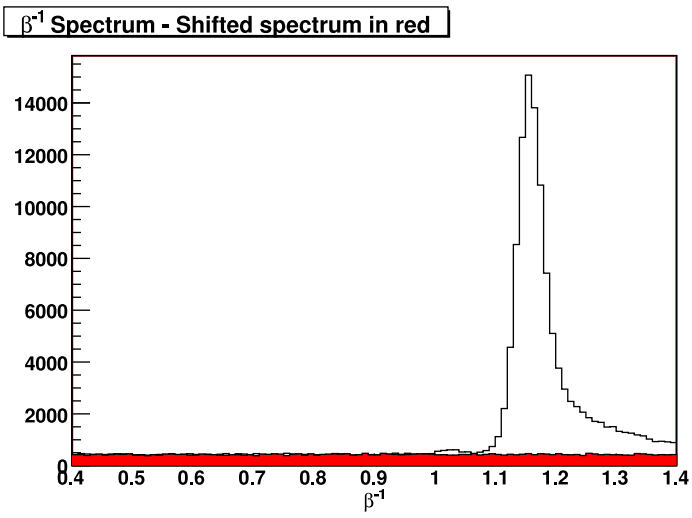

Figure 5.19: β^{-1} spectrum with flat background from β^{-1} shift in red.

and can then be subtracted. Fig. 5.20 shows the background calculated for the $p_{\mathrm{miss},\parallel}$ spectrum after $p_{\mathrm{miss},\perp}$ and W cuts. As confirmation of the time invariance of the spectrum, Fig. 5.21 and Fig. 5.22 shows the raw asymmetry (Section 5.7) and neutral to charged clusters ratio as a function of β^{-1}, respectively. The asymmetry plot is consistent with the idea that the $\beta > 1$ spectrum is invariant with time.

However, the ratio plot, Fig. 5.22, shows that the ratio of accidental uncharged-to-charged in the region $0.5 < \beta^{-1} < 1.0$ is not constant while the region $\beta^{-1} < 0.5$ is. This is due to the 20 ns window for associating veto hits with neutron arm clusters. $\beta > 1$ clusters that are sufficiently in time to the real coincidence region are associated with real coincidence veto hits. Since these veto hits come in locally at a higher rate and different uncharged-to-charged ratio than the accidental background, a larger number of these background clusters are accidentally associated with veto hits causing an artificially high count of background events identified as charged. This reduces the ratio and causes the effect seen.

The size of this effect is consistent with the charge window size. Given a coincidence time window size of 10 ns and a nominal distance of the neutron arm from the target of 10 m, the size of the inverse beta region of this effect, $\Delta\beta^{-1} = (10\text{ ns}) \cdot (0.3\text{ m/ns})/(10\text{ m}) = 0.3$. This is consistent with the region where the deviations occur. This creates a problem when identifying the contributions of charged background and neutral background that need to be subtracted from the quasielastic sample. Fig. 5.22 shows that the ratio of uncharged-to-charged background changes when considered in the presence of real events, which is the correct amount of background to subtract. All that can be determined is an upper limit of the neutral background based upon the amounts seen in the far

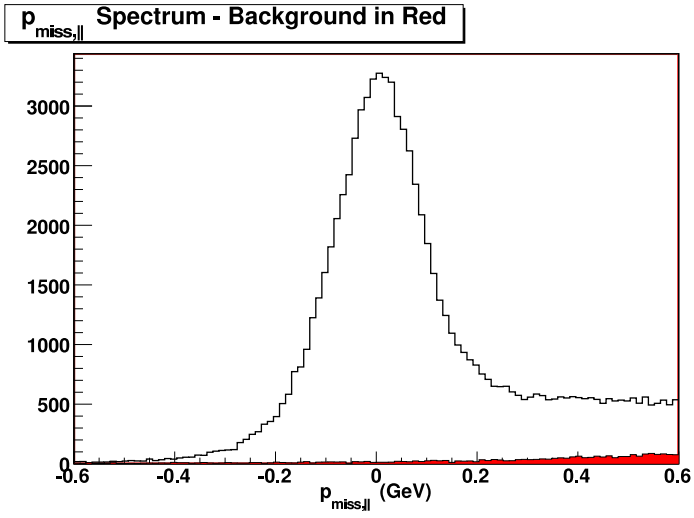

Figure 5.20: $p_{\mathrm{miss},\|}$ spectrum with background from β^{-1} shift in red.

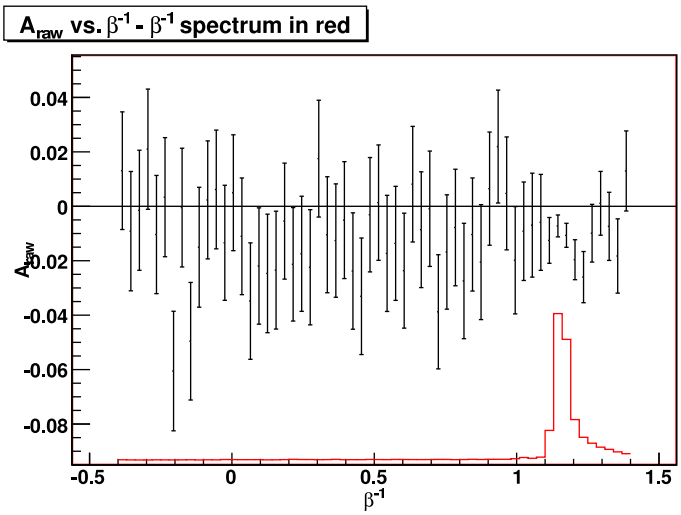

Figure 5.21: Raw asymmetry vs. β^{-1} with β^{-1} inlaid in red for kinematic 4. The asymmetry is consistent with begin constant throughout the $\beta^{-1} < 1$ region.

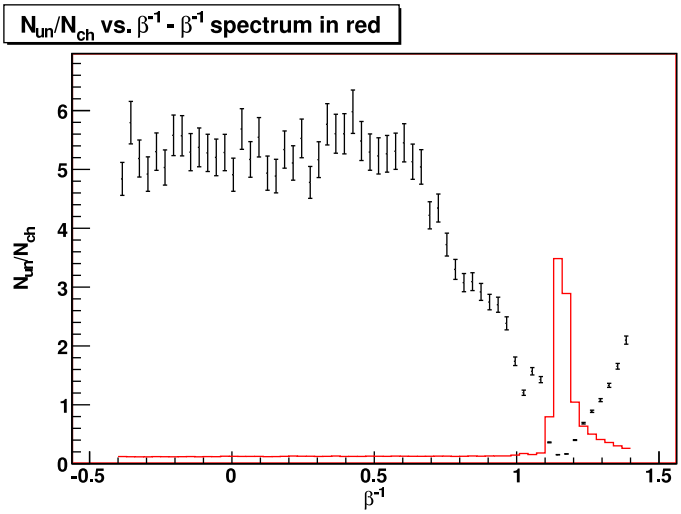

Figure 5.22: Ratio of number of uncharged-to-charged ratio vs. β^{-1} with β^{-1} inlaid in red. The ratio becomes smaller between $0.5 < \beta^{-1} < 1.0$ due to the time window to associate veto hits with neutron arm clusters.

$\beta > 1$ region where the uncharged-to-charged ratio reflects the true nature of the background. A sufficiently large shift of $\beta^{-1} \rightarrow \beta^{-1} + 0.8$ (about 25 ns) is used.

For ease of calculation, we will work with the assumption of no knowledge of how the background changes in the presence of real events. That is, we will say we do not understand the fraction of uncharged background that becomes misidentified. There are two extreme cases for how the neutral background contributes to the signal. For the neutral background, either all the background is unassociated with the quasielastic events or all the neutral background is mistakenly identified as charged. In the former case, the amount of background to subtract is exactly the amount of neutral background after shifting in β^{-1} after cuts. In the latter case, there is no neutral background to subtract. While more sophisticated models of the data can be built, the background contributes a relatively small amount of uncertainty in the final result, as will be shown in Section 6.2. In this light, further analysis of these effects will only produce minor improvements to the measurement and is not done for this work.

For the charged background, the situation is slightly different. All the charged background events will produce a signal in the veto layers and contribute to the background that must be subtracted. This places a lower limit on the amount of charged background. The two extreme cases to consider are no neutral background is misidentified, in which case this lower limit is the background to be subtracted, or all neutral background is misidentified and the amount of charged background to subtract is the total amount of both types.

We identify the amount of both types of background to be subtracted with a systematic uncertainty for the charged signal, $\Sigma^{\text{ch}}_{\text{back}}$, and the neutral signal, Σ_{back}, as

$$\Sigma^{\text{ch}}_{\text{back}} = N_{\text{back,ch}} + \frac{N_{\text{back,un}}}{2} \pm \frac{N_{\text{back,un}}}{\sqrt{12}} \tag{5.7}$$

$$\Sigma_{\text{back}} = \frac{N^{\text{back,un}}}{2} \pm \frac{N^{\text{back,un}}}{\sqrt{12}} \tag{5.8}$$

where $N_{\text{back,ch}}$ and $N_{\text{back,un}}$ is the charged and uncharged background counts measured from the shifted β^{-1} spectrum. The systematic uncertainty of $\frac{N}{\sqrt{12}}$ comes from the RMS value of a flat distribution from $-\frac{N}{2}$ to $\frac{N}{2}$ normalized to 1

$$\langle N \rangle_{\text{RMS}} = \left(\int_{-\frac{N}{2}}^{\frac{N}{2}} \frac{x^2}{N} dx \right)^{1/2} = \frac{N}{\sqrt{12}}. \tag{5.9}$$

5.7 Asymmetries

One of the relevant quantities to measure from the data is the cross section asymmetry with beam helicity. This quantity is directly related to G_E^n through Eq. 3.7. However, these equations assume that one has a perfectly polarized neutron target and a perfectly polarized beam. Furthermore, these equations do not take into account contributions to the neutral quasielastic sample when background from proton charge misidentification and accidental background. Additional false asymmetries may also be introduced from a beam-charge asymmetry, electronics, and analysis.

A table of the notation continuously used in several sections in calculating various asymmetry contributions and dilutions can be found in Table 5.5.

5.7.1 Asymmetry Sign

During the experiment, the apparent sign of the asymmetry would change in accordance with the insertion or removal of a half-wave plate at the injector and with the change of the sign of the target polarization vector. These changes act as a check on the possible systematics of the asymmetry

$N^{\pm}$	Half-wave plate and target sign corrected count for helicity $\pm$.
N_n	The number of correctly identified quasielastically scattered neutrons.
$N_{\rm back}$	The number from accidental coincidence background caused by random hits in time.
N_p	The number of protons misidentified as neutrons in the quasielastic sample.
$N_{\rm N_2}$	The number of events caused by scattering from N_2 in the ^{3}He target in the quasielastic sample.
$N_{\rm other}$	All other contributions in the neutral sample.
$N_{back,{\rm un}}$, $N_{back,{\rm ch}}$	The number of uncharged and charged accidental background hits found by shifting in time, respectively.
Σ_x	The sum $N_x^+ + N_x^-$.
Δ_x	The difference $N_x^+ - N_x^-$.
$A_{\rm phys}$	The physical asymmetry to relate to G_E^n.
$A_{\rm raw}$	The asymmetry measured in the data without corrections to asymmetry contributions and dilutions.
$P_{\rm 3He}$	Polarization of the ^{3}He nucleus.
$P_{\rm n}$	Polarization of the neutron relative to the ^{3}He nucleus polarization.
$P_{\rm beam}$	Polarization of the electron beam.
$D_{\rm back}$	Asymmetry dilution factor due to contributions from accidental background.
$D_{\rm N_2}$	Asymmetry dilution factor due to N_2 contributions from the target.
$D_{\rm p}$	Asymmetry dilution factor due to protons misidentified as neutrons.
$D_{\rm FSI}$	Asymmetry dilution factor from final state interactions.
$D^{\rm ch}_{\rm back}$	Proton asymmetry dilution factor due to contributions from accidental background.
$D^{\rm ch}_{\rm N_2}$	Proton asymmetry dilution factor due to N_2 contributions from the target.
$D^{\rm ch}_{\rm n}$	Proton asymmetry dilution factor due to neutrons misidentified as protons.
$D^{\rm ch}_{\rm FSI}$	Proton asymmetry dilution factor from final state interactions.

Table 5.5: Notation used in calculation of asymmetry contributions and dilutions.

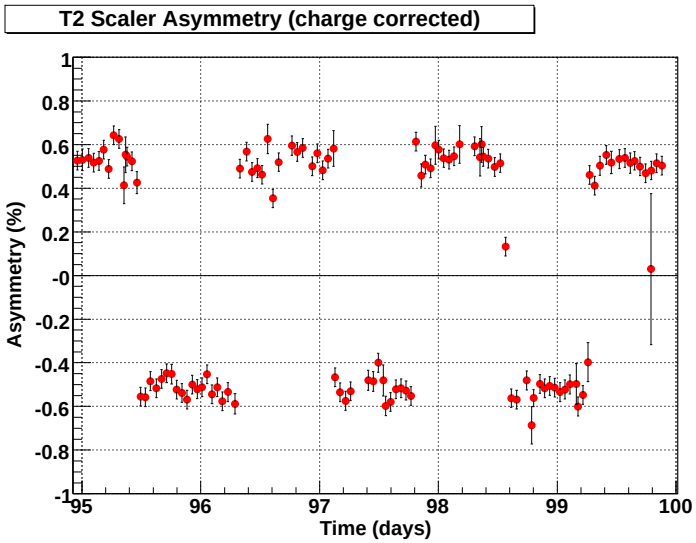

Figure 5.23: Asymmetry of the helicity gated T2 triggers. The change in sign corresponds to changes in the half-wave plate setting and the target polarization direction [81].

during the experiment. The value of the asymmetry can be seen to change sign with the state of the half-wave plate, as shown in Fig. 5.23.

The measured asymmetry, A_{meas}, is equal to

$$A_{\text{meas}} = \frac{N^{+,\text{rec}} - N^{-,\text{rec}}}{N^{+,\text{rec}} + N^{-,\text{rec}}} = f(\hat{T}) \tag{5.10}$$

where $N^{h,\text{rec}}$ is the count of neutral quasielastics with recorded helicity h, $f(\hat{T})$ (more specifically Eq. 3.7) is a function of $\hat{T}$, the unit vector of the target polarization direction and f has the property that $f(\lambda\hat{T}) = \lambda f(\hat{T})$ where $\lambda = \pm 1$. With the insertion of the half-wave plate, the recorded helicities for each state are reversed, meaning A_{meas} will change sign. A similar effect occurs with the change in sign of the target, or $\hat{T} \to -\hat{T}$

$$A_{\text{meas}} = P_{\text{HWP}} P_{\hat{\text{T}}} A_{\text{phys}} \tag{5.11}$$

where P_{HWP} takes the value of $+1$ or -1 given the half-wave plate state and $P_{\hat{\text{T}}}$ is ± 1, based on the direction of the polarization of the target. Multiplying both sides by $P_{\text{HWP}} P_{\hat{\text{T}}}$, the correction on the measured asymmetry based on these states is simply

$$A_{\text{raw}} = P_{\text{HWP}} P_{\hat{\text{T}}} A_{\text{meas}}. \tag{5.12}$$

With knowledge of the target polarization direction, which can be determined from the EPR measurements, and the beam polarization, which comes from the Møller polarimeter measurement, the sign of the asymmetry is fixed. The half-wave plate state is recorded by EPICS and is therefore available on the order of every few seconds during data taking. The half-wave plate was occasionally changed during a run, which is identified by examining this EPICS data over the course of the run. In such cases the run is discarded.

For the remainder of this analysis, the correction of the asymmetry sign based on these factors is assumed.

5.7.2 Asymmetry Corrections

To properly account for all of the contributions and dilutions of the true asymmetry, we must develop a formalism that allows us to take the asymmetry measured from the data, $A_{\rm raw}$ and make corrections such that we can recover the asymmetry that would be measured if these effects were not present, $A_{\rm phys}$. We take $A_{\rm raw}$ to be the sign corrected measured asymmetry

$$A_{\rm raw} = \frac{N^+ - N^-}{N^+ + N^-} \tag{5.13}$$

where $N^{\pm}$ is the count in our quasielastic neutral sample for (corrected) helicity $\pm$. $A_{\rm phys}$ is given by Eq. 3.7. For now we will assume the false instrumental asymmetry contributions are small. These will be treated in Section 5.8. We define our contributions to the neutral quasielastic sample that we will consider for this analysis

1. Accidental random background
2. Protons with misidentified charge
3. Scattering from N_2 present in the target
4. Final state interactions

These contribute as

$$N = N_n + N_{\rm back} + N_p + N_{\rm N_2} + N_{\rm other} \tag{5.14}$$

where N_n is the number of correctly identified quasielastically scattered neutrons, N_p is the number of protons misidentified as quasielastic neutrons, $N_{\rm N_2}$ is the number of events from N_2 present in the target, $N_{\rm back}$ is the number from accidental coincidence background caused by random hits in time, and $N_{\rm other}$ is all other contributions in the neutral sample. N_x^+ and N_x^- will represent the number of x for positive and negative helicity, respectively.

There are also several factors that directly dilute the asymmetry:

1. Less than full polarization of the nucleus, $P_{^3\rm He}$
2. Less than full polarization of the neutron relative to the nucleus, P_n
3. Less than full polarization of the beam, $P_{\rm beam}$

These polarization dilutions change the asymmetry by reducing it by a factor equal to their product

$$P_{^3\rm He} P_{\rm n} P_{\rm beam} A_{\rm phys} = A_{\rm n,meas.} \tag{5.15}$$

where $A_{n,\rm meas.}$ is the true asymmetry of the neutrons measured in the experiment from quasielastic scattering from ^{3}He,

$$A_{n,\rm meas.} = \frac{N_n^+ - N_n^-}{N_n^+ + N_n^-}. \tag{5.16}$$

The raw asymmetry from the data is

$$A_{\rm raw} = \frac{N^+ - N^-}{N^+ + N^-} = \frac{N_n^+ + N_{\rm back}^+ + N_p^+ + N_{\rm N_2}^+ + N_{\rm other}^+ - N_n^- - N_{\rm back}^- - N_p^- - N_{\rm N_2}^- - N_{\rm other}^-}{N_n^+ + N_{\rm back}^+ + N_p^+ + N_{\rm N_2}^+ + N_{\rm other}^+ + N_n^- + N_{\rm back}^- + N_p^- + N_{\rm N_2}^- + N_{\rm other}^-}. \tag{5.17}$$

Defining for type x

$$\Delta_x = N_x^+ - N_x^- \tag{5.18}$$

$$\Sigma_x = N_x^+ + N_x^- \tag{5.19}$$

then,

$$A_{\text{raw}} = \frac{\Delta}{\Sigma} = \frac{\Delta_n + \Delta_{\text{back}} + \Delta_p + \Delta_{\text{N}_2} + \Delta_{\text{other}}}{\Sigma_n + \Sigma_{\text{back}} + \Sigma_p + \Sigma_{\text{N}_2} + \Sigma_{\text{other}}}. \tag{5.20}$$

We define four dilution factors as

$$D_{\text{back}} = 1 - \frac{\Sigma_{\text{back}}}{\Sigma} = \frac{\Sigma_n + \Sigma_p + \Sigma_{\text{N}_2} + \Sigma_{\text{other}}}{\Sigma} \tag{5.21}$$

$$D_{\text{N}_2} = 1 - \frac{\Sigma_{\text{N}_2}}{\Sigma - \Sigma_{\text{back}}} = \frac{\Sigma_n + \Sigma_p + \Sigma_{\text{other}}}{\Sigma_n + \Sigma_p + \Sigma_{\text{N}_2} + \Sigma_{\text{other}}} \tag{5.22}$$

$$D_p = 1 - \frac{\Sigma_p}{\Sigma - \Sigma_{\text{back}} - \Sigma_{\text{N}_2}} = \frac{\Sigma_n + \Sigma_{\text{other}}}{\Sigma_n + \Sigma_p + \Sigma_{\text{other}}} \tag{5.23}$$

$$D_{\text{FSI}} = 1 - \frac{\Sigma_{\text{other}}}{\Sigma - \Sigma_{\text{back}} - \Sigma_{\text{N}_2} - \Sigma_p} = \frac{\Sigma_n}{\Sigma_n + \Sigma_{\text{other}}}. \tag{5.24}$$

The product of these dilutions is

$$D_{\text{back}} D_{\text{N}_2} D_p D_{\text{FSI}} = \frac{\Sigma_n}{\Sigma}. \tag{5.25}$$

A_{raw} can then be written

$$\begin{aligned} A_{\text{raw}} &= D_{\text{back}} D_{\text{N}_2} D_p D_{\text{FSI}} \frac{\Delta_n}{\Sigma_n} + \frac{\Delta_{\text{back}} + \Delta_p + \Delta_{\text{N}_2} + \Delta_{\text{other}}}{\Sigma} \\ &= D_{\text{back}} D_{\text{N}_2} D_p D_{\text{FSI}} A_{n,\text{meas}} + \frac{\Delta_{\text{back}}}{\Sigma} + \frac{\Delta_p}{\Sigma} + \frac{\Delta_{\text{N}_2}}{\Sigma} + \frac{\Delta_{\text{other}}}{\Sigma}. \end{aligned} \tag{5.26}$$

Taking the fact that the N_2 target is not polarized and therefore has no asymmetry, $\Delta_{\text{N}_2} = 0$. Combining Eqs. 5.15 and 5.26, the relation between the raw asymmetry and the asymmetry to relate to G_E^n is

$$A_{\text{phys}} = \frac{A_{\text{raw}} - \frac{\Delta_{\text{back}}}{\Sigma} - \frac{\Delta_p}{\Sigma} - \frac{\Delta_{\text{other}}}{\Sigma}}{P_{^3\text{He}} P_{\text{n}} P_{\text{beam}} D_{\text{back}} D_{\text{N}_2} D_p D_{\text{FSI}}}. \tag{5.27}$$

This leaves the four dilutions and three relative asymmetries to be calculated. D_{back} and Δ_{back} can be calculated directly from the ^{3}He data, as the background counts can be handled by shifting in β^{-1} as described in Section 5.6.

It is also useful to define similar dilutions regarding the charged quasielastic sample, such as in determining the N_2 dilution in the charged sample, as will be used in Section 6.1.4,

$$\Sigma^{\text{ch}} = \Sigma_p^{\text{ch}} + \Sigma_{\text{back}}^{\text{ch}} + \Sigma_n^{\text{ch}} + \Sigma_{\text{N}_2}^{\text{ch}} + \Sigma_{\text{other}}^{\text{ch}} \tag{5.28}$$

where Σ^{ch} is the count of events passing the quasielastic cuts and identified as charged by the vetos, Σ_p^{ch} is the contribution by quasielastic protons from ^{3}He nuclei, $\Sigma_{\text{back}}^{\text{ch}}$ is the contribution of background, Σ_n^{ch} is the contribution of quasielastic neutrons from ^{3}He nuclei, $\Sigma_{\text{N}_2}^{\text{ch}}$ is the contribution from scattering from N_2 nucleons, and $\Sigma_{\text{other}}^{\text{ch}}$ is everything else. We can then define a similar set of dilution factors for the charged spectrum

$$D_{\text{back}}^{\text{ch}} = 1 - \frac{\Sigma_{\text{back}}^{\text{ch}}}{\Sigma^{\text{ch}}} = \frac{\Sigma_p^{\text{ch}} + \Sigma_n^{\text{ch}} + \Sigma_{\text{N}_2}^{\text{ch}} + \Sigma_{\text{other}}^{\text{ch}}}{\Sigma^{\text{ch}}} \tag{5.29}$$

$$D_{\text{N}_2}^{\text{ch}} = 1 - \frac{\Sigma_{\text{N}_2}^{\text{ch}}}{\Sigma^{\text{ch}} - \Sigma_{\text{back}}^{\text{ch}}} = \frac{\Sigma_p^{\text{ch}} + \Sigma_n^{\text{ch}} + \Sigma_{\text{other}}^{\text{ch}}}{\Sigma_p^{\text{ch}} + \Sigma_n^{\text{ch}} + \Sigma_{\text{N}_2}^{\text{ch}} + \Sigma_{\text{other}}^{\text{ch}}} \tag{5.30}$$

$$D_n^{\text{ch}} = 1 - \frac{\Sigma_n^{\text{ch}}}{\Sigma^{\text{ch}} - \Sigma_{\text{back}}^{\text{ch}} - \Sigma_{\text{N}_2}^{\text{ch}}} = \frac{\Sigma_p^{\text{ch}} + \Sigma_{\text{other}}^{\text{ch}}}{\Sigma_p^{\text{ch}} + \Sigma_n^{\text{ch}} + \Sigma_{\text{other}}^{\text{ch}}} \tag{5.31}$$

$$D_{\text{FSI}}^{\text{ch}} = 1 - \frac{\Sigma_{\text{other}}^{\text{ch}}}{\Sigma^{\text{ch}} - \Sigma_{\text{back}}^{\text{ch}} - \Sigma_{\text{N}_2}^{\text{ch}} - \Sigma_n^{\text{ch}}} = \frac{\Sigma_p^{\text{ch}}}{\Sigma_p^{\text{ch}} + \Sigma_{\text{other}}^{\text{ch}}}. \tag{5.32}$$

5.7.3 Nitrogen Dilution

The contribution of N_2 in the data is measured by performing the quasielastic analysis on a N_2 target and scaling the counts proportionally to the relative densities of the targets and to the integrated beam-charge. For a given set of ^{3}He runs and a set of N_2 runs of total beam charge Q, density of N_2 in the target of ρ_{N_2}, neutral quasielastic counts Σ, and quasielastic background counts Σ_{back}, the scaled number of N_2 counts in the ^{3}He quasielastic neutral sample is

$$\Sigma_{N_2} = (\Sigma(N_2) - \Sigma_{\text{back}}(N_2)) \frac{Q(^3\text{He})}{Q(N_2)} \frac{\rho_{N_2}(^3\text{He})}{\rho_{N_2}(N_2)}. \tag{5.33}$$

The dilution factor for N_2, D_{N_2} is then

$$D_{N_2} = 1 - \frac{\Sigma(N_2) - \Sigma_{\text{back}}(N_2)}{\Sigma - \Sigma_{\text{back}}} \frac{Q(^3\text{He})}{Q(N_2)} \frac{\rho_{N_2}(^3\text{He})}{\rho_{N_2}(N_2)}. \tag{5.34}$$

Any varying lengths of the two target cells can be neglected, as identical cuts on the reconstructed vertex position artificially make the effective lengths of the targets equal.

5.7.4 Proton Dilution and Asymmetry

Calculating the number of protons in the neutral sample is done by examining the uncharged-to-charged ratio across three different targets. This allows us to constrain the misidentification probabilities based upon the expected ratios from the nuclei of the targets if there were no misidentifications. Additionally, due to the fact that cuts are placed on missing momentum and due to nuclear effects, one cannot *a priori* expect these ratios to be simply the ratio of neutrons to protons in the nuclei, as covered later in this subsection.

The number of apparently observed quasielastic protons and neutrons, $N^{(p)}$ and $N^{(n)}$ can be written generally as

$$N^{(n)} = N_p^{(n)} + N_n^{(n)} \tag{5.35}$$
$$N^{(p)} = N_p^{(p)} + N_n^{(p)} \tag{5.36}$$

where the subscript refers to the actual particle and the superscript refers to how it is identified. We define a set of mixing coefficients, η, such that

$$N_n^{(n)} \propto \sigma_n \eta_n^{(n)} \tag{5.37}$$
$$N_n^{(p)} \propto \sigma_n \eta_n^{(p)} \tag{5.38}$$
$$N_p^{(n)} \propto f\sigma_p \eta_p^{(n)} \tag{5.39}$$
$$N_p^{(p)} \propto f\sigma_p \eta_p^{(p)} \tag{5.40}$$

where σ_n and σ_p are the single-nucleon cross sections. This definition takes into account the cuts on missing momentum and nuclear effects by parametrizing these effects into a constant f which depends on the target, the effective number of protons to neutrons. The remaining factors are target independent. The ratio of observed uncharged-to-charged quasielastic events in the data can be written

$$R = \frac{N^{(n)}}{N^{(p)}} = \frac{\frac{\sigma_n}{\sigma_p}(\eta_n^{(n)}/\eta_p^{(p)}) + f(\eta_p^{(n)}/\eta_p^{(p)})}{\frac{\sigma_n}{\sigma_p}(\eta_n^{(p)}/\eta_p^{(p)}) + f}. \tag{5.41}$$

By using three different targets, the three ratios of mixing constants in Eq. 5.41 can be constrained. The dilution factor D_p is then

$$D_p = \frac{N_n^{(n)}}{N_n^{(n)} + N_p^{(n)}} = \frac{\frac{\sigma_n}{\sigma_p}\left(\eta_n^{(n)}/\eta_p^{(p)}\right)}{\frac{\sigma_n}{\sigma_p}\left(\eta_n^{(n)}/\eta_p^{(p)}\right) + f\left(\eta_p^{(n)}/\eta_p^{(p)}\right)}. \tag{5.42}$$

Furthermore, the dilution factor for neutrons in the charged sample, $D_n^{\rm ch}$, is given by

$$D_n^{\rm ch} = \frac{N_p^{(p)}}{N_p^{(p)} + N_n^{(p)}} = \frac{f}{\frac{\sigma_n}{\sigma_p}\eta_n^{(p)}/\eta_p^{(p)} + f}. \tag{5.43}$$

As constraints we use the (background subtracted, N_2 subtracted for the ^{3}He data) uncharged-to-charged ratios from the H_2 target, R_{H_2}, the N_2 target, R_{N_2}, and the ^{3}He target, $R_{^3{\rm He}}$

$$R_{H_2} = \eta_p^{(n)}/\eta_p^{(p)} \tag{5.44}$$

$$R_{^3{\rm He}} = \frac{\frac{\sigma_n}{\sigma_p}(\eta_n^{(n)}/\eta_p^{(p)}) + f(\eta_p^{(n)}/\eta_p^{(p)})}{\frac{\sigma_n}{\sigma_p}(\eta_n^{(p)}/\eta_p^{(p)}) + f} \tag{5.45}$$

$$R_{N_2} = \frac{\frac{\sigma_n}{\sigma_p}\eta_n^{(n)}/\eta_p^{(p)} + \eta_p^{(n)}/\eta_p^{(p)}}{\frac{\sigma_n}{\sigma_p}(\eta_n^{(p)}/\eta_p^{(p)}) + 1}. \tag{5.46}$$

Here we have assumed that $f = 0$ for the H_2 target, $f = 1$ for the N_2 target ($Z = N = 7$), but we have allowed that f may be unequal to the ratio of protons to neutron in ^{3}He due to differences in the proton and neutron momentum distributions. These differences could results in a different ratio when cuts on missing momentum are applied. For N_2 with $Z = N = 7$, this is not expected to be a significant effect [80] and the momentum distributions are treated as being identical. It is then simply a matter of solving for the three ratios given these three equations. One arrives at

$$\frac{\eta_p^{(n)}}{\eta_p^{(p)}} = R_{H_2} \tag{5.47}$$

$$\frac{\eta_n^{(p)}}{\eta_p^{(p)}} = \frac{\sigma_p}{\sigma_n}\left(\frac{R_{^3{\rm He}} f - R_{N_2} + R_{H_2}(1-f)}{R_{N_2} - R_{^3{\rm He}}}\right) \tag{5.48}$$

$$\frac{\eta_n^{(n)}}{\eta_p^{(p)}} = \frac{\sigma_p}{\sigma_n}\left(f R_{N_2}\left(\frac{R_{^3{\rm He}} - R_{H_2}}{R_{N_2} - R_{^3{\rm He}}}\right) - R_{H_2}\right). \tag{5.49}$$

Rate Dependence

The analysis above assumes that the efficiencies of detecting one particle as another is rate-independent. However, in the data a variety of luminosities were used on different targets and the accidental background rates will change. Since these rates contribute to factors such as accidental association of neutral particles as charged they must be accounted for when considering uncharged-to-charged ratios of different rates.

To properly evaluate the dilution factor using the method in the previous section all ratios must be corrected for different veto accidental rates. Furthermore, in the regions of time populated purely by accidental hits, there is little correlation between hits in the two veto planes (only 10% have matching hits in both veto layers) and they are treated as independent rates. To do this, we model the rate dependency using the following scheme

$$\begin{aligned} N_n^{\rm obs} = {} & N_n(1 - P_{1,{\rm dead}}P_{2,{\rm dead}}) - N_n[P_{1,{\rm acc}}(1 - P_{1,{\rm dead}}) + P_{2,{\rm acc}}(1 - P_{2,{\rm dead}}) \\ & - P_{1,{\rm acc}}(1 - P_{1,{\rm dead}})P_{2,{\rm acc}}(1 - P_{2,{\rm dead}})] \end{aligned} \tag{5.50}$$

$$\begin{aligned} N_p^{\rm obs} = {} & N_p(1 - P_{1,{\rm dead}}P_{2,{\rm dead}}) + N_n[P_{1,{\rm acc}}(1 - P_{1,{\rm dead}}) + P_{2,{\rm acc}}(1 - P_{2,{\rm dead}}) \\ & - P_{1,{\rm acc}}(1 - P_{1,{\rm dead}})P_{2,{\rm acc}}(1 - P_{2,{\rm dead}})] \end{aligned} \tag{5.51}$$

where $N_n^{\rm obs}$ is the number of observed neutrals, $N_p^{\rm obs}$ is the number of observed charged, N_n is the number of neutrals if there was no accidental backgrounds, N_p is the number of charged if there

was no accidental background, $P_{i,\mathrm{dead}}$ is the probability of an accidental hit in a time window equal to the dead time in veto plane i, and $P_{i,\mathrm{acc}}$ is the probability of an accidental hit in the charge identification window. This model is dependent upon how these probabilities are defined. As the accidental background events are flat in rate, a Poisson distribution can be used to describe the probability of measuring n accidental hits of total rate r on the veto plane in some time interval Δt

$$f(n, kr\Delta t) = \frac{(kr\Delta t)^n e^{-kr\Delta t}}{n!} \tag{5.52}$$

where k parametrizes the spacial window size for accepting a veto hit for a neutron arm cluster. We are interested in finding the probability, P, that we have one or more hits in the interval. This is

$$P = 1 - e^{-kr\Delta t}. \tag{5.53}$$

The probabilities are then

$$P_{i,\mathrm{dead}} = 1 - e^{-kr_i\Delta t_{\mathrm{dead}}} \tag{5.54}$$

$$P_{i,\mathrm{acc}} = 1 - e^{-kr_i\Delta t_{\mathrm{acc}}} \tag{5.55}$$

where r_i is the total rate of accidentals on the ith entire veto plane, $\Delta t_{\mathrm{dead}} = 100$ ns, and $\Delta t_{\mathrm{acc}} = 20$ ns as specified in Section 5.3.

Here k represents the fraction of the veto plane that is considered for any given event. The value of k should vary between 0 and 1 and should be identical for both veto planes, as the cuts are identical. Taking the value of $k \approx 0.2$ as the veto acceptance area of $\Delta x = 1.1$ m and the neutron arm height of 6 m, veto rates generally less than 500 kHz, and the time windows specified above, the amount of deviation compared to that of no veto rate is expected to be about 0.5% which is small.

The dilution analysis should then be performed at the veto rate for the given ^{3}He runs to give an accurate representation of the proton contribution to the quasielastic neutral sample. These rates are typically stable for production running as there was generally little variation in beam current during these time periods.

Missing Momentum Cut Dependence

The effective ratio of protons to neutrons for ^{3}He for our missing-momentum cuts, f, is determined by utilizing a calculation performed by College of William and Mary graduate student Aidan Kelleher [81] using a ^{3}He momentum density distribution provided by Rocco Schiavilla [80]. This calculation determines the momentum distributions of the two nucleon types in the ^{3}He nucleus. Placing cuts on missing-momentum alters the relative ratios measured from quasielastic scattering for protons and neutrons due to these momentum differences.

A plot of the relative ratio of protons to neutrons given our $p_{\mathrm{miss},\parallel}$ and $p_{\mathrm{miss},\perp}$ cuts is shown in Fig. 5.25. From this figure, it is clear that the neutron momentum is generally wider than that of the protons, as the cuts are made more narrow, the relative number of protons to neutron becomes larger. Furthermore, these distributions all have the desired property of asymptotically approaching $\frac{Z}{A-Z}\big|_{^3\mathrm{He}} = 2$ as $p_{\mathrm{miss},\parallel} \to \infty$ and $p_{\mathrm{miss},\perp} \to \infty$.

Effects based on the momentum resolution of the neutron arm are included to determine our values of f, (though are not present in Fig. 5.25). For our cuts of $|p_{\mathrm{miss},\parallel}| < 250$ MeV and $p_{\mathrm{miss},\perp} < 150$ MeV for kinematic 4 a value of $f = 2.15$ is found. For cuts of $|p_{\mathrm{miss},\parallel}| < 400$ MeV and $p_{\mathrm{miss},\perp} < 150$ MeV for kinematic 3, $f = 2.14$.

Proton Asymmetry

The proton asymmetry term $\frac{\Delta_p}{\Sigma}$ can be calculated using the known values of G_E^p and G_M^p by doing a calculation similar to the one used for G_E^n "in reverse". As will be shown in Section 5.10 the physical

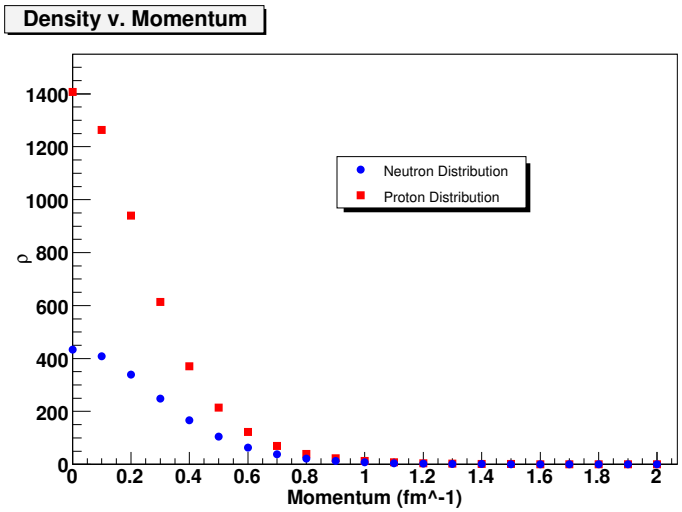

Figure 5.24: Effective proton and neutron densities for ^{3}He vs. the momentum of the nucleon. Density is in arbitrary units.

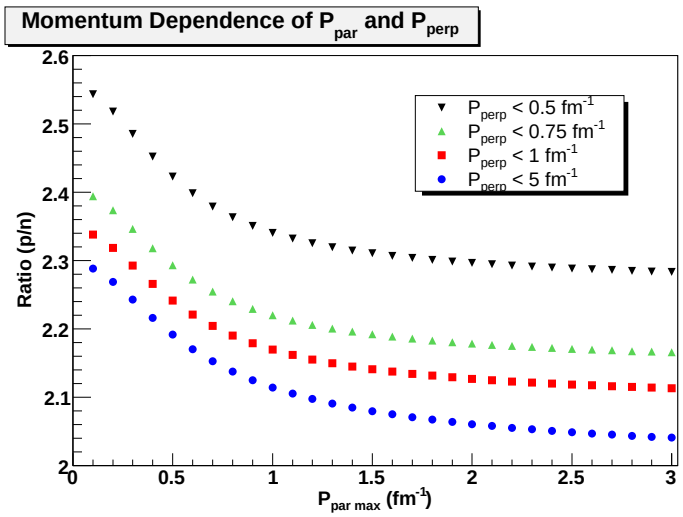

Figure 5.25: Effective proton to neutron ratio for cuts on kinematic variables in ^{3}He quasielastic scattering in units of fm^{-1}. Resolution effects are not present in this plot.

asymmetry for the proton, $A^p_{\rm phys}$, can be related to an expansion of Eq. 3.7 in terms of powers of the ratio $\Lambda = \frac{G^p_E}{G^p_M}$

$$A^p_{\rm phys} = \sum_n \overline{T}_n \Lambda^n(Q^2) \tag{5.56}$$

where the coefficients $\overline{T}_n$ are related to the acceptance of our detectors and the direction of the polarization of the target. These numbers are calculated for G^n_E in our analysis to $n = 5$ and we will treat as known. By using the parametrization by Jim Kelly [36], G^p_E and G^p_M can be calculated given a known value of Q^2, also found during our analysis and described in Section 5.10. All that is left is to calculate $\frac{\Delta_p}{\Sigma}$ given $A^p_{\rm phys}$.

Following an analogous formalism to Section 5.7.2,

$$A_{p,\rm meas} = \frac{N^+_p - N^-_p}{N^+_p + N^-_p} = \frac{\Delta_p}{\Sigma_p} = A^p_{\rm phys} P_{^3\rm He} P_p P_{\rm beam} \tag{5.57}$$

where $P_p \approx -0.03$ as a result of the same calculations that give the polarization of the neutron in the ^{3}He nucleus, as discussed in Section 3.3.3. Using Eqs. 5.21 to 5.23

$$1 - D_p = \frac{\Sigma_p}{\Sigma_n + \Sigma_{\rm other} + \Sigma_p} = \frac{\Sigma_p}{\Sigma} D_{\rm back} D_{\rm N_2}. \tag{5.58}$$

Combining all of these equations, we arrive at our expression for $\frac{\Delta_p}{\Sigma}$

$$\frac{\Delta_p}{\Sigma} = \frac{1 - D_p}{D_{\rm back} D_{\rm N_2}} P_{^3\rm He} P_p P_{\rm beam} \sum_n \overline{T}_n \Lambda^n(Q^2). \tag{5.59}$$

5.7.5 Other Corrections

Final State Interactions

Final state interactions (FSI) also have some effect on the final calculation of G^n_E. These interactions are present due to the rescattering of the struck nucleon with the remaining nucleus. To account for these effects, the Glauber approximation, which treats the nucleons as stationary objects in the nucleus, has been shown to be a reliable theory to describe these interactions for our kinematic regime.

For this analysis a code, called GEA [82], based on the generalized eikonal approximation, was used to estimate the effects of FSI on our final result. While the results for light nuclei are only preliminary, we apply these to our analysis to provide an estimation of these effects on our final result. The preliminary calculations for ^{3}He show that these effects will reduce the asymmetry, $A_{\rm perp}$, the primary contribution to our total asymmetry (see Section 3.1) by about 5% in the presence of charge exchange effects for all of our kinematic points [83], Fig. 5.26.

We set the value for the factor $D_{\rm FSI} = 0.95 \pm 0.05$ as an estimation of these effects. Once more accurate and final calculations become available they may be worked into this analysis.

5.8 False Asymmetries

For this analysis false asymmetry contributions are parametrized as effective efficiencies for each helicity state, as described in Section 3.4.5. These are calculated for each ^{3}He run in the analysis and are the averaged into a total false asymmetry for the run period. For each run, the effective efficiency, ϵ_h, for a helicity state ($\epsilon_h = 1 - r_h$, where r_h is the dead time for a helicity state), h, is

$$\epsilon_h = \prod_i \epsilon_{h,i} = \epsilon_{h,\rm elec} \epsilon_{h,\rm DAQ} \epsilon_{h,\rm track} \epsilon_{h,Q} \tag{5.60}$$

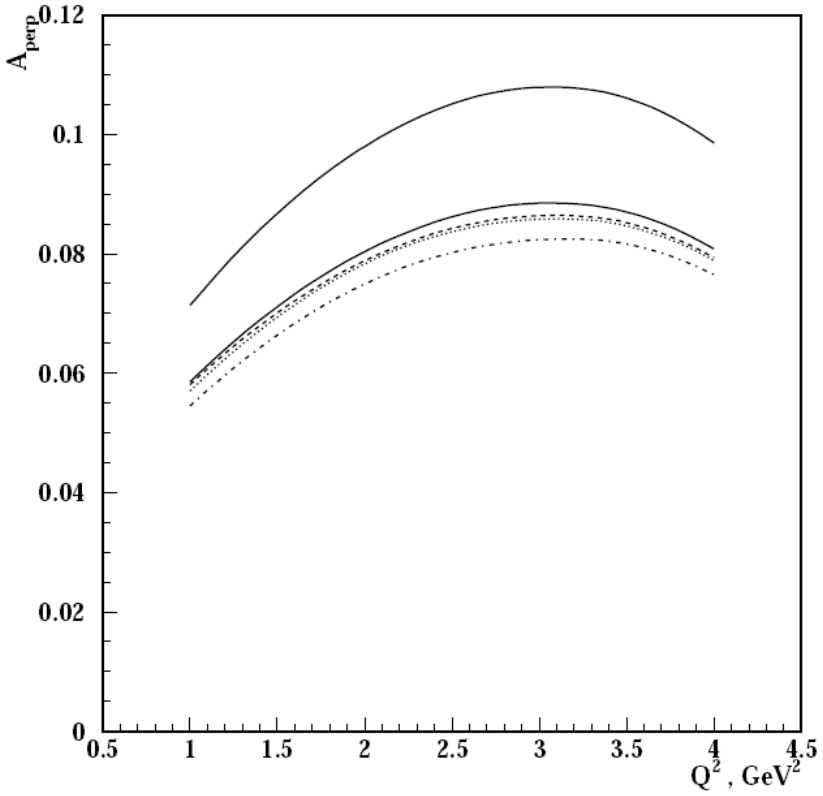

Figure 5.26: The asymmetry $A_{\rm perp}$ calculated by Sargsian [83] in the generalized eikonal approximation. The upper solid line is the result for a 100% polarized neutron at rest. The lower solid line includes a neutron polarization of 82%. The dashed line is the result of a PWIA calculation. The dotted line is the results of a DWIA calculation. The dash-dotted line is the result of the DWIA calcluation with charged exchange effects included.

where the definition of each of the efficiencies is given in Section 3.4.5. For the effective efficiency over a set of runs ϵ where run i has efficiency ϵ_i, event count N_i, and true number of events before dead time effects, N_i^t,

$$\begin{aligned} N_{\pm}^t &= \sum_i N_{i,\pm}^t = \frac{N_{\pm}}{\epsilon_{\pm}} = \sum_i \frac{N_{i,\pm}}{\epsilon_{i,\pm}} \\ \epsilon &= \left(\frac{1}{N} \sum_i \frac{N_i}{\epsilon_i} \right)^{-1}. \end{aligned} \tag{5.61}$$

So, $1/\epsilon$ is just the weighted average of all $1/\epsilon_i$ for all runs. The total false asymmetry for a run period, A_f, that must be subtracted we define as

$$A_f = A - A_t = \frac{N_+ - N_-}{N_+ + N_-} - \frac{N_+^t - N_-^t}{N_+^t + N_-^t} \tag{5.62}$$

where A is the measured asymmetry, A_t is the "true" asymmetry in the absence of these effects, N is the measured number in the asymmetry, N^t is the "true" number, where $\epsilon N^t = N$. For clarity, the total efficiency, ϵ is

$$\epsilon = \frac{\epsilon_+ N_+^t + \epsilon_- N_-^t}{N^t}. \tag{5.63}$$

The false asymmetry can then be written

$$A_f = \frac{(N_+ - \epsilon N_+^t) - (N_- - \epsilon N_-^t)}{N_+ + N_-} = \frac{N_+ \left(1 - \frac{\epsilon}{\epsilon_+}\right) - N_- \left(1 - \frac{\epsilon}{\epsilon_-}\right)}{N_+ + N_-}. \tag{5.64}$$

For kinematic 3 and 4 we find the false asymmetries to be $A_f = -0.0008$ and -0.0014, respectively. As will be shown in the next chapter, these quantities are small compared to the asymmetry uncertainty and are neglected.

5.9 Run Summation

For each kinematic point all the individual runs must be combined together to calculate G_E^n for the entire point. However, the factors for each run, such as the target polarization, are not fixed and may continually vary over time. Here we present the scheme used to take all the ^{3}He runs and produce a single corrected asymmetry, A_{phys}.

The asymmetry A_{phys} for an individual run, i, we will denote as $A_{\text{phys},i}$. For this analysis, we take the dilutions D_{N_2} and D_p to be constant for the experiment. This is acceptable since the relative amount of N_2 in the cell is constant over the kinematic, and the proton contribution should not vary significantly given various background rates, as shown in Section 5.7.4. Furthermore, as the luminosities do not generally change significantly over a kinematic, the background dilution and asymmetry contributions are taken to be constant.

Each individual run is taken as a measurement of A_{phys}. To combine the measurements, $A_{\text{phys},i}$, with statistical uncertainty, σ_i, into a single measurement, we weight by the inverse uncertainty squared

$$A_{\text{phys}} = \frac{\sum_i \frac{A_{\text{phys},i}}{\sigma_i^2}}{\sum_i \frac{1}{\sigma_i^2}}. \tag{5.65}$$

This produces a minimum χ^2 fit of the physical asymmetries. The statistical uncertainty for an asymmetry of N counts goes as $1/\sqrt{N}$, as will be shown in Section 6.1.1. In this case, $\sigma_i \approx \frac{1}{\sqrt{N}}$.

Substituting into Eq. 5.65

$$A_{\rm phys} = \frac{\sum_i N_i A_{{\rm phys},i}}{\sum_i N_i} \tag{5.66}$$

which is simply the average weighted by the counts.

5.10 Finite Acceptance

The asymmetry given by Eq. 3.7

$$\begin{aligned} A_{\rm phys} &= -\frac{2\sqrt{\tau(\tau+1)}\tan(\theta/2)\Lambda\hat{n}\cdot(\hat{q}\times\hat{T})}{\Lambda^2+(\tau+2\tau(1+\tau)\tan^2(\theta/2))} \\ &\quad -\frac{2\tau\sqrt{1+\tau+(1+\tau)^2\tan^2(\theta/2)}\tan(\theta/2)(\hat{q}\cdot\hat{T})}{\Lambda^2+(\tau+2\tau(1+\tau)\tan^2(\theta/2))} \\ &= \frac{\Delta(\theta,\phi)}{\Sigma(\theta,\phi)} \end{aligned} \tag{5.67}$$

assumes fixed values of $\vec{q}$, θ, $\hat{n}$, and $\hat{T}$. However, the acceptance of our detectors allows for a range of $\vec{q}$, $\hat{n}$, and θ. A scheme must be developed to accurately relate the asymmetry measured by the entire acceptance of the spectrometer to the averaged ratio of G_E^n/G_M^n. This acceptance may also have varying efficiencies over the acceptance which must be considered. For this analysis, we use a method formulated by G. B. Franklin [84].

Using Eq. 5.67, we can write the quasielastic neutron asymmetry, $A_{n,\rm meas}$, measured over the acceptance of the spectrometer as an integral over the acceptance Ω

$$A_{\rm n,meas} = \frac{N_n^+ - N_n^-}{N_n^+ + N_n^-} = PA_{\rm phys} = P\frac{\int d\Omega\Delta(\theta,\phi)\epsilon(\theta,\phi)}{\int d\Omega\Sigma(\theta,\phi)\epsilon(\theta,\phi)} \tag{5.68}$$

where $\epsilon(\theta,\phi)$ is the acceptance of a coincidence event with an electron in BigBite and neutron in the neutron arm. We take (θ,ϕ) to be the polar and azimuthal angle of the scattered electron with respect to the nominal beam direction, the LAB coordinate z axis. P is taken as the product of the three polarizations P_n, $P_{^3\rm He}$, and $P_{\rm beam}$.

The efficiency can be formulated by comparing the number of events in an acceptance bin dN to the number we would expect from the differential cross section, which is $\Sigma(\theta,\phi)$

$$\epsilon(\theta,\phi) = \frac{dN^+(\theta,\phi)+dN^-(\theta,\phi)}{\Sigma(\theta,\phi)}. \tag{5.69}$$

Inserting Eq. 5.69 into Eq. 5.68 we get

$$A_{\rm n,meas} = P\frac{\int d\Omega\frac{\Delta(\theta,\phi)}{\Sigma(\theta,\phi)}dN^+(\theta,\phi)+dN^-(\theta,\phi)}{\int d\Omega dN^+(\theta,\phi)+dN^-(\theta,\phi)} \tag{5.70}$$

$$= \frac{P}{N_n^+ + N_n^-}\sum_{\rm QE\ n\ events}\frac{\Delta(\theta,\phi)}{\Sigma(\theta,\phi)}. \tag{5.71}$$

The measured asymmetry $A_{n,\rm meas}$ is then just the average of the asymmetries in each bin weighted by the number of events in that bin. As a side note, we recognize that this form is independent of acceptance effects, which allows one to do this measurement without doing measurements of the absolute cross section. We next write Eqs. 5.67 in simplified terms

$$A_{\rm phys} = \frac{B\Lambda + C}{D+\Lambda^2} \tag{5.72}$$

where

$$B = -2\sqrt{\tau(1+\tau)}\tan(\theta/2)\hat{n}\cdot(\hat{q}\times\hat{T}) \quad (5.73)$$

$$C = -2\tau\sqrt{1+\tau+(1+\tau)^2\tan^2(\theta/2)}\tan(\theta/2)(\hat{q}\cdot\hat{T}) \quad (5.74)$$

$$D = \tau + 2\tau(1+\tau)\tan^2(\theta/2). \quad (5.75)$$

Expanding this in a Taylor series in Λ about $\Lambda = 0$

$$\begin{aligned} A_{\rm phys} &\approx (B\Lambda + C)(1/D - \Lambda^2/D^2 + \Lambda^4/D^2) \\ &= \frac{C}{D} + \frac{B}{D}\Lambda - \frac{C}{D^2}\Lambda^2 - \frac{B}{D^2}\Lambda^3 + \frac{C}{D^3}\Lambda^4 + \frac{B}{D^3}\Lambda^5 \\ &= T_0(\theta,\phi) + T_1(\theta,\phi)\Lambda + T_2(\theta,\phi)\Lambda^2 + T_3(\theta,\phi)\Lambda^3 + T_4(\theta,\phi)\Lambda^4 + T_5(\theta,\phi)\Lambda^5 \end{aligned} \quad (5.76)$$

where

$$T_0 = \frac{C}{D} \quad (5.77)$$

$$T_1 = \frac{B}{D} \quad (5.78)$$

$$T_2 = -\frac{C}{D^2} \quad (5.79)$$

$$T_3 = -\frac{B}{D^2} \quad (5.80)$$

$$T_4 = \frac{C}{D^3} \quad (5.81)$$

$$T_5 = \frac{B}{D^3}. \quad (5.82)$$

Eq. 5.71 tells us to simply take the average of the values for the quasielastic events to get the measured quantity. Taking this average of the T_i values to get $\overline{T_i}$, we arrive at

$$A_{\rm n,meas} = P[\overline{T_0} + \overline{T_1}\Lambda + \overline{T_2}\Lambda^2 + \overline{T_3}\Lambda^3 + \overline{T_4}\Lambda^4 + \overline{T_5}\Lambda^5] \quad (5.83)$$

To fifth order, Monte Carlo results show that this method is accurate to better than 1%.

There is now the question of what the average Q^2 is, given the range of Q^2 over the quasielastic events. To first order, expanding the ratio Λ in Q^2 about some fixed value, Q_n^2, we get

$$\Lambda(Q^2) = \Lambda(Q_n^2) + \alpha(Q^2 - Q_n^2) \quad (5.84)$$

where $\alpha = \frac{d\Lambda}{dQ^2}\big|_{Q^2=Q_n^2}$. Taking Eq. 5.76 just to first order and substituting Eq. 5.84 we get

$$\frac{\Delta}{\Sigma}(Q^2) = T_0(Q^2) + T_1(Q^2)(\Lambda(Q_n^2) + \alpha(Q^2 - Q_n^2)). \quad (5.85)$$

The value of the asymmetry at Q_n is

$$\frac{\Delta}{\Sigma}(Q_n^2) = T_0(Q_n^2) + T_1(Q_n^2)\Lambda(Q_n^2). \quad (5.86)$$

Subtracting Eq. 5.86 from Eq. 5.85 yields

$$\frac{\Delta}{\Sigma}(Q^2) - \frac{\Delta}{\Sigma}(Q_n^2) = T_0(Q^2) - T_0(Q_n^2) + (T_1(Q^2) - T_1(Q_n^2))\Lambda(Q_n^2) + \alpha T_1(Q^2)(Q^2 - Q_n^2). \quad (5.87)$$

Taking the average over the events and recognizing that we wish the average values of $\frac{A}{\Sigma}$, T_0, and T_1 to be identical with those evaluated at the mean value of Q^2, and setting that value to Q_n^2, we get

$$0 = \alpha\overline{T_1(Q^2)Q^2} - \alpha\overline{T_1(Q^2)}Q_n^2 \tag{5.88}$$

or

$$Q_n^2 = \frac{\overline{T_1 Q^2}}{\overline{T_1}}. \tag{5.89}$$

5.11 G_E^n

The calculation of G_E^n from the asymmetry using our finite acceptance model requires finding the root of a 5th order polynomial in Λ given by Eq. 5.76. To solve for this root we employ Newton's method, which utilizes an iterative process based on the derivatives of the function. The specific function we wish to find the root of is

$$f(\Lambda) = A_{\text{phys}} - (\overline{T}_0 + \overline{T}_1\Lambda + \overline{T}_2\Lambda^2 + \overline{T}_3\Lambda^3 + \overline{T}_4\Lambda^4 + \overline{T}_5\Lambda^5). \tag{5.90}$$

For each step, i

$$\Lambda_{i+1} = \Lambda_i - \frac{f(\Lambda_i)}{f'(\Lambda_i)}. \tag{5.91}$$

As an initial value, we use the solution to the expansion in first order

$$\Lambda_0 = \frac{A_{\text{phys}} - \overline{T}_0}{\overline{T}_1} \tag{5.92}$$

which is generally about 10% from the value of Λ for our settings.

While the process can continue indefinitely, we choose to end it when the difference between successive values of Λ is small. Using the dipole parametrization for G_M^n and the Galster parametrization (Section 2.3.5) for G_E^n at the highest Q^2 of 3.47 GeV^2, we obtain a value of $\Lambda \approx -0.15$. Given uncertainties on the order of 10% of Galster, choosing the convergence parameter to be 1×10^{-6} is more than sufficient to ensure an accurate result.

The values of G_M^n to extract G_E^n from Λ are taken from the analysis by Jeff Lachniet [35] and a linear interpolation is used to produce a smooth set of values.

Chapter 6

Results

In this chapter we present the results of our analysis over kinematics 3 and kinematics 4 for E02-013. We will show the various contributions of dilutions and additional asymmetries to the raw measured asymmetry and present their contributions to the uncertainties of our measurement. In particular, the target polarization, the contribution of final state interactions, and the proton contribution to the identified quasielastic neutral sample will have the largest contributions to our uncertainties. The results for our measurements of G_E^n for two of the kinematics will be shown.

6.1 Calculations and Error Propagation

In this section we will show explicitly the calculation of the various quantities necessary to obtain G_E^n as well as the uncertainty for each of those quantities and how it contributes to our uncertainty of G_E^n. In the calculation of uncertainty, we take the approach that the uncertainty for quantity y dependent on a set of (independent) quantities x_i with individual uncertainties δx_i is

$$(\delta y)^2 = \sum_i \left(\frac{\partial y}{\partial x_i} \delta x_i \right)^2 . \tag{6.1}$$

As this analysis is heavily dependent on counting the number of events, we are interested in the uncertainty of these counts. Provided that distribution of these counts form a Poisson distribution, as will be the case if the events occur randomly in time at some fixed mean rate, we expect a Poisson distribution of some mean $\overline{N}$ to have the variance, $\sigma^2 = \overline{N}$. Given this, we will take the uncertainty of a count to be $\delta N = \sqrt{N}$.

6.1.1 Raw Asymmetry

Raw asymmetries are calculated as per Eq. 5.17

$$A_{\text{raw}} = \frac{N^+ - N^-}{N^+ + N^-} \tag{6.2}$$

where N^h are number of identified neutral coincidence events from the data passing the quasielastic cuts with (HWP and target sign corrected) helicity state h. For this analysis, we use the cuts defined in Table 6.1. The uncertainty of this quantity is

$$\delta A_{\text{raw}} = \frac{2\sqrt{N^+ N^-}}{(N^+ + N^-)^{3/2}} \tag{6.3}$$

Cut	Kin. 3	Kin. 4
W	$0.7 < W < 1.05$GeV	$0.7 < W < 1.15$GeV
$p_{\mathrm{miss},\parallel}$	$\lvert p_{\mathrm{miss},\parallel}\rvert < 400$MeV	$\lvert p_{\mathrm{miss},\parallel}\rvert < 250$MeV
$p_{\mathrm{miss},\perp}$	$p_{\mathrm{miss},\perp} < 150$MeV	$p_{\mathrm{miss},\perp} < 150$MeV
m_{miss}	$m_{\mathrm{miss}} < 2.0$ GeV	$m_{\mathrm{miss}} < 2.0$ GeV

Table 6.1: Cuts used for the selection of quasielastic events.

and $N = N^+ + N^-$. We note at the limit where $N^\pm = \frac{N^\pm}{2} \pm \frac{d}{2}$, $N^+ - N^- = d \ll N$

$$\delta A_{\mathrm{raw}} = \frac{2\sqrt{\left(\frac{N}{2}+\frac{d}{2}\right)\left(\frac{N}{2}-\frac{d}{2}\right)}}{N^{3/2}} = \frac{2\sqrt{\frac{N^2}{4}-\frac{d^2}{4}}}{N^{3/2}} \approx \frac{1}{\sqrt{N}} - \frac{d^2}{N^{5/2}} \tag{6.4}$$

so the uncertainty on the asymmetry goes as $1/\sqrt{N}$ for small asymmetries.

6.1.2 Background

Flat background contributes to the raw asymmetry corrections in two forms, the dilution factor D_{back} and the asymmetry contribution $\frac{\Delta_{\mathrm{back}}}{\Sigma}$. D_{back}, expressed in Eq. 5.21 is

$$D_{\mathrm{back}} = 1 - \frac{\Sigma_{\mathrm{back}}}{\Sigma}. \tag{6.5}$$

As explained in Section 5.6, the total amount of uncharged background contributing, N_{back}, is reduced from the amount that would be naively deduced from the $\beta^{-1} < 1$ region. From the analysis in Section 5.6, we obtained a value with systematic uncertainty

$$\Sigma_{\mathrm{back}} = N^+_{\mathrm{back}} + N^-_{\mathrm{back}} = \frac{N_{\mathrm{back,un}}}{2} \pm \frac{N_{\mathrm{back,un}}}{\sqrt{12}}. \tag{6.6}$$

Combining with the statistical uncertainty of $\sqrt{\frac{N_{\mathrm{back,un}}}{2}}$

$$\delta\Sigma_{\mathrm{back}} = \left(\frac{N_{\mathrm{back,un}}}{2} + \frac{(N_{\mathrm{back,un}})^2}{12}\right)^{1/2}. \tag{6.7}$$

The uncertainty for the background dilution factor is

$$\delta D_{\mathrm{back}} = \left(\frac{\delta\Sigma^2_{\mathrm{back}}}{\Sigma^2} + \frac{\Sigma^2_{\mathrm{back}}(\delta\Sigma)^2}{\Sigma^4}\right)^{1/2} = \left(\frac{N_{\mathrm{back,un}}}{2\Sigma^2} + \frac{(N_{\mathrm{back,un}})^2}{12\Sigma^2} + \frac{(N_{\mathrm{back,un}})^2}{4\Sigma^3}\right)^{1/2}. \tag{6.8}$$

For the quantity $\frac{\Delta_{\mathrm{back}}}{\Sigma}$, which describes the asymmetry contribution of the background to the quasielastic neutral sample, using the notation of the previous chapter

$$\frac{\Delta_{\mathrm{back}}}{\Sigma} = \frac{N^+_{\mathrm{back}} - N^-_{\mathrm{back}}}{\Sigma}. \tag{6.9}$$

For the background asymmetry, there is a correlated systematic contribution. The uncertainty taking this into account is

$$\delta\left(\frac{\Delta_{\mathrm{back}}}{\Sigma}\right) = \left(\frac{N^-_{\mathrm{back,un}}}{2\Sigma^2} + \frac{(N^+_{\mathrm{back,un}} - N^-_{\mathrm{back,un}})^2}{12\Sigma^2} + \frac{N^+_{\mathrm{back,un}}}{2\Sigma^2} + \frac{(N^+_{\mathrm{back,un}} - N^-_{\mathrm{back,un}})^2}{4\Sigma^3}\right)^{1/2}. \tag{6.10}$$

The calculations and results for these two quantities for both kinematic 3 and 4 are presented in Table 6.2.

Param	Kin. 3		Kin. 4	
	+	-	+	-
N	7467	7858	73518	82543
$N_{\text{back,un}}$	107	121	5408	5521
D_{back}	0.993		0.965	
δD_{back}	0.004		0.020	
$\delta D_{\text{back}}/D_{\text{back}}$	0.004		0.021	
$\frac{\Delta_{\text{back}}}{\Sigma}$	-0.00046		-0.0004	
$\delta\left(\frac{\Delta_{\text{back}}}{\Sigma}\right)$	0.0007		0.0005	
$\delta\left(\frac{\Delta_{\text{back}}}{\Sigma}\right)/\frac{\Delta_{\text{back}}}{\Sigma}$	1.63		1.43	

Table 6.2: Calculation and results for the background dilution and asymmetry contribution and the associated uncertainties as presented in Section 6.1.2 for kinematics 3 and 4.

6.1.3 Nitrogen Dilution

The nitrogen dilution D_{N_2} is given by Eq. 5.34

$$D_{\text{N}_2} = 1 - \frac{\Sigma(\text{N}_2) - \Sigma_{\text{back}}(\text{N}_2)}{\Sigma - \Sigma_{\text{back}}} \frac{Q(^3\text{He})}{Q(\text{N}_2)} \frac{\rho_{\text{N}_2}(^3\text{He})}{\rho_{\text{N}_2}(\text{N}_2)} \tag{6.11}$$

where Σ_{back} is the uncharged accidental background to be subtracted from the signal, Σ, $Q(x)$ is the accumulated beam charge for the x target runs used for this calculation and $\rho_{\text{N}_2}(x)$ is the density of N_2 in target x. These are calculated from the runs used to obtain Σ, for both the N_2 and ^{3}He runs. The amount of background to subtract is handled in an identical way to all other background subtractions in this analysis.

The uncertainty is

$$\begin{aligned}
\delta D_{\text{N}_2} &= \left[\left(\frac{Q(^3\text{He})}{Q(\text{N}_2)} \frac{\rho_{\text{N}_2}(^3\text{He})}{\rho_{\text{N}_2}(\text{N}_2)} \right)^2 \left(\frac{\delta\Sigma(\text{N}_2)^2}{(\Sigma - \Sigma_{\text{back}})^2} + \frac{\delta\Sigma_{\text{back}}(\text{N}_2)^2}{(\Sigma - \Sigma_{\text{back}})^2} + \frac{(\Sigma(\text{N}_2) - \Sigma_{\text{back}}(\text{N}_2))^2}{(\Sigma - \Sigma_{\text{back}})^4} \left(\delta\Sigma^2 + \delta\Sigma^2_{\text{back}} \right) \right) \right. \\
&\quad \left. + \left(\frac{\delta\rho_{\text{N}_2}(^3\text{He})}{\rho_{\text{N}_2}(^3\text{He})} \right)^2 (1 - D_{\text{N}_2})^2 + \left(\frac{\delta\rho_{\text{N}_2}(\text{N}_2)}{\rho_{\text{N}_2}(\text{N}_2)} \right)^2 (1 - D_{\text{N}_2})^2 \right]^{1/2} \\
&= \left[\left(\frac{Q(^3\text{He})}{Q(\text{N}_2)} \frac{\rho_{\text{N}_2}(^3\text{He})}{\rho_{\text{N}_2}(\text{N}_2)} \frac{1}{\Sigma - \Sigma_{\text{back}}} \right)^2 \left(\Sigma(\text{N}_2) + \frac{N_{\text{back,un}}(\text{N}_2)}{2} + \frac{N^2_{\text{back,un}}(\text{N}_2)}{12} + \right. \right. \\
&\quad \left. \left. \frac{(\Sigma(\text{N}_2) - \Sigma_{\text{back}}(\text{N}_2))^2}{(\Sigma - \Sigma_{\text{back}})^2} \left(\Sigma + \frac{N_{\text{back,un}}}{2} + \frac{N^2_{\text{back,un}}}{12} \right) \right) + \left(\frac{\delta\rho_{\text{N}_2}(^3\text{He})}{\rho_{\text{N}_2}(^3\text{He})} \right)^2 (1 - D_{\text{N}_2})^2 \right. \\
&\quad \left. + \left(\frac{\delta\rho_{\text{N}_2}(\text{N}_2)}{\rho_{\text{N}_2}(\text{N}_2)} \right)^2 (1 - D_{\text{N}_2})^2 \right]^{1/2}.
\end{aligned} \tag{6.12}$$

The results for these calculations for kinematics 3 and 4 are given in Table 6.3.

To properly determine the proton dilution, an identical calculation must be performed for the dilution of charged particles. This formalism is analogous to that of the neutral particles and is also presented in Section 5.7.2. We defined the proton dilution from nitrogen to be

$$D^{\text{ch}}_{\text{N}_2} = 1 - \frac{\Sigma^{\text{ch}}_{\text{N}_2}}{\Sigma^{\text{ch}} - \Sigma^{\text{ch}}_{\text{back}}} \tag{6.13}$$

	Kin. 3	Kin. 4
$Q(^3\mathrm{He})$ (mC)	113.8	99.1
$Q(\mathrm{N_2})$ (mC)	31.7	4.1
$\rho_{\mathrm{N_2}}(^3\mathrm{He})$ (amg)	0.162	0.162
$\rho_{\mathrm{N_2}}(\mathrm{N_2})$ (amg)	4.41	10.09
Σ	369	13693
$N_{\mathrm{back,un}}$	2	689
$\Sigma(\mathrm{N_2})$	146	1979
$N_{\mathrm{back,un}}(\mathrm{N_2})$	14	46
$\delta(\rho_{\mathrm{N_2}}(^3\mathrm{He})/\rho_{\mathrm{N_2}}(^3\mathrm{He})$	0.007	0.007
$\delta(\rho_{\mathrm{N_2}}(\mathrm{N_2})/\rho_{\mathrm{N_2}}(\mathrm{N_2})$	0.007	0.007
$D_{\mathrm{N_2}}$	0.947	0.943
$\delta D_{\mathrm{N_2}}$	0.006	0.002
$\delta D_{\mathrm{N_2}}/D_{\mathrm{N_2}}$	0.006	0.002

Table 6.3: Results for the calculation of the N_2 dilution as described in Section 6.1.3. The units amg, or Amgats, is the ratio of density in the target over the target gas density at STP.

The factor needed to scale the number of N_2 events to obtain $\Sigma^{\mathrm{ch}}_{\mathrm{N_2}}$ is analogous to that for the neutral dilution. The dilution in terms of the counts obtained from the N_2 target is then

$$D^{\mathrm{ch}}_{\mathrm{N_2}} = 1 - \frac{\Sigma^{\mathrm{ch}}_{\mathrm{N_2}}}{\Sigma^{\mathrm{ch}} - \Sigma^{\mathrm{ch}}_{\mathrm{back}}}. \tag{6.14}$$

The background contribution to the charged signal is presented in Section 5.6. The amount of background to subtract from the charged signal is

$$\Sigma^{\mathrm{ch}}_{\mathrm{back}} = N_{\mathrm{back,ch}} + \frac{N_{\mathrm{back,un}}}{2}. \tag{6.15}$$

The uncertainty of the background taking into account statistical and systematic uncertainties is

$$\delta\Sigma^{\mathrm{ch}}_{\mathrm{back}} = \left(N_{\mathrm{back,ch}} + \frac{N_{\mathrm{back,un}}}{2} + \left(\frac{N_{\mathrm{back,un}}}{\sqrt{12}} \right)^2 \right)^{1/2}. \tag{6.16}$$

The uncertainty for the charged dilution is similar to that for the neutral dilution:

$$\begin{aligned}
\delta D^{\mathrm{ch}}_{\mathrm{N_2}} &= \left[\left(\frac{Q(^3\mathrm{He})}{Q(\mathrm{N_2})} \frac{\rho_{\mathrm{N_2}}(^3\mathrm{He})}{\rho_{\mathrm{N_2}}(\mathrm{N_2})} \right)^2 \left(\frac{\delta\Sigma^{\mathrm{ch}}(\mathrm{N_2})^2}{(\Sigma^{\mathrm{ch}} - \Sigma^{\mathrm{ch}}_{\mathrm{back}})^2} + \frac{\delta\Sigma^{\mathrm{ch}}_{\mathrm{back}}(\mathrm{N_2})^2}{(\Sigma^{\mathrm{ch}} - \Sigma^{\mathrm{ch}}_{\mathrm{back}})^2} \right.\right. \\
&+ \left.\left. \frac{(\Sigma^{\mathrm{ch}}(\mathrm{N_2}) - \Sigma^{\mathrm{ch}}_{\mathrm{back}}(\mathrm{N_2}))^2}{(\Sigma^{\mathrm{ch}} - \Sigma^{\mathrm{ch}}_{\mathrm{back}})^4} \left(\delta(\Sigma^{\mathrm{ch}})^2 + \delta(\Sigma^{\mathrm{ch}}_{\mathrm{back}})^2 \right) \right) + \left(\frac{\delta\rho_{\mathrm{N_2}}(^3\mathrm{He})}{\rho_{\mathrm{N_2}}(^3\mathrm{He})} \right)^2 (D^{\mathrm{ch}}_{\mathrm{N_2}})^2 + \left(\frac{\delta\rho_{\mathrm{N_2}}(\mathrm{N_2})}{\rho_{\mathrm{N_2}}(\mathrm{N_2}}) \right)^2 (1 - D^{\mathrm{ch}}_{\mathrm{N_2}})^2 \right]^{1/2} \\
&= \left[\left(\frac{Q(^3\mathrm{He})}{Q(\mathrm{N_2})} \frac{\rho_{\mathrm{N_2}}(^3\mathrm{He})}{\rho_{\mathrm{N_2}}(\mathrm{N_2})} \frac{1}{\Sigma^{\mathrm{ch}} - \Sigma^{\mathrm{ch}}_{\mathrm{back}}} \right)^2 \left(\Sigma^{\mathrm{ch}}(\mathrm{N_2}) + N_{\mathrm{back,ch}}(\mathrm{N_2}) + \frac{N_{\mathrm{back,un}}(\mathrm{N_2})}{2} \right.\right. \\
&+ \frac{N^2_{\mathrm{back,un}}(\mathrm{N_2})}{12} + \left.\left. \frac{(\Sigma^{\mathrm{ch}}(\mathrm{N_2}) - \Sigma^{\mathrm{ch}}_{\mathrm{back}}(\mathrm{N_2}))^2}{(\Sigma^{\mathrm{ch}} - \Sigma^{\mathrm{ch}}_{\mathrm{back}})^2} \left(\Sigma^{\mathrm{ch}} + N_{\mathrm{back,ch}} + \frac{N_{\mathrm{back,un}}}{2} + \frac{N^2_{\mathrm{back,un}}}{12} \right) \right) \right. \\
&+ \left. \left(\frac{\delta\rho_{\mathrm{N_2}}(^3\mathrm{He})}{\rho_{\mathrm{N_2}}(^3\mathrm{He})} \right)^2 (1 - D^{\mathrm{ch}}_{\mathrm{N_2}})^2 + \left(\frac{\delta\rho_{\mathrm{N_2}}(\mathrm{N_2})}{\rho_{\mathrm{N_2}}(\mathrm{N_2})} \right)^2 (1 - D^{\mathrm{ch}}_{\mathrm{N_2}})^2 \right]^{1/2}.
\end{aligned} \tag{6.17}$$

	Kin. 3	Kin. 4
$Q(^3\mathrm{He})$ (μC)	113.8	99.1
$Q(\mathrm{N_2})$ (μC)	31.7	4.1
$\rho_{\mathrm{N_2}}(^3\mathrm{He})$ (amg)	0.162	0.162
$\rho_{\mathrm{N_2}}(\mathrm{N_2})$ (amg)	4.41	10.09
Σ^{ch}	3649	107978
$N_{\mathrm{back,un}}$	2	689
$N_{\mathrm{back,ch}}$	2	55
$\Sigma^{\mathrm{ch}}(\mathrm{N_2})$	1015	8659
$N_{\mathrm{back,un}}(\mathrm{N_2})$	14	46
$N_{\mathrm{back,ch}}(\mathrm{N_2})$	6	3
$\delta(\rho_{\mathrm{N_2}}(^3\mathrm{He})/\rho_{\mathrm{N_2}}(^3\mathrm{He})$	0.007	0.007
$\delta(\rho_{\mathrm{N_2}}(\mathrm{N_2})/\rho_{\mathrm{N_2}}(\mathrm{N_2})$	0.007	0.007
$D^{\mathrm{ch}}_{\mathrm{N_2}}$	0.964	0.969
$\delta D^{\mathrm{ch}}_{\mathrm{N_2}}$	0.001	0.0005
$\delta D^{\mathrm{ch}}_{\mathrm{N_2}}/D^{\mathrm{ch}}_{\mathrm{N_2}}$	0.001	0.010

Table 6.4: Results for the calculation of the N_2 dilution in the charged quasielastic sample as described in Section 6.1.3.

6.1.4 Proton Dilution

The method to evaluate the proton dilution is presented in Section 5.7.4. The basic premise is to take the (background corrected, N_2 corrected) uncharged-to-charged ratios for various targets at various veto rates, fit the ratios and determine their values at a fixed veto rate, and then use these to constrain the various proton/neutron mixing parameters to determine the number of protons contaminating the neutral sample. There may be some uncertainty in the ratio of uncharged-to-charged in the target due to pion contamination, but we make the assumption that it is heavily suppressed due to our W and m_{miss} cuts.

To obtain the uncharged-to-charged ratios to use in our fit, $R = \frac{\Sigma_n+\Sigma_p}{\Sigma^{\mathrm{ch}}_p+\Sigma^{\mathrm{ch}}_n}$, we must first correct for the amount of background in the charged and uncharged sample for each of the three targets. Neglecting other contributions, we found

$$\Sigma^{\mathrm{ch}}_p + \Sigma^{\mathrm{ch}}_n = \Sigma^{\mathrm{ch}} - \Sigma^{\mathrm{ch}}_{\mathrm{back}} = \Sigma^{\mathrm{ch}} - N_{\mathrm{back,ch}} - \frac{N_{\mathrm{back,un}}}{2} \tag{6.18}$$

$$\Sigma_n + \Sigma_p = \Sigma - \Sigma_{\mathrm{back}} = \Sigma - \frac{N_{\mathrm{back,un}}}{2}. \tag{6.19}$$

In determining the uncertainty for the ratio, R, we must take care because the systematic uncertainties for Σ^{ch} and Σ are correlated. This is easily observed by the fact that the more uncharged background that is misidentified, the more background that is included into the charged signal. We can evaluate this by including a number that is misidentified deviating from the mean N_{mis} in the calculation of the uncertainties

$$R = \frac{\Sigma - \frac{N_{\mathrm{back,un}}}{2} - N_{\mathrm{mis}}}{\Sigma^{\mathrm{ch}} - N_{\mathrm{back,ch}} - \frac{N_{\mathrm{back,un}}}{2} + N_{\mathrm{mis}}}. \tag{6.20}$$

This yields the uncertainty

$$\begin{aligned}\delta R^2 &= \left(\frac{\delta\Sigma}{\Sigma^{\rm ch} - N_{\rm back,ch} - \frac{N_{\rm back,un}}{2} + N_{\rm mis}}\right)^2 + \frac{1}{(\Sigma^{\rm ch} - N_{\rm back,ch} - \frac{N_{\rm back,un}}{2} + N_{\rm mis})^4} \\ &\times\left[\delta N^2_{\rm back,un}\left(\frac{1}{2}(\Sigma - \Sigma^{\rm ch} - N_{\rm back,ch}) - N_{\rm mis}\right)^2 + \delta N^2_{\rm mis}\left(\Sigma^{\rm ch} + \Sigma - N_{\rm back,ch} - N_{\rm back,un}\right)^2\right. \\ &\left.+((\delta\Sigma^{\rm ch})^2 + \delta N^2_{\rm back,ch})\left(\Sigma - \frac{N_{\rm back,un}}{2} - N_{\rm mis}\right)^2\right]. \end{aligned} \tag{6.21}$$

$N_{\rm mis}$ takes an average value of 0, but the uncertainty is given by the systematic uncertainty of the background, $\frac{N_{\rm back,ch}}{\sqrt{12}}$. Also, since we've separated the systematic uncertainty from the background, their uncertainties are purely statistical

$$\delta N_{\rm back,ch} = \sqrt{N_{\rm back,ch}} \tag{6.22}$$

$$\delta N_{\rm back,un} = \sqrt{N_{\rm back,un}}. \tag{6.23}$$

This leaves us with the expression

$$\begin{aligned}\delta R &= \left(\frac{\Sigma}{(\Sigma^{\rm ch} - N_{\rm back,ch} - \frac{N_{\rm back,un}}{2})^2} + \frac{1}{(\Sigma^{\rm ch} - N_{\rm back,ch} - \frac{N_{\rm back,un}}{2})^4}\right. \\ &\times\left[N_{\rm back,un}\left(\frac{1}{2}(\Sigma - \Sigma^{\rm ch} - N_{\rm back,ch})\right)^2 + \left(\frac{N_{\rm back,un}}{\sqrt{12}}\right)^2\left(\Sigma^{\rm ch} + \Sigma - N_{\rm back,ch} - N_{\rm back,un}\right)^2\right. \\ &\left.\left.+(\Sigma^{\rm ch} + N_{\rm back,ch})\left(\Sigma - \frac{N_{\rm back,un}}{2}\right)^2\right]\right)^{1/2}. \end{aligned} \tag{6.24}$$

However, this is only valid for the N_2 and H_2 runs. In the case of ^{3}He, there is an additional contribution due to the N_2 in the cell. To correct for this, an additional factor of $\frac{D_{N_2}}{D^{\rm ch}_{N_2}}$ must be included as well. R is then

$$R_{^3{\rm He}} = \frac{D_{N_2}}{D^{\rm ch}_{N_2}}\frac{\Sigma - \frac{N_{\rm back,un}}{2}}{\Sigma^{\rm ch} - N_{\rm back,ch} - \frac{N_{\rm back,un}}{2}} \tag{6.25}$$

and the uncertainty is

$$\begin{aligned}\delta R_{^3{\rm He}} &= \frac{D_{N_2}}{D^{\rm ch}_{N_2}}\left(\frac{\Sigma}{(\Sigma^{\rm ch} - N_{\rm back,ch} - \frac{N_{\rm back,un}}{2})^2} + \frac{1}{(\Sigma^{\rm ch} - N_{\rm back,ch} - \frac{N_{\rm back,un}}{2})^4}\right. \\ &\times\left[N_{\rm back,un}\left(\frac{1}{2}(\Sigma - \Sigma^{\rm ch} - N_{\rm back,ch})\right)^2 + \left(\frac{N_{\rm back,un}}{\sqrt{12}}\right)^2\left(\Sigma^{\rm ch} + \Sigma - N_{\rm back,ch} - N_{\rm back,un}\right)^2\right. \\ &\left.+(\Sigma^{\rm ch} + N_{\rm back,ch})\left(\Sigma - \frac{N_{\rm back,un}}{2}\right)^2\right] \\ &+\left(\frac{\Sigma - \frac{N_{\rm back,un}}{2}}{\Sigma^{\rm ch} - N_{\rm back,ch} - \frac{N_{\rm back,un}}{2}}\right)^2\left(\left[\frac{\delta D_{N_2}}{D_{N_2}}\right]^2 + \left[\frac{\delta D^{\rm ch}_{N_2}}{D^{\rm ch}_{N_2}}\right]^2\right)\Bigg)^{1/2}. \end{aligned} \tag{6.26}$$

These ratios are then given to a program using the Minuit fitter developed at CERN [85] to extrapolate the measurement to zero veto rate. This fitter allows us to not only find the results of

Ratio	Kin. 3			Kin. 4		
Veto 1 Rate (kHz)	540			220		
Veto 2 Rate (kHz)	400			160		
k	0.2			0.2		
$R_{^3\mathrm{He}}$	0.092	$\pm$	0.002	0.121	$\pm$	0.001
R_{H_2}	0.016	$\pm$	0.002	0.032	$\pm$	0.001
R_{N_2}	0.123	$\pm$	0.028	0.214	$\pm$	0.007

Table 6.5: Results for the calculation of the uncharged-to-charged ratios of three target types evaluated at nominal veto rates as presented in Section 6.1.4.

a minimum χ^2 fit, but also obtain the uncertainties for our fits. Once these fits are done, we can then extrapolate the effective uncharged-to-charged ratio for any given veto rate. The uncharged-to-charged ratios for each of our three targets at nominal veto rates representative of the ^{3}He runs are given in Table 6.5. Plots of these fits are shown in Figs. 6.1 and 6.2.

A set of equations relating the target ratios to ratios of the mixing coefficients is given by Eqs. 5.47 to 5.49. These represent the rate a particle of one type, denoted as a subscript, is detected as the type denoted in the superscript in parenthesis (for example, $\eta_p^{(n)}$ are protons detected as neutrons)

$$\frac{\eta_p^{(n)}}{\eta_p^{(p)}} = R_{\mathrm{H}_2} \tag{6.27}$$

$$\frac{\eta_n^{(p)}}{\eta_p^{(p)}} = \frac{\sigma_p}{\sigma_n}\left(\frac{R_{^3\mathrm{He}} f - R_{\mathrm{N}_2} + R_{\mathrm{H}_2}(1-f)}{R_{\mathrm{N}_2} - R_{^3\mathrm{He}}}\right) \tag{6.28}$$

$$\frac{\eta_n^{(n)}}{\eta_p^{(p)}} = \frac{\sigma_p}{\sigma_n}\left(f R_{\mathrm{N}_2}\left(\frac{R_{^3\mathrm{He}} - R_{\mathrm{H}_2}}{R_{\mathrm{N}_2} - R_{^3\mathrm{He}}}\right) - R_{\mathrm{H}_2}\right). \tag{6.29}$$

The uncertainties for these ratios are

$$\delta\left(\frac{\eta_p^{(n)}}{\eta_p^{(p)}}\right) = \delta R_{\mathrm{H}_2} \tag{6.30}$$

$$\delta\left(\frac{\eta_n^{(p)}}{\eta_p^{(p)}}\right) = \frac{\sigma_p}{\sigma_n}\left(\left[\delta R_{^3\mathrm{He}}\frac{(1-f)(R_{\mathrm{H}_2}-R_{\mathrm{N}_2})}{(R_{\mathrm{N}_2}-R_{^3\mathrm{He}})^2}\right]^2 + \left[\delta R_{\mathrm{H}_2}\frac{1-f}{R_{\mathrm{N}_2}-R_{^3\mathrm{He}}}\right]^2 + \left[\delta R_{\mathrm{N}_2}\frac{(1-f)(R_{^3\mathrm{He}}-R_{\mathrm{H}_2})}{(R_{\mathrm{N}_2}-R_{^3\mathrm{He}})^2}\right]^2 + \left[\delta f\frac{R_{^3\mathrm{He}}-R_{\mathrm{H}_2}}{R_{\mathrm{N}_2}-R_{^3\mathrm{He}}}\right]^2\right)^{1/2} \tag{6.31}$$

$$\delta\left(\frac{\eta_n^{(n)}}{\eta_p^{(p)}}\right) = \frac{\sigma_p}{\sigma_n}\left(\left[\delta R_{\mathrm{N}_2}\frac{f R_{^3\mathrm{He}}(R_{\mathrm{H}_2}-R_{^3\mathrm{He}})}{(R_{\mathrm{N}_2}-R_{^3\mathrm{He}})^2}\right]^2 + \left[\delta R_{\mathrm{H}_2}\frac{(f+1)R_{\mathrm{N}_2}-R_{^3\mathrm{He}}}{R_{^3\mathrm{He}}-R_{\mathrm{N}_2}}\right]^2 + \left[\delta R_{^3\mathrm{He}}\frac{f R_{\mathrm{N}_2}(R_{\mathrm{N}_2}-R_{\mathrm{H}_2})}{(R_{\mathrm{N}_2}-R_{^3\mathrm{He}})^2}\right]^2 + \left[\delta f\frac{R_{\mathrm{H}_2}(R_{^3\mathrm{He}}-R_{\mathrm{H}_2})}{R_{\mathrm{N}_2}-R_{^3\mathrm{He}}}\right]^2\right)^{1/2}. \tag{6.32}$$

A table of these ratios and uncertainties for kinematics 3 and 4 is presented in Table 6.6. The ratio of the neutron cross section to proton cross section is determined by using a parametrization of the proton form factors based on the world data for a central Q^2 for each kinematic [36]. Finally,

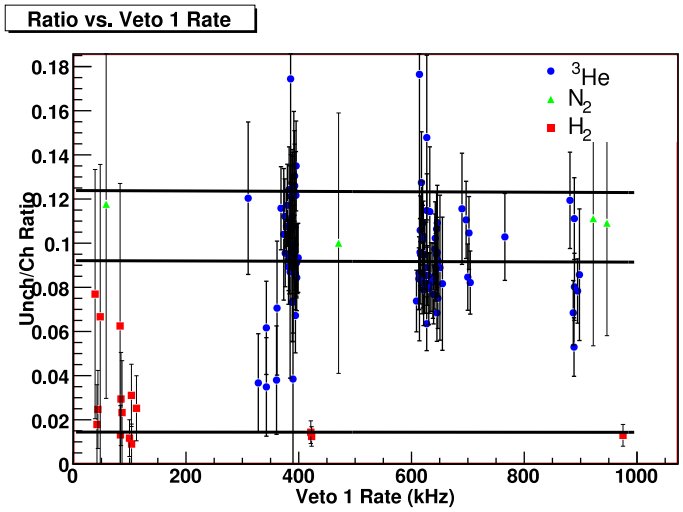

Figure 6.1: Fit of the three target uncharged-to-charged ratios for kinematic 3.

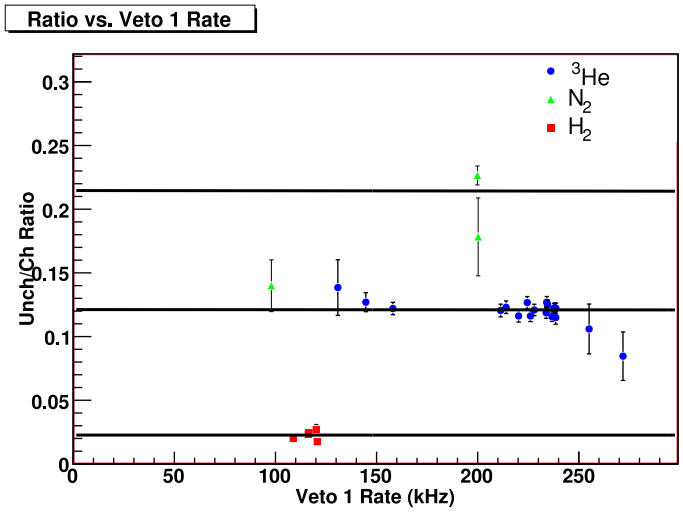

Figure 6.2: Fit of the three target uncharged-to-charged ratios for kinematic 4.

	Kin. 3			Kin. 4		
f	2.14	$\pm$	0.0	2.15	$\pm$	0.0
Q^2 (GeV^2)	3.47			1.72		
σ_n/σ_p	0.445			0.410		
$\eta_p^{(n)}/\eta_p^{(p)}$	0.016	$\pm$	0.002	0.032	$\pm$	0.001
$\eta_n^{(p)}/\eta_p^{(p)}$	Undetermined			0.236	$\pm$	0.210
$\eta_n^{(n)}/\eta_p^{(p)}$	0.72	$\pm$	0.95	0.496	$\pm$	0.045
$\eta_p^{(n)}/\eta_n^{(n)}$	0.022	$\pm$	0.029	0.064	$\pm$	0.006

Table 6.6: Results for the calculation of the three proton/neutron mixing coefficients as presented in Section 6.1.4.

	Kin. 3			Kin. 4		
D_p	0.905	$\pm$	0.063	0.747	$\pm$	0.017
$\delta D_p/D_p$	0.069			0.022		
$D_n^{\rm ch}$	0.552	$\pm$	0.349	0.956	$\pm$	0.036
$\delta D_n^{\rm ch}/D_n^{\rm ch}$	0.633			0.038		

Table 6.7: Results for proton dilution in the neutral sample and neutron dilution in the proton sample as presented in Section 6.1.4.

these mixing coefficients are related to the dilution factors D_p and $D_n^{\rm ch}$ by Eqs. 5.42 and 5.43

$$D_p = \frac{\frac{\sigma_n}{\sigma_p}\left(\eta_n^{(n)}/\eta_p^{(p)}\right)}{\frac{\sigma_n}{\sigma_p}\left(\eta_n^{(n)}/\eta_p^{(p)}\right) + f\left(\eta_p^{(n)}/\eta_p^{(p)}\right)} = \frac{1}{1 + f\frac{\sigma_p}{\sigma_n}\left(\eta_p^{(n)}/\eta_n^{(n)}\right)} \tag{6.33}$$

$$D_n^{\rm ch} = \frac{f}{\frac{\sigma_n}{\sigma_p}\eta_n^{(p)}/\eta_p^{(p)} + f}. \tag{6.34}$$

The uncertainties of these two equations are

$$\begin{aligned}\delta D_p = & \left[\left(\frac{f R_{\rm H_2}(R_{^3{\rm He}} - R_{\rm N_2})\delta R_{\rm H_2}}{R_{^3{\rm H3}}(R_{\rm N_2} - R_{\rm H_2})^2(f-1)}\right)^2 + \left(\frac{f R_{\rm N_2} R_{\rm H_2}\delta R_{^3{\rm He}}}{(f-1)R_{^3{\rm He}}^2(R_{\rm N_2} - R_{\rm H_2})}\right)^2\right. \\ & \left. + \left(\frac{f R_{\rm H_2}(R_{\rm H_2} - R_{^3{\rm He}})\delta R_{\rm N_2}}{(f-1)R_{^3{\rm He}}(R_{\rm N_2} - R_{\rm H_2})^2}\right)^2 + \left(\frac{R_{\rm H_2}(R_{\rm N_2} - R_{^3{\rm He}})\delta f}{(f-1)^2 R_{^3{\rm He}}(R_{\rm N_2} - R_{\rm H_2})}\right)^2\right]^{1/2}\end{aligned} \tag{6.35}$$

$$\begin{aligned}\delta D_n^{\rm ch} = & \left[\left(\frac{f(R_{\rm H_2} - R_{^3{\rm He}})\delta R_{\rm H_2}}{(f-1)(R_{\rm N_2} - R_{\rm H_2})^2}\right)^2 + \left(\frac{f\delta R_{^3{\rm He}}}{(f-1)(R_{\rm H_2} - R_{\rm N_2})}\right)^2\right. \\ & \left. + \left(\frac{f(R_{^3{\rm He}} - R_{\rm H_2})\delta R_{\rm N_2}}{(f-1)(R_{\rm N_2} - R_{\rm H_2})^2}\right)^2 + \left(\frac{(R_{^3{\rm He}} - R_{\rm N_2})\delta f}{(f-1)^2(R_{\rm N_2} - R_{\rm H_2})}\right)^2\right]^{1/2}.\end{aligned} \tag{6.36}$$

The results for this calculation for kinematics 3 and 4 are given in Table 6.7.

The proton asymmetry contribution is defined in Eq. 5.59

$$\frac{\Delta_p}{\Sigma} = \frac{1 - D_p}{D_{\rm back} D_{\rm N_2}} P_{^3{\rm He}} P_p P_{\rm beam} \sum_n T_n \Lambda^n(Q^2) \tag{6.37}$$

Param	Kin. 3			Kin. 4		
P_p	-0.028	$\pm$	0.004	-0.028	$\pm$	0.004
G_E^p	0.018	$\pm$	0.004	0.077	$\pm$	0.007
G_M^p	0.089	$\pm$	0.004	0.262	$\pm$	0.006
$\frac{\Delta_p}{\Sigma}$	-0.00017	$\pm$	0.00004	-0.00055	$\pm$	0.00010
$\delta\frac{\Delta_p}{\Sigma}/\frac{\Delta_p}{\Sigma}$	0.23			0.19		

Table 6.8: Values used to obtain the proton asymmetry contribution to the quasielastic neutral sample. Proton form factor numbers are calculated from the Kelly parametrization [36].

The uncertainty for this quantity is

$$\begin{aligned}\delta\left(\frac{\Delta_p}{\Sigma}\right) &= \left(\frac{\Delta_p}{\Sigma}\right)^2\left[\left[\frac{\delta D_p}{D_p}\right]^2+\left[\frac{\delta D_{\rm back}}{D_{\rm back}}\right]^2+\left[\frac{\delta D_{\rm N_2}}{D_{\rm N_2}}\right]^2+\left[\frac{\delta P_{^3{\rm He}}}{P_{^3{\rm He}}}\right]^2+\left[\frac{\delta P_p}{P_p}\right]^2+\left[\frac{\delta P_{\rm beam}}{P_{\rm beam}}\right]^2\right.\\ &\left.+\left[\frac{\sum_{n=1}^5 \overline{T}_n\left(\frac{G_E^p}{G_M^p}\right)^{n-1}}{\sum_{n=0}^5 \overline{T}_n\left(\frac{G_E^p}{G_M^p}\right)^{n}}\right]^2\left(\frac{G_E^p}{G_M^p}\right)^2\left(\left[\frac{\delta G_E^p}{G_E^p}\right]^2+\left[\frac{\delta G_M^p}{G_M^p}\right]^2\right)\right]^{1/2}. \qquad (6.38)\end{aligned}$$

To evaluate this we simply use an average target polarization, as it may vary over individual runs. The parameters used in this calculation are presented in Tables 6.8, 6.9, and 6.11.

6.1.5 $A_{\rm phys}$

The calculation of $A_{\rm phys}$ from experimental values is given in Eq. 5.27

$$A_{\rm phys} = \frac{A_{\rm raw} - \frac{\Delta_{\rm back}}{\Sigma} - \frac{\Delta_p}{\Sigma} - \frac{\Delta_{\rm other}}{\Sigma}}{P_{^3{\rm He}}P_{\rm n}P_{\rm beam}D_{\rm back}D_{\rm N_2}D_pD_{\rm FSI}} \qquad (6.39)$$

Since various quantities may vary over the course of each kinematic, each parameter is taken to be constant only over individual runs. This produces a set of measurements of $A_{\rm phys}$ which must then be combined together, as presented in Section 5.9. For each individual run, the uncertainty is

$$\begin{aligned}\delta A_{{\rm phys},i} &= \left(\frac{\delta A_{\rm raw}^2+\delta\left(\frac{\Delta_p}{\Sigma}\right)^2}{(P_{^3{\rm He}}P_{\rm n}P_{\rm beam}D_{\rm back}D_{\rm N_2}D_pD_{\rm FSI})^2}+A_{{\rm phys},i}^2\left(\left[\frac{\delta P_{^3{\rm He}}}{P_{^3{\rm He}}}\right]^2+\left[\frac{\delta P_{\rm n}}{P_{\rm n}}\right]^2\left[\frac{\delta P_{\rm beam}}{P_{\rm beam}}\right]^2\right.\right.\\ &\left.\left.+\left[\frac{\delta D_{\rm N_2}}{D_{\rm N_2}}\right]^2+\left[\frac{\delta D_p}{D_p}\right]^2+\left[\frac{\delta D_{\rm FSI}}{D_{\rm FSI}}\right]^2\right)+(\delta_{\rm back})^2\right)^{1/2}. \qquad (6.40)\end{aligned}$$

The uncertainty for the background, $\delta_{\rm back}$, has been reduced in terms of the independent counts of $N_{\rm back}^+$ and $N_{\rm back}^-$ to take into account the correlated uncertainties and takes the form

$$\begin{aligned}\delta_{\rm back} &= \left[\left(\frac{A_{\rm phys}}{D_{\rm back}}-\frac{1}{P_{^3{\rm He}}P_{\rm n}P_{\rm beam}D_{\rm back}D_{\rm N_2}D_pD_{\rm FSI}}\right)^2\left(\frac{\delta N_{\rm back}^+}{2\Sigma}\right)^2\right.\\ &+\left(\frac{A_{\rm phys}}{D_{\rm back}}+\frac{1}{P_{^3{\rm He}}P_{\rm n}P_{\rm beam}D_{\rm back}D_{\rm N_2}D_pD_{\rm FSI}}\right)^2\left(\frac{\delta N_{\rm back}^-}{2\Sigma}\right)^2.\\ &\left.+\left(\left(\frac{A_{\rm phys}(1-D_{\rm back})}{D_{\rm back}}-\frac{\Delta_{\rm back}}{\Sigma}\frac{1}{P_{^3{\rm He}}P_{\rm n}P_{\rm beam}D_{\rm back}D_{\rm N_2}D_pD_{\rm FSI}}\right)\frac{1}{\sqrt{12}}\right)^2\right]^{1/2} \qquad (6.41)\end{aligned}$$

Param	Kin. 3			Kin. 4		
$\overline{P}_{\rm nucl}$	0.478	$\pm$	0.020	0.485	$\pm$	0.020
$P_{\rm n}$	0.86	$\pm$	0.02	0.86	$\pm$	0.02
$P_{\rm beam}$	0.835	$\pm$	0.011	0.835	$\pm$	0.011
$D_{\rm back}$	0.993	$\pm$	0.004	0.965	$\pm$	0.020
$D_{\rm N_2}$	0.947	$\pm$	0.012	0.943	$\pm$	0.002
D_p	0.905	$\pm$	0.063	0.747	$\pm$	0.017
$D_{\rm FSI}$	0.95	$\pm$	0.05	0.95	$\pm$	0.05
$\frac{\Delta_{\rm back}}{\Sigma}$	-0.00046	$\pm$	0.0008	-0.0004	$\pm$	0.0005
$\frac{\Delta_p}{\Sigma}$	-0.00017	$\pm$	0.00004	-0.00050	$\pm$	0.00010

Table 6.9: Parameters used in the calculation of $A_{\rm phys}$ as presented in Section 6.1.5.

Param	Kin. 3	Kin. 4
$N_{\rm QE}$	15325	156061
$A_{\rm raw}$	-0.026	-0.058
$\delta A_{\rm raw}$	0.008	0.003
$\delta A_{\rm raw}/A_{\rm raw}$	0.311	0.044
$A_{\rm phys}$	-0.117	-0.256
$\sigma_{\rm sys}$	0.012	0.020
$\sigma_{\rm sys}/A_{\rm phys}$	0.104	0.077
$\sigma_{\rm stat}$	0.036	0.011
$\sigma_{\rm stat}/A_{\rm phys}$	0.311	0.044

Table 6.10: Calculation of $A_{\rm phys}$ and statistical and systematic uncertainties as presented in Section 6.1.5.

The statistical uncertainty is contained in $A_{\rm raw}$, so the statistical contribution in $A_{{\rm phys},i}$

$$\sigma_{\rm stat} = \frac{\delta A_{\rm raw}}{P_{^3{\rm He}} P_{\rm n} P_{\rm beam} D_{\rm back} D_{\rm N_2} D_p D_{\rm FSI}}. \tag{6.42}$$

The remaining systematic uncertainty is

$$\begin{aligned}\sigma_{\rm sys} \;=\; & \left(\frac{\delta\left(\frac{\Delta_p}{\Sigma}\right)^2}{(P_{^3{\rm He}} P_{\rm n} P_{\rm beam} D_{\rm back} D_{\rm N_2} D_p D_{\rm FSI})^2} + A_{{\rm phys},i}^2 \left(\left[\frac{\delta P_{^3{\rm He}}}{P_{^3{\rm He}}}\right]^2 + \left[\frac{\delta P_{\rm n}}{P_{\rm n}}\right]^2 \left[\frac{\delta P_{\rm beam}}{P_{\rm beam}}\right]^2 \right.\right. \\ & \left.\left. + \left[\frac{\delta D_{\rm back}}{D_{\rm back}}\right]^2 + \left[\frac{\delta D_{\rm N_2}}{D_{\rm N_2}}\right]^2 + \left[\frac{\delta D_p}{D_p}\right]^2 + \left[\frac{\delta D_{\rm FSI}}{D_{\rm FSI}}\right]^2 \right) + (\delta_{\rm back})^2 \right)^{1/2}. \end{aligned} \tag{6.43}$$

There are two parameters in the systematic uncertainty that vary over the runs, the target polarization $P_{^3{\rm He}}$ and the physical asymmetry $A_{\rm phys}$. For this analysis we simply take the average of the beam polarizations and the uncertainty weighted average of $A_{\rm phys}$. Values for dilutions, polarizations, and asymmetry contributions are found in Table 6.9. The systematic uncertainty and the final values of $A_{\rm phys}$ for kinematics 3 and 4 is presented in Table 6.10.

Param	Kin. 3	Kin. 4
$\overline{T}_0$	0.034	-0.063
$\overline{T}_1$	0.721	1.002
$\overline{T}_2$	-0.019	0.086
$\overline{T}_3$	-0.432	-1.348
$\overline{T}_4$	0.011	-0.118
$\overline{T}_5$	0.262	1.843
Q^2 (GeV^2)	3.47	1.72
Λ	-0.213	-0.206
$\delta\Lambda$	0.057	0.028
$\delta\Lambda/\Lambda$	0.268	0.14

Table 6.11: Parameters used in the calculation of G_n^E from A_{phys} as presented in Section 6.2.

Param	Kin. 3					Kin. 4				
Λ	-0.213	$\pm$	0.057			-0.206	$\pm$	0.028		
G_M^n	-0.055	$\pm$	0.001			-0.166	$\pm$	0.003		
Q^2 (GeV^2)	3.47					1.72				
G_E^n	0.0117	$\pm_{\text{stat}}$	0.0030	$\pm_{\text{sys}}$	0.0010	0.0342	$\pm_{\text{stat}}$	0.0023	$\pm_{\text{sys}}$	0.0040

Table 6.12: Calculated value of G_E^n. For G_E^n the first uncertainty is statistical while the second is systematic.

6.2 Results

With A_{phys} calculated, the remaining pieces involve evaluating the finite acceptance parameters as described in Section 5.10 and then solving for G_E^n. This is given by Eq. 5.76

$$A_{\text{phys}} = \overline{T}_0 + \overline{T}_1\Lambda + \overline{T}_2\Lambda^2 + \overline{T}_3\Lambda^3 + \overline{T}_4\Lambda^4 + \overline{T}_5\Lambda^5. \tag{6.44}$$

To evaluate the uncertainty, we first relate the uncertainty of Λ in terms of A_{phys}. We get

$$\delta\Lambda = \frac{\delta A_{\text{phys}}}{\left|\sum_{i=n}^{5} n\overline{T}_n\Lambda^{n-1}\right|}. \tag{6.45}$$

The values for $\overline{T}_n$, Q^2, and Λ are given in Table 6.11.

The uncertainty for $G_E^n = G_M^n\Lambda$ is then

$$\delta G_E^n = \left([\delta G_M^n\Lambda]^2 + [G_M^n\delta\Lambda]^2\right)^{1/2}. \tag{6.46}$$

The values for the final calculation of G_E^n can be found in Table 6.12. A breakdown of the various systematic contributions can be found in Table 6.13. The value for G_M^n was produced from data from a recent analysis from CLAS by Jeff Lachniet [35] (shown in Fig. 2.4. A plot of the world data for G_E^n with the results of this experiment are shown in Fig. 6.3.

The uncertainty for kinematic 3 is dominated by statistical uncertainty, while the uncertainty for kinematic 4 is mostly systematic. In both cases major contributions to the systematic uncertainty are from the target polarization and nuclear effects based on a Glauber calculation. In kinematic 3, the uncertainty in the proton dilution also contributes a significant amount.

	Kin. 3 (δ/G_E^n)	Kin. 4 (δ/G_E^n)
δG_E^n	0.268	0.135
$\delta_{\rm sys}$	0.087	0.118
$\delta_{\rm stat}$	0.253	0.067
$\delta D_{\rm FSI}$	0.043	0.080
$\delta P_{^3{\rm He}}$	0.035	0.063
δD_p	0.057	0.035
δP_n	0.019	0.035
δG_M^n	0.019	0.017
$\delta P_{\rm beam}$	0.011	0.020
$\delta_{\rm back}$	0.017	0.018
$\delta D_{\rm N2}$	0.010	0.003
$\delta \frac{\Delta_p}{\Sigma}$	0.001	0.003

Table 6.13: Contributions to the systematic uncertainty of G_E^n as a fraction of G_E^n.

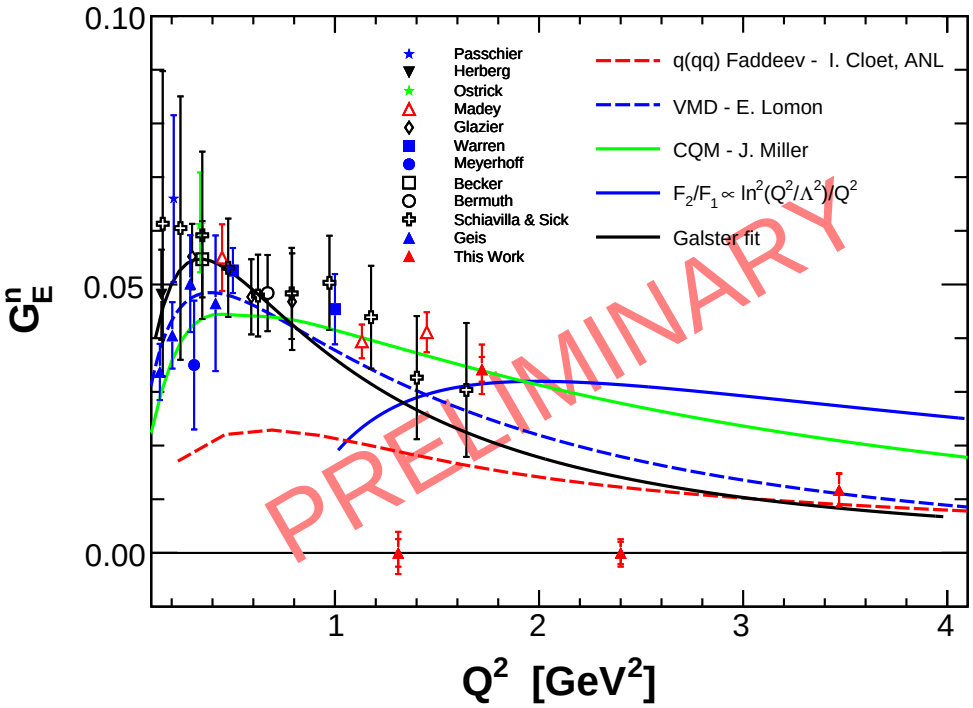

Figure 6.3: G_E^n from this work with selected world data. Inner error bars for our points are statistical uncertainty only. Miller q-only represents his calculation in the absence of the pion cloud. The curve for F_2/F_1 pQCD behavior has been scaled to match our kinematic 4 point.

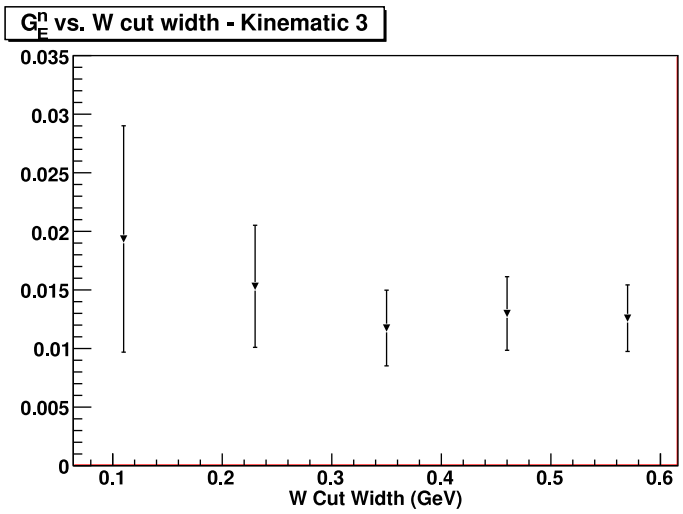

Figure 6.4: G_E^n as the W cut is varied for kinematic 3. Each cut is centered around the value of $W = 0.925$ GeV. Nominal value is 0.35 GeV.

6.3 Sensitivity to Cuts

A repetition of this analysis was done varying the quasielastic cuts to observe the sensitivity of G_E^n on these values. For each cut on W, $p_{\mathrm{miss},\parallel}$, and $p_{\mathrm{miss},\perp}$, the width of the cut was varied while the remaining two cuts were kept constant. This allows us to systematically examine the effect that each cut has upon our final result and provides a direct method to examine how the value is sensitive to effects we attempted to minimize. For example, as the cuts are widened, it is expected that pion electroproduction will provide a greater contribution to the quasielastic neutral sample.

For kinematic 3, shown in Figs. 6.4 to 6.6, wider cuts in W and $p_{\mathrm{miss},\perp}$ both produce slightly higher values of G_E^n. This effect is likely due to the larger contributions of pion electroproduction into the sample. A similar but weaker effect is seen as as $p_{\mathrm{miss},\parallel}$ is widened. Since the cut in m_{miss} explicitly cuts out higher values of $p_{\mathrm{miss},\parallel}$, the new contributions as the cut is widened are events with lower $p_{\mathrm{miss},\parallel}$, which are less likely to be associated with inelastic events. This explains why G_E^n is roughly stable as cuts are widened. Tighter cuts predictably produce larger error bars and values are within agreement with our final values.

For kinematic 4, shown in Figs. 6.7 to 6.9, pion electroproduction should play a much weaker role, so wider cuts were generally produced more stable results than seen in kinematic 3. Reducing statistics produces slightly different values for G_E^n, but the error bars do not increase substantially as the uncertainty of this point is dominated by systematic uncertainties.

Overall, the data for both points appears to behave as expected as cuts are varied. The cuts chosen to produce G_E^n should then provide a clean sample of quasielastic events while maximizing

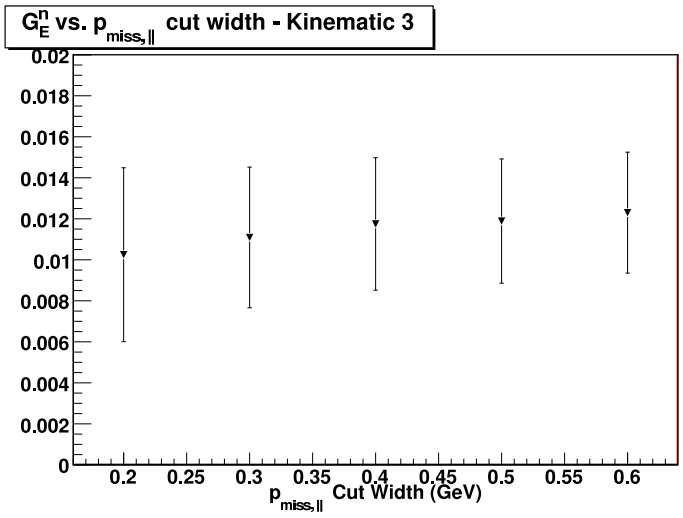

Figure 6.5: G_E^n as the $p_{\mathrm{miss},\parallel}$ cut is varied for kinematic 3. Each cut is centered around the value of $p_{\mathrm{miss},\parallel} = 0$. Nominal value is 0.40 GeV/c.

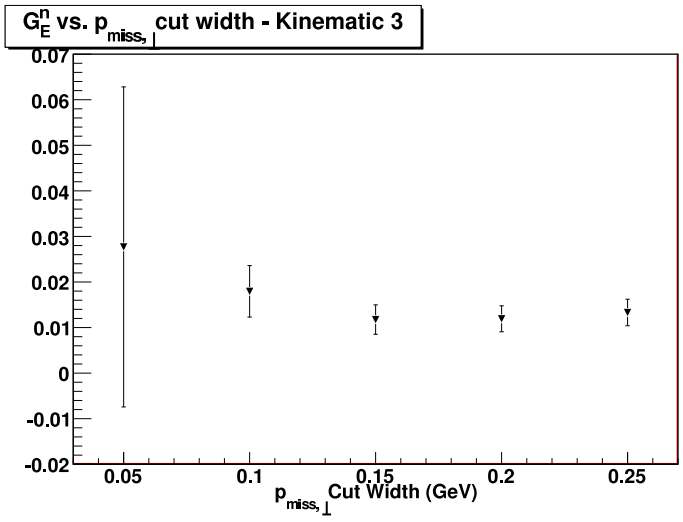

Figure 6.6: G_E^n as the $p_{\mathrm{miss},\perp}$ cut is varied for kinematic 3. Each cut has a lower bound of $p_{\mathrm{miss},\perp} = 0$. Nominal value is 0.15 GeV/c.

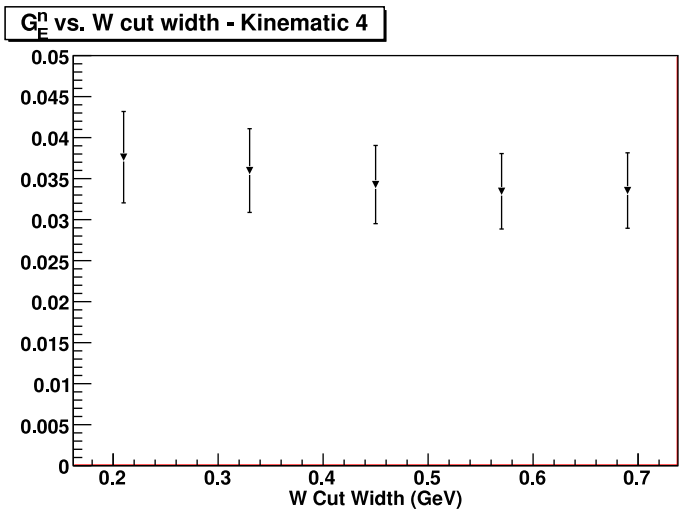

Figure 6.7: G_E^n as the W cut is varied for kinematic 4. Each cut is centered around the value of $W = 0.925$ GeV. Nominal value is 0.45 GeV.

available statistics.

6.4 Conclusions and Future

The electric form factor of the neutron,G_E^n, was measured at $Q^2 = 1.7$ and 3.4 GeV^2. This was done by measuring the quasielastic helicity dependent cross section asymmetry through the reaction $^3\overrightarrow{He}(\vec{e}, e'n)pp$. The polarized ^{3}He nucleus acts as an effective neutron source and was polarized using spin exchange optical pumping. The degree of polarization was monitored using EPR and NMR techniques. A newly developed set of detectors were constructed and calibrated to detect the scattered electron and recoiling nucleon. For the electron arm, the BigBite spectrometer provided a momentum resolution $\delta p/p = 1\%$ utilizing a 1.0 T $\cdot$ m field integral magnet and set of multiple wire drift chambers providing high-resolution hit based tracking. The hadron arm was constructed using a multi-layered wall of scintillator matching BigBite's acceptance. This arm measured the momentum of the nucleon through time of flight and performed charge identification on the nucleon to differentiate between protons and neutrons.

The result for $Q^2 = 1.7$ GeV^2, or kinematic 4, is in line with the CQM model from Miller, which also agrees with the previous data points above 1 GeV^2. This point also appears to be in rough agreement with other data at lower Q^2 and with the Schiavilla and Sick analysis.

For $Q^2 = 3.5$ GeV, or kinematic 3, we are in agreement with Lomon's VMD parametrization and the Galster fit. The CQM model by Miller seems to over predict the value for our point despite

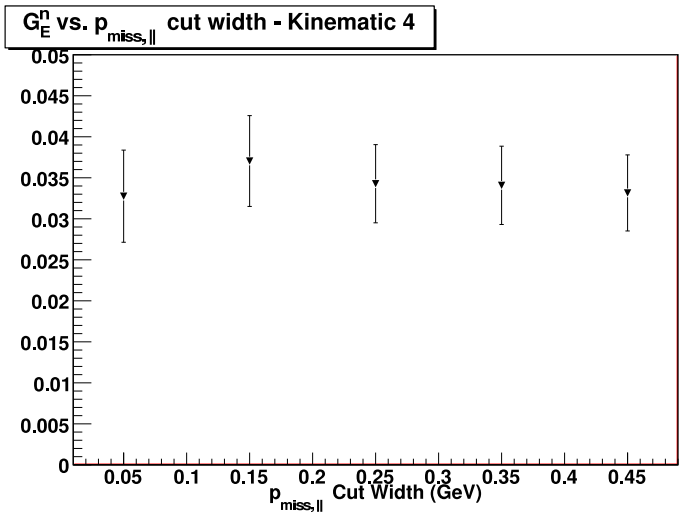

Figure 6.8: G_E^n as the $p_{\mathrm{miss},\parallel}$ cut is varied for kinematic 4. Each cut is centered around the value of $p_{\mathrm{miss},\parallel} = 0$. Nominal value is 0.25 GeV/c.

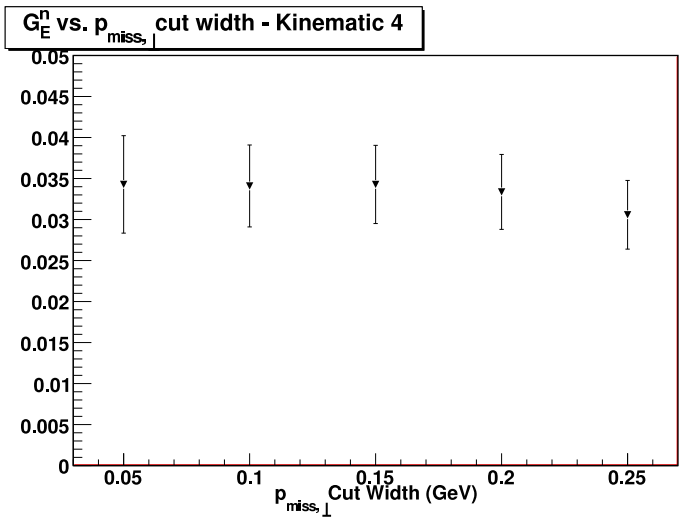

Figure 6.9: G_E^n as the $p_{\mathrm{miss},\perp}$ cut is varied for kinematic 4. Each cut has a lower bound of $p_{\mathrm{miss},\perp} = 0$. Nominal value is 0.15 GeV.

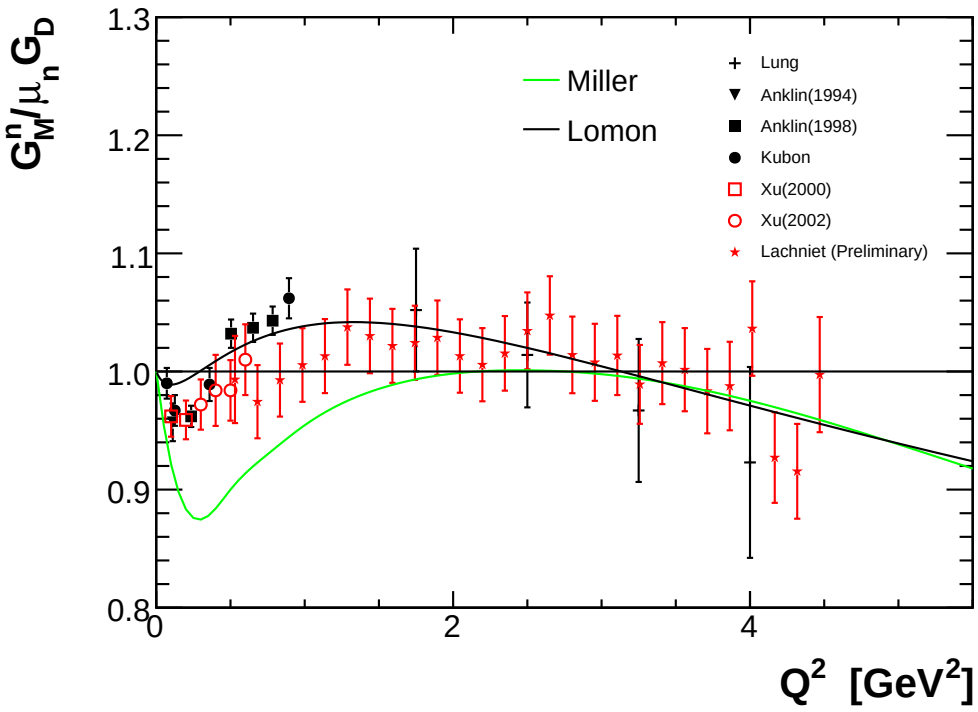

Figure 6.10: $G_M^n/(\mu_n G_D)$ with selected world data.

success at lower values of Q^2. Setting the pQCD prediction for F_2/F_1 to our kinematic 4 point, we do not attain agreement with our kinematic 3 point, suggesting unsurprisingly that we are not yet in the region where pQCD applies.

Both Galster and the VMD seem to continue to have the greatest accuracy in modeling G_E^n for a wide range of the measured Q^2. It is interesting to note that Miller overpredicts the value of G_E^n for higher Q^2 while it has general success with the three other form factors, Figs. 6.10 to 6.12.

Outlook and Further Work

Improvements to this analysis can be made in the future as further efforts are made. As mentioned before, calculations describing the final state interactions are forthcoming, which will improve the accuracy of the correction made for charge exchange. This represents one of the larger contributions to our systematic uncertainty. Currently, work on the BigBite tracking code utilizing a more sophisticated drift chamber hit pattern matching technique is being developed which may yield an increase in statistics (possibly as high as 50%), which would improve the uncertainty on kinematic 3.

For E02-013, there still remain two other data points to be analyzed by other students within the collaboration for the experiment. Their efforts and analysis will also yield independent verification of this work before final publication.

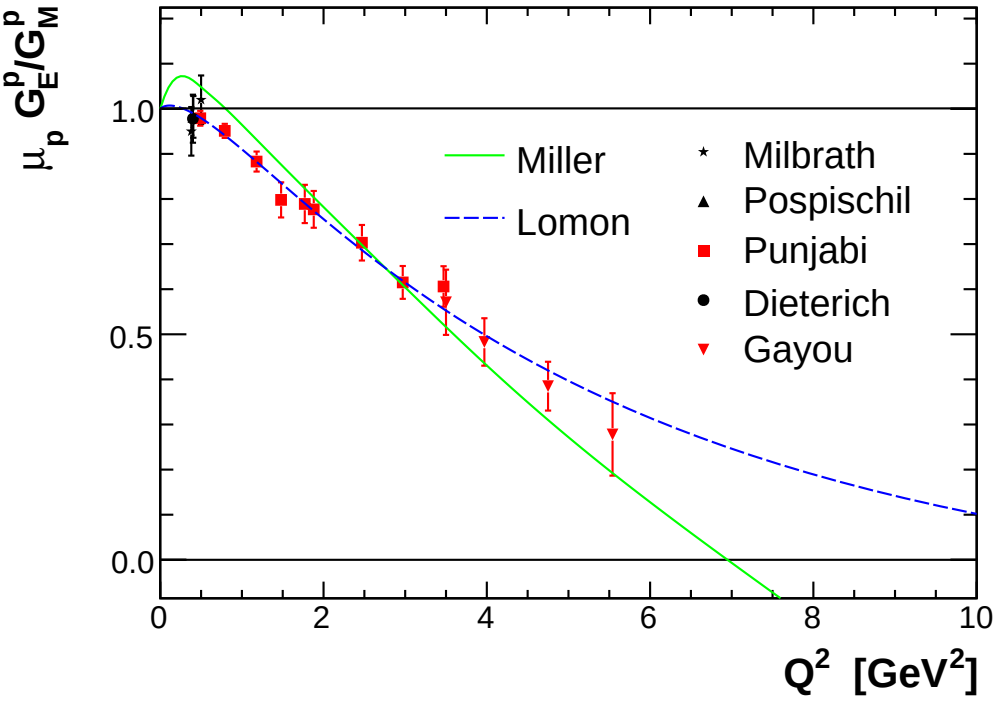

Figure 6.11: $\mu_p G_E^p/G_M^p$ with selected world data.

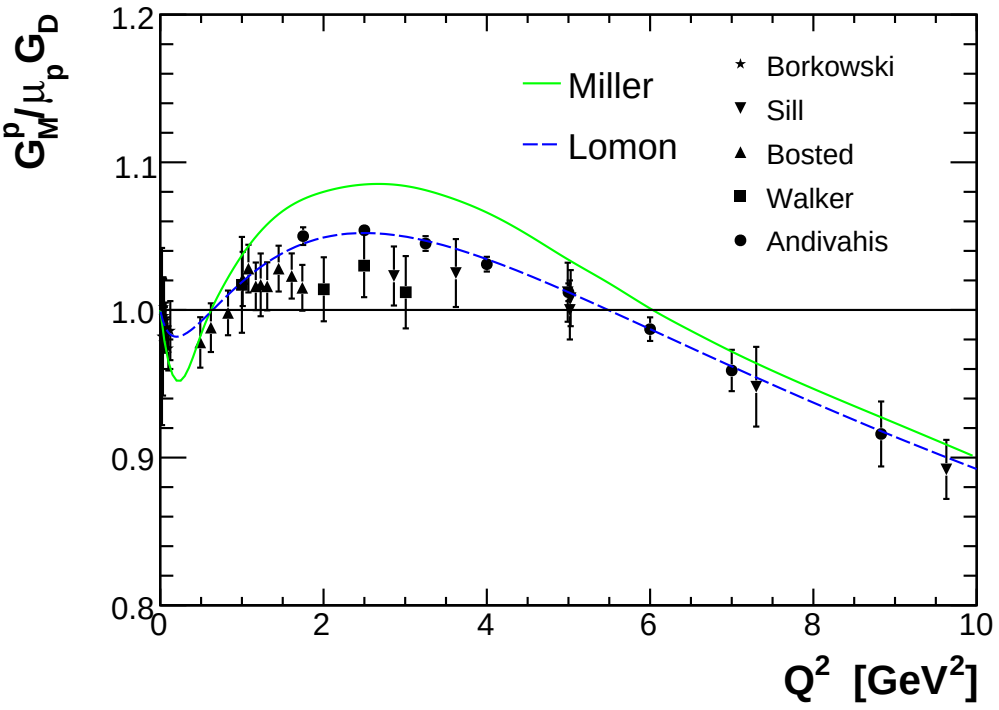

Figure 6.12: $\mu_p G_M^p/(\mu_p G_D)$ with selected world data.

Appendix A

Survey Reports

Jefferson Lab Alignment Group

Data Transmittal

TO: E. Chudakov, B. Wojtsekhowski, E. Folts, J. LeRose		**DATE:** 08 Feb 2006
FROM: Kelly Tremblay	**Checked:**	**# :** A1039r

DETAILS: Data: m:\algin\data\step2b\halla\bigbite\060207a

The Hall A Gen 2 experiment Big Bite magnet and detector assemblies were surveyed February 7th, 2006. The assembly was located at the ideal angle of 56.5° clockwise looking downstream from the standard Hall A target. The magnet origin is located 1.1 meters from the hall target and is the front face of the steel core. The origin for the detector is the front face of the assembly. The coordinate system shown is in millimeters with the hall A target center being the origin, +z being the downstream along the main beamline, +x being transverse beam left and +y being up. The angular results are in degrees, with the +yaw being clockwise about the y axis, +pitch is positive counter clockwise about the x axis and +roll is clockwise about the z axis.

	Ideal			Found			Deltas bfs		
	Z	X	Y	z	x	y	dz	dx	dy
Magnet	607.1	-917.3	0.0	594.5	-913.5	-0.3	-10.1	-8.4	-0.3
Detector	1252.8	-1892.8	151.6	1255.6	-1872.6	164.8	-15.3	13.5	13.2

	Ideal Angles			Found Angles			Delta Angles		
	Yaw	Pitch	Roll	Yaw	Pitch	Roll	dYaw	dPitch	dRoll
Magnet	56.50	0.00	0.00	56.26	-0.35	0.06	-0.24	-0.35	0.06
Detector	56.50	10.00	0.00	56.21	10.05	-0.09	-0.29	0.05	-0.09

Jefferson Lab Alignment Group

Data Transmittal

TO: Eugene Chudakov, Bogdan Wojtsekhowski, John LeRose		**DATE:** 22 Feb 2006
FROM: Chris Curtis	**Checked:**	**# :** A1041

DETAILS: Data: m:\algin\data\step2b\halla\bigbite\060214a

Given below are the results of the Big Bite detector survey carried out on February 14th, 2006. The center of each of the three chambers is shown, together with the four corners of each detector plane. This information is derived from the as found location survey of the external fiducials (Feb 14th), and the fiducialization survey carried out after the planes were shimmed on December 22nd. Some distortion of the external fiducials was apparent between these two surveys. The coordinates are in millimeters, with the Hall A target as origin, +z being downstream along the main beamline, +x being transverse beam left, and +y being up with respect to gravity (not pitched).

	Z	X	Y
Ch1 Center	1256.2	-1872.4	167.1
Ch1 Bot L	1682.0	-1776.7	-717.4
Ch1 Top L	1506.5	-1516.4	1052.2
Ch1 Bot R	1005.9	-2228.4	-718.0
Ch1 Top R	830.5	-1968.1	1051.5
Ch2 Center	1453.4	-2167.2	221.3
Ch2 Bot L	1989.4	-2063.2	-970.0
Ch2 Top L	1756.6	-1710.7	1411.8
Ch2 Bot R	1150.4	-2623.7	-969.1
Ch2 Top R	917.3	-2271.4	1412.6
Ch3 Center	1640.2	-2450.9	289.5
Ch3 Bot L	2174.7	-2348.2	-902.9
Ch3 Top L	1945.5	-1993.1	1479.3
Ch3 Bot R	1334.8	-2908.9	-900.9
Ch3 Top R	1105.8	-2553.5	1482.3

Jefferson Lab Alignment Group

Data Transmittal

TO: Eugene Chudakov, Bogdan Wojtsekhowski, John LeRose		**DATE:** 07 Jul 2006
FROM: James Dahlberg	**Checked:**	**# :** A1067

DETAILS: Data: m:\algin\data\step2b\halla\gen\060516a

Note: The previous data transmittal #A1061 was incorrectly referenced to the May 10th survey and is actually for the May 16th survey. A revised DT for #A1061 will be published.

Given below are the results of the Big Bite detector survey carried out on May 10th, 2006. The center of each of the three chambers is shown, together with the four corners of each detector plane. This information is derived from the as found location survey of the external fiducials (May 10th), and the fiducialization survey carried out after the detector was shifted from the running position on May 16th. The coordinates are in millimeters, with the Hall A target as origin, +z being downstream along the main beam line, +x being transverse beam left, and +y being up with respect to gravity (not pitched).

	Z	X	Y
Ch1 center	1405.89	-1760.85	168.66
Ch1 topbr	988.98	-1890.52	1053.03
Ch1 topbl	1626.12	-1385.20	1053.73
Ch1 botbr	1185.66	-2136.42	-716.39
Ch1 botbl	1822.82	-1631.27	-715.75
Ch2 center	1626.60	-2038.74	222.40
Ch2 topbr	1100.28	-2185.05	1413.64
Ch2 topbl	1891.38	-1558.27	1412.66
Ch2 botbr	1361.80	-2519.17	-967.79
Ch2 botbl	2152.94	-1892.49	-968.91
Ch3 center	1836.25	-2306.59	290.00
Ch3 topbr	1312.07	-2451.56	1483.09
Ch3 topbl	2103.32	-1825.05	1479.51
Ch3 botbr	1569.20	-2788.47	-899.66
Ch3 botbl	2360.41	-2161.27	-902.95

Appendix B

Reconstruction Matrix

A 15×4 matrix used to reconstruct a track in the BigBite drift chambers for the configuration used in E02-013. It was designed to produce four track parameters for a given set of hits such that the χ^2 is minimized.

The plane names are used to represent the position they measure. For example u_1 is the position measured by plane u_1.

$$\begin{pmatrix} x \\ x' \\ y \\ y' \end{pmatrix} = \begin{pmatrix} 0.1579 & 0.1563 & 0.0684 & -0.026085 & -0.024515 \\ -0.24855 & -0.2441 & 0.0016925 & 0.24905 & 0.24495 \\ 0.4632 & 0.45855 & 0.2025 & 0.0753 & 0.07085 \\ -0.7265 & -0.7135 & -0.006545 & -0.724 & -0.7125 \end{pmatrix} \begin{pmatrix} u_1/\sigma_{u_1} \\ u_2/\sigma_{u_2} \\ u_3/\sigma_{u_3} \\ u_4/\sigma_{u_4} \\ u_5/\sigma_{u_5} \end{pmatrix}$$

$$+ \begin{pmatrix} 0.1862 & 0.18335 & 0.08145 & -0.02688 & -0.022805 \\ -0.28625 & -0.27855 & -0.003614 & 0.28855 & 0.2776 \\ -0.01393 & -0.01376 & -0.006905 & -0.00172 & -0.001882 \\ 0.017775 & 0.017795 & 0.01851 & 0.02516 & 0.024905 \end{pmatrix} \begin{pmatrix} x_1/\sigma_{x_1} \\ x_2/\sigma_{x_2} \\ x_3/\sigma_{x_3} \\ x_4/\sigma_{x_4} \\ x_5/\sigma_{x_5} \end{pmatrix}$$

$$+ \begin{pmatrix} 0.1636 & 0.1619 & 0.0699 & -0.01875 & -0.01729 \\ -0.2451 & -0.2407 & -0.001144 & 0.2453 & 0.2412 \\ -0.4659 & -0.46105 & -0.1975 & -0.05355 & -0.04924 \\ 0.6995 & 0.687 & -0.006685 & 0.7005 & 0.689 \end{pmatrix} \begin{pmatrix} v_1/\sigma_{v_1} \\ v_2/\sigma_{v_2} \\ v_3/\sigma_{v_3} \\ v_4/\sigma_{v_4} \\ v_5/\sigma_{v_5} \end{pmatrix}$$

Bibliography

[1] J. Ashman et al. *Nucl. Phys.*, B 328:1, 1989.

[2] F. Halzen and D. Martin. *Quarks & Leptons: An Introductory Course in Modern Particle Physics*. John Wiley and Sons, Inc., 1984.

[3] R. G. Sachs. *Phys. Rev.*, 126:2256, 1962.

[4] L. N. Hand, D.G. Miller, and R. Wilson. *Rev. Mod. Phys.*, 35:335, 1963.

[5] C.F. Perdrisat, V. Punjabi, and M. Vanderhaeghen. *Progress in Particle and Nuclear Physics*, 59:694–764, 2007.

[6] M. Gourdin. *Nuovo Cimento*, 33:533, 1963.

[7] S. Galster, J. Moritz H. Klien, K. H. Schmidt, D. Wegener, and J. Bleckwenn. *Nucl. Phys.*, B 32:221 – 237, 1971.

[8] Akhiser, Rozentsveig, and Shmushkevich. *Sov. Phys. JTEP*, 6:588, 1958.

[9] A. I. Akhieser and M. P. Rekalo. *Sov. Phys. Dokl.*, 13:572, 1968.

[10] A. I. Akhieser and M. P. Rekalo. *Sov. J. Part. Nucl.*, 4:277, 1974.

[11] R. G. Arnold, C. E. Carlson, and F. Gross. *Phys. Rev.*, C 23:363, 1981.

[12] T. Eden et al. *Phys. Rev.*, C 50:1749, 1994.

[13] C. Herberg et al. *Eur. Phys. J*, A 5:131, 1999.

[14] M. Ostrick et al. *Phys. Rev. Lett.*, 83:276, 1999.

[15] D. Glazier et al. *Eur. Phys. J*, A 24:101, 2005.

[16] R. Madey et al. *Phys. Rev. Lett.*, 91:122022, 2003.

[17] I. Passchier et al. *Phys. Rev. Lett.*, 82:4988, 1999.

[18] G. Warren et al. *Phys. Rev. Lett.*, 92:042301, 2004.

[19] N. Dombey. *Rev. Mod. Phys.*, 41:236, 1969.

[20] B. Blankleider and R.M. Woloshyn. *Phys. Rev.*, C 29:538, 1984.

[21] M. Meyerhoff et al. *Phys. Lett. B*, 327:201, 1994.

[22] J. Becker et al. *Eur. Phys. J.*, A 6:329, 1999.

[23] J. Golak et al. *Phys. Rev.*, C 63:034006, 2001.

[24] J. Bermuth et al. *Phys. Lett.*, B 564:199, 2003.

[25] E02-013 Collaboration et al. Measurement of the neutron electric form factor g_e^n at high q^2. December 2001. `http://hallaweb.jlab.org/experiment/E02-013/GEN_files/prop_GEN.pdf`.

[26] R. Schiavilla and I. Sick. *Phys. Rev.*, C 64:041002, 2001.

[27] O. Gayou et al. *Phys. Rev. Lett.*, 88:092301, 2002.

[28] A. V. Belitsky, Xiandong Ji, and Feng Yuan. *Phys. Rev. Lett.*, 91:092003, 2003.

[29] F. Iachello, A. D. Jackson, and A. Lande. *Phys. Lett.*, 43 B:191 – 196, 1973.

[30] M. F. Gari and W. Krümpelmann. *Phys. Lett.*, B 274:159 – 162, 1992.

[31] E. Lomon. *Phys. Rev.*, C 66:045501, 2002.

[32] R. Bijker and F. Iachello. *Phys. Rev.*, C 69:068201, 2004.

[33] Hyde-Wright and de Jager. *Annu. Rev. Nucl. Part. Sci*, 54:217–267, 2004.

[34] G. Miller. *Phys. Rev.*, C 66:032201, 2002.

[35] J. Lachniet. *A high precision measurement of the neutron magnetic form factor using the CLAS detector*. PhD thesis, Carnegie Mellon University, 2005.

[36] J. J. Kelly. *Phys. Rev.*, C 70:068202, 2004.

[37] T.W. Donnelly and A. S. Raskin. Considerations of polarization in inclusive electron scattering from nuclei. *Ann. Phys.*, 169:247–351, 1986.

[38] L.D Faddeev. *Mathematical Aspects of the Three-Body Problem*. Daniel Davey and Co., Inc., New York, 1965.

[39] J. L. Friar et al. *Phys. Rev.*, C 42:2310, 1991.

[40] C. Ciofi degli Atti and S. Scopetta. *Phys. Lett.*, B 404:223, 1997.

[41] R. M. Woloshyn. *Nucl. Phys.*, A 496:749, 1989.

[42] C. Ciofi degli Atti, S. Scopetta, E. Pace, and G. Salme. *Phys. Rev*, C 48:968, 1993.

[43] R.W Schulze and P.U. Sauer. *Phys. Rev*, C 56:2293, 1997.

[44] F. Bissey, A.W. Thomas, and I.R. Afnan. *Phys. Rev*, C 64:024004, 2001.

[45] C. Leemann, D. Douglas, and G. Krafft. *Ann. Rev. of Nucl. and Part. Sci.*, 51:413–450, 2001.

[46] Hall A Collaboration. *Nucl. Instr. and Meth.*, A 522:294, 2004.

[47] K. Unser. *IEEE Trans. on Nucl. Sci.*, NS 28 3:2344, 1981.

[48] A. V. Glamazdin et al. Electron beam moeller polarimeter at jlab hall a. *Fizika*, B8:91–95, 1999.

[49] Thad G. Walker and William Happer. *Rev. Mod. Phys.*, 69:629, 1997.

[50] M. A. Bouchiat, T. R. Carver, and C. M. Varnum. *Phys. Rev. Lett.*, 5:373, 1960.

[51] S. Kadlecek, L.W. Anderson, and T. Walker. *Nucl. Inst. and Meth.*, A 402:208, 1998.

[52] Earl Babcock, Ian Nelson, Steve Kadlecek, Bastiaan Driehuys, L. W. Anderson, F. W. Hersman, and Thad G. Walker. Hybrid spin-exchange optical pumping of ^3he. *Phys. Rev. Lett.*, 91(12):123003, Sep 2003.

[53] A. Abragam. *Principles of Nuclear Magnetism*. Oxford University Press, Amen House, London, 1961.

[54] M. V. Romalis and G. D. Cates. *Phys. Rev.*, A58:3004–3011, 1998.

[55] A. S. Barton, N. R. Newbury, G. D. Cates, B. Driehuys, H. Middleton, and B. Saam. Self-calibrating measurement of polarization-dependent frequency shifts from rb$-^3$he collisions. *Phys. Rev. A*, 49(4):2766–2770, Apr 1994.

[56] A. Kolarkar. Private communication.

[57] A. Kelleher et al. Private communication, July 2007.

[58] B. Wojtsekhowski et al. Holding field directions for the polarized target in gen-experiment. 2008. Technical notes, to be written.

[59] J. Miller. Private communication.

[60] A. Shahinyan. Private communication.

[61] A. Gavalya. Private communication.

[62] Bigbite is reborn. *Jefferson Lab OnTarget*, August 2006.

[63] Hall a status report 2007. January 2008.

[64] M. Kubantsev, V Verebrioussov, and B. Wojtsekhowski. Monte-carlo of shower electron identifier for gen experiment. April 2003.

[65] Coda homepage. `http://coda.jlab.org/`.

[66] I. Rachek. Private communication.

[67] Cern root homepage. `http://root.cern.ch`.

[68] The hall a root/analyzer. `http://hallaweb.jlab.org/root/index.html`.

[69] B. Craver. Beam position calibration for gen. November 2007. `http://www.jlab.org/~bcraver/docs/pdf/beam_cal.pdf`.

[70] J. Singh et al. Private communication, December 2006.

[71] T. Ngo. Neutron arm study and calibration for the gen experiment at thomas jefferson national laboratory. Master's thesis, California State University, Los Angeles, July 2007.

[72] E. Chudakov. Gen geometry and surveys. August 2006. `http://hallaweb.jlab.org/experiment/E02-013/surveys.html`.

[73] M. Steenbakkers. *Quasi-free π^0 and π^- electroproduction on ^{4}He in the Δ-resonance region*. PhD thesis, Vrije Universiteit Amsterdam, 2004.

[74] W. M. Yao et al. Review of Particle Physics. *Journal of Physics G*, 33:1+, 2006. `http://pdg.lbl.gov`.

[75] J. Schwinger. Quantum electrodynamics. iii. the electromagnetic properties of the electronradiative corrections to scattering. *Physical Review*, 76:790–817, 1949.

[76] Yung-Su Tsai. Radiative corrections to electron-proton scattering. *Phys. Rev.*, 122:1898, 1961.

[77] D.R. Yennie and H. Suura. *Phys. Rev.*, 105:1378, 1957.

[78] J. Friedrich. Radiation tail and radiative corrections for elastic electron scattering. *Nucl. Inst. and Meth.*, 129:505, 1975.

[79] Maid photo- and electroproduction of pions, etas and kaons on the nucleon. `http://www.kph.uni-mainz.de/MAID/`.

[80] R. Schiavilla. Private communication.

[81] A. Kelleher. Private communication.

[82] M. Sargsian. Selected topics in high energy semi-exclusive electro-nuclear reactions. *International Journal of Modern Physics E*, 10:405, 2001.

[83] M. Sargsian. Private communication.

[84] G.B. Franklin. Gen asymmetry corrections for finite angular acceptance. Nov. 2006.

[85] Minuit. `www.cern.ch/minuit`.